



UNIVERSITY OF LEEDS

**Relaxor-PbTiO₃ single crystals and polycrystals:
processing, growth and characterisation**

Laura Andreea Stoica

Submitted in accordance with the requirements for the degree of
Doctor of Philosophy

The University of Leeds

School of Chemical and Process Engineering

Faculty of Engineering

September 2016

The candidate confirms that the work submitted is her own and that appropriate credit has been given where reference has been made to the work of others.

This copy has been supplied on the understanding that it is copyright material and that no quotation from the thesis may be published without proper acknowledgement.

©2016 The University of Leeds and Laura Andreea Stoica

The right of Laura Andreea Stoica to be identified as Author of this work has been asserted by her in accordance with the Copyright, Designs and Patents Act 1988.

"If things were easy to find, they wouldn't be worth finding."

Extremely Loud & Incredibly Close (2011)

Abstract

Acoustic transducers operate using polycrystalline lead zirconate titanate (PZT) since the 1950s'. Recently, relaxor-lead titanate (relaxor-PT) single crystals have been developed and exhibit up to 650% higher piezoelectric charge coefficient and up to 50% higher electromechanical coupling factor, compared with PZT. Transducers built with relaxor-PT crystals show increased bandwidth, lower power consumption and increased sensitivity. Despite the significant advantages over PZT, a growth method for relaxor-PT single crystals that is both economical and able to produce homogeneous, highly dense crystals is yet to be found. Furthermore, one of the most important relaxor-PT solid solution is Mn modified $\text{Pb}(\text{In}_{1/2}\text{Nb}_{1/2})\text{O}_3\text{-Pb}(\text{Mg}_{1/3}\text{Nb}_{2/3})\text{O}_3\text{-PbTiO}_3$ due to its thermal stability and low electrical and mechanical losses compared with other relaxor-PT solid solutions. However, the behaviour of Mn in this compound is not fully understood and control of properties, such as the mechanical quality factor, is difficult. The aim of this study was to compare Bridgman and Solid State techniques for growth of single crystalline $\text{Pb}(\text{In}_{1/2}\text{Nb}_{1/2})\text{O}_3\text{-Pb}(\text{Mg}_{1/3}\text{Nb}_{2/3})\text{O}_3\text{-PbTiO}_3$. Subsequent to this, several Mn modified compositions were designed and investigated to determine the mechanisms by which mechanical and electrical losses are lowered upon Mn incorporation. Bridgman experiments have shown that a 20 mm \varnothing x 60 mm length and highly dense single crystal can be obtained, with (011) the natural growth direction. Seeded Bridgman was also investigated as a method of controlling the orientation of the grown crystal, but was proven challenging due to nucleation of several crystallites. Solid State experiments, which involve attaching a single crystal seed to a polycrystalline matrix and promoting boundary migration of the seed into the matrix, showed that crystal growth is encouraged when a Pb-based interlayer exists in between the seed and matrix. An epitaxially deposited, uniform thin film as interlayer was found particularly beneficial. More research is needed to determine conditions for growth of a single crystal of useful size by Solid State. Analysis of several relaxor-PT compositions modified with the same amount of Mn revealed that alterations of the relaxor-PT formulation affects behaviour of the multi-valent Mn which in turn influences electromechanical properties. These findings are of use to the industrial and scientific communities. Crystal growth results indicate Bridgman as suitable method if growth of crystals is desired in a short time frame, whilst Solid State results provide the basis of a new approach for growing relaxor-PT crystals. The study of Mn modified compositions provides new insights into the role of Mn substitution for manipulating the electrical and mechanical properties of complex, relaxor-PT solid solutions.

Acknowledgements

First and foremost, I would like to thank my supervisor, Professor Andrew Bell, for his outstanding guidance, the freedom offered, his expertise, constant advice and for teaching me to always question and critically evaluate literature - *Thanks, Andy. It has been an honour and I hope this has been only the start of an exciting collaboration.*

I acknowledge EPSRC and Thales who provided funding for this work. Special thanks to Alan Elliott for constant support, transducer design lessons, Royal Navy stories and for encouraging my career as a researcher. I would like to express my gratitude to Dr Faye Esat and Dr Tim Comyn for their support and advice particularly in the early stages of the PhD. I am greatly indebted to Rob Simpson for his invaluable technical support (including platinum crucible cutting skills and patience with fixing thermocouples). I greatly appreciate the support with experiments of Dr Jim Bennett, Dr Tim Stevenson, Diane Cochrane and the staff in LEMAS, particularly Dr Richard Walshaw and Stuart Micklethwaite for help with electron microscopy.

Greatly appreciated is the support from Thales UK and Australia with my industrial placement, which was a great experience and opportunity to explore wonderful Australia. Special thanks to Ian Bedwell for invaluable technical advice, encouragement and SMH comics not only during the placement, but constantly throughout my PhD. I am thankful to Peter Bryant for extremely useful ceramic manufacturing conversations and for providing support in the laboratory (especially when my "Leeds recipe" turned out not to work in Australia). I also greatly appreciate the support provided by Tim Cain, Valsala Kurusingal and everyone at Thales Australia who made my placement a wonderful one. I would also like to acknowledge The Australian Synchrotron, Dr Peter Kappen, Dr Bernt Johannessen and Dr Tamsyn Ross for XAS measurements. At The University of New South Wales I want to thank Professor Nagarajan Valanoor for support during my visit and Peggy Zhang who helped with PFM measurements.

Thanks are also due to "the 2.50ers": Rob, Faye, Jim, Leo, Stephen, Anton, Sam, Tom for the great atmosphere in the office and for putting up with my manganese passion as well as to all my colleagues in IMR for making the overall experience unforgettable. Special thanks to Tom for proofreading and to Julian for his feedback on my drafts.

I would also like to thank my friends from all corners of the world, particularly in Romania and Leeds.

Finally I would like to thank my family, particularly my parents for being incredibly supportive - I could not have done it without you.

Contents

Publication statement	i
Abstract	iii
Acknowledgements	iv
Contents	vi
List of Figures	xii
List of Tables	xxi
Abbreviations	xxii
Symbols	xxiv
1 Introduction	1
1.1 Background and motivation	1
1.2 Research subject	3
1.3 Aims and objectives	5
1.4 Thesis organisation	5
2 Introduction to Piezoelectricity and Piezoelectric Materials	7
2.1 Introduction	7
2.2 Crystallography of piezoelectric materials	9
2.2.1 Crystal systems, point groups and space groups	9
2.2.2 The perovskite structure	12
2.2.3 Definition of polycrystalline and single crystals	14
2.2.4 Operation modes - engineering notation	15
2.3 Properties of piezoelectric materials	17
2.3.1 Dielectric properties	17
2.3.2 Piezoelectric properties	19

2.3.2.1	Electrostriction	19
2.3.2.2	Piezoelectricity and piezoelectric coefficients	20
2.3.2.3	Electromechanical coupling factor	22
2.3.2.4	Mechanical Quality Factor	23
2.3.3	Ferroelectric properties	24
2.3.3.1	Hysteresis loop and Curie point	24
2.3.3.2	Phase Transitions	25
2.3.3.3	Morphotropic Phase Boundary	26
2.3.3.4	Domains	29
2.3.4	Relaxor ferroelectric properties	30
2.4	Contributions to piezoelectricity	32
2.5	Piezoelectric materials	33
2.5.1	Lead zirconate titanate	33
2.5.2	Relaxor-PT single crystals	34
2.5.2.1	Generation I	35
2.5.2.2	Generation II	38
2.5.2.3	Generation III	39
2.6	Applications	39
2.6.1	Medical ultrasound transducer	40
2.6.2	Underwater projector	40
2.6.3	Underwater receiver (hydrophone)	41
2.6.4	Other applications	41
3	Introduction to Single Crystal Growth	42
3.1	Introduction	42
3.2	Generic single crystal growth methods	43
3.3	Relaxor-PT single crystal growth	44
3.3.1	Solution	45
3.3.1.1	Flux	45
3.3.1.2	Top-seeded solution growth	48
3.3.1.3	Flux Bridgman	50
3.3.2	Modified Bridgman (Bridgman-Stockbarger, Vertical Bridgman or Bridgman)	50
3.3.3	Solid State Conversion Growth	54
3.3.3.1	Grain growth in polycrystalline systems	56
3.3.3.2	Single crystal growth studies	58
	Liquid film approach	58
	Grain size in the polycrystalline matrix	58
	Seed orientation	59
	Discussion	59
3.4	Conclusion	59
4	Powder Synthesis	61
4.1	Introduction and Background	61

4.1.1	Introduction	61
4.1.2	Background	62
4.1.2.1	Pre-synthesis steps	62
4.1.2.2	Choice of composition	63
4.2	Experimental Procedure	64
4.2.1	Drying and weighing	65
4.2.2	Attrition milling (1)	65
4.2.3	Drying	65
4.2.4	Calcination	66
4.2.5	Attrition milling (2)	66
4.2.6	Binder addition	66
4.2.7	Pressing	66
4.2.8	Sintering	67
4.3	Characterisation of powder prepared	67
4.3.1	X-ray Diffraction	67
4.3.2	Scanning Electron Microscopy	69
4.4	Summary	70
5	Bridgman Grown Single Crystals	71
	Abstract	71
5.1	Introduction	72
5.2	Experimental Procedures	72
5.2.1	Growth Preparation	72
5.2.1.1	Growth Equipment	73
5.2.1.2	Choice of Crucible	73
5.2.1.3	Thermal Profile of the Furnace	74
5.2.1.4	Material Loading	76
5.2.1.5	Sealing	77
5.2.1.6	Crucible loading	77
5.2.2	Growth Parameters	79
5.2.3	Characterisation	81
5.2.3.1	Polishing	81
5.2.3.2	X-Ray Powder Diffraction	83
5.2.3.3	X-Ray Pole Figures	83
5.2.3.4	Optical Microscope	83
5.2.3.5	Electron Back-Scatter Diffraction (EBSD)	84
5.2.3.6	Energy Dispersive X-Ray Diffraction (EDX)	84
5.2.3.7	Piezoresponse Force Microscopy	85
5.2.3.8	Permittivity versus temperature	85
5.2.3.9	Polarisation versus electric field	85
5.3	Results and Discussion	85
5.3.1	Unseeded Growth B1	85
5.3.1.1	Energy Dispersive X-Ray Spectroscopy	87
5.3.1.2	Pole Figures	87

5.3.1.3	X-Ray Diffraction	88
5.3.1.4	Piezoresponse Force Microscopy (PFM)	89
5.3.1.5	Impedance Spectroscopy	92
5.3.1.6	Permittivity versus temperature	93
5.3.1.7	Polarisation and Strain versus Field	94
5.3.1.8	Preparation for next run	94
5.3.2	Seeded Growth B2	97
5.3.2.1	Growth direction - Pole figures	97
5.3.2.2	Electron Back Scatter Diffraction	98
5.3.2.3	Energy Dispersive X-ray Spectroscopy	99
5.3.2.4	Preparation for next run	101
5.3.3	Seeded Growth B3	102
5.3.3.1	Growth direction - Pole figures	102
5.3.3.2	Optical micrographs	103
5.3.3.3	Preparation for next run	104
5.3.4	Seeded Growth B4	105
5.3.4.1	Optical micrographs	105
5.3.5	Discussion	107
5.4	Summary and Conclusions	109
5.5	Limitations and Future Trends	111
5.5.1	Bridgman method variations	112
5.5.1.1	Continuous Feed Growth	112
5.5.1.2	Multiround Growth	113
5.5.1.3	Double Melt Approach	114
5.5.1.4	Vertical Gradient Freeze	114
5.5.1.5	Float Zone Technique	115
5.5.2	Non-melt Crystal Growth Techniques	115
5.5.2.1	Non-melt Bridgman	115
5.5.2.2	Solid State Conversion Growth	116
6	Solid State Conversion Growth	117
	Abstract	117
6.1	Introduction	118
6.2	Experimental procedure	119
6.2.1	Sample preparation for grain growth investigations	119
6.2.2	Crystal growth experiments	120
6.3	Results and discussion	122
6.3.1	Polycrystalline precursor processing	122
6.3.1.1	Particle size of synthesized powder	122
6.3.1.2	Phase analysis by X-ray diffraction	123
6.3.1.3	Density and weight loss	125
6.3.1.4	Grain size analysis	128
6.3.2	Crystal growth experiments	132
6.3.2.1	Growth from a PMN-PT nucleus grain	132

6.3.2.2	Growth from a BT nucleus grain	133
6.4	Summary and conclusions	135
6.5	Limitations and future trends	136
7	Advances in Understanding Mn behaviour in PIN-PMN-PT	138
	Abstract	138
7.1	Introduction and Background	139
7.1.1	Introduction	139
7.1.2	Background	140
7.1.2.1	Mechanical Quality Factor	140
7.1.2.2	Contribution to losses	143
7.1.2.3	Internal Bias Field	144
7.1.2.4	Non-stoichiometry	144
	Mn and Nb simultaneous doping in PZT	146
	Mn, Nb and Ni simultaneous doping in PT	146
	Mn \ Mg and F simultaneous doping in PZT	147
	Processing atmosphere and temperature	147
7.2	Experimental Procedures	148
7.2.1	Investigated Compositions	148
7.2.2	Sample Preparation	150
7.2.3	Characterisation Techniques	152
7.2.3.1	Investigations during sample preparation	152
7.2.3.2	X-ray Absorption Spectroscopy	152
7.2.3.3	Polarisation versus Electric Field	152
7.2.3.4	Impedance Spectroscopy	153
7.2.3.5	Permittivity versus Temperature	154
7.2.3.6	Mechanical quality factor	154
7.3	Results and Discussion	154
7.3.1	Investigations during sample preparation	154
7.3.2	Mn Valence State	159
7.3.3	Permittivity versus Electric Field	161
7.3.4	Polarisation versus Electric Field	164
7.3.5	Impedance Spectroscopy	165
7.3.5.1	Complex Impedance Spectrum	165
7.3.5.2	Relaxation times	173
7.3.5.3	Origin of the Relaxation Process	177
7.3.5.4	Conductivity	182
	Oxygen Vacancies Formation	182
	Polaron Hopping	183
	Ionic Conduction	185
	Defect Dipole Formation	185
7.3.6	Dielectric measurements versus temperature	187
7.3.7	Mechanical Quality Factor	191
7.3.8	Property Comparison	191

7.4	Summary and Conclusions	193
7.5	Future Work	195
	Summary and Conclusions	197
	Further work	199
	A Pole figures technique	201
	B Design of Platinum Crucibles for Seeded Growth	204
	C Archimedes' principle for determining sample density	207
	D Conferences and other activities	209
	Bibliography	211

List of Figures

1.1	Piezoelectric charge coefficient d_{33} comparison between various compositions of polycrystalline PZT and various compositions of relaxor-PT single crystals. Data from [6].	2
1.2	Electromechanical coupling factor k_{33} comparison between various compositions of polycrystalline PZT and various compositions of relaxor-PT single crystals. Data from [6].	2
1.3	World wide principal companies involved with relaxor-PT single crystal manufacturing: A - CTS Advanced (Bridgman), B - TRS Technologies (Bridgman), C - Microfine (Solution), D - Sinoceramics (Bridgman), E - iBule (Bridgman), Ceracomp (Solid State Conversion Growth), F - JFE Mineral (Bridgman). Blank world map from [7].	4
1.4	Thesis workflow	6
2.1	Development of piezoelectric materials since their discovery. The abbreviations represent the following compounds: KDP: KH_2PO_4 ; ADP: $(\text{NH}_4)_2\text{H}_2\text{PO}_4$; BT: BaTiO_3 ; LN: LiNbO_3 ; PZT: $\text{Pb}(\text{Zr},\text{Ti})\text{O}_3$; PN: PbNb_2O_6 ; PMN: $\text{Pb}(\text{Mg}_{1/3}\text{Nb}_{2/3})\text{O}_3$; PMN-PT: $\text{Pb}(\text{Mg}_{1/3}\text{Nb}_{2/3})\text{O}_3\text{-PbTiO}_3$. The figure highlights two key points in the development of piezoelectric materials - the perovskite structure and the Morphotropic Phase Boundary concept in PZT [6].	8
2.2	The 14 Bravais lattices [12]	10
2.3	Schematic diagram showing the link between crystallographic structure and piezoelectric, pyroelectric and ferroelectric properties. Adapted from [10, 12, 13].	11
2.4	PbTiO_3 unit cell as example of perovskite structure ABO_3 . The octahedral site with the central Ti atom is highlighted. Structure generated with CrystalMaker software.	13
2.5	Octahedral sites with the A ion sitting at the centre of the cuboctahedron within a perovskite structure. From [12].	13
2.6	Graphic representation of a polycrystalline and a single crystal material (top, not to scale) and optical micrograph showing polished surfaces of Mn-modified PIN-PMN-PT in a polycrystalline form and a single crystalline form (bottom). The materials were prepared within this work.	15
2.7	Deformation directions of piezoelectric materials. The poling direction is the 3 direction. Adapted from [10].	16
2.8	Various polarisation mechanisms [13].	18

2.9	Dependency of permittivity (real and imaginary) on frequency and associated polarisation mechanisms which lead to dielectric dispersion. Space charge and dipolar mechanisms depend strongly on temperature, whilst ionic and atomic are temperature independent [13].	19
2.10	Power vs frequency plot showing frequencies at half power [22].	23
2.11	Typical hysteresis loop in a ferroelectric material, D - displacement, E - electric field, P_{SAT} - saturation polarisation, P_S - spontaneous polarisation, P_R - remanent polarisation, E_c - coercive field [9].	24
2.12	Phase transformation of $BaTiO_3$ from the high symmetry cubic phase to lower symmetry phases tetragonal, orthorhombic and rhombohedral upon cooling from $T_C=130^\circ C$ to $-90^\circ C$. The direction of the dipole is highlighted for the non-cubic structures. [13]	26
2.13	Initial phase diagrams of PZT, PZN-PT and PMN-PT, C - cubic, R - rhombohedral, T - tetragonal [24]	27
2.14	Updated phase diagrams. X represents the concentration of PT. In PZT, a monoclinic phase is revealed in between rhombohedral (R) and tetragonal (T) phase. In addition the R phase is found to exist with different space groups at lower and higher temperatures. In PZN-PT an orthorhombic (O) has been identified in between R and T . In PMN-PT a type of monoclinic phase is present between R and T [24].	28
2.15	Phase diagram of PIN-PMN-PT at room temperature [25].	28
2.16	Updated PIN-PMN-PT phase diagram as a function of temperature [26]	29
2.17	Domain engineered single crystals [6]	30
2.18	Dielectric response shown over a range of frequencies $10-10^7$ Hz of the relaxor PMN. The arrows highlight the frequency dispersion of the response, adapted from [30]	31
2.19	Strain levels achieved in single crystals compared with polycrystalline PMN-PT, soft PZT (5H) and hard PZT (8)[38].	36
2.20	Piezoelectric charge coefficient d_{33} (top) and electromechanical coupling factor k_{33} (bottom) as a function of transition temperature for conventional polycrystalline material and single crystals [3].	37
2.21	Curie point for ABO_3 - $PbTiO_3$ solid solutions with MPB compositions as a function of the ABO_3 tolerance factor [39].	39
3.1	Schematic of the experimental design for crystal growth from flux – generally, a box resistive heating furnace is used; this schematic, however, also shows a system for oxygen gas flow which offers the advantage of local cooling and therefore, better nucleation control [2]	46
3.2	Experimental design of the Top Cooled Solution Growth; similarly with the conventional flux method, a Pt crucible is used for the growth inside a box furnace; the difference is the use of a cooling system triggered by a Pt wire; nucleation occurs around the wire [55]	47

3.3	Typical single crystals grown by flux technique – in addition to a main crystal, other, undesirable crystals are also obtained such as satellite crystals which are growing at the periphery of the main crystal, parasitic crystals which are growing on the surface of the main crystal, side-wall nucleations and also crystals of pyrochlore [3]	47
3.4	A flux-grown PIN-PMN-PT crystal; for the growth, 50% precalcined 16PIN-51PMN-33PT has been dry mixed with 40% PbO and 10% B ₂ O ₃ (mol%); following 2 pre-melts at 1000°C for 1 h, the mixture has been heated at 1230°C, equilibrated for 5 h and allowed to cool with a rate of 1.2°C/h down to 850°C and then 100°C/h to room temperature; the main crystal has been removed from the crucible in 50% strength boiling acetic acid for 24 h [3]	48
3.5	Experimental set-up for TSSG; the design is very similar to that for conventional flux growth, however, a seed single crystal is used to induce nucleation within the solution, which is attached to a Pt wire, in turn, supported by an alumina rod [3]	49
3.6	19PIN-46PMN-35PT grown by TSSG by Li et al. [58].	49
3.7	Graphic representation of the Bridgman technique: Bridgman furnace (left) and associated thermal profile (right). A crucible containing the material to be grown is placed into the upper (hot) zone of a furnace and slowly lowered through a thermal gradient towards the second (cold) zone of the furnace so that nucleation is induced and the crystal grows from one end to another.	51
3.8	0.5mol% Mn-doped 15PIN-55PMN-30PT Bridgman grown single crystal. From [63].	51
3.9	25PIN-44PMN-31PT single crystal, 55 mm diameter and 100 mm length grown from a (110) oriented seed. From [65].	52
3.10	Compositional variation of the chemical constituents along a PMN-35PT single crystal boule. Ti concentration is seen to increase along the boule, particularly towards the end. From [67].	53
3.11	Variation of the electromechanical coupling factor k_{33} versus Curie point T_C measured along a PMN-31PT single crystal boule. k_{33} increases from one end of the boule to the other following the increase in Ti content due to segregation. From [3].	53
3.12	SSCG concept proved in BaTiO ₃ - electron micrograph (A) and Electron Back-Scatter Diffraction image (B). The polycrystalline BaTiO ₃ sample has been sintered at 1290°C for 2 h and a BaTiO ₃ seed has been diffusion bonded via heat treatment at 1200°C for 2 h with a 1 kg weight. Crystal growth was promoted at 1350°C. The experiment was conducted as trial crystal growth within this work to prove the SSCG concept and is not presented in future sections.	55
3.13	Two dimensional representation of grains with different sizes in a polycrystalline matrix. Direction of growth upon heat treatment depends on the curvature of grain boundaries and it is marked by the arrows. From [72].	56

3.14	Schematic representation of size distributions for Normal growth (top) and Discontinuous growth (bottom). From [72].	57
4.1	Phase diagram of PIN-PMN-PT. The purple line represents the boundary between the rhombohedral and tetragonal crystal structures, whilst the red dot marks the composition studied within this work	64
4.2	Flow chart of the processing path for material preparation. The purple boxes indicate processing experimental methods, whilst the brown boxes indicate characterisation techniques.	65
4.3	X-ray diffraction patterns of calcined compounds.	68
4.4	SEM micrographs for calcined powders - InNbO_4 (A), MgNb_2O_6 (B), PIN-PMN-PT (C) and the fracture surface of a sintered PIN-PMN-PT pellet (D)	69
5.1	Crystal growth furnace at The University of Leeds. The five zone tube furnace is located on the right hand side, whilst the controls for translation/rotation movement together with temperature controls for each of the five zones of the furnace are located on the left hand side.	73
5.2	Crucible design for unseeded crystal growth - orthographic projection (left) and trimetric projection (right). Courtesy of Rob Simpson.	74
5.3	Crucible design for seeded crystal growth - orthographic projection (left) and trimetric projection (right). Courtesy of Rob Simpson.	74
5.4	Thermal profile measured in between the hot and cold zones (1355°C and 1150°C) using a conical bottom platinum crucible. The red cross marks the position of the thermocouple tip used for mapping.	75
5.5	Thermal profile measured in between the hot and cold zones (1355°C and 1150°C) using a seed pocket platinum crucible. The red and black crosses mark the position of two thermocouples used during mapping.	76
5.6	Alumina support system during growth for a self-seed crucible type. The gap in between the platinum crucible and the outer alumina crucible has been filled with yttria stabilised zirconia media. Courtesy of Rob Simpson.	78
5.7	Alumina support system during growth for a seed pocket crucible type. The gap in between the platinum crucible and the outer alumina crucible has been filled with yttria stabilised zirconia media. The seed pocket was surrounded only by the alumina tube. Courtesy of Rob Simpson.	78
5.8	Liquid solid interface shapes within a stationary rod for materials with low ($H=0.4$), medium ($H=1$) and high ($H=2$) Biot number and different values of the temperatures within the hot/cold zones represented by Φ , from [103].	80
5.9	Simulated interaction volume for the studied samples, accelerating voltage 20 kV, material's density 8.2 g/cm^2 , Casino software. Courtesy of Stuart Micklethwaite.	84
5.10	Crystal grown during the first run, i.e. unseeded growth B1	86

5.11	Crystal grown during the first run, i.e. unseeded growth as seen under a flashlight	86
5.12	Electron image of a single crystal plate (top) and elemental maps of region highlighted in yellow for Mg, In, Ti, O, Nb and Pb	87
5.13	Pole figures acquired for (001), (011) and (111) crystallographic planes (left to right). When the distribution of (011) plane was analysed (centre figure), a centre pole is observed which is associated with a preferred (011) growth direction of the crystal.	88
5.14	XRD pattern obtained from a single crystal sample crushed into powder. A pure perovskite phase has been obtained with no secondary phases or other impurities.	89
5.15	Unit cell within the investigated sample rotated such that the plane (011) is parallel to the surface. The arrows mark the eight directions possible for the spontaneous polarisation within the rhombohedral structure.	90
5.16	Piezoresponse Force Microscopy images on a (011) oriented sample extracted from the bottom region of the crystal.	91
5.17	Impedance Spectra at various temperatures measured on one sample. The full semicircles obtained at higher temperatures are associated with a single response from the bulk of the sample.	93
5.18	Permittivity versus temperature analysis implying a relaxor behavior due to the frequency dispersion.	94
5.19	Hysteresis loop of a 5x5 mm ² single crystal sample	96
5.20	Strain loop of a 5x5 mm ² single crystal sample	96
5.21	B2 (001) seeded crystal	97
5.22	Pole figures obtained from a sample cut halfway through the boule so that the direction of growth can be analysed. The figure shows distribution of the plane (001) (left), (011) (centre) and (111) (right)	98
5.23	Image of the entire single crystal boule grown (left), cross sectional electron micrograph of the seed pocket (middle, courtesy of Buehler customer service laboratory) and three different areas investigated with Electron Back scatter Diffraction (right). The EBSD figures are mirror images of the regions highlighted in red on the electron micrograph and reveal regions with different crystallographic orientations (different colours) associated with grains.	99
5.24	Energy Dispersive X-ray Spectroscopy performed at the interface seed - crystallised compound. The top-left image represents the electron micrograph revealing the seed in the bottom half of the image and the crystallised grains in the upper half of the image. The following images are chemical maps showing the distribution of each element in the compound for the same region as the electron micrograph. All chemical elements are homogeneously distributed.	100

5.25	Influence of the moving rate on the liquid-solid interface shape and position. Pe is the ratio of heat carried by movement to heat conduction and is therefore associated with the moving speed. $Pe=0$ for a stationary ampoule and increases with increasing moving rate. The interface becomes increasingly concave with Pe increasing from 0.1 to 1 and then 2, adapted from [103].	101
5.26	Single crystal boule grown during the third run, B3, as it is being removed from the platinum crucible	102
5.27	Pole figures obtained from a sample cut halfway through the seed pocket to investigate whether the crystal grew from the seed or nucleation has occurred as previously. The presence of multiple grains is confirmed by each pole figure, (001) (left) , (011) (centre) and (111) (right).	103
5.28	Optical micrograph of the B3 grown crystal - seed pocket region (left) and zoom in two regions (right). The scale bar of the left image is 5 mm and of the right 400 μm . Some grains have been numbered on the top right image to easily distinguish them.	104
5.29	Single crystal grown during the fourth experimental run, B4 during removal from the platinum crucible	105
5.30	Optical micrograph of the crystal grown within B4 experiment - seed pocket region (left) and zoom in two regions (right). The scale bar is 4 mm for the left image and 400 μm for the right images.	106
5.31	Progression of the thermal profile inside the crucible, as it moves from the hot towards the cold zone. The length of the crucible in this study was 11 times the diameter. From [106]	109
5.32	At constant lowering rate, the crystal growth speed accelerates if the diameter of the seed pocket is much smaller than the body of the crucible (left). The growth speeds remains constant for smaller differences in diameter. [3]	109
5.33	Summary of the Bridgman runs presenting the key parameters, as well as the result (in green) and the action taken for the subsequent run (red)	111
5.34	Ti concentration along a PMNT crystal obtained by Continuous Feed Growth (CFG) and a PMNT crystal obtained by Conventional Bridgman Growth (CBG). Ti content is normalised at 5% of the crystal position. CFG grown crystal shows a more uniform distribution of the Ti content, with variation controlled at 6% compared with 20% within the CBG crystal. From [108].	113
5.35	PbTiO_3 concentration along a crystal grown by the Multiround Growth approach. Section I and II are grown within the first run, whilst II and III are grown in the second run. Section II is remelted in the second run so that the first crystal acts as seed for the second. The grey area represents the Morphotropic Phase Boundary. Therefore, the graph shows that most of the crystal maintains a composition within the MPB. From [66].	114
6.1	Binder burnout profile	119

6.2	Particle size distribution of PIN-PMN-PT powder by number and by volume	122
6.3	X-ray diffraction patterns recorded on all compositions prepared, sintered at different temperatures	124
6.4	Density of samples sintered at different temperatures for 24 h, without PbO excess (top) and with PbO excess (bottom)	126
6.5	Weight loss of samples sintered at different temperatures for 24 h, without PbO excess (top) and with PbO excess (bottom)	127
6.6	Optical micrographs of polished and chemically etched samples with no excess PbO, sintered at 1150 and 1200°C. Samples sintered at 1250°C proved difficult to etch and are not shown.	129
6.7	Optical micrographs of polished and chemically etched samples with PbO excess, sintered at 1150, 1200 and 1250°C.	130
6.8	Average grain size for samples with no excess PbO (A) and with excess PbO (B)	131
6.9	Growth from a PMN-PT seed (left) and growth from a PMN-PT seed with a Pb(II) 2-ethylhexanoate-based interlayer (right)	132
6.10	X-ray diffraction pattern of the BT seed and the subsequent thin film deposited	134
6.11	The surface of the deposited thin film imaged by Atomic Force Microscopy	134
6.12	Growth from a BT seed (left) and growth from a BT seed with a PIN-PMN-PT thin film deposited by Pulsed Laser Deposition (right)	135
7.1	Mn valence state scenarios in PIN-PMN-PT. The possibilities of valence change in the case of Nb, Ti and Pb have been ignored as the number of scenarios is too large.	145
7.2	Binder burnout profile measured during the process	151
7.3	Sintering profile measured during the process	151
7.4	Method for calculation of real permittivity from PE loops	153
7.5	Thermogravimetric analysis of the powder containing binder	156
7.6	X-ray patterns for calcined powders.	156
7.7	Optical micrographs of calcined powders. The scale bar is 400 μ m.	157
7.8	Optical Micrographs of sintered samples. The images have been taken on the unpolished, unetched surface. The scale bar is 400 μ m.	158
7.9	Density of samples obtained via Archimedes method	159
7.10	X-Ray Absorption Spectrum of Mn-modified samples investigated in this study (The samples In, Mg, Ti, Nb1, Nb2, All are here labelled LC2, LC3, LC4, LC5, LC6, LC7). The spectrum from Mn modified single crystal B4 (B4 XTAL) is also presented. PC samples are not investigated here. Measurements conducted at The Australian Synchrotron.	160
7.11	Valence state as a function of absorption edge energy for commercial oxides, B4 single crystal (B4 XTAL) and sample analysed within this study (The samples In, Mg, Ti, Nb1, Nb2, All are here labelled LC2, LC3, LC4, LC5, LC6, LC7). PC samples are not investigated here. Data provided by The Australian Synchrotron.	160

7.12	Real part of relative permittivity as a function of electric field	162
7.13	Real part of permittivity versus electric field. The scale is different for Sample 0 plot compared to the plots for the Mn-modified samples. . .	163
7.14	Polarisation versus electric field loops	164
7.15	Internal bias field (absolute values) calculated from hysteresis loops. .	165
7.16	Nyquist plots. The caption under each figure represents the name of the sample as well as the temperature range of measured data in °C . .	167
7.17	Nyquist plot for all samples at 400°C	168
7.18	Imaginary impedance as a function of frequency at 400°C	168
7.19	Imaginary part of the impedance versus frequency plots	169
7.20	Nyquist plots fitted using ModuLab XM Software	170
7.21	Evolution of parameter n with increasing temperature shown separately for each sample	172
7.22	Relaxation times obtained with $\tau = \frac{1}{f_0}$, where f_0 is the frequency of maximum $-Z''$	175
7.23	Relaxation times obtained with $\tau = RQ$	176
7.24	Activation energies for relaxation plotted for $\tau = \frac{1}{f_0}$ and $\tau = RQ$	177
7.25	Modulus versus frequency plots	179
7.26	Imaginary part of the modulus for all samples at 300°C	180
7.27	Imaginary part of the modulus for all samples at 400°C	181
7.28	Conductivity versus the inverse of temperature and their and their calculated activation energies	184
7.29	Relative permittivity measured in the frequency range 0.1 - 100 kHz .	188
7.30	Dissipation factor measured in the frequency range 0.1 - 100 kHz . . .	189
7.31	Relative permittivity measured at 100 kHz for all samples	190
7.32	Dissipation factor measured at 100 kHz for all samples	190
7.33	Mechanical quality factor	191
7.34	Normalised property values for investigated samples. The frequency of measurement for $\tan\delta_e$ was 100 kHz. The permittivity has been determined from polarisation - electric field loop using a triangular signal at 1 kHz (see Section 7.2.3.3)	192
7.35	Properties plotted against mechanical quality factor	193
A.1	Schultz geometry used to investigate orientation of single crystals or the degree of preferred orientation in textured crystalline samples. The X-ray beam is fixed at θ angle (red), whilst the sample is rotated 360 about the normal to the sample surface (β) and tilted 90 from the normal to the sample surface (α). Adapted from [104].	202
A.2	Representation of the sample movement by varying α and β angles during investigation. The red arrows represent the fixed X-ray beam. The variation of diffracted X-rays intensity is represented on a stereographic projection [104].	202
A.3	The α and β angles on a pole figure [104].	203
A.4	Typical pole figures of a cubic single crystal sample for the (111), (100) and (110) crystallographic planes [104].	203

C.1 Schematic diagram of the set-up used to determine the weight of samples immersed in water to subsequently determine the density using Archimedes' principle	208
---------------------------------------------------------------------------------------------------------------------------------------------------------------------------	-----

List of Tables

2.1	Symbols and their units used in piezoelectric relationships [17]	16
2.2	Conversion from engineering to tensor coefficients for engineering strain [16]	16
2.3	Symbols and their units used in piezoelectric relationships [17]	21
2.4	Typical values for various properties of soft and hard PZT. From [27].	34
3.1	Generic growth methods for single crystals	44
4.1	Dielectric, piezoelectric and ferroelectric properties of [001] poled PIN-PMN-PT grown by Bridgman with nominal compositions in the MPB area. <i>Description of symbols and abbreviations are listed in the beginning of the thesis.</i>	64
5.1	Summary of growth conditions for each of the four experiments	81
5.2	Polishing procedure for sample imaging. Advice and products from Buehler (B) and Struers (S)	82
6.1	Polishing procedure. Advice and products from Buehler.	121
7.1	Brief summary of mechanical quality factor in single domain rhombohedral 1R and tetragonal 1T single crystals, multi-domain single crystals 2R, 4R (see Section 2.3.3.4 for domain engineered single crystals) and polycrystalline materials P. In the case of single crystals where the poling direction or crystallographic phase is not specified, the domain configuration is referred to as single crystals S C only.	142
7.2	Ionic radii for elements in the perovskite structure studied within this work. A-site (Pb) ionic radii is given for a 12 coordination number, whilst B site (In, Mg, Nb, Ti, Mn) 6 coordination number [132]	146
7.3	Summary of compositions studied	149
7.4	R-CPE parameters obtained for each fitting process	171
7.5	Capacitance and associated relaxation origin, classification by Irvine, Sinclair and West [146]	180
7.6	Pseudocapacitance (F) calculated calculated using the parameters R, Q, n obtained from fitting data with R-CPE _C equivalent circuit	181
7.7	Temperature of maximum dielectric permittivity	187

Abbreviations

ABO ₃	general formula of the perovskite structure
AGG	Abnormal Grain Growth
BCSG	Bottom Cooled Solution Growth
BT	BaTiO ₃
B1, B2, B3, B4	The four Bridgman experiments conducted
C	cubic
CPE	Constant Phase Element
EBS	Electron Back-Scatter Diffraction
EDX	Energy Dispersive X-Ray Diffraction
M	monoclinic
Mn:PIN-PMN-PT	Mn modified PIN-PMN-PT
MPB	Morphotropic Phase Boundary
O	orthorhombic
PAGG	Primary Abnormal Grain Growth
PFM	Piezoresponse Force Microscopy
PIN-PMN-PT	Pb(In _{1/2} Nb _{1/2})O ₃ -Pb(Mg _{1/3} Nb _{2/3})O ₃ -PbTiO ₃ (lead indium niobate - lead magnesium niobate - lead titanate)
PMN-PT	Pb(Mg _{1/3} Nb _{2/3})O ₃ -PbTiO ₃ (lead magnesium niobate - lead titanate)
PNRs	Polar Nano Regions
PT	PbTiO ₃ (lead titanate)
PZN-PT	Pb(Zn _{1/3} Nb _{2/3})O ₃ -PbTiO ₃ (lead zinc niobate -lead titanate)
PZT	Pb(Zr _x Ti _{1-x})O ₃ (lead zirconate titanate)
R	rhombohedral
relaxor-PT	relaxor-lead titanate system

SAGG	Secondary Abnormal Grain Growth
SEM	Scanning Electron Microscopy
SONAR (also sonar)	SOund Navigation And Ranging
SSCG	Solid State Conversion Growth
T	tetragonal
TCSG	Top Cooled Solution Growth
TSSG	Top Seeded Solution Growth
XRD	X-Ray Diffraction

Symbols

B	Biot number
C	capacitance
C	Curie constant
C_0	capacitance of the sample at low frequency
d	piezoelectric charge coefficient
d_{33}	d with induced polarisation in direction 3 (parallel to the direction in which material has been poled) per unit stress applied in direction 3 OR induced strain in direction 3 per unit electric field applied in direction 3
D	dielectric displacement
e	piezoelectric coefficient (relates strain to displacement or electric field to stress)
E	electric field
E_a	activation energy
E_c	coercive field
ε (also ε^*)	permittivity (complex permittivity)
ε'	real permittivity
ε''	imaginary permittivity
ε_r	relative permittivity
ε'_r	real part of the relative permittivity
ε_0	permittivity of free space (8.85×10^{-12} F/m)
f_m	frequency of minimum impedance
f_n	frequency of maximum impedance
g	piezoelectric voltage coefficient
k_{33}	electromechanical coupling factor (subscripts as for d_{33})

M^*	complex modulus
M'	real modulus
M''	imaginary modulus
n	parameter which describes the distribution of relaxation times, $n=1$ narrow distribution, $n<1$ broader distribution
P	polarisation
P_R	remanent polarisation
P_S	spontaneous polarisation
P_{SAT}	saturated polarisation
Q	parameter which describes the Constant Phase Element
Q	electrostriction coefficient
Q_m	mechanical quality factor
R	resistance
ρ_{dc}	DC resistivity
s	compliance
s^E	compliance under constant electric field
$(s^E)'$	real compliance under constant electric field
$(s^E)''$	imaginary compliance under constant electric field
s^T	compliance under constant stress
σ	conductivity
t	tolerance factor related to the perovskite structure
T	stress
T_c	temperature in the cold zone of the Bridgman furnace
T_C	Curie point
T_{FF}	ferroelectric to ferroelectric phase transition temperature
T_h	temperature in the hot zone of the Bridgman furnace
T_i	temperature at the liquid-solid interface
T_m	temperature of maximum dielectric permittivity ($^{\circ}\text{C}$)
T_{RT}	rhombohedral to tetragonal phase transition temperature
T_0	Curie temperature
$\tan\delta_e$	dielectric loss or dissipation factor

$\tan\delta_m$	mechanical loss (inverse of Q_m)
τ	relaxation time
Φ	parameter which described the shape of the liquid-solid interface
w_m	mechanical losses
W_m	mechanical energy stored
x (also S)	strain
Z_m	value of minimum impedance
Z^*	complex impedance
Z'	real impedance
Z''	imaginary impedance

To my parents.

Chapter 1

Introduction

1.1 Background and motivation

The demonstration of piezoelectricity in certain materials at the end of the 19th century began a technological era where conversion from mechanical energy into electrical energy and/or vice-versa could be performed on demand, leading to development of a completely new range of sensor, transducer and actuator devices [1–3]. Subsequently, the field of piezoelectric materials has seen increasingly rapid advances with the most important discovery represented by the compound lead zirconate titanate (PZT) in a polycrystalline form in the 1950s'. Today PZT is still the material of choice for a broad range of applications due to its high piezoelectric response with values of the piezoelectric charge coefficient d_{33} up to 700 pC/N and the electromechanical coupling factor k_{33} up to 0.75. In addition, the composition and shape of PZT can be tailored to meet demands, whilst the manufacturing method is simple, inexpensive and suitable for production of large quantities. However, since the late 1990s' research has consistently shown that relaxor-lead titanate (relaxor-PT) solid solutions in a single crystalline form exhibit a remarkably higher piezoelectric response with d_{33} up to 2500 pC/N and k_{33} up to 0.9. Figures 1.1 and 1.2 graphically show a comparison of several compositions of PZT and relaxor-PT crystals for d_{33} and k_{33} . The improved charge coefficient and coupling factor of relaxor-PT crystals are highly advantageous for many applications. For example in underwater acoustics advantages include miniaturisation, increased bandwidth, increased sound levels, decreased power consumption, higher sensitivity or higher signal-to-noise ratio [4]. Another example where relaxor-PT are advantageous is in the area of medical imaging. As a result of the increased bandwidth,

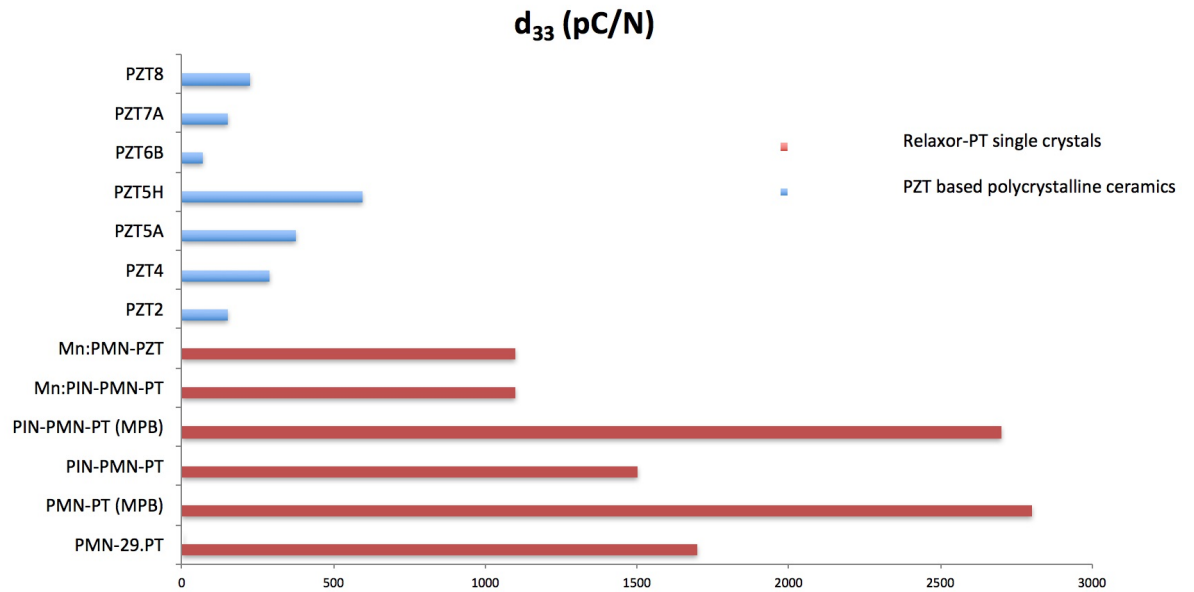


FIGURE 1.1: Piezoelectric charge coefficient d_{33} comparison between various compositions of polycrystalline PZT and various compositions of relaxor-PT single crystals. Data from [6].

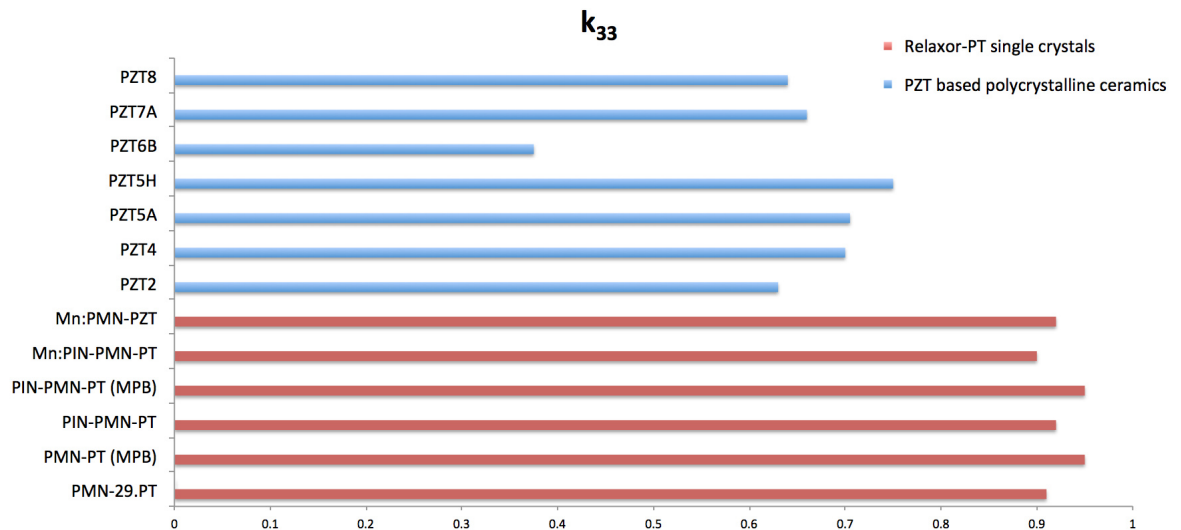


FIGURE 1.2: Electromechanical coupling factor k_{33} comparison between various compositions of polycrystalline PZT and various compositions of relaxor-PT single crystals. Data from [6].

a single crystal transducer can cover the frequency range of two traditional transducers and therefore the same device may be used for a greater range of patients [5].

Therefore, single crystals represent the subject of a revolutionary upgrade particularly in underwater systems and medical industry. However, investigations are still needed to identify an advantageous growth method as well as to explore the relationship between chemical composition and properties. Both areas make the subject of this thesis. The findings up to date are briefly presented in the following section.

1.2 Research subject

The identification of high piezoelectric performance in relaxor-PT crystals has triggered an important amount of innovative scientific work with two major aims:

1. Identify a crystal growth method with no (or minimal) disadvantages.
2. Develop chemical formulations of relaxor-PT solid solutions that, in addition to high piezoelectric performance, exhibit thermal stability and low mechanical and electrical losses.

First, developments up to date in terms of crystal growth are briefly presented. Three principal growth methods are currently explored, namely Solution, Bridgman and Solid State¹. A number of companies have already established commercialisation of certain relaxor-PT single crystal compounds - Figure 1.3. From the three techniques, Bridgman is dominant amongst manufacturers due the ability to provide large, highly dense crystals. Unfortunately, crystals grown by this technique exhibit an unpreventable compositional gradient which results in variation of properties and ultimately in a cost increase. Crystals grown by Solution are impractical for use in certain devices due to their size limitation. Solid State is a technique not sufficiently explored, the understanding of the underlying growth mechanisms is currently minimal. Consequently, more research is needed to develop a technique able to produce large, high quality crystals at low cost. Based on the advantages and disadvantages of the three methods reviewed here, Bridgman and Solid State seem to be the crystal growth methods that need further attention for growing high performance piezoelectric crystals.

Second, the progress made to date in terms of chemical formulations of relaxor-PT

¹Detailed description of the methods will be given in Chapter 3.



FIGURE 1.3: World wide principal companies involved with relaxor-PT single crystal manufacturing: A - CTS Advanced (Bridgman), B - TRS Technologies (Bridgman), C - Microfine (Solution), D - Sinoceramics (Bridgman), E - iBule (Bridgman), Ceracomp (Solid State Conversion Growth), F - JFE Mineral (Bridgman). Blank world map from [7].

solid solutions is outlined. The high piezoelectric performance has been first proved in pseudo-binary solid solutions such as $\text{Pb}(\text{Mg}_{1/3}\text{Nb}_{2/3})\text{O}_3\text{-PbTiO}_3$ (PMN-PT). Subsequently, a pseudo-ternary formulation has been developed, namely $\text{Pb}(\text{In}_{1/2}\text{Nb}_{1/2})\text{O}_3\text{-Pb}(\text{Mg}_{1/3}\text{Nb}_{2/3})\text{O}_3\text{-PbTiO}_3$ (PIN-PMN-PT) which has increased thermal stability compared to the pseudo-binary compound. Furthermore, a third formulation which consists of modifying the pseudo-ternary compound with manganese has been developed (Mn:PIN-PMN-PT). The Mn modification¹ has the advantage of lowering electrical and mechanical losses of the material. Additional information regarding the different compounds outlined here is given in Chapter 3. Mn modified crystals are highly desirable particularly for high power devices where materials with low losses are required to minimise the heating effect. However, the availability and fundamental understanding of the Mn modified crystals are limited. Further investigation and experimentation are strongly recommended.

¹Within this work as well as in the literature related to this subject, the words "doped" and "modified" are used interchangeably - an explanation is provided in Chapter 7.

1.3 Aims and objectives

The first aim of this study is to compare Bridgman and Solid State Conversion by means of experimental research and determine which method maintains a satisfactory balance between cost, microstructural quality and size of grown crystals. Consequently, the readiness for industrial production is to be established for the two methods. Objectives are set as follows:

- Perform experimental crystal growth runs by Bridgman where parameters such as growing speed, crucible thickness, the use of crystal seeds for control of orientation are to be varied. A conclusion with respect to encountered challenges is to be drawn.
- Perform a basic study of grain growth behaviour in polycrystalline PIN-PMN-PT and Mn:PIN-PMN-PT. Consequently, establish the experimental conditions which would lead to conversion to a single crystal and perform growth experiments.

The second aim is to advance the fundamental understanding of Mn:PIN-PMN-PT, particularly to determine the influence that the complex chemical medium of PIN-PMN-PT has on the multi-valent Mn ion. Objectives are established as follows:

- Design several formulations of PIN-PMN-PT and modify them with the same amount of Mn.
- Prepare polycrystalline samples for each designed formulation.
- Determine the average valence state of Mn within each compound prepared.
- Perform various electrical measurements.
- Identify whether varying the composition of PIN-PMN-PT influences the behaviour of Mn.

1.4 Thesis organisation

The structure of the thesis takes the form of seven sections. Chapter 1 has given the background information of the research topic. An introduction to piezoelectricity and

piezoelectric materials with focus on single crystals will be given in Chapter 2, whilst Chapter 3 details single crystal growth methods. The following chapters present the experiments conducted in this study. Chapter 4 describes the processing route for preparation of compounds from raw oxide powders and presents the results of basic analysis on the compounds prepared. Chapter 5 and 6 present the investigations with respect to crystal growth via Bridgman and Solid State. Chapter 7 reveals the study performed on Mn modified PIN-PMN-PT formulations. For clarity, the organisation of the thesis is schematically presented in Figure 1.4.

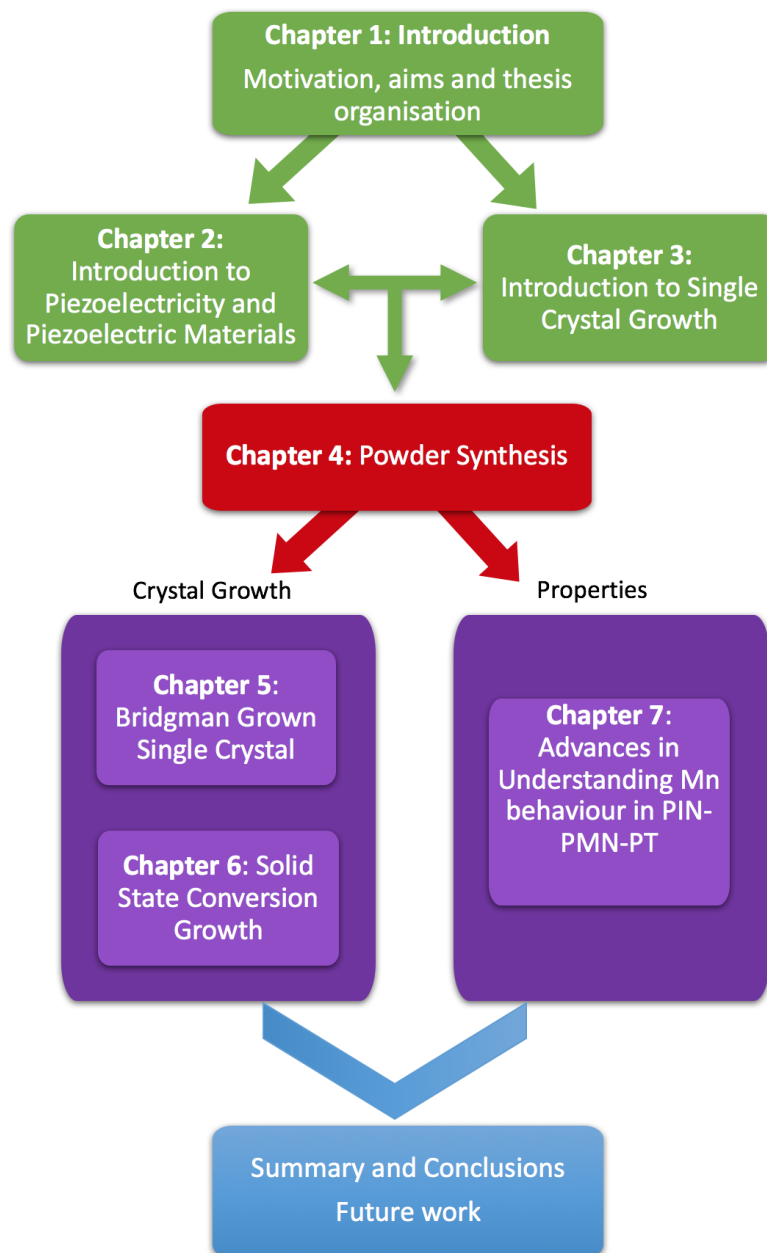


FIGURE 1.4: Thesis workflow

Chapter 2

Introduction to Piezoelectricity and Piezoelectric Materials

2.1 Introduction

The phenomenon of piezoelectricity has been discovered by the Curie brothers in 1880. It has then been found that when certain materials such as Rochelle salt, quartz or cane sugar are subject to mechanical force they generate a voltage and the polarity changes sign in agreement with either compression or tension. Subsequently it has been found that the converse effect is also true - when subject to an electric field, the examined materials compress or expand according to the polarity of the field. The first effect was named the *direct piezoelectric effect*, whilst the second the *inverse piezoelectric effect* [8, 9]. The origin of the label *piezo-* is from the Greek word *piezein* which means to press [1].

Since their discovery, piezoelectric materials have received increased attention and their use spans across a broad range of applications. Some applications make use of the direct piezoelectric effect (where the output is the electrical energy) such as gas lighters, airbag sensors or microphones and some other make use of the inverse effect (mechanical energy as output) such as positioning stages in microscopes, acoustic transducers or loudspeakers. There are also applications based on both effects like medical imaging, hearing aids, sonar, parking sensors, wristwatches or micro-processors [10]. Innovations continue to occur in the world of applications due to the continuous improvement of properties in piezoelectric materials. Although discovered in naturally occurring materials as mentioned in the beginning of this chapter,

many compounds have been also developed. Figure 2.1 shows the development of piezoelectric materials in chronological order. A notable compound is BaTiO_3 (BT) developed during World War II. Another notable piezoelectric material is $\text{Pb}(\text{Zr,Ti})\text{O}_3$ (PZT) which was developed in the 50's and is still in use to date. However, in the late 90's a new class of piezoelectric materials started to attract a lot of attention due to their ultrahigh piezoelectric performance - relaxor-PT single crystals.

The aim of this chapter is to present the basics of piezoelectric materials in terms of crystallographic structure and properties. A section is dedicated to relaxor-PT crystals.

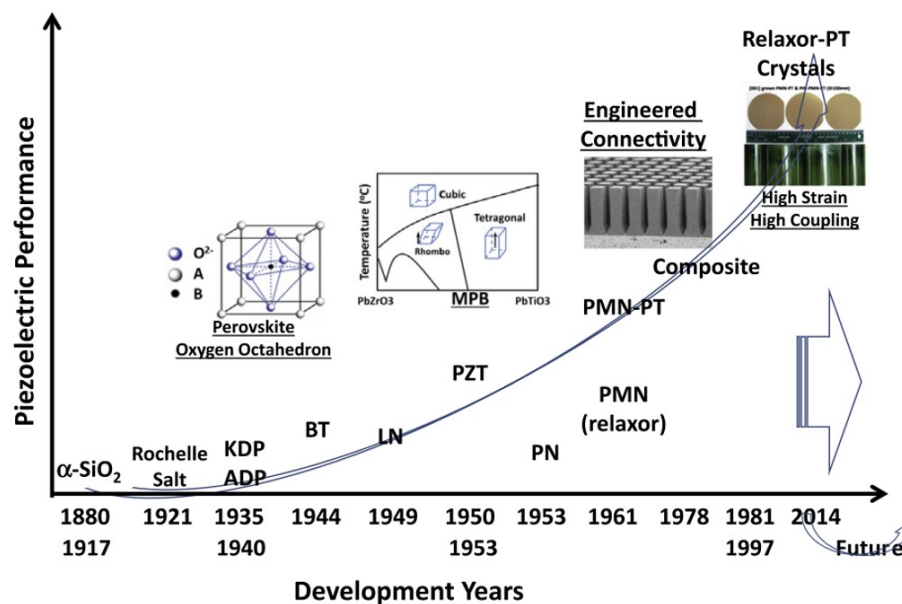


FIGURE 2.1: Development of piezoelectric materials since their discovery. The abbreviations represent the following compounds: KDP: KH_2PO_4 ; ADP: $(\text{NH}_4)\text{H}_2\text{PO}_4$; BT: BaTiO_3 ; LN: LiNbO_3 ; PZT: $\text{Pb}(\text{Zr,Ti})\text{O}_3$; PN: PbNb_2O_6 ; PMN: $\text{Pb}(\text{Mg}_{1/3}\text{Nb}_{2/3})\text{O}_3$; PMN-PT: $\text{Pb}(\text{Mg}_{1/3}\text{Nb}_{2/3})\text{O}_3\text{-PbTiO}_3$. The figure highlights two key points in the development of piezoelectric materials - the perovskite structure and the Morphotropic Phase Boundary concept in PZT [6].

2.2 Crystallography of piezoelectric materials

2.2.1 Crystal systems, point groups and space groups

Crystalline materials can be classified into 7 basic crystal systems which together with their different lattice centering types give rise to 14 Bravais lattices - Figure 2.2. A number of point symmetry elements may be applied to the lattices which result in 32 point groups. The properties of materials depend on the arrangement of atoms and their symmetries and therefore, one use of the point groups is to describe materials' properties. Piezoelectricity is a phenomenon directly related to the symmetry elements of a crystalline material. From the 32 point groups, 21 have no centre of symmetry, 20 being piezoelectric. The exception is a point group which, although non-centrosymmetric, exhibits other symmetry elements which cancel the occurrence of a dipole. From those, 10 are polar or pyroelectric, as they exhibit polarity, i.e. the centre of positive charge differs from the centre of negative charge. Pyroelectric crystals generate a voltage upon a change in temperature. A linked property to pyroelectricity is ferroelectricity. In ferroelectric materials, the polarisation may be switched between equivalent stable states by the application of an electric field. A schematic representation of crystal classification and their related properties is shown in Figure 2.3. An extensively studied crystallographic structure which exhibits ferroelectricity is the perovskite structure¹, described in the following section.

¹Only a limited number of perovskites exhibit ferroelectricity [11].

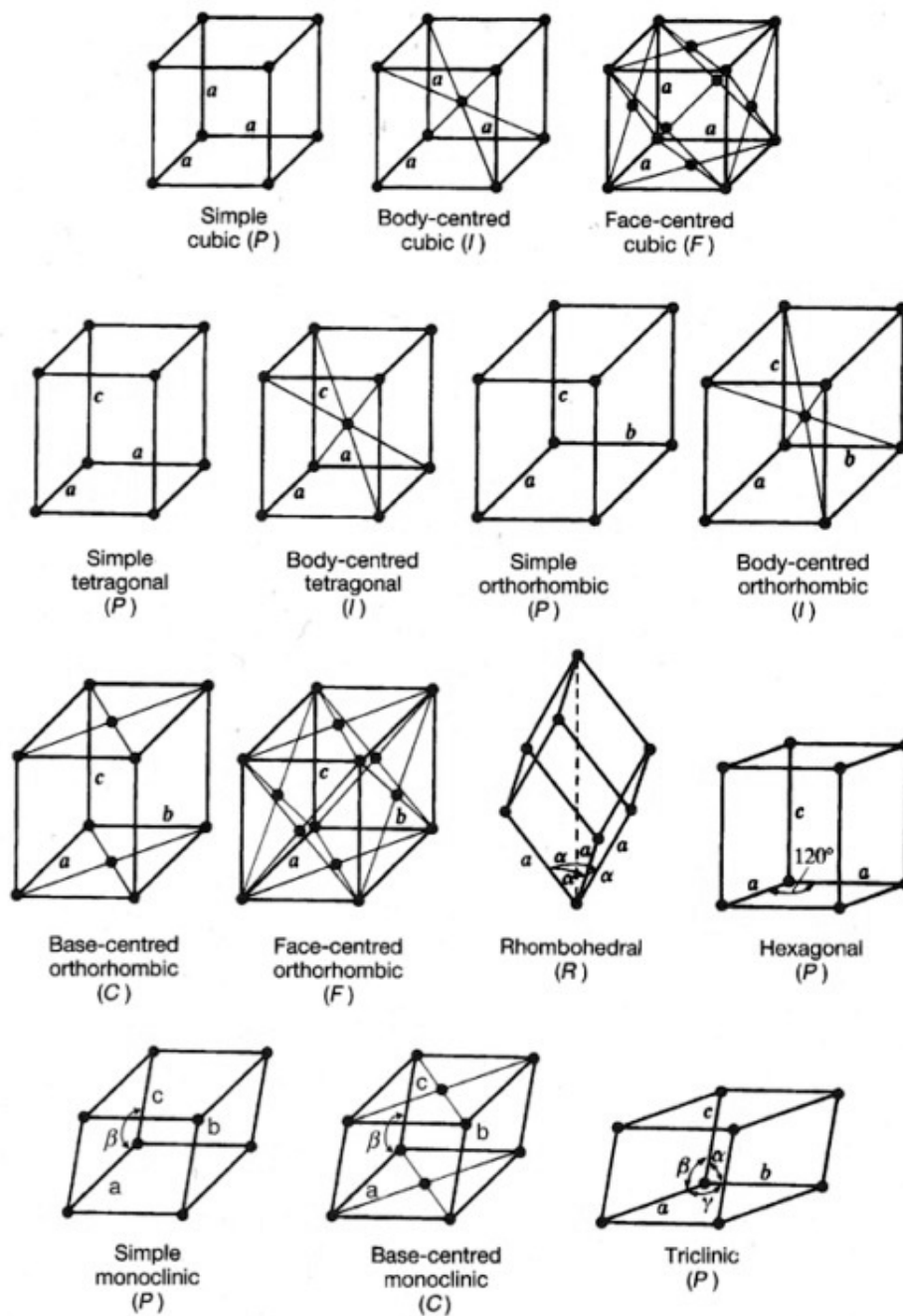


FIGURE 2.2: The 14 Bravais lattices [12]

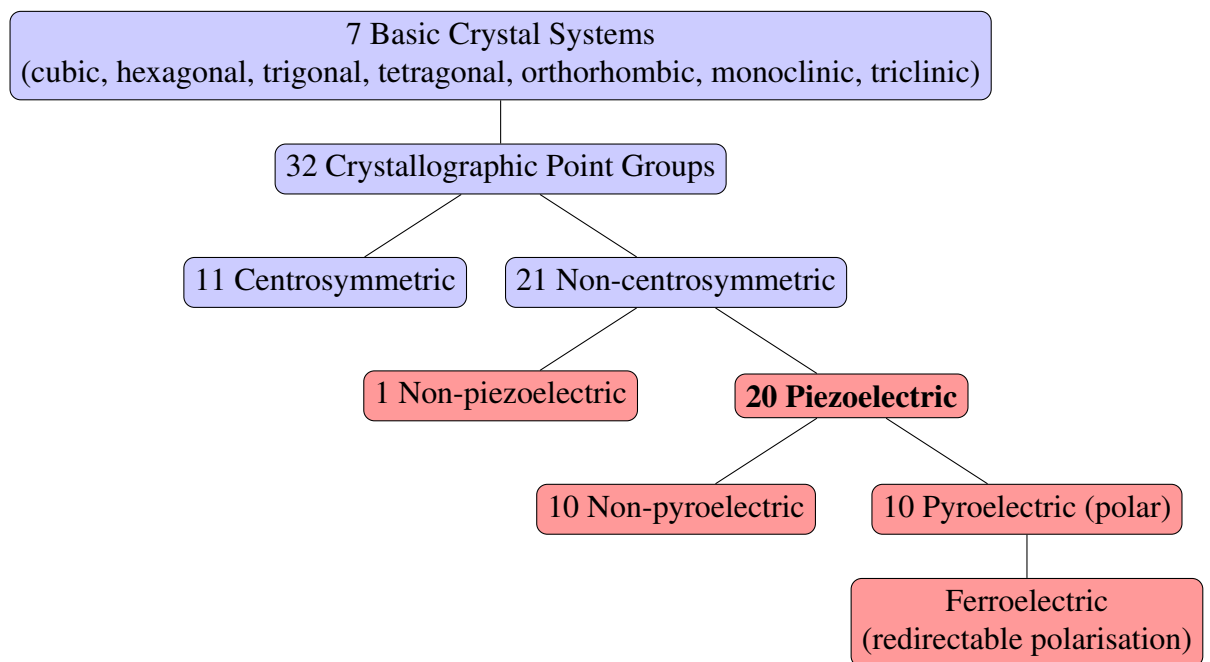


FIGURE 2.3: Schematic diagram showing the link between crystallographic structure and piezoelectric, pyroelectric and ferroelectric properties. Adapted from [10, 12, 13].

2.2.2 The perovskite structure

A broad range of piezoelectric applications make use of materials with this particular structure. Originally the term *perovskite* referred to the mineral CaTiO_3 . However, the term has been generalised to compounds with a chemical formula ABO_3 , where A and B are cations. The B ion occupies octahedral sites - Figure 2.4, whilst the A ion occupies cubeoctahedral sites - Figure 2.5. Under certain conditions, the cation B is displaced from its centred position and the structure becomes non-centrosymmetric and therefore may exhibit piezoelectricity.

In a cubic ABO_3 structure, the lattice parameter a may be calculated as follows:

$$a = \sqrt{2}(r_O + r_A) = 2(r_O + r_B) \quad (2.1)$$

where r_A and r_B are the ionic radii of A and B atoms. Many cations of different sizes may crystallise in the perovskite structure and the Goldschmidt tolerance factor is used to predict the stability of a given compound in a cubic form:

$$t = (r_O + r_A) / \sqrt{2}(r_O + r_B) \quad (2.2)$$

A wide variety of cations can be accommodated in the perovskite structure. As a result, the structure may distort to accommodate cations of various ionic radii. Typically, a tolerance factor of 0.9-1 is associated with an ideal perovskite structure, whilst values between 0.71-9 are linked to a distorted perovskite structure such as rhombohedral or orthorhombic. Tolerance factors <0.71 and >1 are associated with non-perovskite structures. Notable are values slightly higher than 1 which tend to be tetragonal [9, 14, 15].

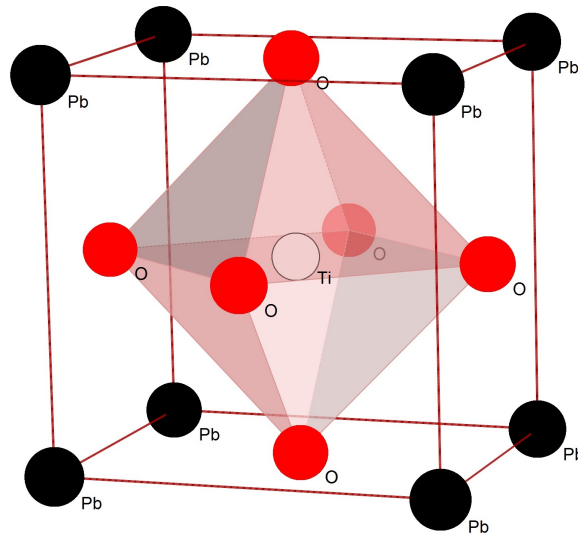


FIGURE 2.4: PbTiO_3 unit cell as example of perovskite structure ABO_3 . The octahedral site with the central Ti atom is highlighted. Structure generated with CrystalMaker software.

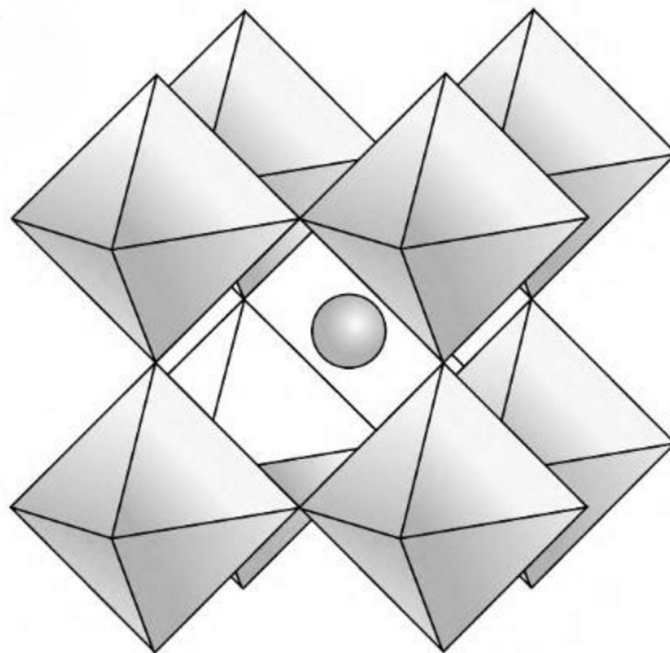


FIGURE 2.5: Octahedral sites with the A ion sitting at the centre of the cuboctahedron within a perovskite structure. From [12].

2.2.3 Definition of polycrystalline and single crystals

The microstructural difference between a polycrystalline and a single crystal is shown in Figure 2.6. A polycrystalline material is an arrangement of unit cells into so-called grains. Within each grain the unit cells are ordered and have the same crystallographic orientation. Generally, the orientation from grain to grain differs, being random throughout the material. On the contrary, a single crystal shows complete translational symmetry of the unit cell throughout the material. For these materials to become piezoelectric, a poling process is required which involves application of an electric field resulting in a macroscopic polarisation. As a consequence, certain properties of both polycrystalline materials and single crystals will depend upon the measurement direction. These properties are called anisotropic and examples include polarisation produced by mechanical stress and deformation caused by an electric field [16]. In single crystals, the anisotropy is much stronger than that in polycrystalline materials due to their complete translational symmetry. The strong anisotropy of single crystals means that novel modes of operations may be designed [2].

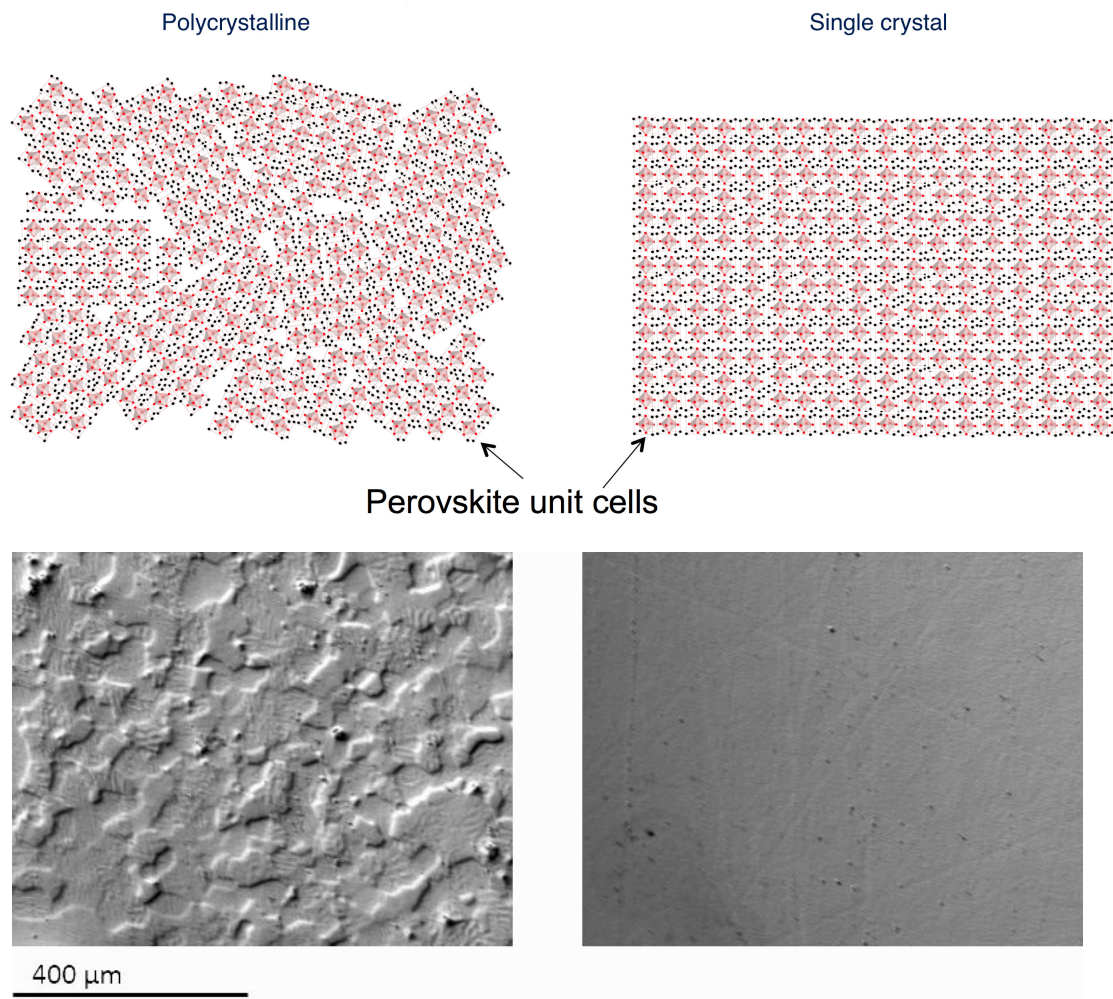


FIGURE 2.6: Graphic representation of a polycrystalline and a single crystal material (top, not to scale) and optical micrograph showing polished surfaces of Mn-modified PIN-PMN-PT in a polycrystalline form and a single crystalline form (bottom). The materials were prepared within this work.

2.2.4 Operation modes - engineering notation

To account for the anisotropy of the certain properties of piezoelectric materials, the direction of the electrical quantity (electric field or displacement) and the direction of the mechanical quantity (strain or stress) must be defined. In other words, the material's mode of operation must be specified. The engineering notation is commonly used. This notation is achieved with subscripts from 1 to 6 added to the different piezoelectric parameters (briefly discussed in the following subsections). Subscripts 1, 2 and 3 define a *normal* deformation in the x, y and z directions. Subscripts 4, 5 and 6 define *shear* deformation around x, y and z. Figure 2.7 shows a graphic representation.

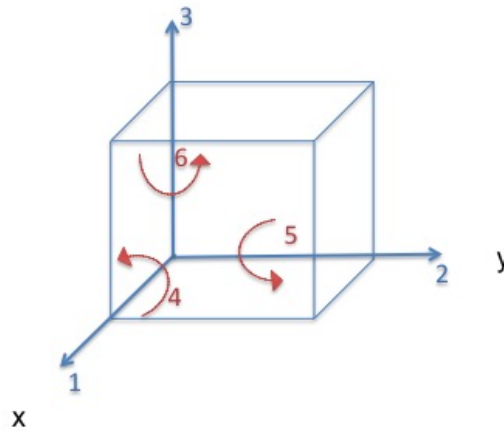


FIGURE 2.7: Deformation directions of piezoelectric materials. The poling direction is the 3 direction. Adapted from [10].

The general difference between engineering and tensor subscripts is summarised in Table 2.1. Special care must be taken when a conversion from engineering to tensor is made in the case of shear strain as a "factor of 2" appears - Table 2.2.

TABLE 2.1: Symbols and their units used in piezoelectric relationships [17]

Engineering xyz	Engineering contracted	Tensor
x	1	11
y	2	22
z	3	33
yz	4	23, 32
xz	5	13, 31
xy	6	12, 21

TABLE 2.2: Conversion from engineering to tensor coefficients for engineering strain [16]

Engineering contracted	Tensor
e_1	e_{11}
e_2	e_{22}
e_3	e_{33}
e_4	$2e_{23}$
e_5	$2e_{13}$
e_6	$2e_{12}$

2.3 Properties of piezoelectric materials

To characterise newly designed piezoelectric materials and to evaluate changes in their behavior upon variations in processing or chemical composition, a number of parameters and constants are to be determined. Characterisation may be divided in three sections (i) dielectric, (ii) piezoelectric and (iii) ferroelectric properties.

2.3.1 Dielectric properties

A dielectric material is widely regarded as an insulating material. It responds to an applied electric field by becoming polarised [18]. There are various polarisation mechanisms such as atomic (electronic), ionic, dipolar and space charge. The mechanisms are illustrated in Figure 2.8. Atomic polarisation is a displacement of the electrons in an atom relative to the nucleus and is found in all materials. Ionic materials, in addition to electronic polarisation, experience a displacement of the cations and anions relative to each other. Dipolar polarisation occurs in dipolar materials such as water, where an electric field causes the molecules to reorient accordingly. Space charge polarisation is associated with the movement of free charge carriers until they encounter a potential barrier such as a grain boundary [13].

An elementary dipole moment is defined as two charges of opposite signs +Q and -Q separated by a distance δx :

$$p = Q\delta x \quad (2.3)$$

The dipole moment per unit volume constitutes the polarisation of the material and accounts only for the bound charges in the material. However, the total charge density (bound and free) is equivalent to the electric displacement D:

$$D = \varepsilon_0 E + P \quad (2.4)$$

where $\varepsilon_0 = 8.85 \times 10^{-12}$ F/m is the permittivity of free space, E the electric field and P the polarisation. When P is proportional to the electric field:

$$P = \chi_e \varepsilon_0 E \quad (2.5)$$

where χ_e is the electric susceptibility. A parameter related to the electric susceptibility is permittivity of the material ε , which represents the extent to which the electric field

affects the dielectric and is defined as:

$$\varepsilon = \varepsilon_0 + \varepsilon_0 \chi_e \quad (2.6)$$

Subsequently, ε_r may be extracted which is the value of the permittivity relative to the permittivity of free space:

$$\frac{\varepsilon}{\varepsilon_0} = 1 + \chi_e = \varepsilon_r \quad (2.7)$$

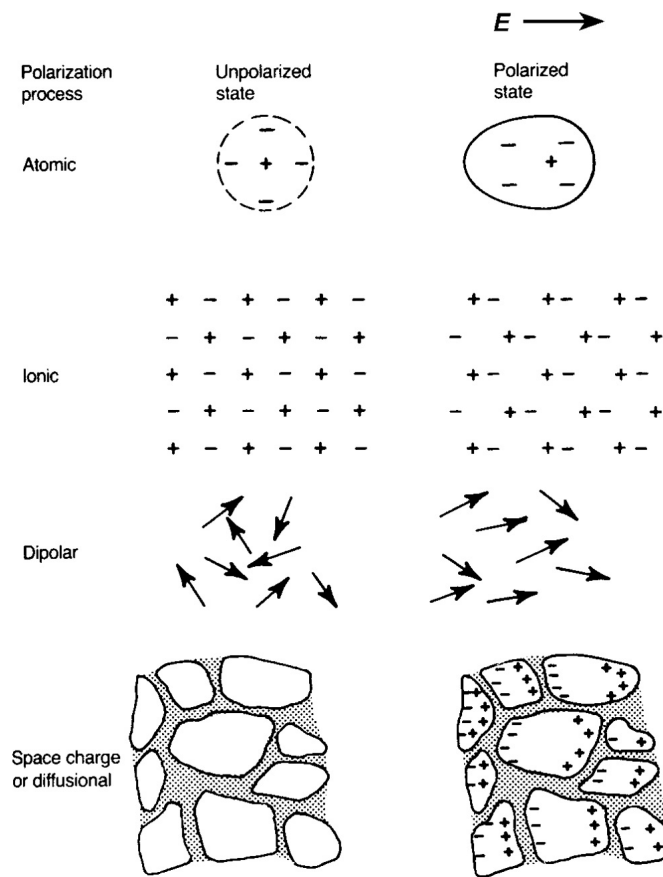


FIGURE 2.8: Various polarisation mechanisms [13].

Permittivity is complex as has a real component and an imaginary (lossy) component:

$$\varepsilon^* = \varepsilon' - i\varepsilon'' \quad (2.8)$$

The loss component, also called dissipation factor is caused by lossy mechanisms in a dielectric such as conduction or rotation or movement of atoms or molecules. The dissipation factor is defined as the ratio between the imaginary and real components of

the permittivity [9, 19]:

$$\tan\delta_e = \frac{\epsilon''}{\epsilon'} \quad (2.9)$$

The real permittivity as well as the dissipation factor are both frequency dependent. The various polarisation mechanisms cause a dielectric dispersion and occur at well distinguished frequencies - Figure 2.9 [13].

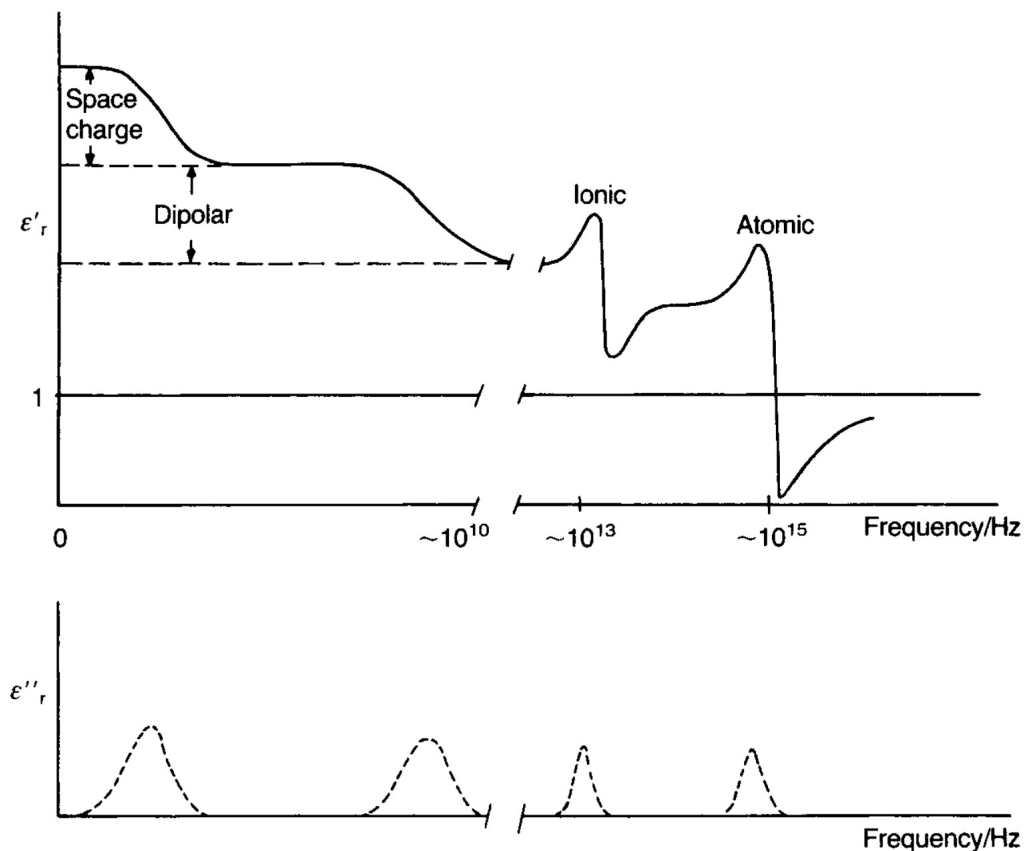


FIGURE 2.9: Dependency of permittivity (real and imaginary) on frequency and associated polarisation mechanisms which lead to dielectric dispersion. Space charge and dipolar mechanisms depend strongly on temperature, whilst ionic and atomic are temperature independent [13].

2.3.2 Piezoelectric properties

2.3.2.1 Electrostriction

Electrostriction is a phenomenon describing deformation which occurs under applied electric field. It is a property of *all* non-conductive materials crystalline or amorphous.

As opposed to piezoelectric effects, deformation caused by electrostriction is independent of the polarity of the field and is proportional to its square.

Electrostriction is a weak phenomenon and the response in piezoelectric materials is predominantly a result of true piezoelectric effects [8, 9]. Electrostriction may be described as follows:

$$T_h = -c_{hi}^P S_i + q_{hkl} P_k P_l \quad (2.10)$$

$$S_i = -s_{ij}^P T_j + Q_{imn} P_m P_n \quad (2.11)$$

where T and S are stress and strain components at constant polarisation P, c and s elastic stiffness and compliance. The electrostriction constants q and Q are related as follows (by substitution of the equation 2.10 into 2.11):

$$q_{hmn} = c_{hi}^P Q_{imn} \quad (2.12)$$

$$Q_{imn} = s_{ih}^P q_{hmn} \quad (2.13)$$

The electrostriction coefficients are fourth rank tensors and the Voigt notation with three suffixes has been used in the above equations. The h and i suffixes are associated with 6 values where T_1, T_2, T_3 are compressive stresses, T_4, T_5, T_6 shear stresses and S_1, S_2, S_3 extension strains, S_4, S_5, S_6 shear strains. The suffixes k and m take three values only [20].

2.3.2.2 Piezoelectricity and piezoelectric coefficients

The direct piezoelectric effect is associated with the creation of an electric charge upon application of stress. Contrarily, the inverse piezoelectric effect is described as the generation of strain upon application of an electric field. The basic piezoelectric relations may be defined in four different ways [17]:

$$D = \varepsilon^T E + dT \quad (2.14)$$

$$S = d_t E + s^E T \quad (2.15)$$

$$D = \varepsilon^S E + eS \quad (2.16)$$

$$T = -e_t E + c^E S \quad (2.17)$$

$$E = \beta^T E - gT \quad (2.18)$$

$$S = g_t D + s^D T \quad (2.19)$$

$$E = \beta^S D - h S \quad (2.20)$$

$$T = -h_t D + c^D S \quad (2.21)$$

where the symbols are given in Table 2.3.

TABLE 2.3: Symbols and their units used in piezoelectric relationships [17]

Symbol	Description	Unit
S	Strain	m/m
T	Stress	N/m ²
D	Electric displacement	C/m ²
E	Electric field strength	V/m
ϵ	Permittivity	F/m
β	Dielectric impermeability	m/F
s	Elastic compliance	m ² /N
c	Elastic stiffness	N/m ²
d	Piezoelectric strain (or charge) coefficient	C/N or m/V
e	Piezoelectric stress constant	C/m ² or N/Vm
g	Piezoelectric strain constant	Vm/N or m ² /C
h	Piezoelectric stress constant	V/m or N/C

The equations 2.14 through to 2.21 are matrix equations relating the electric field or displacement vector (three components) with the stress or strain tensor (six components). The subscript t indicates the transposed matrices.

The four piezoelectric constants d , g , e and h may be defined as partial derivatives:

$$d = \left(\frac{\partial S}{\partial E}\right)_T = \left(\frac{\partial D}{\partial T}\right)_E \quad (2.22)$$

$$g = \left(\frac{-\partial E}{\partial T}\right)_D = \left(\frac{\partial S}{\partial D}\right)_T \quad (2.23)$$

$$e = \left(\frac{-\partial T}{\partial E}\right)_S = \left(\frac{\partial D}{\partial S}\right)_E \quad (2.24)$$

$$h = \left(\frac{-\partial T}{\partial D}\right)_S = \left(\frac{-\partial E}{\partial S}\right)_D \quad (2.25)$$

where the subscripts represent boundary conditions: constant stress (T), constant strain (S), constant displacement (D) and constant field (E).

2.3.2.3 Electromechanical coupling factor

The electromechanical coupling factor k is associated with the strength of the electromechanical effect and is defined as the square root of the ratio between converted energy (electrical or mechanical) and input energy (mechanical or electrical):

$$k^2 = \frac{\text{converted energy (mechanical or electrical)}}{\text{input energy (electrical or mechanical)}} \quad (2.26)$$

Most used electromechanical coupling coefficients are the following (for polycrystalline materials or crystals of class 6mm [17]):

$$k_{15} = \frac{d_{15}}{\sqrt{s_{44}^E \varepsilon_1^T}} \quad (2.27)$$

where all strain components are 0 except S_5 , and the electric displacement is constant at antiresonance frequency;

$$k_{33} = \frac{d_{33}}{\sqrt{s_{33}^E \varepsilon_3^T}} \quad (2.28)$$

where all stress components are 0 except T_1 , and the electric displacement is constant at antiresonance frequency;

$$k_{31} = \frac{d_{31}}{\sqrt{s_{11}^E \varepsilon_3^T}} \quad (2.29)$$

where all stress components are 0 except T_1 , and the electric field is constant at resonance frequency;

$$k_p = \frac{d_{31}}{\sqrt{2/(s_{11}^E + s_{12}^E) \varepsilon_3^T}} = k_{31} \sqrt{2(1 - \sigma)} \quad (2.30)$$

where the subscript p indicates a *planar mode* with all stress components are 0 except $T_1=T_2$, and the electric field is constant at resonance frequency;

$$k_t = \frac{e_{33}}{\sqrt{c_{33}^D \varepsilon_{33}^S}} \quad (2.31)$$

where the subscript t indicates a *thickness mode* with all strain components are 0 except S_3 , and the electric displacement is constant at antiresonance frequency.

Additional information regarding the electromechanical coupling coefficients may be found elsewhere [9, 16, 17].

2.3.2.4 Mechanical Quality Factor

The mechanical quality factor Q_m is a measure of the energy lost to mechanical damping and is proportional to the ratio between stored mechanical energy and losses during a vibration cycle of a vibrating body:

$$Q_m = \omega_r \frac{U_s(\omega_r)}{W_d(\omega_r)} = \frac{2\pi U_s(\omega_r)}{T_r W_d(\omega_r)} \quad (2.32)$$

where $U_s(\omega_r)$ is the energy stored in the mass at the resonance frequency ω_r , $W_d(\omega_r)$ the time average dissipated power at ω_r , and T_r is the period of one oscillation at the resonance.

Q_m may also be expressed as the ratio between the resonance frequency and the peak width of the power vs frequency plot when the power drops by half - Figure 2.10. Q_m will take the following expression:

$$Q_m = \frac{\omega_r}{\omega_2 - \omega_1} \quad (2.33)$$

When the power drops by half, the admittance drops by $1/\sqrt{2}$, commonly referred to as the *3 dB point* as the response is within 3 dB of the response at resonance [21]. Measurement of the admittance as a function of frequency is the common approach for determining Q_m :

$$Q_m = \frac{\omega_r}{(\Delta\omega)_{3dB}} \quad (2.34)$$

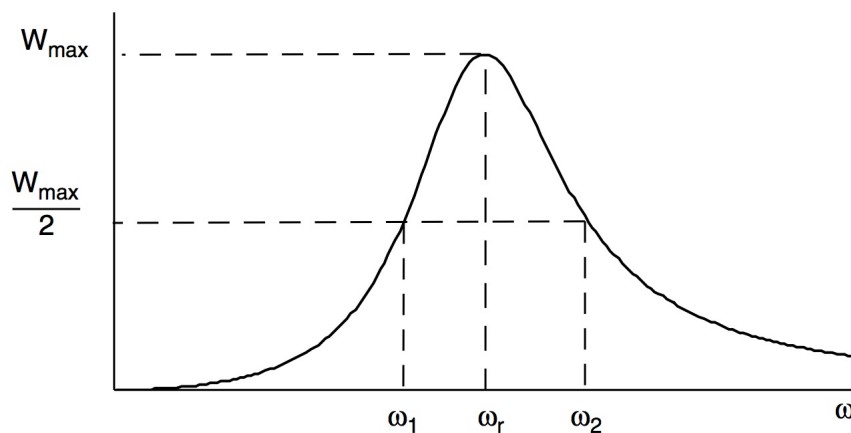


FIGURE 2.10: Power vs frequency plot showing frequencies at half power [22].

2.3.3 Ferroelectric properties

2.3.3.1 Hysteresis loop and Curie point

As briefly mentioned in Section 2.2.1, in certain polar crystals a reversibility of the dipole is possible by means of an electric field. Materials exhibiting this property are said to be ferroelectric. A measure of ferroelectricity is the polarisation, P . Typically, P is determined by means of displacement (D) versus electric field measurements with $P \cong D$. In a ferroelectric material D versus E gives rise to a hysteresis loop - Figure 2.11. Certain parameters are marked on the loop such as P_{SAT} which marks the saturation of the polarisation within the material, P_S is the spontaneous polarisation obtained by extrapolating P_{SAT} at high fields, P_R is the remanent polarisation when removing the electric field. P_{SAT} and P_R may be equivalent in certain materials. E_C is the coercive field, i.e. the electric field required by a ferroelectric material to change the direction of the polarisation (e.g. the position of the B-site atom in a perovskite structure). Another

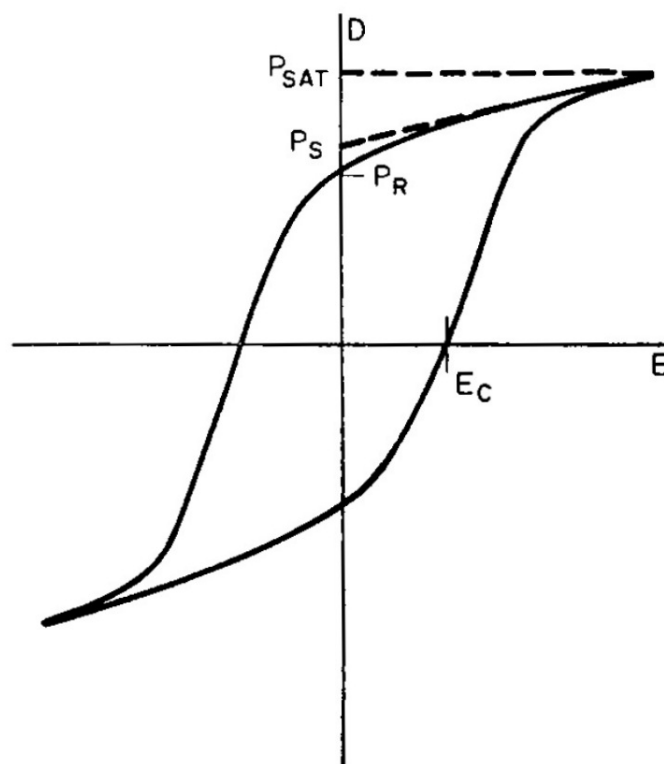


FIGURE 2.11: Typical hysteresis loop in a ferroelectric material, D - displacement, E - electric field, P_{SAT} - saturation polarisation, P_S - spontaneous polarisation, P_R - remanent polarisation, E_C - coercive field [9].

characteristic of ferroelectric materials is the Curie point, T_C which is the temperature

above which the system changes its structure to a non-polar one and becomes non-ferroelectric. Above T_C , the dielectric permittivity of the material follows the Curie-Weiss law:

$$\epsilon_r - 1 = \frac{C}{T - T_0} \quad (2.35)$$

where C is the Curie constant and has a value between 10^3 and 10^5 degrees and T_0 is the Curie temperature (more commonly referred to as Curie-Weiss temperature). T_0 , a constant obtained by extrapolation, is not to be confused with T_C which is the temperature at which a structural transformation takes place, from a polar crystal structure (ferroelectric phase) to a non-polar one (non-ferroelectric phase), for example to the non centrosymmetric cubic structure. For 2^{nd} order transformations (continuous) T_0 equals T_C , however for 1^{st} order transformations (discontinuous) the two values can differ.

2.3.3.2 Phase Transitions

Below T_C the structure may exhibit one or several crystallographic structures. This behavior may be exemplified in BaTiO_3 - Figure 2.12, which transforms to a tetragonal phase at 130°C , to an orthorhombic at 0°C and further to a rhombohedral phase at -90°C . Except temperature, other external stimuli such as electric fields or stress, may also cause phase transitions. Furthermore, of particular interest are phase transformations upon changes in composition of a compound. This subject will be treated separately in the following subsection.

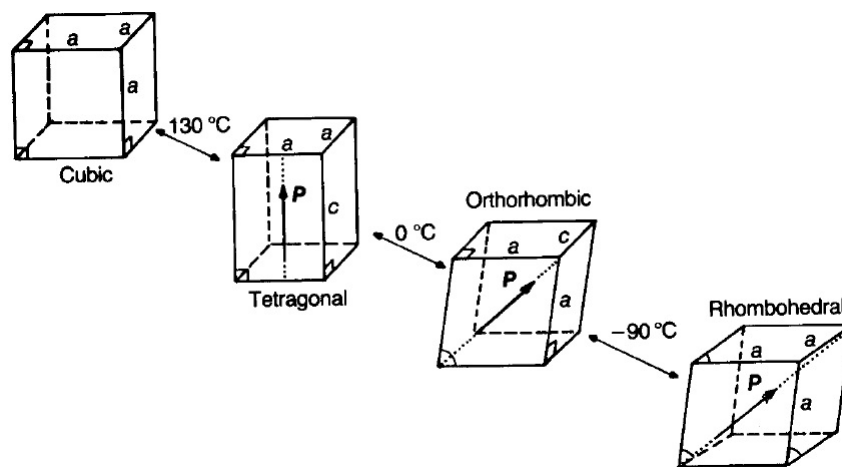


FIGURE 2.12: Phase transformation of BaTiO₃ from the high symmetry cubic phase to lower symmetry phases tetragonal, orthorhombic and rhombohedral upon cooling from $T_C=130^\circ\text{C}$ to -90°C . The direction of the dipole is highlighted for the non-cubic structures. [13]

2.3.3.3 Morphotropic Phase Boundary

An interesting aspect of perovskites is that structures with more than one type of A site and/or B site atom may be obtained. Examples include solid solutions such as:

- $(\text{Ba}_x\text{Ca}_{1-x})\text{TiO}_3$ (BCT)
- $\text{Pb}(\text{Zr}_x\text{Ti}_{1-x})\text{O}_3$ (PZT)
- $\text{Pb}(\text{Zr}_x\text{Ti}_y\text{Nb}_{1-x-y})\text{O}_3$ (PZTN)
- $(\text{Pb}_x\text{Sr}_{1-x})(\text{Zr}_y\text{Ti}_z\text{Mn}_{1-y-z})\text{O}_3$ (PSZTM)
- $\text{Pb}(\text{Zn}_{1/3}\text{Nb}_{2/3})\text{O}_3\text{-PbTiO}_3$ (PZN-PT)
- $\text{Pb}(\text{Mg}_{1/3}\text{Nb}_{2/3})\text{O}_3\text{-PbTiO}_3$ (PMN-PT)
- $\text{Pb}(\text{In}_{1/2}\text{Nb}_{1/2})\text{O}_3\text{-PbTiO}_3$ (PIN-PT)
- $\text{Pb}(\text{In}_{1/2}\text{Nb}_{1/2})\text{O}_3\text{-Pb}(\text{Mg}_{1/3}\text{Nb}_{2/3})\text{O}_3\text{-PbTiO}_3$ (PIN-PMN-PT).

In solid solutions two (or more) crystallographic phases may be stable depending on the ratios of the components. The point which marks a phase transformation as a result of a change in compositions is named *Morphotropic Phase Boundary* (MPB) and may vary with temperature. Figure 2.13 shows phase diagrams for PZT, PZN-PT and PMN-PT

as a function of temperature. Rhombohedral and tetragonal phases are stable below T_C and a cubic phase above T_C . The MPB is the region below T_C marking the transition from rhombohedral to tetragonal. However, more in depth studies (for example high resolution synchrotron studies in PMN-PT by Ye et al [23]) have subsequently proven the existence of additional phases below T_C such as monoclinic or orthorhombic. Figure 2.14 shows the updated phase diagrams for PZT, PZN-PT and PMN-PT. A similar path has been followed for the pseudo-ternary compound PIN-PMN-PT. Figure 2.15 shows a room temperature phase diagram, where rhombohedral and tetragonal phases have been found stable. However, further studies suggest a monoclinic phase is present in between rhombohedral and tetragonal. An updated phase diagram as a function of temperature is shown in Figure 2.16.

The MPB plays a critical role in the performance of a piezoelectric material. The structural instability at the MPB leads to a flat free energy profile which enhances the piezoelectric response [2]. Most of piezoelectric compounds are explored in the vicinity of their MPB.

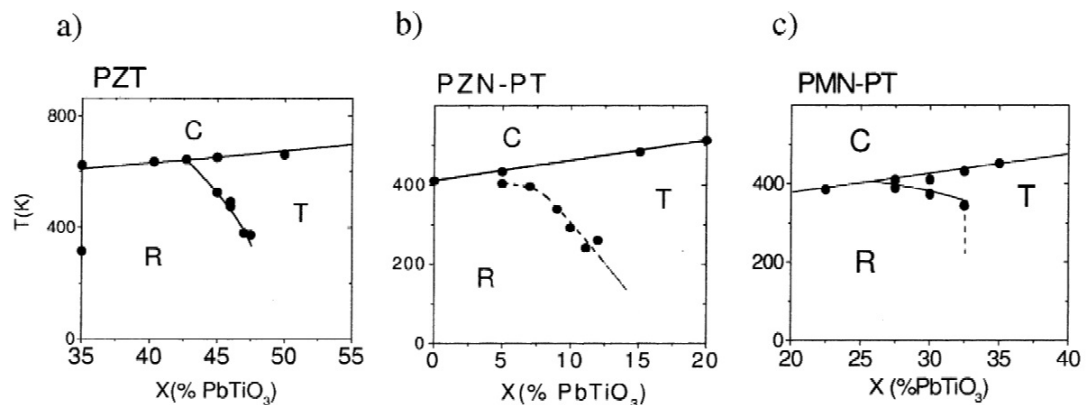


FIGURE 2.13: Initial phase diagrams of PZT, PZN-PT and PMN-PT, C - cubic, R - rhombohedral, T - tetragonal [24]

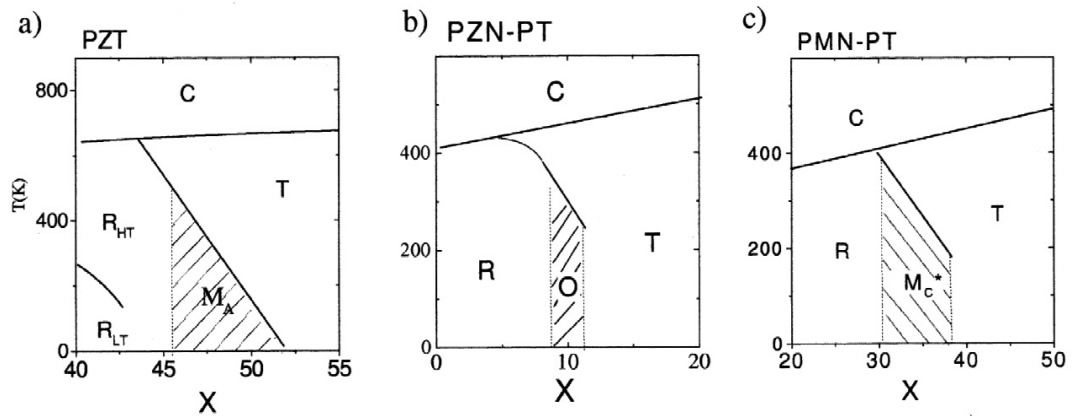


FIGURE 2.14: Updated phase diagrams. X represents the concentration of PT. In PZT, a monoclinic phase is revealed in between rhombohedral (R) and tetragonal (T) phase. In addition the R phase is found to exist with different space groups at lower and higher temperatures. In PZN-PT an orthorhombic (O) has been identified in between R and T. In PMN-PT a type of monoclinic phase is present between R and T [24].

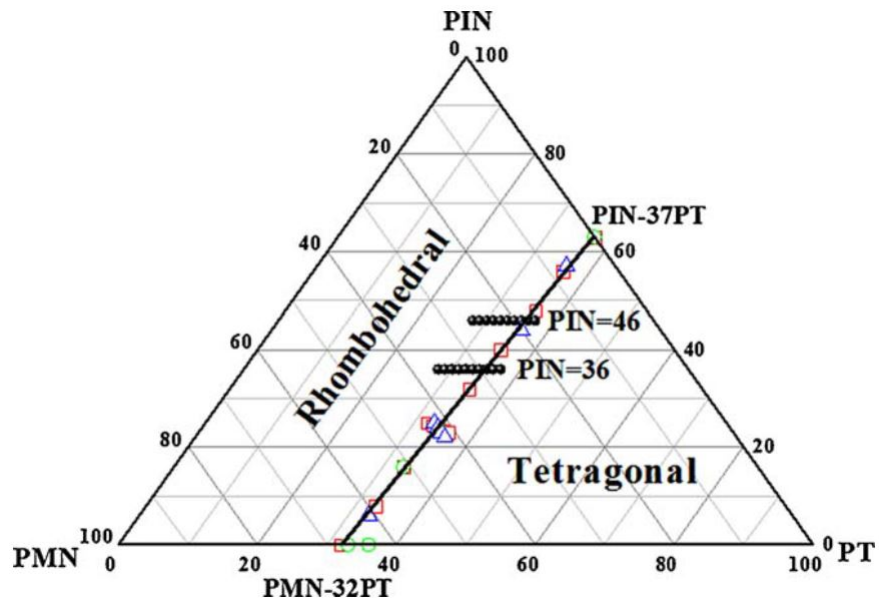


FIGURE 2.15: Phase diagram of PIN-PMN-PT at room temperature [25].

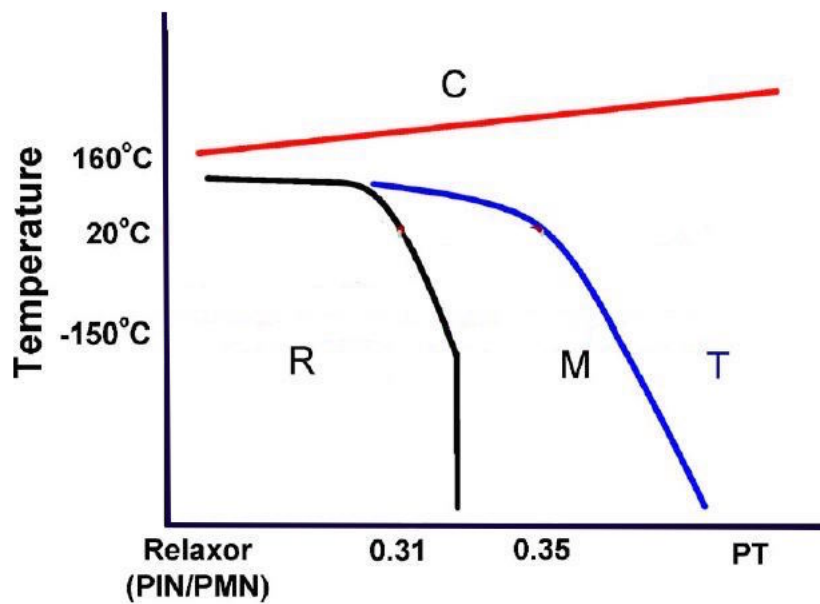


FIGURE 2.16: Updated PIN-PMN-PT phase diagram as a function of temperature [26]

2.3.3.4 Domains

When a ferroelectric material is cooled through T_C , a phase transition from the cubic, non-ferroelectric to a ferroelectric phase takes place. Some regions within the material cool faster than others as an isotherm throughout the material is difficult to achieve. These regions act as nucleating sites for the ferroelectric phase (i.e. where a dipole is present). As multiple directions of the polarisation are stable, different nucleating sites assume different directions and domains are formed. A domain is a volume of the material in which the spontaneous polarisation exhibits the same direction resulting in a net dipole moment. However, the polarisation direction differs from domain to domain and the resultant net polarisation is zero. The boundary which marks the transition from one domain to another is represented by a domain wall. Domain walls are named by the angle the polarisation makes across the wall. Therefore, in a material with tetragonal distortion 90° and 180° domain walls are present. Similarly, in a material with rhombohedral distortion 71° , 109° and 180° walls occur [27].

In a polycrystalline material, the existence of differently aligned grains (from a crystallographic point of view) leads to polarisation being randomly oriented throughout the material. Within each grain, several domains may form. With the application of a sufficiently large electric field, the domains try to align with the field. However the

polarisation is restricted by the crystallographic orientation of the grain. Therefore, domains will align with the equivalent polar direction which is closest to the direction of the applied field. The alignment process referred to as poling is required to induce piezoelectric activity within the material [13].

In a single crystal, the microstructure (complete translational symmetry of the unit cell throughout the material) allows domains to be engineered. Crystals poled along their natural crystallographic directions such as rhombohedral poled along $[111]$ or tetragonal poled along $[001]$ exhibit a single domain state. However, single crystals may be poled along non-natural directions such as a rhombohedral crystal poled along $[001]$. In this scenario, several polar directions are stable after the poling process and the material is said to be in a multi-domain state. Figure 2.17 depicts various poling scenarios for rhombohedral, orthorhombic and tetragonal crystals.

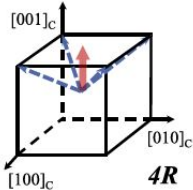
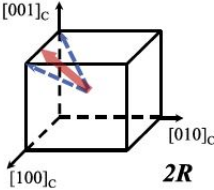
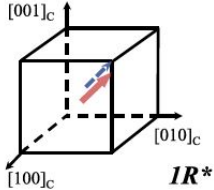
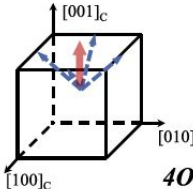
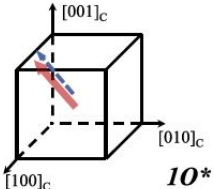
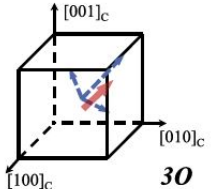
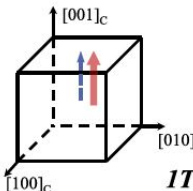
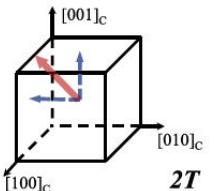
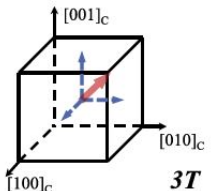
Phase	Symmetry			
	$[001]_c$ poled $4mm$	$[011]_c$ poled $mm2$	$[111]_c$ poled $3m$	
Rhombohedral	 $4R$	 $2R$	 $1R^*$	
Orthorhombic	 $4O$	 $1O^*$	 $3O$	
Tetragonal	 $1T^*$	 $2T$	 $3T$	

FIGURE 2.17: Domain engineered single crystals [6]

2.3.4 Relaxor ferroelectric properties

Relaxor-ferroelectric behavior is shown by a range of compounds with a perovskite structure and complex compositions¹. Examples include $\text{Pb}(\text{Mg}_{1/3}\text{Nb}_{2/3})\text{O}_3$ (PMN),

¹A relaxor behavior is also observed in a number of tungsten bronze systems [28], however these materials are not of interest within this work.

$\text{Pb}(\text{In}_{1/2}\text{Nb}_{1/2})\text{O}_3$ (PIN), $\text{Pb}(\text{Zn}_{1/3}\text{Nb}_{2/3})\text{O}_3$ (PZN), $\text{Pb}(\text{Mg}_{1/3}\text{Ta}_{2/3})\text{O}_3$ and are characterised by intriguing dielectric properties. Figure 2.18 shows the dielectric response in PMN. The characteristics of relaxor ferroelectrics may be summarised as follows:

- the peaks in the dielectric permittivity versus temperature measurements are wider when compared to conventional ferroelectrics;
- contrary to ferroelectrics where the maximum dielectric permittivity is frequency independent and the temperature at which the maximum occurs is associated with the Curie point T_C (see Section 2.3.3.1), in a relaxor, the temperature of maximum permittivity, T_m shows a frequency dependence and is not associated with a structural phase transition as the relaxor systems exhibit a macroscopically cubic structure below T_m ;
- above T_m , the dielectric response does not follow the Curie-Weiss law as in conventional ferroelectrics (see Section 2.3.3.1);
- although typically present in non-cubic crystals, ferroelectricity is observed in relaxors, clearly proven by P-E measurements which show hysteresis, hence the name relaxor ferroelectrics [9, 28, 29].

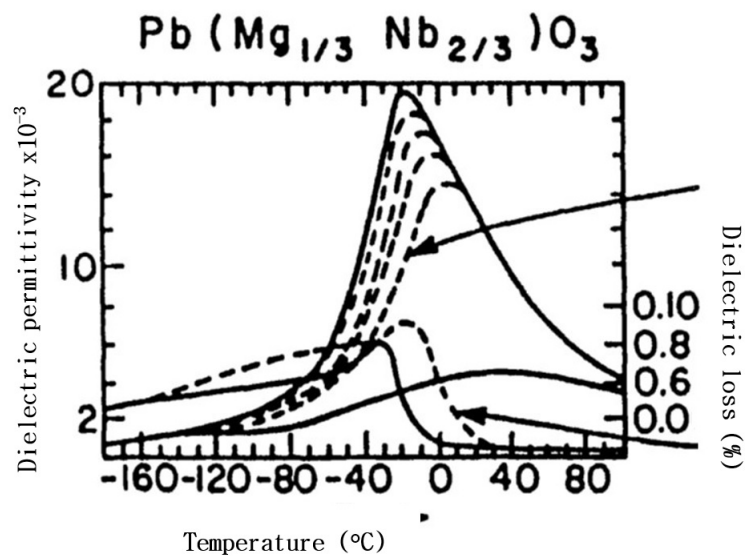


FIGURE 2.18: Dielectric response shown over a range of frequencies $10\text{-}10^7$ Hz of the relaxor PMN. The arrows highlight the frequency dispersion of the response, adapted from [30]

A common feature for all relaxor ferroelectrics is the cation disorder, for example Mg^{2+} and Nb^{5+} in PMN. This disorder leads to the appearance of Polar Nano Regions (PNRs), which may be described as polar regions with limited length exhibiting coherence in polarisation. PNRs appear in the vicinity of T_m and are responsible for the broad dielectric peak as follows: upon cooling through T_m a field induced alignment of PNRs (growth) takes place and the relaxation of the polarisation mechanism results in a broad and frequency dependent dielectric peak. Overall, the properties of relaxor ferroelectrics arise from the competition of two factors, i.e. the promotion of ferroelectric (polar) order and the cation disorder which disrupts the ferroelectric order. From a crystallographic point of view, several structures exist in relaxor ferroelectrics, although macroscopically the system is cubic [28, 29, 31]. For a complete picture describing the behaviour and underlying mechanisms of relaxor ferroelectrics additional studies are required, as a common description has not been agreed by the scientific community.

2.4 Contributions to piezoelectricity

Contributions to piezoelectricity are classified into extrinsic and intrinsic. The main mechanism for extrinsic contributions is attributed to domain wall motion, but other contributions may arise such as grain boundary effects [32]. The intrinsic contributions are lattice-related, such as extension or rotation of the polarisation. The ratio of extrinsic and intrinsic contributions within polycrystalline and single crystal ceramics depend on a number of factors including composition and crystallographic structure. Generally, in polycrystalline ceramics such as PZT the intrinsic contribution is in the range 50-75% [33]. In single crystals the intrinsic contribution is greater due to the high stability of domain engineered configurations. For example, the intrinsic contribution is 95% for rhombohedral PIN-PMN-PT poled along [001]. However, it decreases when the composition of the compound is shifted towards the MPB as a result of phase instability in the vicinity of the MPB [26].

2.5 Piezoelectric materials

2.5.1 Lead zirconate titanate

Lead zirconate titanate (PZT) is one of the most studied piezoelectric materials, widely used in various sensors, actuators or transducer devices. PZT is a solid solution between PbTiO_3 and PbZrO_3 . PbTiO_3 is a ferroelectric with a perovskite structure exhibiting a tetragonal phase below 490°C - the transition temperature from the cubic phase. A relatively high tetragonal strain with a $c/a=1.063$ causes PbTiO_3 to mechanically fracture as it is cooled from the sintering temperature through the phase transition temperature and therefore very difficult to work with [27]. PbZrO_3 is also a perovskite, but exhibits antiferroelectricity (adjacent cells are oppositely polarised resulting in 0 net polarisation [9]) and therefore cannot manifest piezoelectricity. However, a solid solution between the two compounds results in a material with interesting structural and piezoelectric properties. $\text{Pb}(\text{Zr}_{1-x}\text{Ti}_x)\text{O}_3$ exhibits a Morphotropic Phase Boundary at $x\approx 0.47$ where the crystallographic phase changes from rhombohedral to tetragonal [34]. The T_C for compositions in the vicinity of the MPB is $\approx 360^\circ\text{C}$. The phase diagram of PZT has been presented in Section 2.3.3.3.

Jaffe et al. [35] were the first to reveal the high piezoelectric response in PZT with compositions around the MPB. However, PZT is very rarely used in a "pure" form and various dopants or modifiers are utilised to obtain PZT with desired properties, which may be broadly classified into *soft* and *hard* properties. Soft PZT is obtained by substituting B-site ($\text{Ti}^{4+}/\text{Zr}^{4+}$) ions with donors such as Nb^{5+} , Ta^{5+} , the A-site (Pb^{2+}) with ions such as La^{3+} and O^{2-} with F^{1-} . The higher valence state of the cation (or lower valence of the anion) introduced causes lead vacancies which results in a material with the following characteristics (relative to unmodified PZT): increased dielectric constant, high dielectric loss, low mechanical quality factor, low coercive fields. Contrarily, acceptor substitutions such as Fe^{3+} , Mn^{2+} at the B-site and K^{1+} at the A-site cause oxygen vacancies. The associated characteristics of the material (relative to unmodified PZT) are: low dielectric constant, low dielectric loss, high mechanical quality factor, high coercive fields [9]. The most common and also the most controversial acceptor dopant is Mn. A detailed study on Mn substitutions is conducted in Chapter 7. Typical values for soft and hard PZT are given in Table 2.4.

TABLE 2.4: Typical values for various properties of soft and hard PZT. From [27].

	d_{33}	k_t	Q_m	ϵ_{33}	$\tan \delta$
Soft	450	0.47	<100	1,800	0.02
Hard	290	0.47	1,000	1,300	0.005

PZT is used in a broad variety of acoustic applications in a polycrystalline form. The method of fabrication is well established making the material widely available. Furthermore, PZT thin and thick films are also available, being particularly utilised for microelectromechanical systems (MEMS) [27]. However, single crystalline PZT is extremely challenging to obtain due to incongruent melting of the material. Very limited data is available on single crystalline PZT [36].

2.5.2 Relaxor-PT single crystals

Dielectric and piezoelectric coefficients which greatly exceeded those of polycrystalline PZT have been revealed for the first time in $\text{Pb}(\text{Zn}_{1/3}\text{Nb}_{2/3})\text{O}_3\text{-PbTiO}_3$ (PZN-PT) with composition in the vicinity of the MPB on the rhombohedral side (see phase diagram in Section 2.3.3.3) and grown by a solution method [37]. High piezoelectric charge coefficient $d_{33} \approx 1500$ pC/N and electromechanical coupling factor $k_{33} \approx 0.9$ were obtained for rhombohedral PZN-PT poled along the pseudocubic direction [001]. Interestingly, the d_{33} value for PZN-PT single crystal poled along the non-polar [001] direction (here referred to as d_{33}^* to avoid confusion) was found almost double the value of d_{33} for crystals poled along the polar [111] (1500 vs ≈ 750 pC/N). The explanation was given in terms of the following equations, under the assumption that four types of domains equally distributed exist when the crystal is poled along [001]:

$$d_{33}^* = 2/\sqrt{3}Q_{11}P_S\epsilon_{11}^T \quad (2.36)$$

$$d_{33} = 2/3(Q_{11} + 2Q_{12} + Q_{44})P_S(\epsilon_{11}^T + \epsilon_{12}^T) \quad (2.37)$$

$$d_{33}^*/d_{33} = \sqrt{3}Q_{11}/(Q_{11} + 2Q_{12} + Q_{44}) \quad (2.38)$$

where Q are the electrostrictive coefficients, ϵ the dielectric constants, P_S the polarisation along the polar direction [111] and $\epsilon_{12}^T \ll \epsilon_{11}^T$. By substituting $Q_{11} = 2.4 \times 10^{-2}$, $Q_{12} = -0.86 \times 10^{-2}$, $Q_{44} = 1.6 \times 10^{-2} \text{ m}^4 \text{ C}^{-2}$ the ratio d_{33}^*/d_{33} equals 1.8.

Although these findings were revealed in 1981, the phenomenon of ultrahigh piezoelectric effect in relaxor-PT single crystal was not exploited until recently. The work

published in 1997 by Park and Shrout [38] on PZN-PT and PMN-PT single crystals triggered work on single crystal growth and structural and electrical characterisation. Various compositions have been developed and currently single crystals are classified in three generations [2] which will be separately discussed in the following subsections.

2.5.2.1 Generation I

The first generation of piezoelectric single crystals comprises pseudo-binary compounds such as PZN-PT or PMN-PT with various formulations. The addition of the ferroelectric PT end member to the relaxor ferroelectric PZN or PMN makes the compound ferroelectric (i.e. non cubic structure) at room temperature, whilst retaining relaxor characteristics.

When compared with the polycrystalline counterpart PZT, generation I single crystals show increased piezoelectric performance. Strain levels up to 0.6% with low hysteresis have been observed in PMN-PT single crystals, whereas PZT exhibits strain up to 0.2% for "soft" compositions (PZT-5H)- Figure 2.19. In addition, the piezoelectric coefficient d_{33} exhibited by PMN-PT may reach 2500 pC/N and the electromechanical coupling factor k_{33} may be as high as 0.9. Polycrystalline PZT exhibits a d_{33} in the range of 400-700 pC/N and k_{33} of 0.7. Figure 2.20 shows the comparison between single crystals and their polycrystalline counterparts for d_{33} and k_{33} .

Nevertheless, materials from this generation are not thermally stable due to low temperatures at which piezoelectric performance is degraded or even lost. The ferroelectric phase transition temperature T_{RT} (transition from a rhombohedral crystallographic phase to a tetragonal one) is in the range of 50-75°C, whilst Curie point T_C is in the range 150-179°C. Furthermore, the low coercive field E_c in the range 2-2.5 kV/cm questions the performance of PMN-PT under various drive conditions. In addition, the low mechanical quality factor Q_m of approximately 100 (some PZT compositions modified with dopants such as Mn may reach $Q_m > 1000$) represents a concern for use of this generation of crystals in high power transducers.

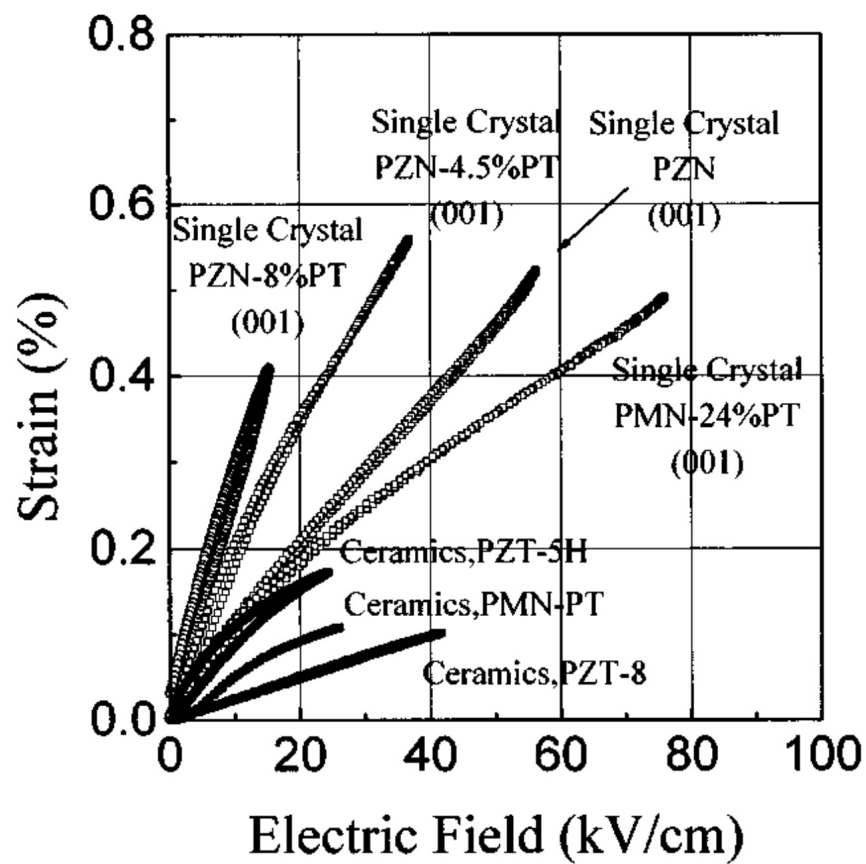


FIGURE 2.19: Strain levels achieved in single crystals compared with polycrystalline PMN-PT, soft PZT (5H) and hard PZT (8)[38].

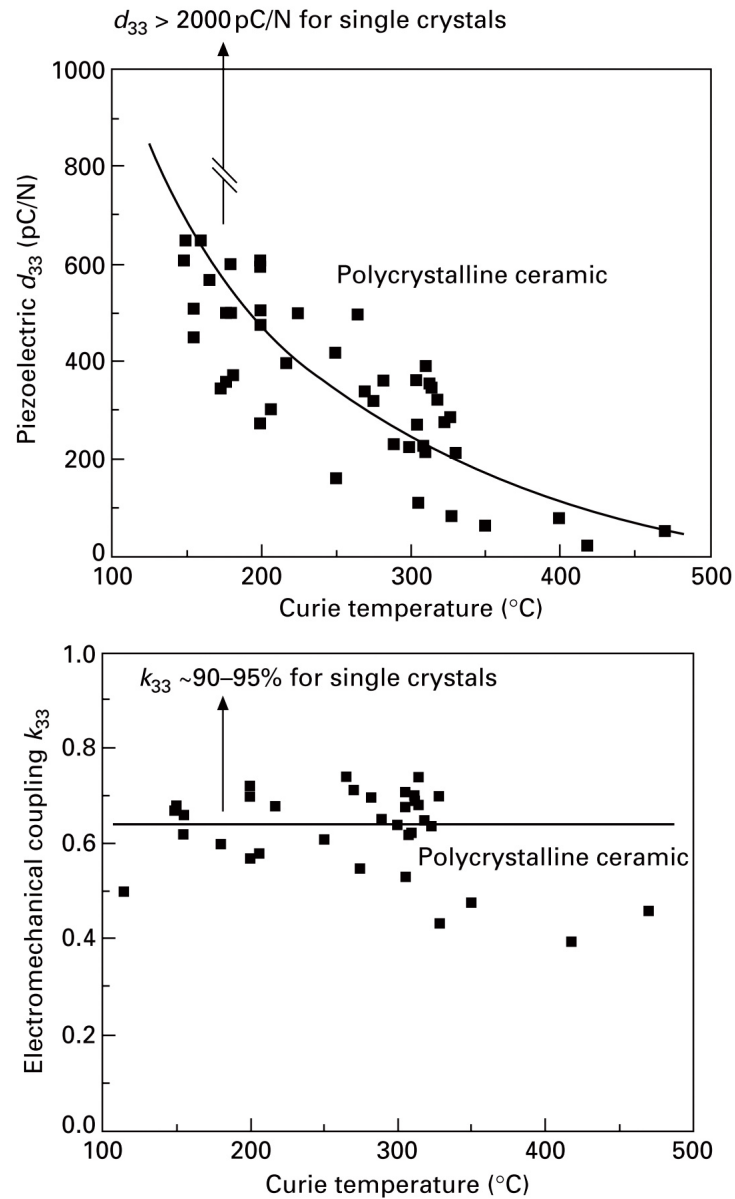


FIGURE 2.20: Piezoelectric charge coefficient d_{33} (top) and electromechanical coupling factor k_{33} (bottom) as a function of transition temperature for conventional polycrystalline material and single crystals [3].

2.5.2.2 Generation II

To overcome some of the problems exhibited by Generation I, a new single crystal compound has been developed, i.e. the pseudo-ternary PIN-PMN-PT. The addition of lead indium niobate brings the advantage of improved thermal and field stability. PIN-PMN-PT crystals show coercive field E_c in the range 4.5-11 kV/cm, a ferroelectric phase transition T_{RT} between 120-140°C and a Curie point T_C between 160-200°C. The T_C increase might be related to the tolerance factor (see Section 2.2.2) of the perovskite structure. It has been shown that a high Curie point is related to a low tolerance factor within the ABO_3 structure in ABO_3 - $PbTiO_3$ solid solutions [15]. Figure 2.21 shows transition temperature for ABO_3 - $PbTiO_3$ compounds with compositions at the morphotropic phase boundary against the ABO_3 tolerance factor. It has been suggested that $T_C > 400^\circ\text{C}$ for $t < 0.94$ [39].

Although Generation II piezoelectric single crystals may be used in a broader range of applications given their improved thermal and field stability, they are unsuitable for high power transducer applications due to their high losses. The mechanical quality factor Q_m does not improve when compared with Generation I and remains on the order of 100.

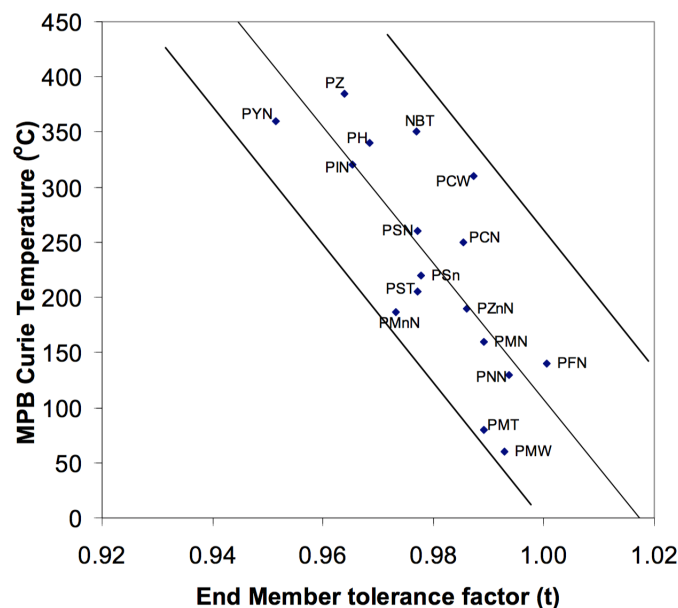


FIGURE 2.21: Curie point for ABO_3 - $PbTiO_3$ solid solutions with MPB compositions as a function of the ABO_3 tolerance factor [39].

2.5.2.3 Generation III

Mn modifications in conventional polycrystalline piezoelectrics have been known to decrease both electrical and mechanical losses. In single crystals Mn modifications have been proven to have the same effect. Mechanical quality factor Q_m is improved for both Generation I and Generation II crystals when Mn is introduced. However, Generation III consists of Mn modified pseudo ternary PIN-PMN-PT only. A detailed review of modifications with Mn in both polycrystalline and single crystal materials is given in Chapter 7.

2.6 Applications

This section aims to give a brief overview of piezoelectric applications whilst highlighting the advantages of using relaxor-PT single crystals in relation to state-of-art piezoelectric materials, such as PZT. Compared with PZT, relaxor-PT single crystals allow domain engineering and exhibit higher anisotropy which results in ultrahigh piezoelectric performance with electromechanical coupling factor $k_{33} > 90\%$ and piezoelectric charge coefficient $d_{33} > 2000$ pC/N. In addition, relaxor-PT crystals may be explored in novel vibration modes not achievable with PZT which may result in development of innovative devices.

Typical relaxor-PT single crystals explored for implementation in various devices are PZN-PT, PMN-PT, PIN-PMN-PT, Mn:PIN-PMN-PT with compositions approaching MBP from the rhombohedral side and poled along the non-polar direction [001].

Areas where relaxor-PT crystals are of particular interest are medical ultrasound transducers and sonar systems (projectors and hydrophones). Other applications include accelerometers, tactile sensors, acoustic tweezers, ultrasonic motors or pyroelectric devices.

2.6.1 Medical ultrasound transducer

One key parameter for a medical ultrasound transducer is the electromechanical coupling factor k_{33} which is related to the resolution of the device. Typically, soft PZT is the material of choice [40] with $k_{33} \approx 0.75$. The low mechanical quality factor of soft PZT $Q_m < 100$ benefits a sharp pulse detection. Relaxor-PT crystals exhibit similar

$Q_m \approx 100$, but significantly higher $k_{33} \approx 0.9$ and offer an increase in bandwidth $>15\%$ and sensitivity >3 dB which results in improved resolution. In addition, single crystals provide deeper penetration depth (or lower excitation amplitudes) and improve the signal to noise ratio of the ultrasound transducer [2].

2.6.2 Underwater projector

The projector of a sonar system requires high acoustic levels and it is used under high electrical drive conditions with high duty cycles. Hard PZT is typically used [41]. Investigations using relaxor-PT crystals revealed their higher piezoelectric charge coefficient (up to 650% higher) results in 10-15 dB higher source level or same source level for 10-15 dB lower drive field. In addition, the lower Young's modulus (up to 78% lower) results in significant miniaturisation [4] which is particularly beneficial for autonomous underwater vehicles (AUVs). The most advantageous crystal composition for underwater projector is Generation III Mn:PIN-PMN-PT which exhibits a similar Q_m as for hard PZT (≈ 1000) [2].

2.6.3 Underwater receiver (hydrophone)

Although a sonar system may have a projector and hydrophone as part of the same device, often the two are separated as the requirements are different. A receiver is used to detect underwater acoustic pressure and therefore sensitivity is a critical parameter. As opposed to projectors where typically hard PZT is preferred due to stability under high drive fields, soft PZT is desired for a receiver which exhibits higher sensitivities than hard PZT [41]. When relaxor-PT single crystals are considered, recent studies revealed that hydrophones may benefit from 7 dB higher sensitivity or 15 dB higher signal to noise ratio due to the increased piezoelectric charge coefficient compared with PZT [4].

2.6.4 Other applications

Relaxor-PT single crystals may benefit numerous other applications. One example is the piezoelectric tactile sensor. A tactile sensor is a device able to respond to external

stimuli such as pressure or temperature via contact and may be used as intraocular pressure sensors, touchscreen or fingerprint reader. Typically, poly(vinylidene fluoride), quartz and hard PZT are piezoelectric materials of choice for such devices. Relaxor-PT crystals are promising candidates not only for their higher piezoelectric performance compared with state of the art materials, but new types of tactile sensors may be designed. Specifically, the face-shear mode of relaxor-PT crystals has drawn attention due to high piezoelectric coefficient $d_{36}=1600-2800$ pC/N and high elastic compliance $s_{66}^E > 120$ pm²/N which allows a novel sensor configuration [42].

Another example is represented by acoustic tweezers which are used to manipulate particles using sound waves. Traditional materials for sono-tweezers are PZT, ZnO and LiNbO₃. Here, the stimulus for using relaxor-PT is the miniaturisation of the ultrasound transducer.

Other examples where relaxor-PT crystals are promising candidates include but are not limited to energy harvesting devices, thermal imaging, transformers, ultrasonic motors and cryogenic ultrasonic motors [2, 42, 43].

Chapter 3

Introduction to Single Crystal Growth

3.1 Introduction

Relaxor-PT single crystals play a critical role in the development of devices, particularly in underwater systems and medical applications, as highlighted in the previous chapter. It is therefore essential to establish a growth technique able to provide high quality single crystals. This chapter aims to review and discuss the available growth methods. A technique with no drawbacks is yet to be found and therefore, advantages and disadvantages are examined for each method. The level of success of a given technique is discussed in terms of the following key points:

- quality (i.e. density, cracks, defects, impurities)
- size of the grown crystal
- homogeneity
- reproducibility
- simplicity of the method (i.e. requirement for specialised equipment)
- suitable for growth of incongruent melting compounds
- requirement for post processing (alignment, slicing/dicing)
- cost of single crystal material obtained
- cost of production line set up for crystal growth.

First, generic single crystals growth methods are presented Section 3.2. Subsequently, the methods suitable for growth of relaxor-PT will be presented and discussed in Section 3.3. Section 3.4 presents the concluding remarks and explains the focus of this thesis on Bridgman and Solid State Conversion Growth.

3.2 Generic single crystal growth methods

Single crystal growth methods may be broadly classified as follows: (i) solution growth, (ii) melt growth and (iii) solid state growth. Based on this classification, Table 3.1 presents a number of methods for growth of various single crystals.

TABLE 3.1: Generic growth methods for single crystals

Melt growth		
Verneuil (or Flame fusion)	Fine particles of desired material are melted and subsequently they fuse and fall onto the upper surface of a crystalline peak. When the desired crystal size has been reached the system is cooled.	[44]
Czochralski	A seed crystal is dipped into a crucible with molten material and then slowly withdrawn.	[45]
Kyropoulos	A single crystal seed connected to an air cooled platinum finger is dipped into the melt. Crystallisation is induced by increasing the air flow through the cooling finger or by cooling the melt. In addition, a Pt wire may be used instead of a seed.	[46]
Bridgman	Crystal growth is induced from molten material by movement through a temperature gradient.	[47]
Floating zone	A small length of a polycrystalline sample in the form of a rod is melted and the molten region is moved across the crystal. The molten zone is suspended between the two solid parts of the sample. A single crystal seed might be used at one end of the sample to control the growth crystallographic direction.	[48]
Solution growth		
Solution	(Flux) Relies on spontaneous nucleation and growth from a solution upon slow cooling.	[47]
Hydrothermal	Crystallization occurs under conditions of high temperature and pressure.	[47]
Solid state growth		
Templated (Seeded)	(Solid State Conversion Growth) A seed crystal is placed on a powder compact and, under heat treatment, grows into a large single crystal.	[49, 50]

3.3 Relaxor-PT single crystal growth

The high melting point of approximately 1300°C [51] and the high volatility of Pb [3, 52] which requires a sealed crucible, reduce the number of suitable methods for growth of relaxor-PT single crystals to three, namely Solution, Bridgman and Solid State Conversion [2]. The following subsections present the growth principles for each of the three cases.

3.3.1 Solution

This technique has three main variations, i.e. Flux, Top Seeded and Flux Bridgman. Each will be discussed separately in the following subsections.

3.3.1.1 Flux

The flux method is widely explored for the growth of single crystals. It is based on spontaneous nucleation from a solution upon super-saturation during the cooling process [2]. A schematic of the experimental design is shown in Figure 3.1. The charge – a mixture of the material to be crystallised together with a flux, is placed in a platinum crucible with a platinum lid which in turn, is placed in a sealed alumina crucible. This system is then placed in a box furnace and the compound is allowed to melt and equilibrate. Subsequently, a cooling process is set up – in the range 0.5-1°C/min. When the temperature reaches a value at which crystal growth stops, the cooling is set at a higher rate, typically in the range 50-100°C/min. Once the entire process ends, nitric acid and/or acetic acid is used to dissolve the flux and remove the crystals from the crucible [2, 53]. For improved control of the nucleation a cooling system may be used at the bottom of the crucible – see Figure 3.1. This process is sometimes referred to as Bottom Cooled Solution Growth (BCSG) [54]. Another variation of the solution growth is the Top Cooled Solution Growth (TCSG). The experimental set up is shown in Figure 3.2. This technique does not make use of a seed and therefore must not be confused with the Top Seeded Solution Growth (TSSG) technique [55], presented in the next subsection. The flux method has been mostly used for the growth of PMN-PT and PZN-PT materials [2, 3, 51, 56]. Systems such as BiFeO₃-PbTiO₃ (BFPT) have also been investigated, having in view their potential high piezoelectric properties [53]. In addition, the method has been employed for the growth of ternary PIN-PMN-PT [3]. Generally, a mix of PbO and B₂O₃ is used as flux [2, 3, 51, 53, 56]. Successful growth of PIN-PT has also been reported, where a PbO-PbF₂-B₂O₃ flux has been used [57]. Unfortunately, crystals grown by flux technique are not suitable for commercialisation and implementation into devices due to several problems, as follows: compositional segregation, multiple nucleation points as well as satellite crystals, parasitic crystals, side-wall crystallisation – see Figure 3.3. In addition, important issues are represented by cracking, platinum inclusions and the relatively small size. The compositional segregation is of extreme importance as it is the reason for high variation regarding the piezoelectric and dielectric properties of the grown material. Especially for compounds

with MPB compositions or for systems where the PT content is high, the property variation is increased. Consequently, the composition of the material to be grown, as well as the choice of flux is of paramount importance [3]. The reported size of the grown crystals is typically in the mm range: ≥ 35 mm edge length for PZN-PT and ≥ 25 mm edge length for PMN-PT and PIN-PMN-PT. A flux grown PIN-PMN-PT crystal is shown in Figure 3.4. The small size results in a lack of different orientation cuts needed for property measurements. In addition, the method is costly, mainly due to the Pt crucible used [2, 3]. Probably further research regarding the flux growth technique is needed to overcome all the stated problems and to commercialise the crystals. Alternatively, the growth of single crystals may be directed towards other, more efficient methods of growth.

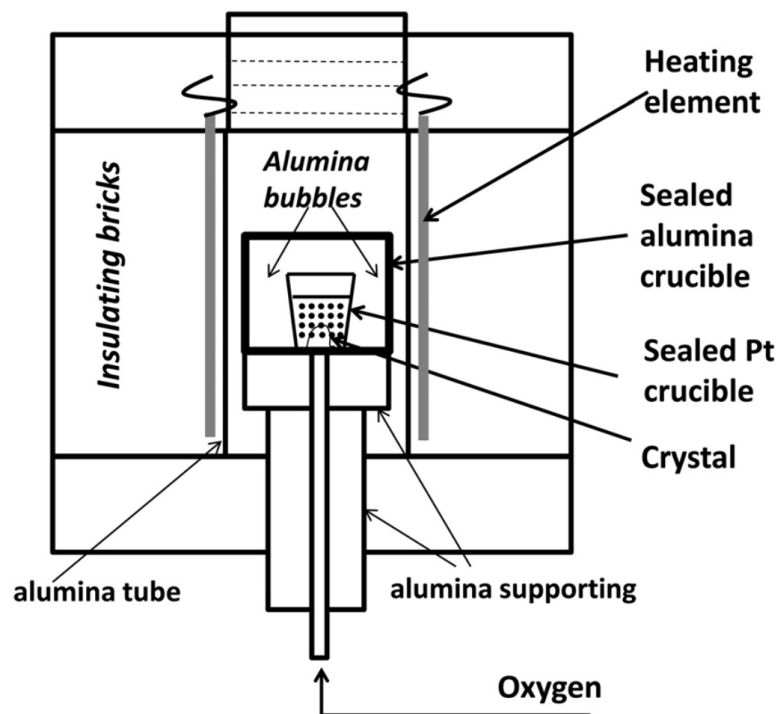


FIGURE 3.1: Schematic of the experimental design for crystal growth from flux – generally, a box resistive heating furnace is used; this schematic, however, also shows a system for oxygen gas flow which offers the advantage of local cooling and therefore, better nucleation control [2]

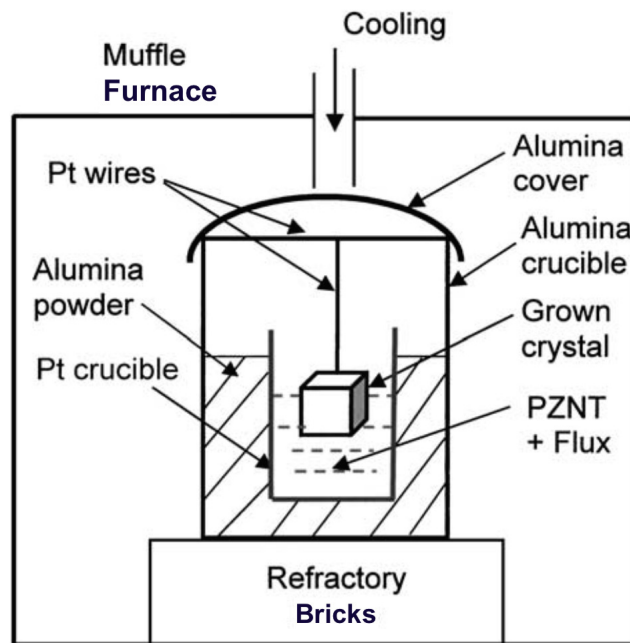


FIGURE 3.2: Experimental design of the Top Cooled Solution Growth; similarly with the conventional flux method, a Pt crucible is used for the growth inside a box furnace; the difference is the use of a cooling system triggered by a Pt wire; nucleation occurs around the wire [55]

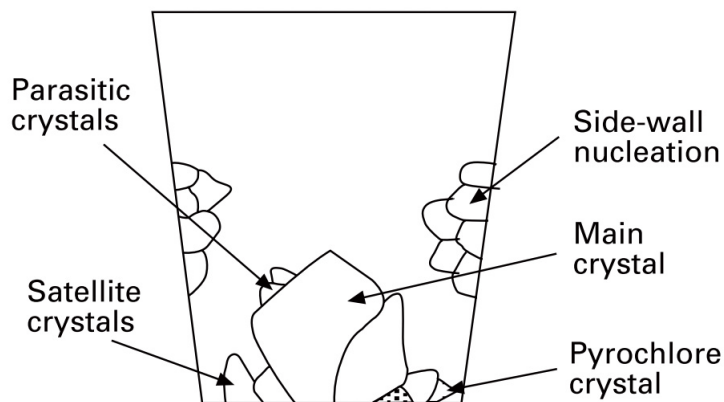


FIGURE 3.3: Typical single crystals grown by flux technique – in addition to a main crystal, other, undesirable crystals are also obtained such as satellite crystals which are growing at the periphery of the main crystal, parasitic crystals which are growing on the surface of the main crystal, side-wall nucleations and also crystals of pyrochlore

[3]

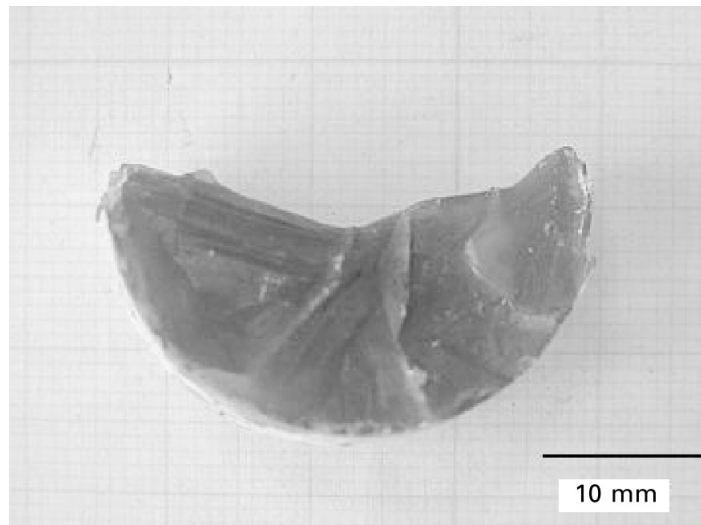


FIGURE 3.4: A flux-grown PIN-PMN-PT crystal; for the growth, 50% precalcined 16PIN-51PMN-33PT has been dry mixed with 40% PbO and 10% B₂O₃ (mol%); following 2 pre-melts at 1000°C for 1 h, the mixture has been heated at 1230°C, equilibrated for 5 h and allowed to cool with a rate of 1.2°C/h down to 850°C and then 100°C/h to room temperature; the main crystal has been removed from the crucible in 50% strength boiling acetic acid for 24 h [3]

3.3.1.2 Top-seeded solution growth

This method of obtaining single crystals has been developed as an extension to the conventional flux growth method. It has been proved that TSSG offers better nucleation control and hence, larger crystals may be obtained. Another advantage is the possibility of controlling the crystallographic direction of growth.

As the name suggests, the principle of this technique is based on a small single crystal, i.e. a seed, which is attached to a Pt wire and lowered into the platinum crucible to make contact with the molten material. A schematic of the experimental design is shown in Figure 3.5. TSSG of PIN-PMN-PT has been investigated by Li. et al [58, 59] and the size of the obtained crystals was approximately 35 x 35 x 15 mm³ - Figure 3.6, which shows an improvement when compared to crystals grown by conventional flux method [58, 59]. Nevertheless, the size remains relatively small and further research is required.

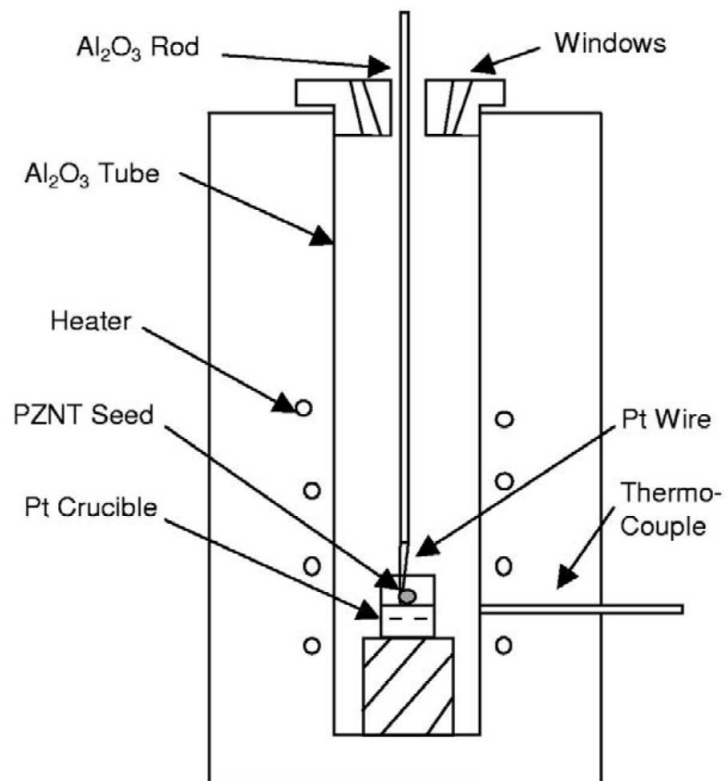


FIGURE 3.5: Experimental set-up for TSSG; the design is very similar to that for conventional flux growth, however, a seed single crystal is used to induce nucleation within the solution, which is attached to a Pt wire, in turn, supported by an alumina rod [3]

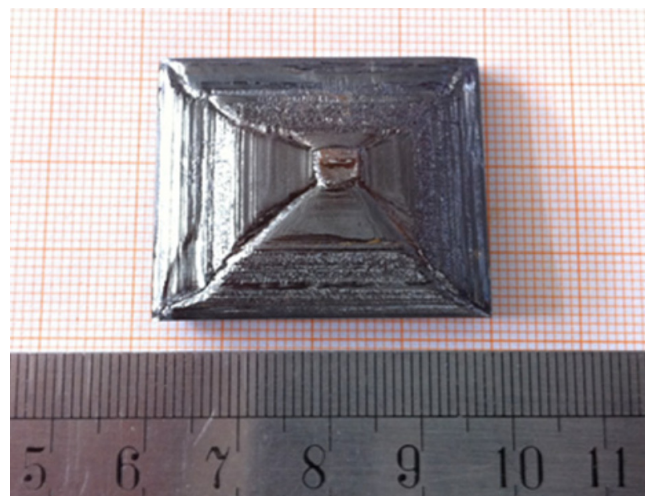


FIGURE 3.6: 19PIN-46PMN-35PT grown by TSSG by Li et al. [58].

3.3.1.3 Flux Bridgman

The flux Bridgman is a combination between conventional flux growth and modified Bridgman (following subsection). Generally, Bridgman method consists of growing single crystals in a vertical furnace in which a hot zone and a cold zone exist, so that a thermal gradient is created between the two. The flux Bridgman is particularly used for the growth of PZN-PT crystals, because PZN-PT melt is stable in a perovskite phase only in PbO flux [60]. The technique consists of loading a platinum crucible with the precursor material and PbO flux and subsequently sealing it. The crucible is then placed into an outer alumina crucible. Often, alumina powder is used to fill in the gap between the two crucibles. An oxygen cooling system is set at the bottom of the crucible to induce nucleation – similar to the conventional flux growth - Figure 3.1. Once the material melted, the crucible system is lowered through the temperature gradient with a rate of 0.1-0.6 mm/h. Growth of large crystals has been reported, up to 75 mm in diameter and 55 mm in length and with varying orientations from [111] to [100] [2].

3.3.2 Modified Bridgman (Bridgman-Stockbarger, Vertical Bridgman or Bridgman)

Bridgman was the first who, in 1925, obtained single crystals by passing a container with molten material through a thermal gradient. The procedure involved lowering the container directly outside the furnace. Therefore, crystallisation was induced from one end, along the length [61]. Later, in 1936, Stockbarger used two furnaces on top of each other. Within the first one, a temperature above the melting point of the material to be grown was set, whilst in the second, a temperature below the melting point was set. Hence, a thermal gradient was created in between the two furnaces and crystal growth was induced by lowering a crucible from the first furnace towards the second one [62]. This method is particularly beneficial as by adjusting the temperatures in the two zones, the thermal gradient can be tuned and thermal shock is avoided. The set-up evolved in that a single furnace with two (or more) independently controlled zones is now used. The method is referred to as *Bridgman-Stockbarger*, *Modified Bridgman*, *Vertical Bridgman* or simply *Bridgman* throughout the literature. Within this thesis the method is referred to as Bridgman. A schematic diagram of the method is shown in Figure 3.7 and typical Bridgman-grown crystals are shown in 3.8.

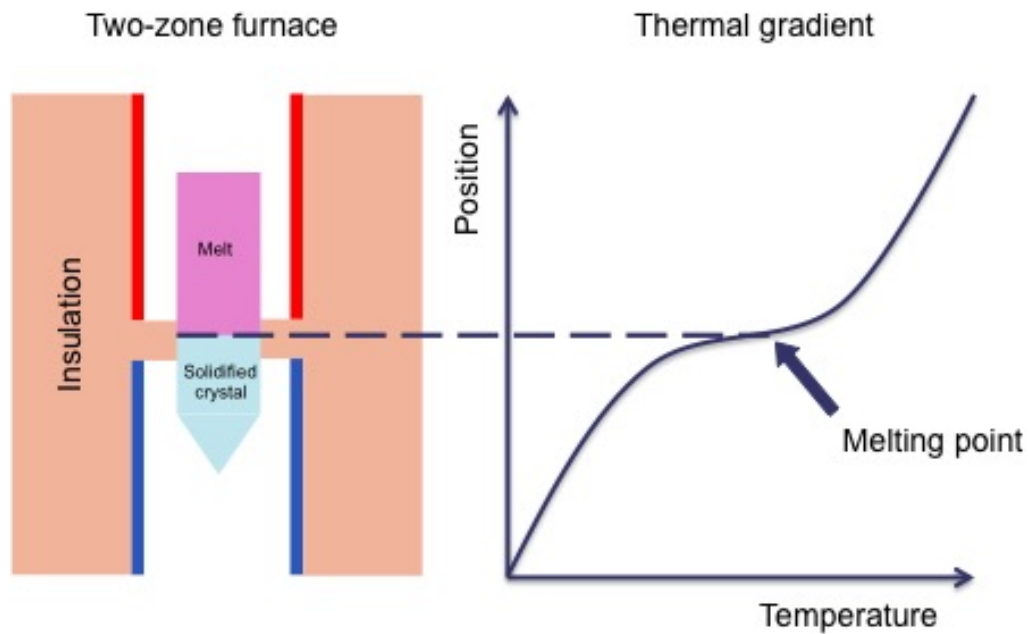


FIGURE 3.7: Graphic representation of the Bridgman technique: Bridgman furnace (left) and associated thermal profile (right). A crucible containing the material to be grown is placed into the upper (hot) zone of a furnace and slowly lowered through a thermal gradient towards the second (cold) zone of the furnace so that nucleation is induced and the crystal grows from one end to another.

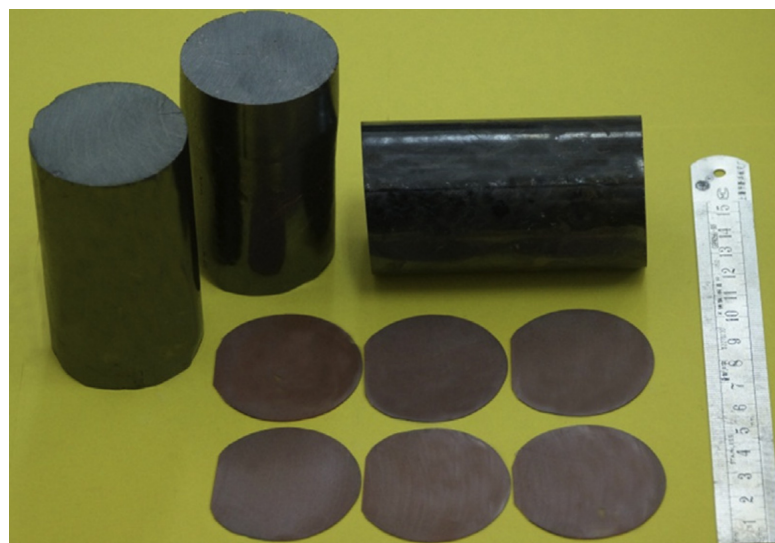


FIGURE 3.8: 0.5mol% Mn-doped 15PIN-55PMN-30PT Bridgman grown single crystal. From [63].

For growth of relaxor-PT crystals, a Pt crucible is used as container, due to the harsh conditions, i.e. high melting point and corrosive materials. The Pt container is single use as it needs to be cut to remove the crystal at the end of the process. The lowering rate through the thermal gradient is typically in the range 0.1-1 mm/h and the thermal gradient between the two zones is in the range 30-50°C/cm.

The orientation of the grown crystal may be controlled by placing a single crystal seed at the bottom of the crucible. In this case, the position of the crucible inside the furnace must be carefully chosen so that part of the seed will be below the melting point and part above. Consequently, the crystal will grow with the same orientation as the seed [2, 64]. This strategy is particularly useful since relaxor-PT exhibit high piezoelectric performance along certain crystallographic directions. Moreover, growing a crystal with known direction of growth facilitates the process of sample dicing. A single crystal grown from a seed is shown in Figure 3.9.



FIGURE 3.9: 25PIN-44PMN-31PT single crystal, 55 mm diameter and 100 mm length grown from a (110) oriented seed. From [65].

A major disadvantage of the Bridgman method is a compositional gradient developed along the direction of growth as a result of Ti segregation. The segregation behavior is described by the following equation:

$$C_S = C_0 e^{\frac{1}{k-1}x} \quad (3.1)$$

where C_S is the concentration in the solid, C_0 the initial melt concentration, k the effective segregation coefficient and x the length of the crystal [66]. The segregation coefficient of Ti is <1 , i.e. in the range 0.83-0.85 [67, 68] and therefore segregates at the liquid/solid boundary by diffusion to the liquid phase. Consequently, the composition varies along the length of the boule - Figure 3.10. As a result, properties of the material also vary along the length [64, 69, 70]. Therefore, only a certain percentage of the crystal will have required properties.

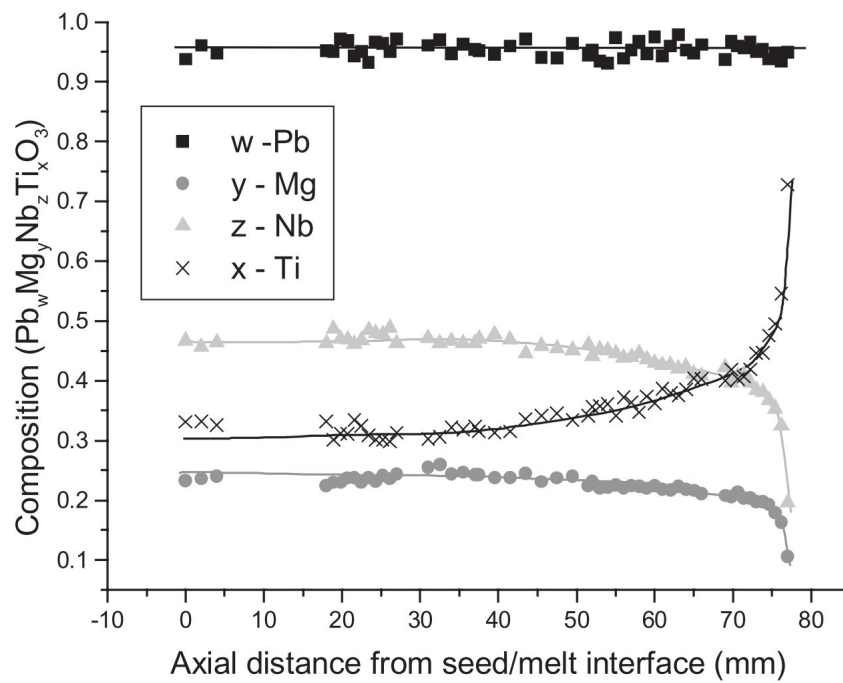


FIGURE 3.10: Compositional variation of the chemical constituents along a PMN-35PT single crystal boule. Ti concentration is seen to increase along the boule, particularly towards the end. From [67].

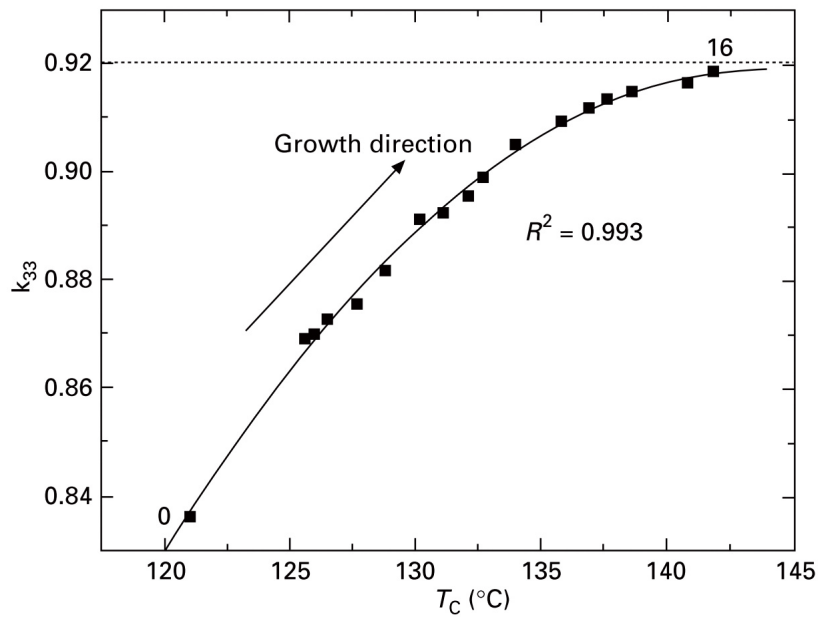


FIGURE 3.11: Variation of the electromechanical coupling factor k_{33} versus Curie point T_C measured along a PMN-31PT single crystal boule. k_{33} increases from one end of the boule to the other following the increase in Ti content due to segregation. From [3].

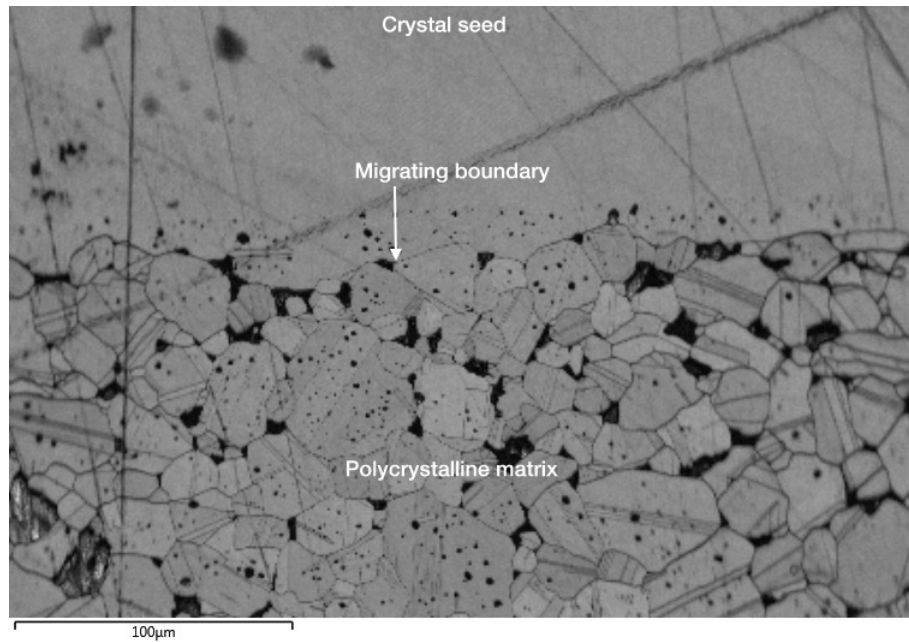
To improve the homogeneity along the boule a number of new approaches have been suggested. These will be presented in Section 5.5 of Chapter 5, as they are not established techniques, but rather suggestions for future investigations.

In addition to the homogeneity problem, the cost is another issue that needs to be addressed. The cost of Bridgman grown crystals is relatively high, partly due to the varying properties along the boule and partly due to the use of Pt crucibles. In addition, relative to conventional technologies of ceramic material processing, the technique requires expensive specialised equipment. As a result, ceramic processing industry of conventional piezomaterials may find this an impediment and delay or even refuse the production and commercialisation of the new generations of piezomaterial such as single crystals.

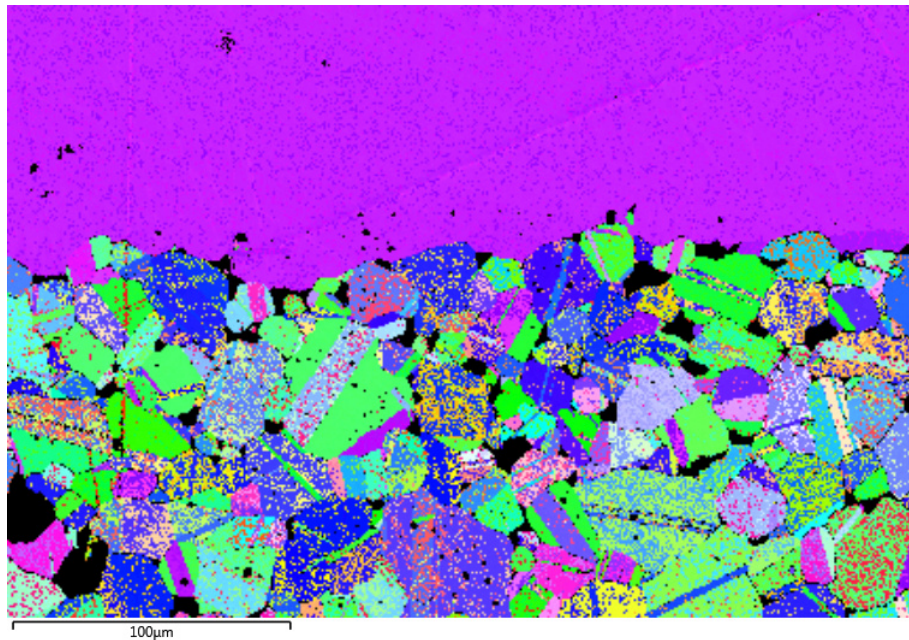
3.3.3 Solid State Conversion Growth

Solid State Conversion Growth (SSCG) is a solid to solid transformation where a polycrystalline material is converted into a single crystal via heat treatment. The initial polycrystalline sample is prepared by conventional ceramic processing techniques. Subsequently, a single crystal seed is bonded by diffusion to the sintered polycrystalline sample (or embedded in calcined powder) and annealed at temperatures 100-200°C below the melting point of the material to be grown. The seed grows by consuming the grains in the polycrystal (*Ostwald ripening*) or, in other words, the seed boundary migrates through the polycrystal. The concept is illustrated in Figure 3.12. The single crystal used as seed may be grown by other methods such as Bridgman or flux and it has to be chemically stable within the polycrystal, as well as to be compatible from a crystallographic point of view. BaTiO_3 , $\text{Ba}(\text{Zr}_x\text{Ti}_{1-x})\text{O}_3$ or $\text{Pb}(\text{Mg}_{1/3}\text{Nb}_{2/3})\text{O}_3$ - PbTiO_3 have been used as seeds for the growth of relaxor-PT single crystals. SrTiO_3 has also been studied, however it has been proved to be chemically unstable in relaxor-PT systems [2, 3, 71].

The conversion mechanism is based on grain growth mechanisms and therefore a good understanding of the grain growth behavior in the polycrystalline matrix is critical and will be discussed in the following subsection.



(A) Scanning Electron micrograph showing the SSCG concept - the boundary of a single crystal seed migrates through the polycrystalline matrix promoting crystal growth. Note the single crystal seed is pore free, whilst the grown crystal and the polycrystalline matrix contain pores. Any pores or other defects present in the polycrystalline matrix are transferred to the grown single crystal.



(B) Electron Back-Scatter Diffraction image showing the conversion of grains into a single crystal of the same orientation as the seed (purple) and grains within the matrix with different crystallographic orientations (different colors).

FIGURE 3.12: SSCG concept proved in BaTiO_3 - electron micrograph (A) and Electron Back-Scatter Diffraction image (B). The polycrystalline BaTiO_3 sample has been sintered at 1290°C for 2 h and a BaTiO_3 seed has been diffusion bonded via heat treatment at 1200°C for 2 h with a 1 kg weight. Crystal growth was promoted at 1350°C . The experiment was conducted as trial crystal growth within this work to prove the SSCG concept and is not presented in future sections.

3.3.3.1 Grain growth in polycrystalline systems

When a polycrystalline material is heat treated, the size of grains within the matrix increases. The reason for this process is a decrease in interfacial energy per unit volume as the boundary area decreases. The driving force for grain growth is related to the curvature of the grain boundaries. Boundaries move towards their centre of curvature and therefore a grain with more than six sides will expand, whilst a grain with less than six sides will be consumed. Grains with six sides do not exhibit curvature and boundaries equal in energy meet at three grain junction with 120° angles. This is a two-dimensional case and a schematic representation is shown in Figure 3.13. In a three-dimensional scenario the net curvature of the grain determines the direction of boundary migration.

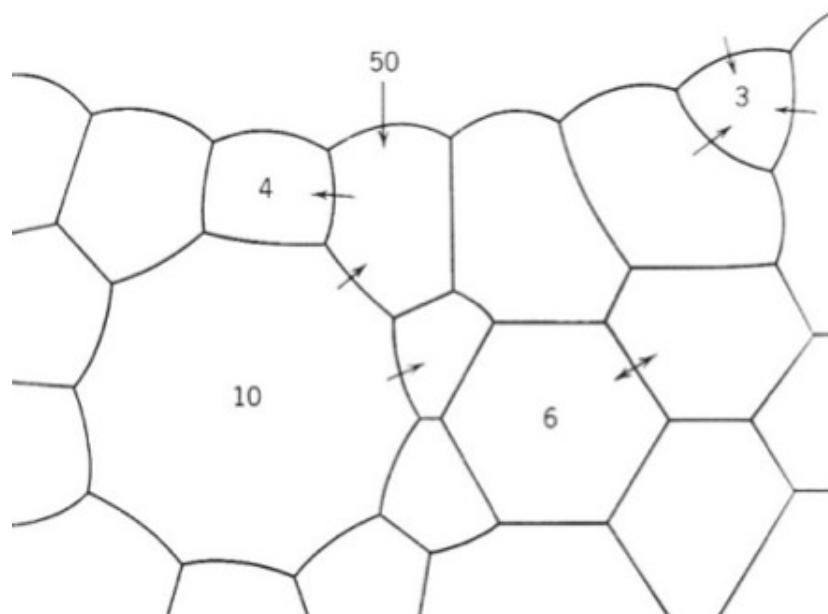


FIGURE 3.13: Two dimensional representation of grains with different sizes in a polycrystalline matrix. Direction of growth upon heat treatment depends on the curvature of grain boundaries and it is marked by the arrows. From [72].

In theory, polycrystalline systems exhibit two types of grain growth behavior, i.e. normal and non-normal. The first scenario, normal growth, is characterised by a single modal size distribution where the size of all grains increases in the same manner. In the second scenario, non-normal (or discontinuous) growth, some grains grow faster and therefore larger than others. An extreme case of non-normal growth is represented by Abnormal Grain Growth (AGG) where a bi-modal size distribution is present. Figure 3.14 shows a representation of the size distributions for normal and abnormal

growth.

In practice, a normal growth behavior is rare and most systems exhibit non-normal grain growth.

Although under investigation, several mechanisms have been suggested to influence grain growth (including AGG), as follows:

- grain boundary complexion transitions (phase transformations which occur at the grain boundaries) [73]
- pore drag mechanism (pores that are attached to the grain exert a drag force and decrease the velocity of the migrating boundary) [72]
- liquid film at the grain boundaries (secondary phases at grain boundaries which become liquid at the sintering/annealing temperature and increase or, in certain cases, decrease boundary mobility) [72]

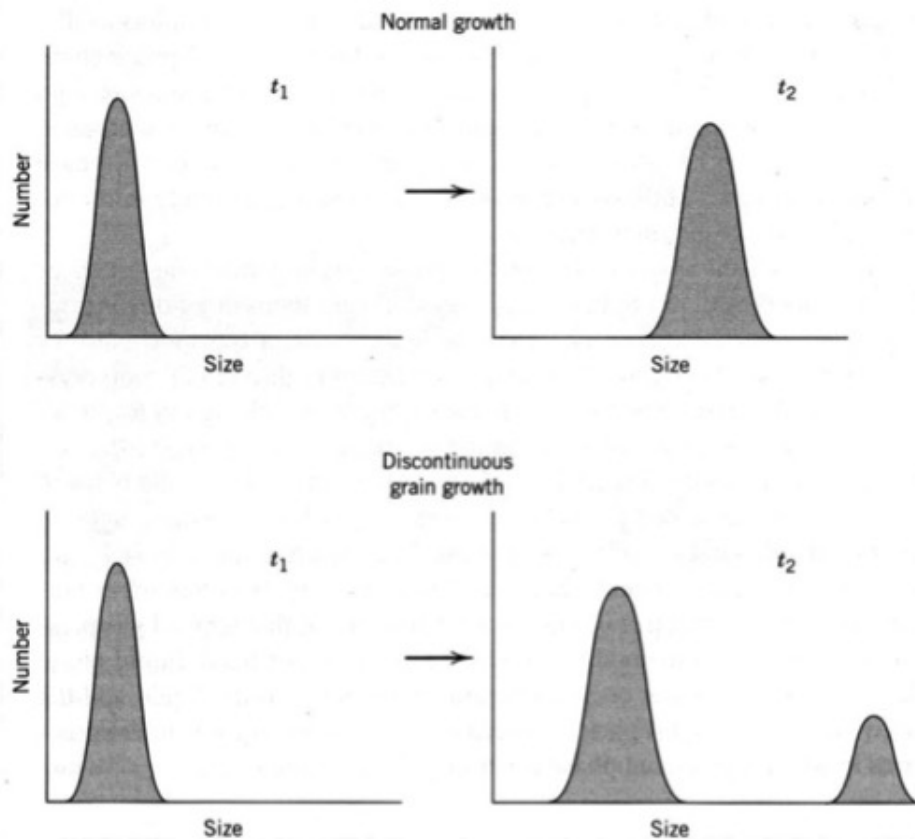


FIGURE 3.14: Schematic representation of size distributions for Normal growth (top) and Discontinuous growth (bottom). From [72].

3.3.3.2 Single crystal growth studies

Grain growth in polycrystalline materials is a complex process [72] and the level of complexity increases for single crystal growth from polycrystalline materials. This subsection presents a limited number of factors with impact on crystal conversion.

Liquid film approach

A common approach for crystal growth from the solid state is the use of a liquid film at the grain boundaries which enhances boundary mobility. A liquid film in relaxor-PT systems is typically achieved via additions of PbO which becomes liquid at the annealing temperature ($>800^{\circ}\text{C}$). Growth of 5 mm thick single crystal has been reported for PMN-PT with 8mol% excess PbO from a (011) oriented BaTiO₃ seed when annealing at 1200°C for 200 h [74].

Grain size in the polycrystalline matrix

To successfully convert a polycrystalline material into a single crystal via heat treatment from a seed, growth at the seed-polycrystal interface must be promoted, whilst grain growth within the matrix must be suppressed. Therefore, an important role in this respect is played by the size of the grains in the initial polycrystalline system and their growth behavior upon annealing.

Ideally, the matrix should be very fine as the smaller the grain size the higher the boundary velocity [72]. However, during annealing of a fine grained matrix it is very likely that grain growth will occur and therefore the chances to obtain a relatively large crystal decrease dramatically. Therefore, one must find a way to stop growth within the matrix, but promote growth at the seed-matrix interface. One suggested approach is based on the Primary and Secondary Abnormal Grain Growth (PAGG and SAGG). PAGG is completed when all grains within a matrix have been replaced by abnormal grains and occurs at a specific temperature. Once PAGG is completed, if the polycrystalline material is heat treated again at a higher temperature than that when PAGG occurs, the abnormal grains may start growing again to even larger sizes leading to SAGG [75]. It is suggested that annealing for crystal conversion should occur at a lower temperature than that where SAGG starts, in a matrix where PAGG is completed. For PIN-PMN-PT system, it is suggested that grain size should be in the range 80-160 μm [71].

Seed orientation

The crystallographic orientation of the seed (i.e. the growth direction of the crystal) influences the quality of the converted crystal, particularly when conversion of a matrix which contains excess PbO is considered. When a (111) oriented seed is used, the crystal is of lower quality as large amounts of trapped PbO are observed. However, when (001) seed is used no trapped PbO is observed. (001) is the slowest growth direction and therefore PbO moves along with the growth front rather than being left behind and trapped as for (111) [76].

Discussion

Although mechanisms of grain growth in polycrystalline materials and subsequently mechanisms for crystal conversion are yet to be understood, SSCG is a very promising technique. First, homogeneous crystals may be grown as the technique does not involve melting and therefore segregation is avoided. Second, crystals with predetermined shape and already aligned in the desired crystallographic orientation may be grown thus bypassing the need for post-processing. Third, materials which melt incongruently such as PZT may be grown. In addition, platinum crucibles are not required anymore and conventional alumina ware may be used thus reducing the cost. Finally, the method does not require any specialised equipment and once established it can be easily implemented in any factory which processes conventional ceramics. Although the grown crystals may be of lower quality (i.e. less dense) when compared with crystals grown from the melt, SSCG might be the preferred technique for mass production of single crystals as a result of the advantages presented. Therefore, greater efforts are needed to understand the mechanisms involved in grain/crystal growth and to ensure reproducibility of the technique.

3.4 Conclusion

This chapter has presented the three methods suitable for growth of relaxor-PT crystals, namely Solution, Bridgman and SSCG. It was decided not to explore the Solution technique within this work as a consequence of the limited crystal size which can be obtained. Small crystals are difficult to characterise and are impractical in applications such as low-frequency devices which require large crystals.

Therefore, this work explores Bridgman and SSCG techniques. Bridgman is the most

successful technique for growth of relaxor-PT single crystals despite the inhomogeneity along the boule and the cost. Large, high quality single crystals may be grown with a high degree of reproducibility. Furthermore, SSCG is a promising technique owing to the possibility of obtaining homogeneous crystals with pre-determined shape at the same cost as for conventional ceramics. However, a considerable amount of work is required.

Chapter 4

Powder Synthesis

4.1 Introduction and Background

4.1.1 Introduction

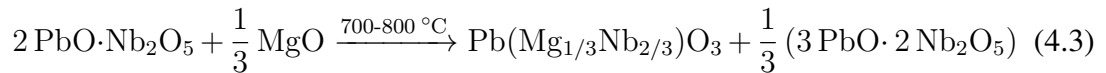
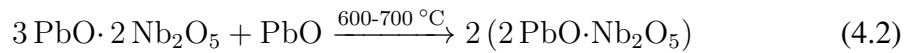
This chapter aims to give a general review of the method used to synthesize ceramic material. Specific conditions or any modifications to the this method are given alongside every experiment presented within the thesis.

PIN-PMN-PT in a powder form has been prepared via the mixed oxide route. The method consists of mixing in a stoichiometric manner raw oxides, i.e. PbO , In_2O_3 , $(\text{MgCO}_3)_4 \cdot \text{Mg}(\text{OH})_2 \cdot 5\text{H}_2\text{O}$, Nb_2O_5 and TiO_2 together with binders and dopants or modifiers such as MnO_2 and heating the compound to a certain temperature below the melting point to drive a solid state reaction between the constituents [13]. A two step method has been employed. The columbite-like MgNb_2O_6 and wolframite-like InNbO_4 have been pre-synthesised prior to mixing with the rest of the oxides to obtain the final PIN-PMN-PT compound. The composition has been chosen in the vicinity of the Morphotropic Phase Boundary. These aspects are detailed in Section 4.1.2. The experimental procedures are presented in Section 4.2. X-Ray Diffraction (PANalytical X'Pert Diffractometer, Phillips, The Netherlands) has been used to asses the purity and phase of the synthesized powder. Scanning Electron Microscopy (Carl Zeiss EVO MA15, Carl Zeiss Microscopy, Germany) has been used to analyse the particle size and shape. The results are presented in Section 4.3. A summary will be provided at the end of the chapter in Section 4.4.

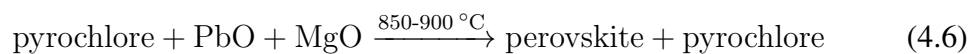
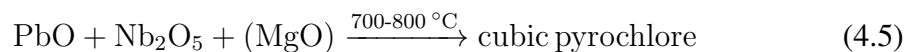
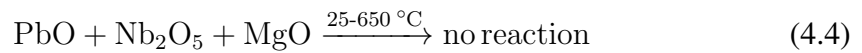
4.1.2 Background

4.1.2.1 Pre-synthesis steps

The rationale behind presynthesising MgNb_2O_6 and InNbO_4 is given in this subsection. Pre-synthesis of niobium and magnesium oxides has been first suggested by Swartz and ShROUT [77] as a method to fabricate $\text{Pb}(\text{Mg}_{1/3}\text{Nb}_{2/3})\text{O}_3$ with a pure perovskite phase. Without the pre-synthesis step, that is if PbO , Nb_2O_5 and MgO are all mixed in a single step, a stable pyrochlore forms as a result of a reaction between PbO and Nb_2O_5 . A pyrochlore structure is generally described by the formula $\text{A}_2\text{B}_2\text{O}_7$ which is isostructural to the mineral pyrochlore $(\text{NaCa})(\text{NbTa})\text{O}_6\text{F}(\text{OH})$. The structure is described in detail in a review by Subramanian et al. [78]. When processing $\text{Pb}(\text{Mg}_{1/3}\text{Nb}_{2/3})\text{O}_3$ without the pre-synthesis step, Inada [79] suggested the following reactions occurring during the thermochemical reaction:



where $\text{Pb}_3\text{Nb}_4\text{O}_{13}$ is a cubic pyrochlore and $\text{Pb}_2\text{Nb}_2\text{O}_7$ a rhombohedral pyrochlore. A perovskite phase could only be obtained by multiple calcination steps with long dwell times (24 h) which considerably increased the processing time. Swartz and ShROUT [77] also suggested formation of intermediate phases although with no formation of the rhombohedral pyrochlore, as follows:

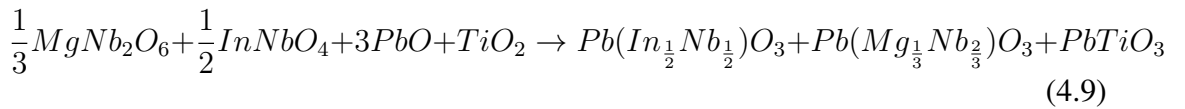
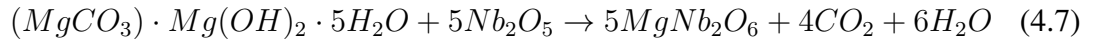


The study concluded that a pure $\text{Pb}(\text{Mg}_{1/3}\text{Nb}_{2/3})\text{O}_3$ with a perovskite phase may be obtained via bypass of the lead and niobium oxides reaction. It has been proved that pre-reaction of niobium and magnesium oxides to form MgNb_2O_6 prior to mixing with PbO is essential to avoid unwanted phases.

Following the same reasoning, pre-synthesis of indium and niobium oxides is a common practice [80]. However, Wang et al. [81] suggested that this step is unnecessary

as In_2O_3 reacts more readily with Nb_2O_5 rather than PbO and no secondary phases are formed.

It is beyond the scope of this study to examine the reactivity of oxides and therefore both MgNb_2O_6 and InNbO_4 have been pre-synthesised. For each step, chemical equations are provided in the following lines:



4.1.2.2 Choice of composition

Due to the increased performance of relaxor-PT solid solutions with compositions in the Morphotropic Phase Boundary (MPB) area as discussed in Chapter 3, the formulation of the material studied within this work has been chosen in this region. Table 4.1 presents typical compositions at the MPB of Bridgman grown PIN-PMN-PT and their dielectric, piezoelectric and ferroelectric properties. As a result of the compositional gradient along the Bridgman grown crystal, properties will depend on the location along the boule. Consequently, for crystals with the same nominal composition different properties may be reported as shown in Table 4.1.

The thesis does not engage with studying a range of compositions and therefore only one is used for experiments throughout the work. When choosing the formulation, Ti segregation during Bridgman growth has been taken into account. As a result of the segregation, the upper side of the boule is Ti rich and results in a tetragonal structure. Therefore, the formulation has been chosen slightly on the rhombohedral side of the phase diagram - Figure 4.1, to ensure the overall composition of the boule is across the MPB.

TABLE 4.1: Dielectric, piezoelectric and ferroelectric properties of [001] poled PIN-PMN-PT grown by Bridgman with nominal compositions in the MPB area. Description of symbols and abbreviations are listed in the beginning of the thesis.

Nominal composition			Dielectric properties		Piezoelectric properties		Ferroelectric properties		Reference
PIN	PMN	PT	ϵ_r	$\tan\delta$ (%)	d_{33} (pC/N)	k_{33} (%)	T_{FF} (°C)	E_c (kV/cm)	
28	40	32	4400	0.4	1500	92	130	5	[82]
28	40	32	5200	0.5	1700-2200	92	119	10.88	[83]
27	40	33	7244	≤ 2	2742	95	96	5.5	[84]
25-35		30-32	4000-4400	≤ 2	1130-1510	89-92	125	5.5	[85]
24	44	32	4289	≤ 0.5	1301	86	110	5.88	[64]

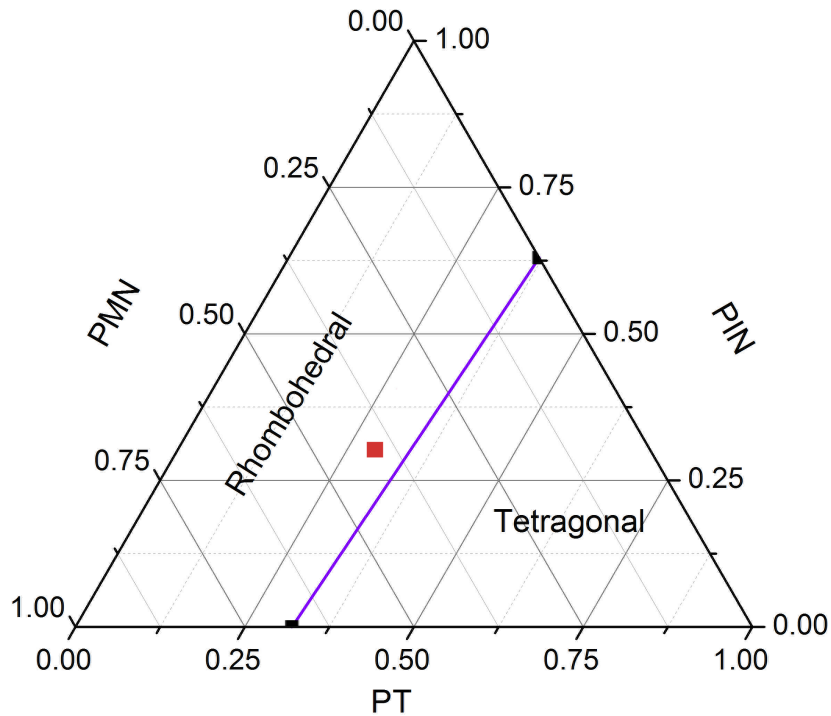


FIGURE 4.1: Phase diagram of PIN-PMN-PT. The purple line represents the boundary between the rhombohedral and tetragonal crystal structures, whilst the red dot marks the composition studied within this work

4.2 Experimental Procedure

Commercially available raw oxides have been used as starting materials for synthesis of PIN-PMN-PT, as follows: PbO 99.9+%, In_2O_3 99.99%, $(\text{MgCO}_3)_4 \cdot \text{Mg}(\text{OH})_2 \cdot 5\text{H}_2\text{O}$ >99%, TiO_2 99.9+% and Nb_2O_5 99.9% (Sigma-Aldrich). The processing path is

shown in the flow chart of Figure 4.2. The next subsections give details for each of the steps.

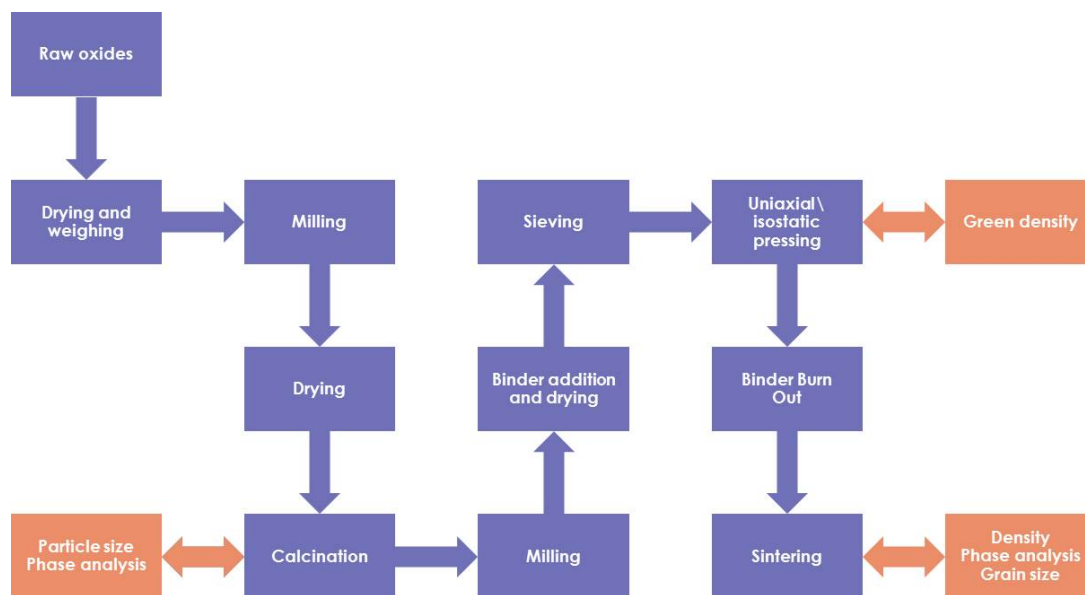


FIGURE 4.2: Flow chart of the processing path for material preparation. The purple boxes indicate processing experimental methods, whilst the brown boxes indicate characterisation techniques.

4.2.1 Drying and weighing

The starting chemicals were dried at 120-130°C (≥ 24 h) to remove moisture. This step ensures accurate weighing and therefore a stoichiometric mixture of the raw materials.

4.2.2 Attrition milling (1)

Powders were mixed in iso-propan-2-ol for 60 minutes, using 0.3 or 0.5 mm diameter yttria stabilised zirconia media in a DYNO Mill (KDLA, Switzerland) attrition mill unless otherwise stated. Milling was necessary to homogenize the mixture and obtain a more uniform particle size.

4.2.3 Drying

Following milling, powders were dried in a kitchen mixer Kenwood Cooking Chef KM080 with induction heating. The apparatus ensured thorough mixing whilst drying,

which resulted in a homogeneous compound. Subsequently, the powder was sieved through a 300 μm plastic mesh to obtain a free flowing powder.

4.2.4 Calcination

This step offers the conditions for a thermochemical reaction which enables the constituents of the powder to interact. As presented in the first section of this chapter, PIN-PMN-PT has been synthesised in two steps - first MgNb_2O_6 and InNbO_4 were prepared and in a final step PIN-PMN-PT. MgNb_2O_6 has been calcined at 1150°C [86, 87], whilst InNbO_4 at 1100°C [88, 89]. PIN-PMN-PT has been calcined at 800°C [25, 90, 91]. In all cases a heating and cooling rates of 300°C/h and a dwell of 4 h have been set.

4.2.5 Attrition milling (2)

Calcined powders were ground using pestle and mortar and subsequently sieved. A second attrition mill step at this stage ensured homogeneity. The milling was performed under the same conditions as the first milling step.

4.2.6 Binder addition

Following milling, the compound has been placed in the mixer with 0.2solids% dispersing additive (BYK-154, BYK Additives and Instruments, Germany) and 1% binder (Glascol HA4, Allied Colloids, United Kingdom). The dried compound has been subsequently sieved and a free flowing powder has been obtained.

4.2.7 Pressing

Calcined powder was then pressed into shapes of various sizes depending on the intended experiment. Typically, samples were uniaxially pressed using a hydraulic press and dies of various sizes at 20 MPa. To increase green density, samples were further cold isostatically pressed at 200 MPa for 5-10 min.

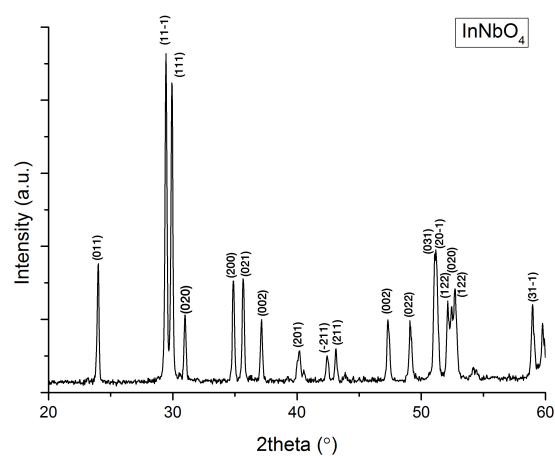
4.2.8 Sintering

Sintering regimes will be provided separately within each experiment. PIN-PMN-PT is generally sintered at temperatures between 1100 and 1250°C for different dwell times [88].

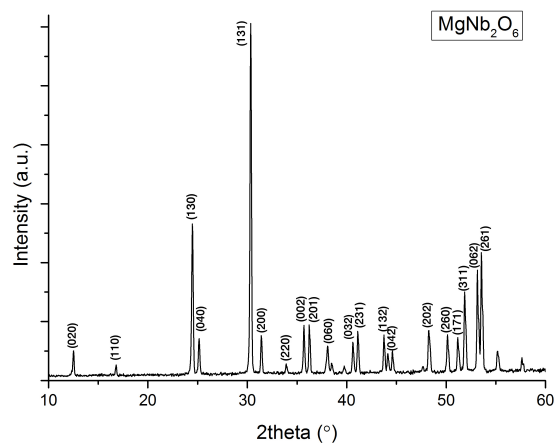
4.3 Characterisation of powder prepared

4.3.1 X-ray Diffraction

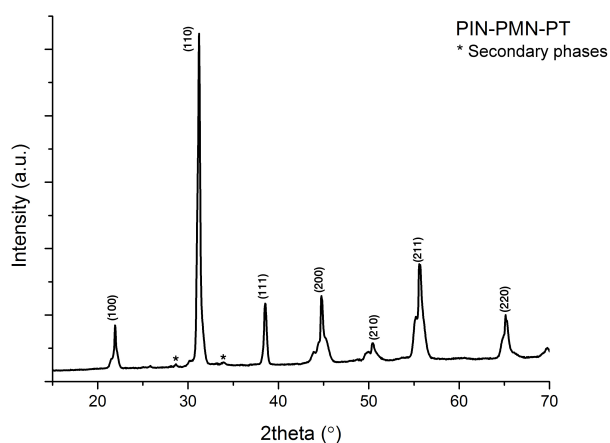
X-ray diffractograms for calcined MgNb_2O_6 , InNbO_4 and PIN-PMN-PT are shown in Figure 4.3. MgNb_2O_6 and InNbO_4 have been obtained with a pure phase with no secondary phase or impurities. PIN-PMN-PT has been obtained mainly with a perovskite phase, however minor peaks are present which may be related to residual secondary phases. The minor peaks may be associated with $\text{Pb}_3\text{Nb}_4\text{O}_{13}$, $\text{Nb}_2\text{Pb}_{1.5}\text{O}_{6.5}$, $\text{Pb}_{1.45}\text{Nb}_2\text{O}_{6.26}$ and/or PbO as revealed by analysing data obtained with Highscore software in conjunction with PDF4 database of the International Centre for Diffraction Data.



(A) Powder XRD pattern for InNbO_4 calcined at 1100°C for 4 h. Literature [92] confirms a pure phase InNbO_4 has been obtained.



(B) Powder XRD pattern for MgNb_2O_6 calcined at 1150°C for 4 h. Literature [93] confirms a pure phase MgNb_2O_6 has been obtained.



(C) Powder XRD pattern for PIN-PMN-PT calcined at 800°C for 4 h. Literature [69] confirms a PIN-PMN-PT with a perovskite structure has been obtained with a minor amount of secondary phases.

FIGURE 4.3: X-ray diffraction patterns of calcined compounds.

4.3.2 Scanning Electron Microscopy

Electron micrographs of the powders synthesized as well as the fracture surface of a sintered pellet are shown in Figure 4.4. The powders show agglomerated particles. MgNb_2O_6 powder has more rounded particles, whilst InNbO_4 and PIN-PMN-PT present more irregular shapes. Observed particle sizes are 0.5-1 μm for InNbO_4 and 0.5-3 μm for MgNb_2O_6 . For PIN-PMN-PT powder it is more difficult to distinguish the range of diameters. Sintered PIN-PMN-PT shows a grain size of up to 10 μm .

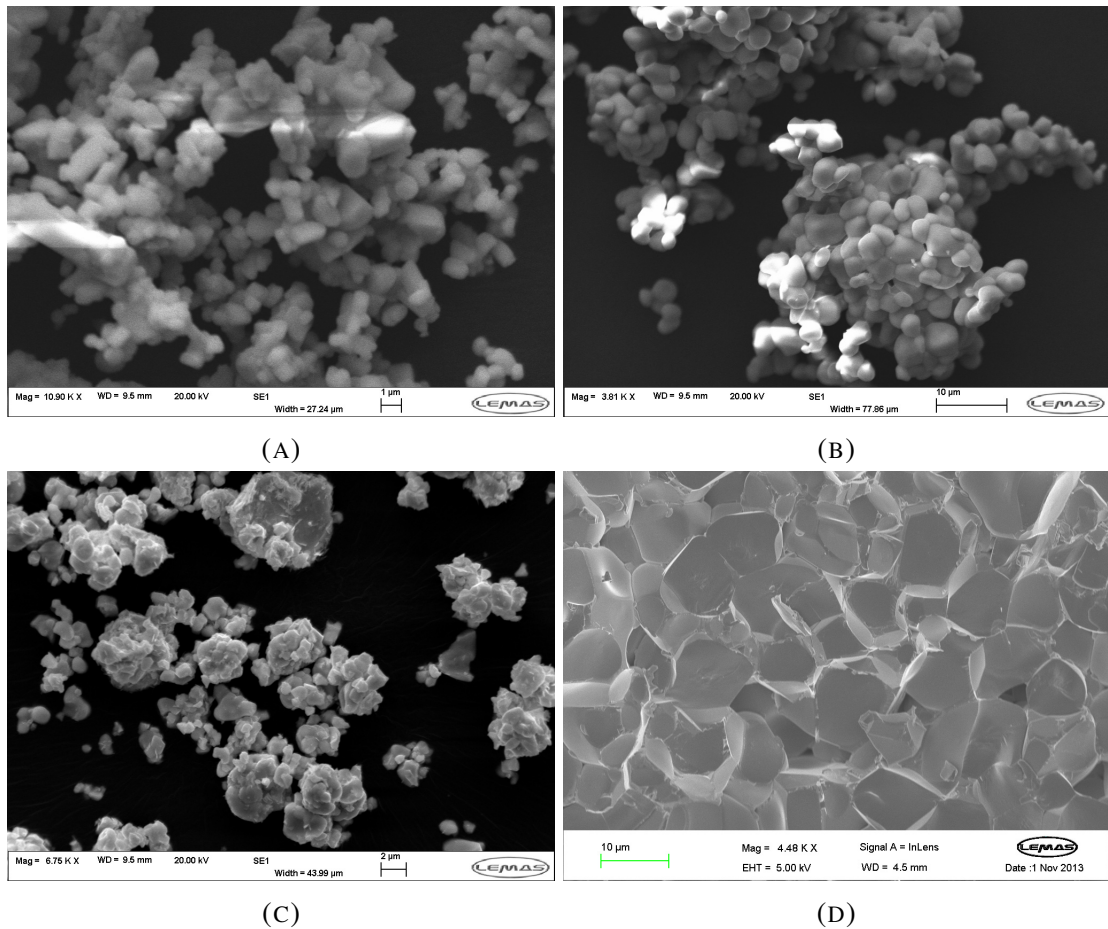


FIGURE 4.4: SEM micrographs for calcined powders - InNbO_4 (A), MgNb_2O_6 (B), PIN-PMN-PT (C) and the fracture surface of a sintered PIN-PMN-PT pellet (D)

4.4 Summary

The aim of this chapter was to present the method for synthesis of PIN-PMN-PT in a powder form, subsequently used for the experimental work. The mixed oxide route has been employed where raw, commercially available oxides have been used as precursor material. A composition in the vicinity of the Morphotropic Phase Boundary, slightly on the rhombohedral side has been selected.

To avoid formation of pyrochlore or other secondary phases and ensure PIN-PMN-PT is obtained with a pure perovskite structure, the two-step precursor approach has been chosen, where MgNb_2O_6 and InNbO_4 are presynthesized.

X-ray diffraction patterns have confirmed all compounds have been prepared with a single phase. No impurities or secondary phases have been observed. The particle size and shape has been analysed with Scanning Electron Microscopy.

Chapter 5

Bridgman Grown Single Crystals

Abstract

Due to the promising properties of relaxor-PbTiO₃ single crystals, particularly for use in SONAR devices and medical imaging, there is a great interest for a production method that is both cost-effective and able to produce high quality material. To date, literature suggests Bridgman is the most successful method. Although Bridgman is a relatively well understood crystal growth technique, not enough details are available regarding growth conditions and their influence on the quality of the grown material. The aim of this study was to grow non-seeded (or self-seeding) as well as seeded crystals and to identify the critical success factors. Therefore, PIN-PMN-PT and Mn:PIN-PMN-PT crystals have been grown in a multi-zone furnace using platinum crucibles. The first crystal growth experiment was self-seeding whilst for the following three runs an attempt at controlling the orientation by means of seed crystals has been made. The initial crucible thickness was 1 mm and this has been reduced to 0.6 and then to 0.4 mm in the final run with the aim of finding the optimal thickness, i.e. thin enough to be cost effective, but thick enough to support the growing material without posing a risk of crucible failure. The crystals have been grown at 0.5 and 0.2 mm/h speeds. A high quality single crystal has been obtained during the unseeded growth run, with a growth preference for the (011) direction. When seeds have been used, unwanted nucleation has occurred which resulted in a boule formed by several crystals. Unwanted grains nucleated even when the growing speed was reduced or when the orientation of the seeds had been changed. One factor believed to have contributed to the undesirable nucleation is the set up of the alumina support system of the platinum crucible which may have caused ineffective heat transfer from the furnace to the melt. Another factor is presumably the end-effect, i.e. an acceleration of the solidification speed as a result of the limited length of the crucible at constant lowering speed. The observations made within this study provide valuable information for crystal growers. Specifically, the study highlights the difficulty in controlling the orientation of single crystals and provides an overview of the variables which need to be taken into account for successful crystal growth.

5.1 Introduction

Although a Bridgman growth procedure may be found [3] and a growing body of literature reports investigations on Bridgman-grown crystals [15, 67, 81, 94, 95], the technique does not seem straight forward. For example a growing rate between 0.1 and 1 mm/h is generally reported [2, 3, 43, 67, 96, 97]. At the same time, it is reported that (111) is the fastest growing direction, followed by (110) and subsequently (001) [76, 98, 99]. However, specific optimal growing rates for each orientation cannot be found. Moreover, limited information is available regarding crucible dimensions (i.e. crucible diameter, seed pocket length and diameter, thickness) [3] which is believed to influence the growth. Within this work, the focus has been on growing unseeded and seeded crystals and identify the critical success factors. Variables such as crucible thickness, lowering speed or seed orientation have been explored.

The experimental techniques in terms of growth preparation, growth procedure and post-growth characterisation are detailed in Section 5.2. Four growth experiments have been run, the results of which are presented in Section 5.3. The work is summarised in Section 5.4. The limitations of the method together with suggestions for future work are presented in Section 5.5.

5.2 Experimental Procedures

This section will give a brief overview of the equipment used and the procedures followed to prepare for crystal growth. Subsequently growth parameters are presented and post-growth characterisation techniques are introduced.

5.2.1 Growth Preparation

The following subsections will briefly describe the apparatus, the crucible design, understanding the thermal profile of the furnace, loading of material, sealing and finally crucible loading.

5.2.1.1 Growth Equipment

A special five zone split tube furnace equipped with a Crystalox CRT4000 Crucible Rotation/Translation Unit has been used for crystal growth (Lenton, United Kingdom). The centre zone made of three out of five modules was capable of 1400°C, whilst the top and bottom modules were capable of 1200°C. Within this work, two of the three centre zones were used for crystal growth. The two zones were associated with the hot and cold zones, respectively. The equipment is shown in Figure 5.1.



FIGURE 5.1: Crystal growth furnace at The University of Leeds. The five zone tube furnace is located on the right hand side, whilst the controls for translation/rotation movement together with temperature controls for each of the five zones of the furnace are located on the left hand side.

5.2.1.2 Choice of Crucible

Custom made platinum crucibles (99.95% KPL Scientific, Canada and 99.99% Johnson Matthey, United Kingdom) were used within this work due to low reactivity with the metal oxide to be grown and high operating temperature [100].

Figure 5.2 shows crucible design used for unseeded growth. The entire material load is melted within this experiment and therefore, a crucible with conical bottom is desired. Once lowering towards the cooler zone begins, crystallization occurs at the tip of the cone and a single crystal grows.

Furthermore, Figure 5.3 shows the design for seeded growth. Here, a pocket is desired at the bottom of the crucible in which single crystal seeds are placed.

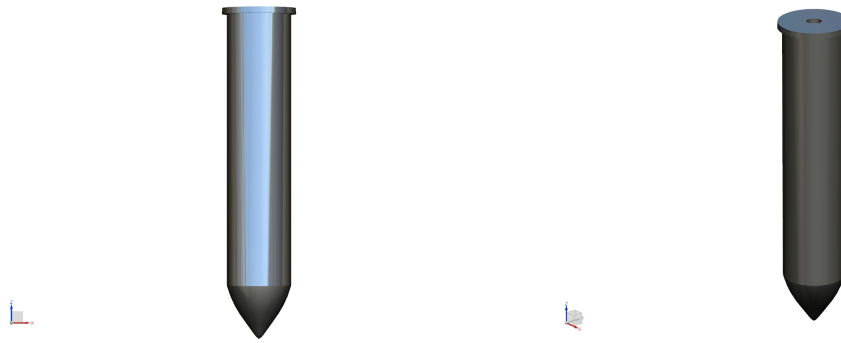


FIGURE 5.2: Crucible design for unseeded crystal growth - orthographic projection (left) and trimetric projection (right). Courtesy of Rob Simpson.

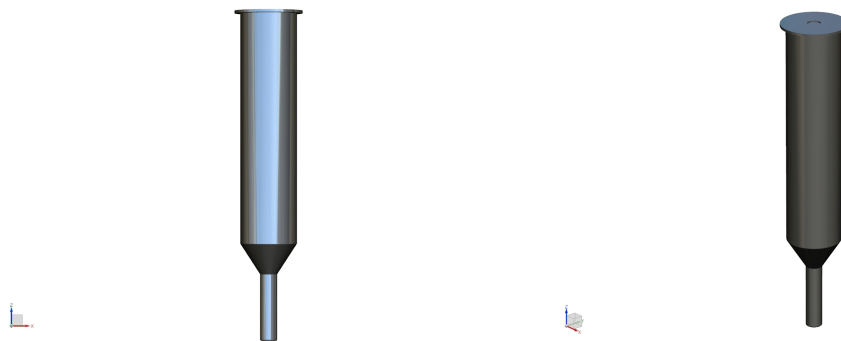


FIGURE 5.3: Crucible design for seeded crystal growth - orthographic projection (left) and trimetric projection (right). Courtesy of Rob Simpson.

5.2.1.3 Thermal Profile of the Furnace

R-type thermocouples (TC Direct, United Kingdom) have been used to map the thermal profile of the furnace prior to crystal growth experiments. The profile has been mapped on a small region in between the hot and cold zones which were set at 1355 and 1150°C, respectively. The choice of temperatures for the two zones will be discussed in Section 5.2.2. The thermal profile has been mapped inside both a conical platinum crucible

and a seed pocket crucible.

Figure 5.4 shows the profile mapped inside a conical crucible with the thermocouple placed at the bottom. A thermal gradient of $2.5^{\circ}\text{C}/\text{mm}$ has been observed.

Figure 5.5 shows the profile mapped inside a seed pocket crucible. In this case two thermocouples have been used - one placed at the bottom of the seed pocket and a second one at a higher point, where the crucible's main body starts. It has been noticed that the temperature decreases more rapidly in the seed pocket ($3.1^{\circ}\text{C}/\text{mm}$) when compared with the main body of the crucible ($1.5^{\circ}\text{C}/\text{mm}$).

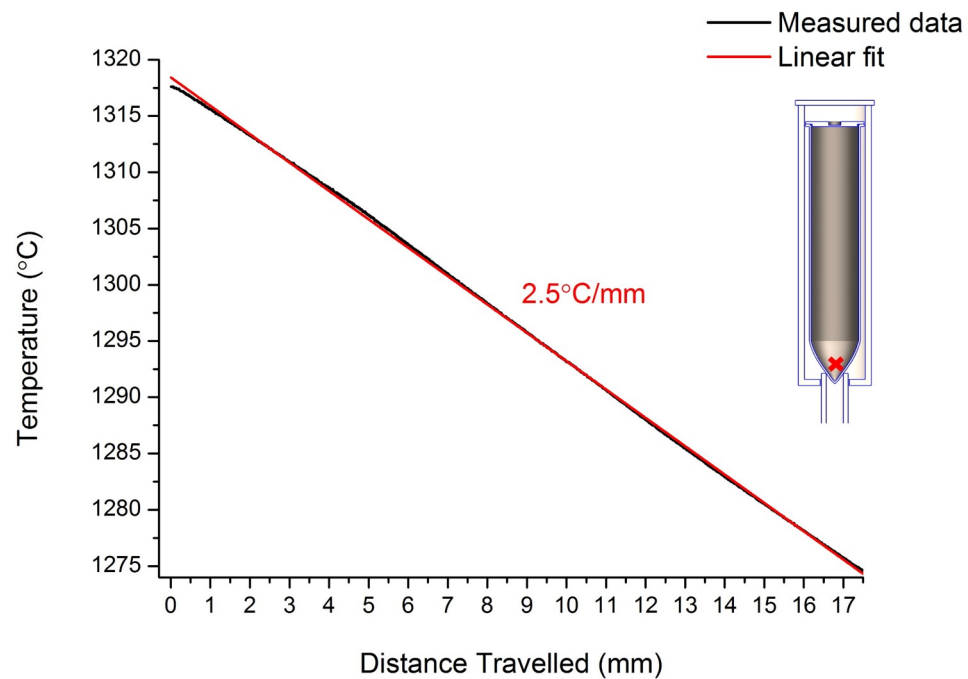


FIGURE 5.4: Thermal profile measured in between the hot and cold zones (1355°C and 1150°C) using a conical bottom platinum crucible. The red cross marks the position of the thermocouple tip used for mapping.

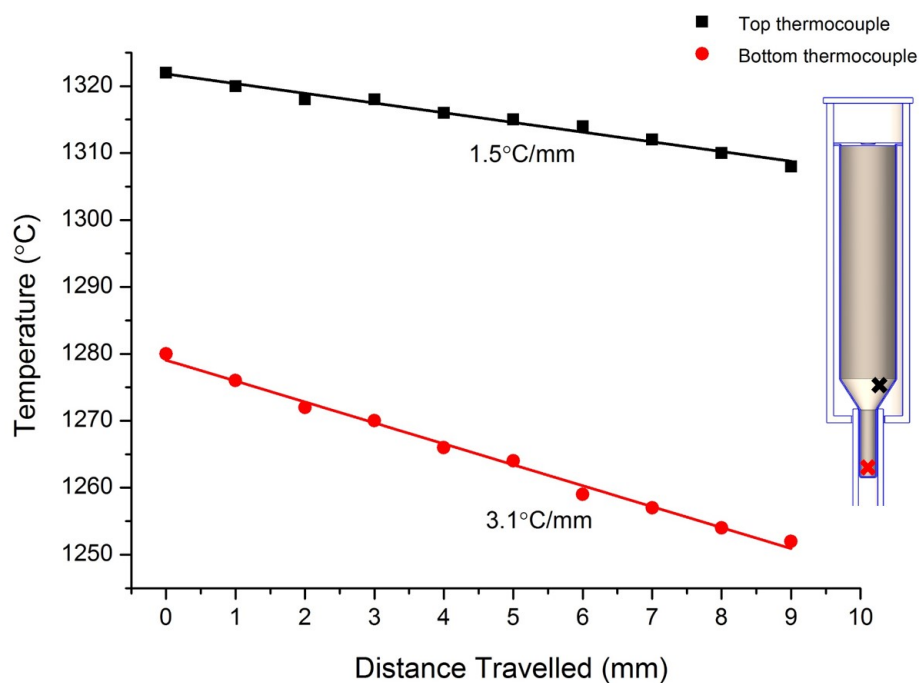


FIGURE 5.5: Thermal profile measured in between the hot and cold zones (1355°C and 1150°C) using a seed pocket platinum crucible. The red and black crosses mark the position of two thermocouples used during mapping.

5.2.1.4 Material Loading

Raw material composition and synthesis procedures have been presented in Chapter 4. The prepared powder has been uniaxially pressed into circular discs of 20 mm diameter and 5 mm height and isopressed at 200 MPa. Subsequently, the pellets have been sintered for 2 h at 1250°C. Sintered samples have increased density which means more material can be placed inside the crucible and consequently a larger crystal can be obtained. However, due to the difficulty of pressing a cone-shaped pellet, the conical region of the crucibles has been filled with powder, namely a stoichiometric mix of MgNb_2O_6 , InNbO_4 , TiO_2 and Pb_3O_4 . Pb_3O_4 has been chosen over PbO due to the increased content of oxygen. If PbO is used, it has been shown that as the temperature inside the crucible raises, oxygen is absorbed in the temperature range 430-520°C and Pb_3O_4 is formed. Above 600°C, oxygen is released and the compound returns to PbO . If there is an oxygen deficiency inside the crucible, metallic Pb may be generated which may promote formation of a low melting point alloy with platinum and consequently leakage of the crucible [3].

5.2.1.5 Sealing

A pinhole with 0.2 mm diameter has been drilled through the lid of the crucible prior to sealing to allow the release of pressure built-up at high temperature. Subsequently, the lid was welded to the crucible using a laser (ORLAS Station, O.R. Lasertechnologie GmbH, Germany). A platinum wire has been used as feed material in between lid and crucible lip. The laser settings were: pulse width 7 ms, frequency 1.6 Hz, energy 22 J, crucible rotation speed during welding 1 rpm.

5.2.1.6 Crucible loading

Following sealing, the crucible has been placed inside an alumina crucible supported by an alumina rod. The alumina support system formed by crucible and rod is schematically shown in Figure 5.6 and 5.7 for a conical and a seed-pocket platinum crucible, respectively. The gap around the platinum crucible has been filled with 0.5 mm diameter yttria stabilised zirconia media (Tosoh, Japan).

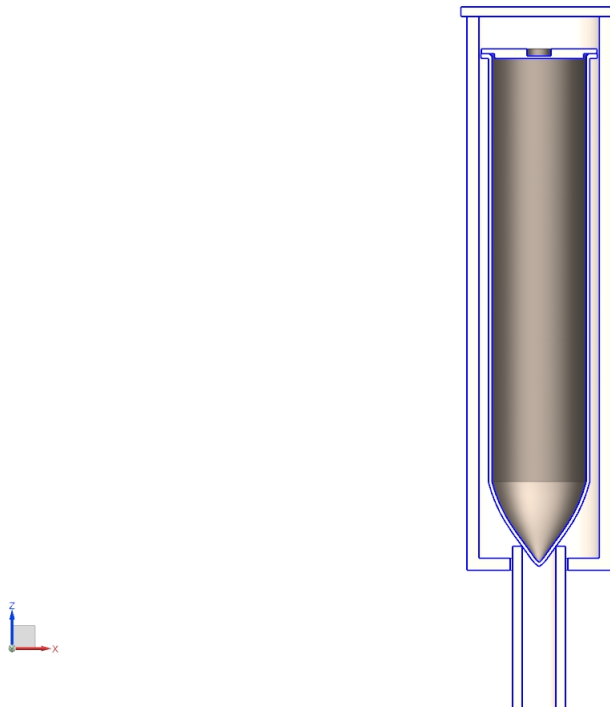


FIGURE 5.6: Alumina support system during growth for a self-seed crucible type. The gap in between the platinum crucible and the outer alumina crucible has been filled with yttria stabilised zirconia media. Courtesy of Rob Simpson.

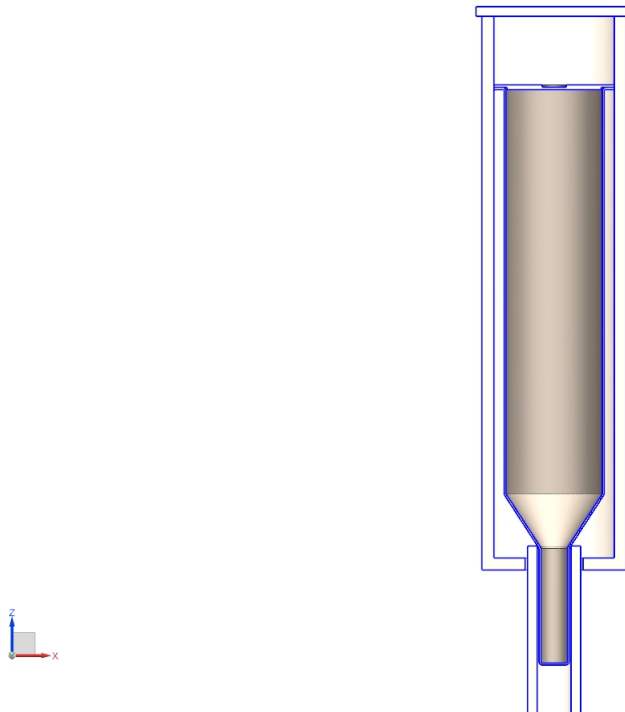


FIGURE 5.7: Alumina support system during growth for a seed pocket crucible type. The gap in between the platinum crucible and the outer alumina crucible has been filled with yttria stabilised zirconia media. The seed pocket was surrounded only by the alumina tube. Courtesy of Rob Simpson.

5.2.2 Growth Parameters

One of the most important steps when setting up the growth parameters for Bridgman experiments is choosing the temperature for the hot and cold zone, respectively. First, the melting point of the compound to be grown needs to be considered. PIN-PMN-PT has a melting point of $\approx 1300^\circ\text{C}$ [51, 68, 97, 101, 102]. The temperature in the hot zone will be chosen above the melting point, whilst the temperature in the cold zone below the melting point, to allow directional solidification when the crucible is lowered. The temperature values must be carefully selected as this will affect the shape of the liquid-solid interface, which, in turn, may affect the quality of the crystal grown. Generally, a planar interface is known to be beneficial as the thermal stresses are minimal. However, a convex shape (with respect to the liquid) is believed to be advantageous during directional solidification as nucleation on the crucible wall can be avoided.

Chang et al. [103] have shown that a flat interface requires the melting point be exactly the mean between the temperature in the hot zone and that in the cold zone. If, for example, the temperature in the hot zone is chosen to be 55°C higher than the melting point, i.e. 1355°C , the cold zone temperature must be 1245°C for the interface to be flat. Lowering the temperature in the hot and/or cold zone(s), results in their mean value being lower than the melting point of the material and the interface moves towards the hot zone, i.e. becomes convex. On the contrary, increasing the temperature in the hot and/or cold zone(s), leads to the interface moving towards the cold zone, i.e. becomes concave.

A material-specific parameter which further influences the degree of convexity/concavity of the liquid-solid interface is the thermal conductivity of the material. The more conductive the material, the more pronounced the change of the interface shape upon temperature change. This concept may be described in terms of Biot number, H , which is defined as the ratio of heat loss from surface to heat conduction. Therefore, a material with high thermal conductivity will have a low Biot number and vice-versa.

A schematic diagram presenting the influence of the two factors, i.e. temperatures in the hot/cold zones and the Biot number, on the interface shape is shown in Figure 5.8. The interface shape is described by Φ , which is calculated as follows:

$$\Phi = \frac{T_i - T_c}{T_h - T_c} \quad (5.1)$$

where T_i is the temperature at the interface, i.e. 1300°C , T_c is the temperature within the cold zone and T_h is the temperature within the hot zone. The diagram shows that the interface is flat when $\Phi=0.5$. Φ increases when one or both hot/cold zone temperatures

are decreased and vice-versa. In addition, low (0.1), medium (1) and high (2) Biot numbers are considered. It is assumed that a lower Biot number (i.e. 0.4) is typical for the compound studied within this thesis due to the high melting point. Higher Biot number values are associated with low melting point compounds such as organics. Therefore, by using these studies it has been decided that a temperature of 1355°C in the hot zone and 1150°C in the cold zone which gives $\Phi=0.73$ would result in a liquid-solid interface with a satisfying theoretical convex shape. A higher Φ , i.e. a higher level of convexity, may lead to segregation of Ti in plane in addition to the segregation along the boule.

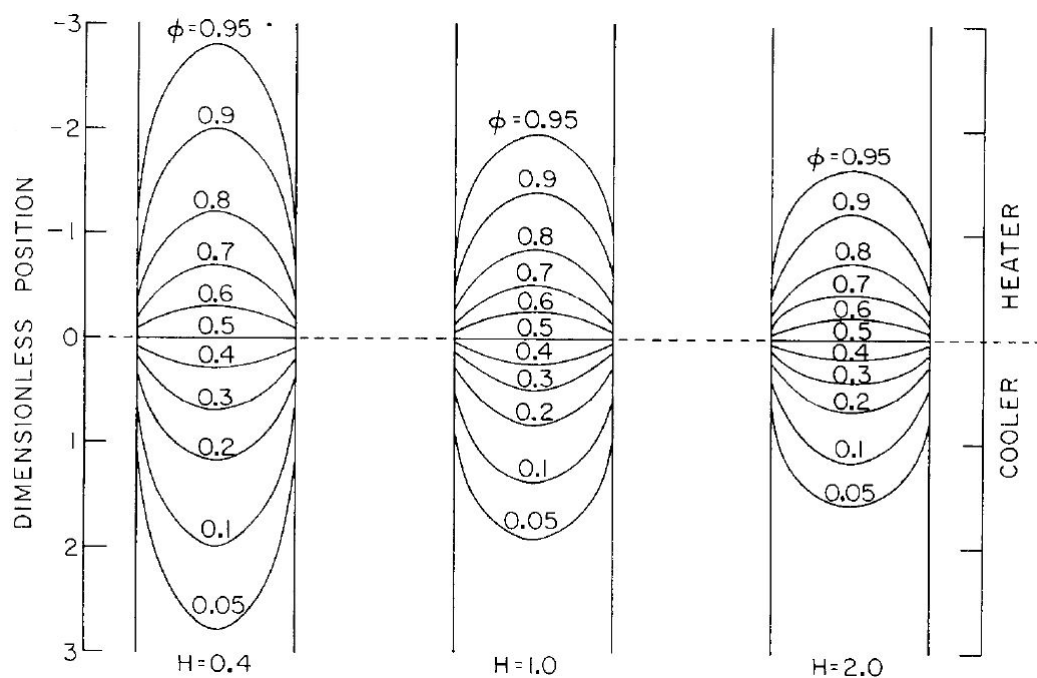


FIGURE 5.8: Liquid solid interface shapes within a stationary rod for materials with low ($H=0.4$), medium ($H=1$) and high ($H=2$) Biot number and different values of the temperatures within the hot/cold zones represented by Φ , from [103].

Another important growth parameter which must be carefully selected is the lowering speed of the platinum crucible during growth. The speed must be relatively low so that each layer of material has enough time to fully crystallise (solidify) before other upper layers of materials start to solidify. As specified in the introduction of this chapter, growth rates in the range 0.1-1 mm/h are generally used. Within this work, an initial growth rate of 0.5 mm/h has been used, which has been later lowered to 0.2 mm/h. An

explanation for growth parameters change will be given throughout the chapter. The full set of growth parameters are summarised in Table 5.1.

TABLE 5.1: Summary of growth conditions for each of the four experiments

	Bridgman 1	Bridgman 2	Bridgman 3	Bridgman 4
Composition	PIN-PMN-PT	Mn:PIN-PMN-PT	Mn:PIN-PMN-PT	Mn:PIN-PMN-PT
Platinum crucible	conical 20 mm dia 1 mm thick	seed pocket 19 mm dia 0.6 mm thick	seed pocket 19 mm dia 0.6 mm thick	seed pocket 19 mm dia 0.4 mm thick
Seed orientation	-	(001)	(001)	(011)
Heating rate	100°C/h	100°C/h	100°C/h	100°C/h
Soaking time	5 h	5 h	5 h	5 h
Hot zone	1355°C/h	1355°C/h	1355°C/h	1355°C/h
Cold zone	1150°C/h	1150°C/h	1150°C/h	1150°C/h
Lowering speed	0.5 mm/h	0.5 mm/h	0.2 mm/h	0.2 mm/h
Cooling rate	60°C/h	60°C/h	60°C/h to 250°C 6°C/h to 20°C	60°C/h to 250°C 6°C/h to 20°C

5.2.3 Characterisation

This section briefly presents the techniques used to characterise the grown crystals. Microstructural analysis was performed to understand the growth mechanisms and determine the challenges that Bridgman method poses. Selected electrical measurements have been performed to assess the quality of the grown material and not to provide a full-set of properties.

5.2.3.1 Polishing

Samples with a high degree of polishing have been required to investigate the microstructure under optical and electron microscopes. Unless otherwise stated, samples have been polished during the industrial placement in Rydalmere, Australia using a semi-automatic TegraSystem grinder and polisher (Struers). The polishing route is summarised in Table 5.2.

TABLE 5.2: Polishing procedure for sample imaging. Advice and products from Buehler (B) and Struers (S)

Step	Surface	Abrasive Lubricant	Force (N/specimen)	Time (mm:ss)	Platen Speed (rpm)	Head Speed (rpm)	Relative Rotation
1	SiC Foil MD-Gekko + MD Piano	220 600/1200 water	35	Until plane	150	150	Comp
2	MD/DP-Pan (S)	9 μm diamond suspension (B) diamond lubricant (B)	35	12:00	150	150	Comp
3	MD/DP-Pan (S)	3 μm diamond suspension (B) diamond lubricant (B)	30	9:00	150	150	Comp
4	MD/DP-Mol (S)	1 μm diamond suspension (B) diamond lubricant (B)	25	1:00	150	150	Comp
5	ChemoMet (B)	Colloidal Silica (B)	25	1:30	150	150	Contra

5.2.3.2 X-Ray Powder Diffraction

PANalytical X'Pert Diffractometer (Phillips, The Netherlands) with a Bragg-Brentano configuration has been used for phase determination. Two types of sample stages have been used, depending on the sample to be investigated: PW3064/00 Sample Spinner and PW3071/60 spring loaded sample holder (Phillips, The Netherlands). The X-Ray generator was set at 40 mA and 40 kV. A 10 mm (or 5 mm, depending on the size of the sample) mask was used to control the illuminated area. Step sizes in the range 0.01 to 0.03°2theta and total scan times in the range 2 to 60 min were used, depending on the level of detail required for the scans. All diffractograms have been acquired at room temperature with Cu as anode material. Samples in the form of powder (either calcined or crushed sintered pellets) and bulk sintered pellets have been investigated. The powders have been pressed into the sample holder to ensure a flat surface, whilst the bulk samples have been fixed into the holder with modelling clay. Prior to mounting, the sintered samples have been mechanically ground to ensure the bulk of the material is analysed rather than any secondary phases formed on the surface. Grinding has been achieved using SiC paper, first with relatively coarse grit size and subsequently finer grit sizes. All steps have been performed under wet conditions, using tap water.

5.2.3.3 X-Ray Pole Figures

PANalytical X'Pert Diffractometer (Phillips, The Netherlands) has also been used for investigation of the single crystals with Bragg-Brentano configuration and a specialised PW3068/00 Automatic Texture Cradle ATC-3 in the Schulz reflection geometry (see Appendix A). As-cut single crystals have been mounted with modelling clay onto the sample stage.

5.2.3.4 Optical Microscope

OLYMPUS OLS4100 optical microscope has been used to investigate polished surfaces of B2 and B3 in the seed pocket region. The samples have been imaged in Rydalmere, Australia.

5.2.3.5 Electron Back-Scatter Diffraction (EBSD)

A FEI Quanta 650 Field Emission Gun Environmental Scanning Electron Microscope has been used to assess the single crystalline nature of B2 crystal. The accelerating voltage was 15 kV, the specimen tilt 70° and the mapping step size in the range 4 - 15 μm . The sample analysed has been polished courtesy of Buehler customer service laboratory prior to EBSD investigations. Furthermore, to eliminate charging effects, the sample area to be mapped has been coated with a 5 nm thick gold layer, whilst the rest of the sample has been coated with a 200 nm thick gold layer.

5.2.3.6 Energy Dispersive X-Ray Diffraction (EDX)

EDX was used within this work to identify the distribution of chemical elements in a given sample. The apparatus was a Carl Zeiss EVO MA15 Scanning Electron Microscope with Oxford Instruments AZtecEnergy EDX system. The interaction volume with the sample has been simulated using Casino software - Figure 5.9. The interaction width (i.e. spatial resolution) is $\approx 1 \mu\text{m}$, however 90% of the X-ray energy arises from $\approx 100 \text{ nm}$.

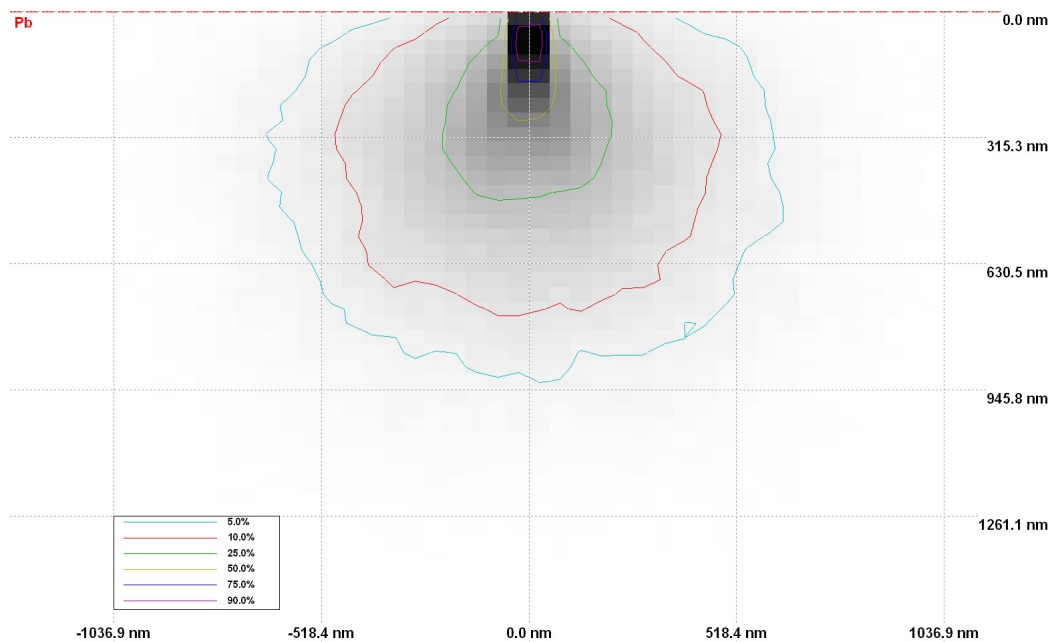


FIGURE 5.9: Simulated interaction volume for the studied samples, accelerating voltage 20 kV, material's density 8.2 g/cm^2 , Casino software. Courtesy of Stuart Micklethwaite.

5.2.3.7 Piezoresponse Force Microscopy

A Cypher S (Asylum Research) with Dual AC Resonance Tracking (DART) scanning technique has been used to determine domain structure. The tip was a Multi75 (Budget Sensors) with Cr/Pt conductive coating. This analysis has been done at The University of New South Wales, Australia.

5.2.3.8 Permittivity versus temperature

The permittivity versus temperature across a range of frequencies has been acquired by measuring the capacitance of the samples via an Agilent 4192A (Agilent, USA) apparatus in conjunction with a Pyrotherm tube furnace and a LabView data acquisition software. A K-type thermocouple has been used to monitor the temperature in the vicinity to the sample.

5.2.3.9 Polarisation versus electric field

Polarisation versus field measurements have been performed using a Precision LC Ferroelectric Tester (Radiant Technologies, USA) together with a TREK 5/80 high voltage power amplifier. The measurements were controlled by Vision Data Acquisition and Management System Software.

5.3 Results and Discussion

This section presents and discusses the results of the Bridgman experiments. Each crystal growth run is treated separately.

5.3.1 Unseeded Growth B1

Figure 5.10 shows the crystal grown during the first run, i.e. unseeded growth. The color of the crystal changes from yellow to a darker color in the direction of growth. This behavior is associated with a compositional gradient as previous studies have confirmed [3, 67]. In addition, secondary phases can be observed at the top of the crystal. Figure 5.11 shows the same crystal as seen when a flashlight is placed underneath. This

way it is possible to observe any major defects such as cracks. The initial observations indicated a high quality crystal with secondary phases formed only at the top, as expected. In addition, the density of the crystal was determined via Archimedes' method and has a value of 8.2 g/cm^3 . This value represents 99% of the theoretical value of 8.3 g/cm^3 which has been calculated from an ideal unit cell using PANalytical Highscore Plus software.

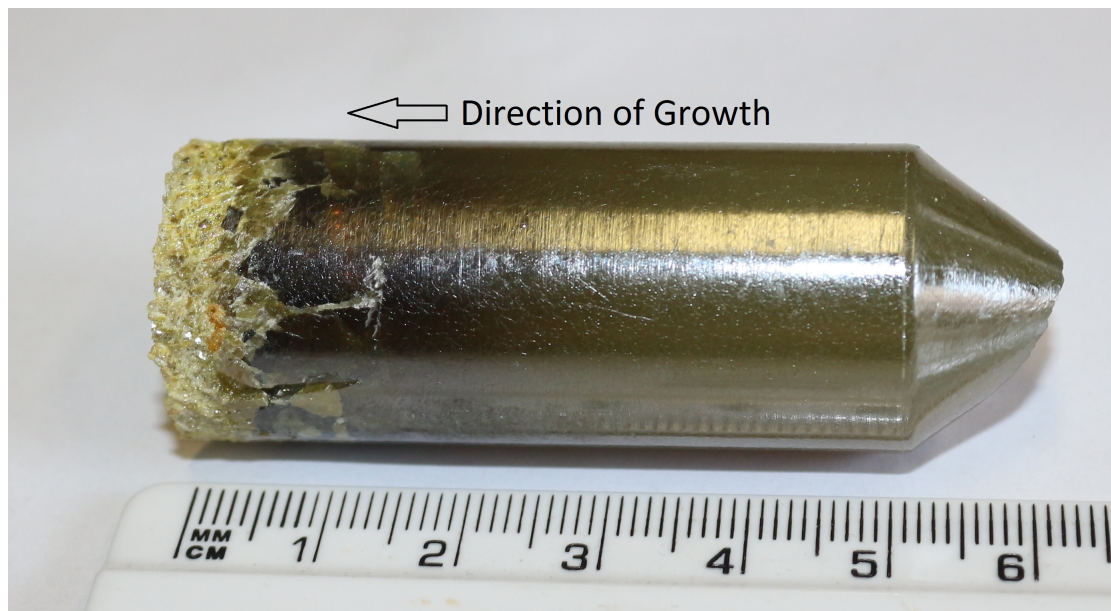


FIGURE 5.10: Crystal grown during the first run, i.e. unseeded growth B1



FIGURE 5.11: Crystal grown during the first run, i.e. unseeded growth as seen under a flashlight

5.3.1.1 Energy Dispersive X-Ray Spectroscopy

Qualitative microanalysis has been performed on a random plate to verify the homogeneity on a small scale. Figure 5.12 shows elemental maps of the selected region on the crystal sample. There is no segregation observed. Each chemical element is uniformly distributed throughout the studied sample.

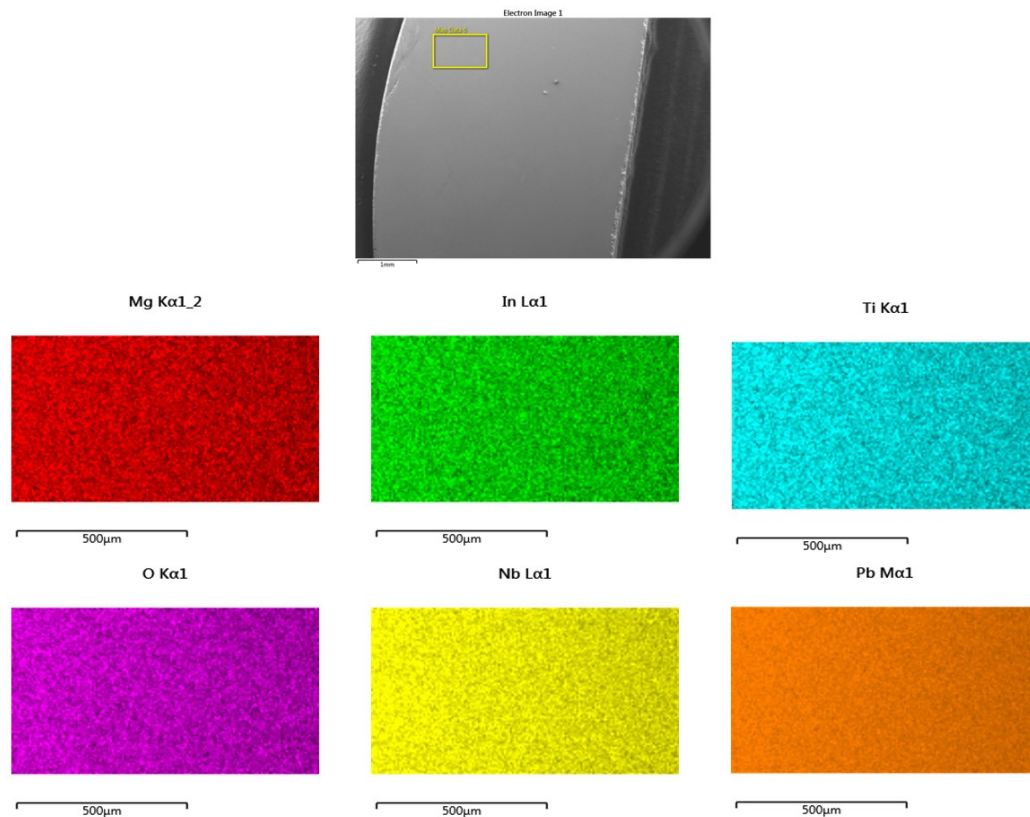


FIGURE 5.12: Electron image of a single crystal plate (top) and elemental maps of region highlighted in yellow for Mg, In, Ti, O, Nb and Pb

5.3.1.2 Pole Figures

Pole figures (see Appendix A) were used to determine the growth direction of the single crystal boule. In addition, the single crystalline nature of the investigated sample is also assessed. Pole figures were recorded at the Bragg angle 22.071° for the (001) crystallographic plane, 31.359° for (110) and 38.626° for (111) on a sample from the bottom region of the boule. The results are shown in Figure 5.13. The analysis of the (011) plane (Figure 5.13 centre) reveals a pole very close to the centre which implies the growth direction of the crystal is (011) with $\approx 2^\circ$ tilt relative to the axis of the

crystal boule. The tilt might be the result of a slightly inclined crucible during growth. To ensure the same orientation was kept along the crystal boule an additional sample from the top region of the crystal has been analysed revealing the same pole figures and hence the same orientation as the bottom one.

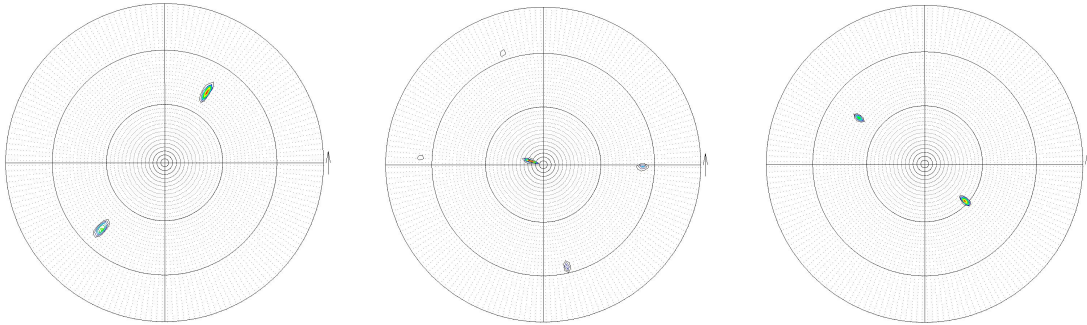


FIGURE 5.13: Pole figures acquired for (001), (011) and (111) crystallographic planes (left to right). When the distribution of (011) plane was analysed (centre figure), a centre pole is observed which is associated with a preferred (011) growth direction of the crystal.

5.3.1.3 X-Ray Diffraction

Powder X-Ray Diffraction has been performed on a crushed single crystal sample to determine the phase. The scan is shown in Figure 5.14 and suggests a pure material with a perovskite phase was obtained with no traces of secondary phases or impurities down to the signal to noise ratio of the diffractometer.

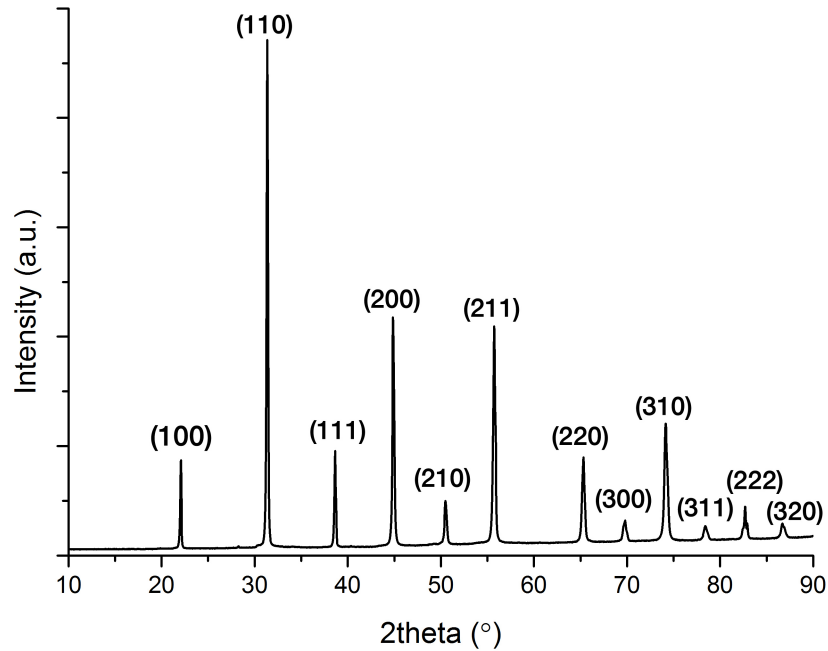


FIGURE 5.14: XRD pattern obtained from a single crystal sample crushed into powder. A pure perovskite phase has been obtained with no secondary phases or other impurities.

5.3.1.4 Piezoresponse Force Microscopy (PFM)

To visualise ferroelectric domains, a sample with (011) orientation has been cut from the lower part of the single crystal boule and polished. No poling process has been applied. The crystallographic phase expected for this region is rhombohedral as the nominal composition has been chosen slightly on the rhombohedral side of the Morphotropic Phase Boundary and, in addition, the real composition within this region is moved further away from the MPB towards the rhombohedral side due to the Ti segregation during crystal growth (see Section 4.1.2.2 for phase diagram). Therefore, eight polarisation directions are possible within this structure which are highlighted in Figure 5.15.

Figure 5.16a shows the topography of a $12 \times 12 \mu\text{m}^2$ area of the sample. A surface roughness of approximately 8 nm is observed. Figure 5.16b and 5.16c show the amplitude PFM response which is related to the local piezoelectric constant d_{33} . Five regions have been identified with no correlation with topography and therefore have been attributed to ferroelectric domains. The orientation of the domains may be analysed from the phase response images - Figure 5.16d and 5.16e. The vertical phase image

reveals 180° domains which could be associated with either the blue or red directions in Figure 5.15. The lateral image shows two major types of domains. It is believed that both 71° and 109° domains contribute to the signal. However, the images must be interpreted with caution. Comparison of the vertical and lateral signals reveal similar domain patterns although phase vertical and phase lateral images suggest different angles between the domains. This might be explained in terms of polarisation direction. The red and blue directions in Figure 5.15 have an out-of-plane component which will cause a vertical signal as well as an in-plane component which will cause a lateral signal. To clearly distinguish between the different domain types further studies are required.

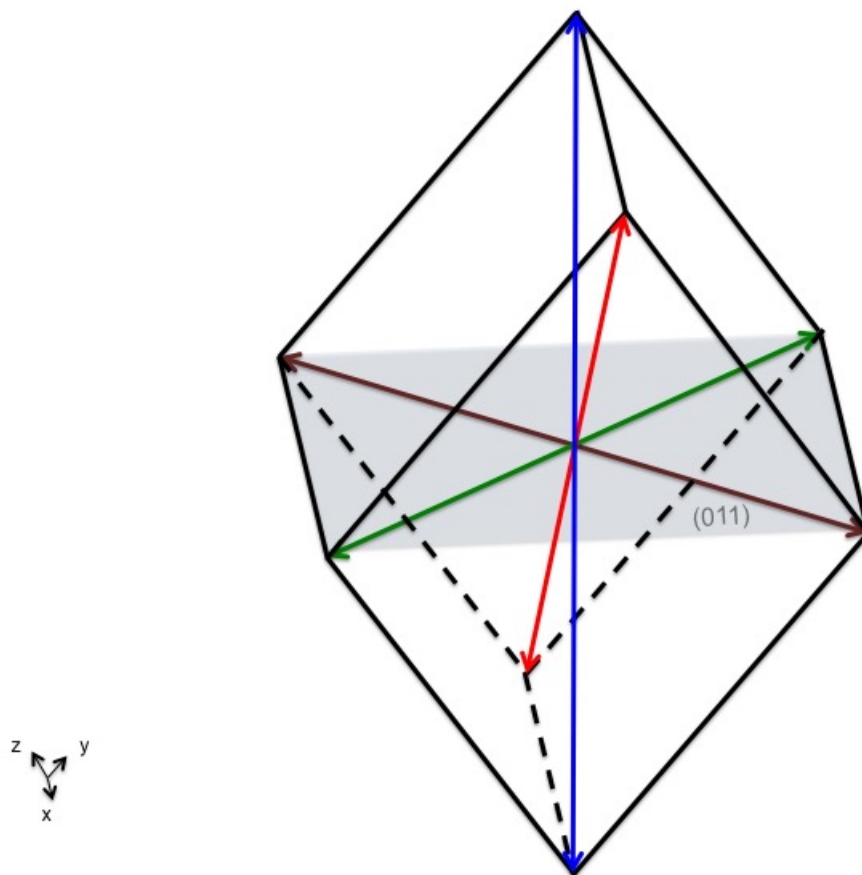


FIGURE 5.15: Unit cell within the investigated sample rotated such that the plane (011) is parallel to the surface. The arrows mark the eight directions possible for the spontaneous polarisation within the rhombohedral structure.

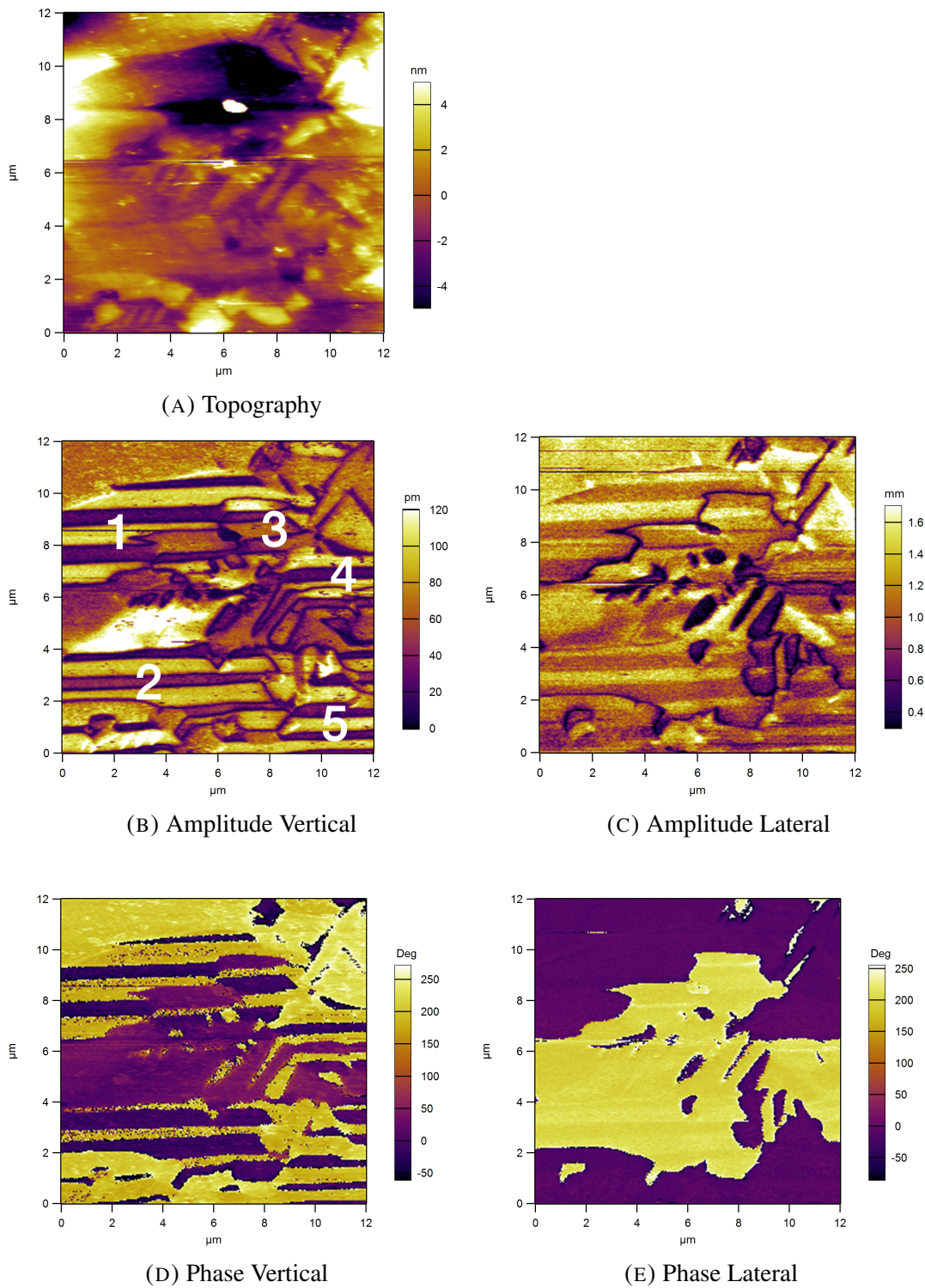


FIGURE 5.16: Piezoresponse Force Microscopy images on a (011) oriented sample extracted from the bottom region of the crystal.

5.3.1.5 Impedance Spectroscopy

Impedance Spectroscopy data has been acquired in the form of complex impedance - Equation 7.3

$$Z^* = Z' + iZ'' \quad (5.2)$$

where Z' is the real part and Z'' the imaginary part of the complex impedance. Nyquist diagrams, i.e. $-Z''$ versus Z' at various temperatures are shown in Figure 5.17. Full semicircles start to be observed at 400°C. Single semicircles have been obtained at all temperatures studied which suggest response from the bulk of the samples, with no secondary phases or impurities.

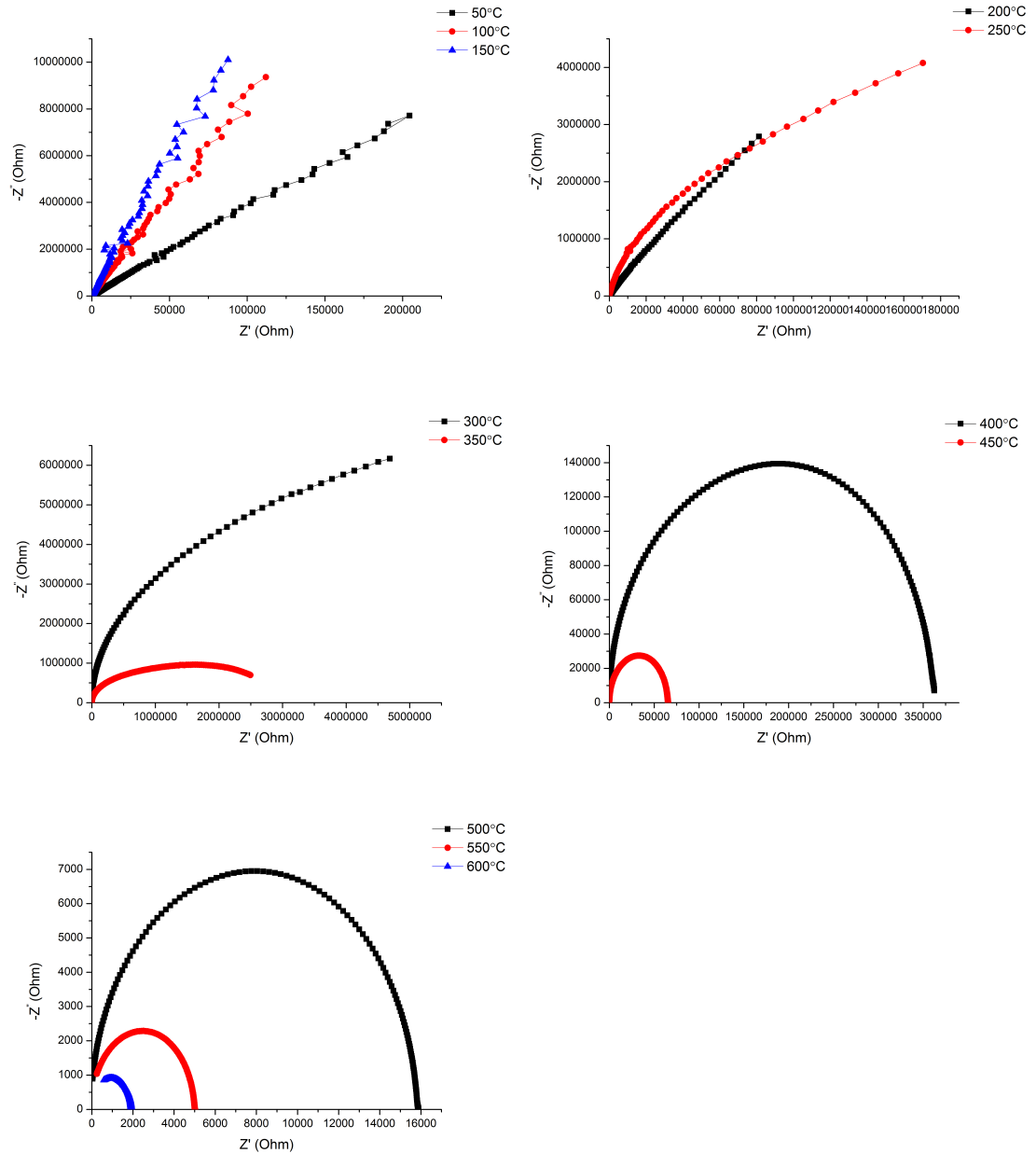


FIGURE 5.17: Impedance Spectra at various temperatures measured on one sample. The full semicircles obtained at higher temperatures are associated with a single response from the bulk of the sample.

5.3.1.6 Permittivity versus temperature

Permittivity data acquired in the frequency range 1 kHz - 1 MHz from room temperature up to 250°C is shown in Figure 5.18. The frequency dispersion suggests a typical relaxor behavior.

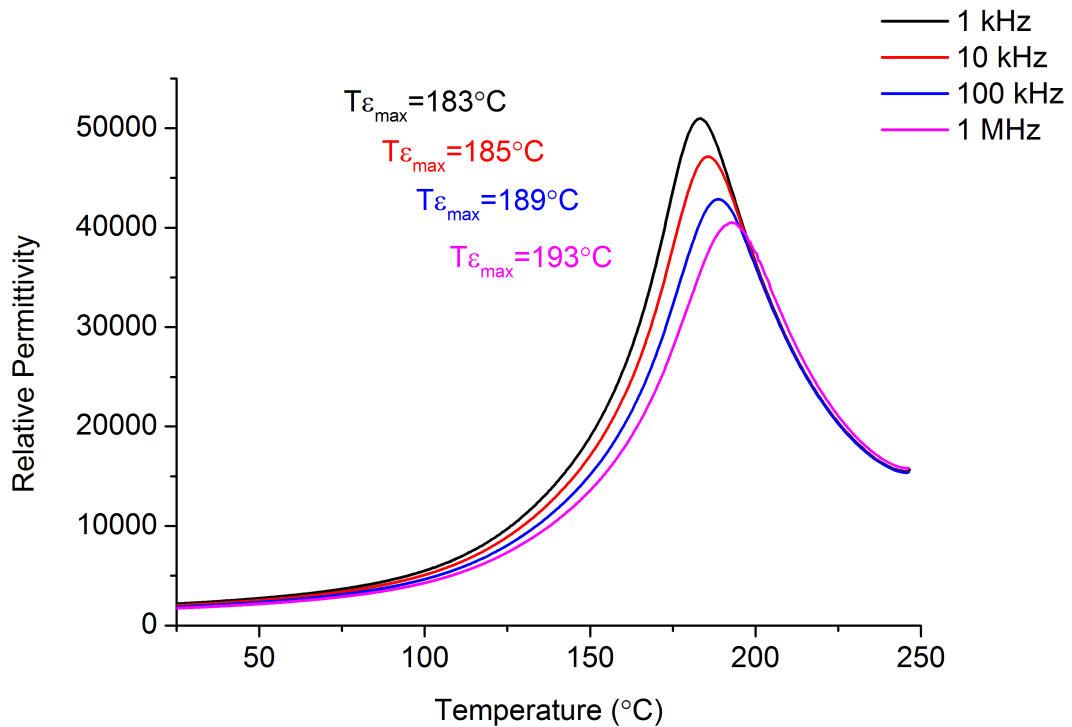


FIGURE 5.18: Permittivity versus temperature analysis implying a relaxor behavior due to the frequency dispersion.

5.3.1.7 Polarisation and Strain versus Field

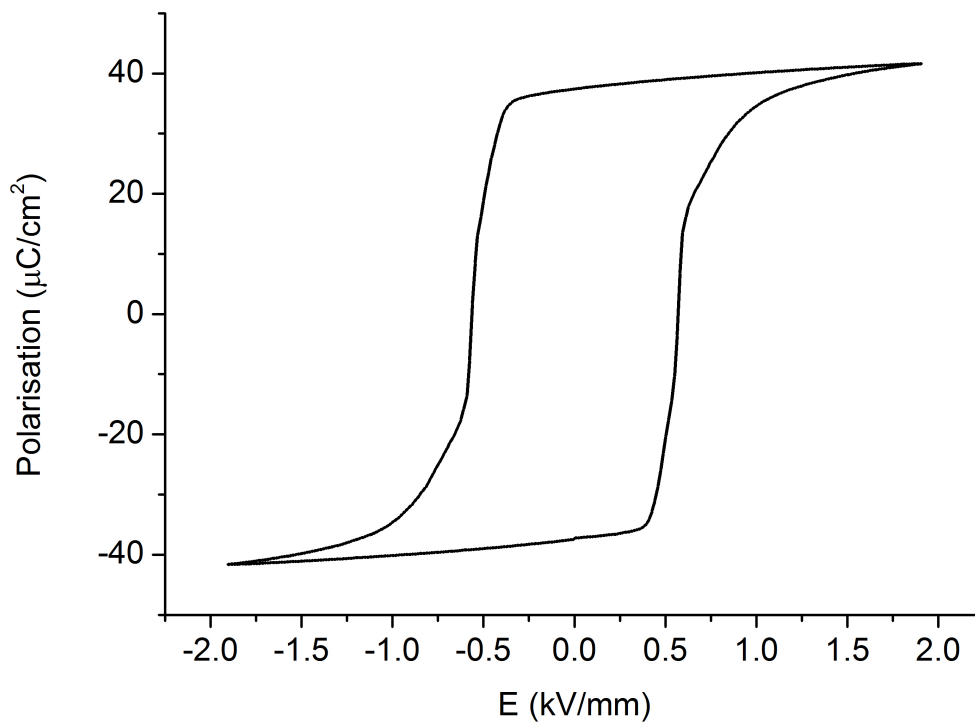
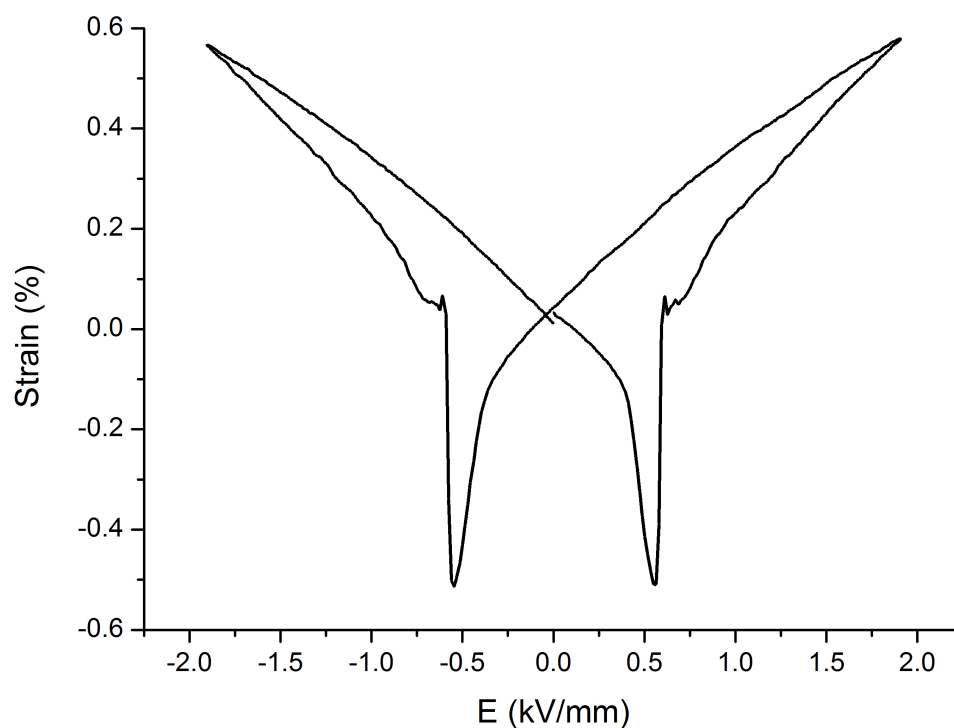
Polarisation and strain have been tested on a 5x5 mm² sample and a 10 Hz signal was applied. Figure 5.19 shows the hysteresis loop with a remanent polarisation P_r of approximately 40 $\mu\text{C}/\text{cm}^2$ and a coercive field E_c of approximately 0.5 kV/mm. Figure 5.20 shows the strain loop with a typical butterfly shape. The loop indicates a piezoelectric behavior due to the negative strain achieved. The small bump around 0.5 kV/mm suggests a crystallographic phase change.

5.3.1.8 Preparation for next run

The results of this experiment showed that a PIN-PMN-PT single crystal may be easily grown by the unseeded Bridgman method. A high quality single crystal, with no visible defects such as cracks, homogeneous and with a density of 99% of the theoretical has been grown at a rate of 0.5 mm/h. The preferred growth direction was (011).

However, growing oriented crystals is important due to the requirement for piezoelectric single crystals with specific properties which can only be achieved in specific crystallographic orientations. Cutting samples with a different orientation than the direction of growth may lead to compositional gradients within a sample due to the Ti segregation along the boule. Therefore, it is desired to grow oriented single crystals, since samples are homogeneous within a wafer cut perpendicular to the direction of growth.

Consequently, the next experiment will focus on controlling the growth orientation by means of a single crystal seed.

FIGURE 5.19: Hysteresis loop of a 5x5 mm² single crystal sampleFIGURE 5.20: Strain loop of a 5x5 mm² single crystal sample

5.3.2 Seeded Growth B2

Within this experiment a Mn modified PIN-PMN-PT crystal has been grown and the orientation of the seed was (001). Full details of the growth parameters were listed in Table 5.1 of Section 5.2.2. The crystal grown within this run is shown in Figure 5.21. The main body has been cut and separated from the seed pocket side during removal from the crucible. The following subsections present investigations on the single crystal grown.

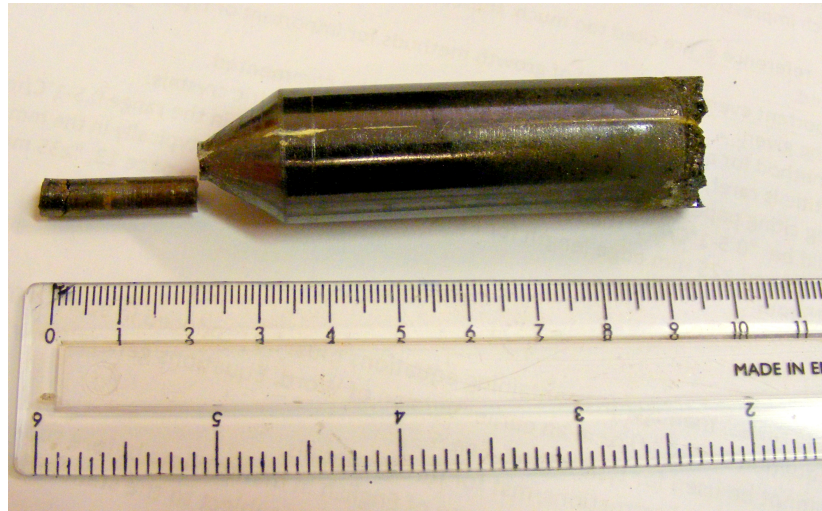


FIGURE 5.21: B2 (001) seeded crystal

5.3.2.1 Growth direction - Pole figures

To verify whether the growth direction followed the seed orientation, i.e. (001), a sample has been extracted from the middle region of the boule and investigated by X-Ray texture analysis. Three crystallographic planes have been analysed (001), (011) and (111) and the results are shown in Figure 5.22. The number of poles for the (001) and (011) planes are greater than what would be expected for a single crystal [104] and suggest the existence of multiple crystals or grains. The pole figure for (111) indicates that all grains in the area analysed are oriented (111). To understand what happened during growth it has been decided to investigate in detail the part of the crystal in the seed pocket where growth was initiated. The technique of choice was Electron Back Scatter Diffraction which, in addition to electron micro-graphs, provides information of regions with different crystallographic orientation if they exist.

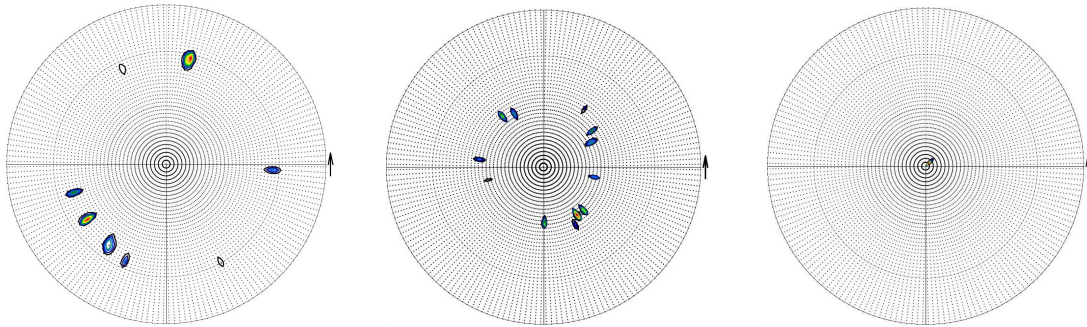


FIGURE 5.22: Pole figures obtained from a sample cut halfway through the boule so that the direction of growth can be analysed. The figure shows distribution of the plane (001) (left) , (011) (centre) and (111) (right)

5.3.2.2 Electron Back Scatter Diffraction

EBS D has been the method of choice for investigating the initial phase of single crystal growth due to its capability of providing crystallographic information. To determine whether the crystal started to grow following the orientation of the seed, the seed pocket has been investigated. Figure 5.23 (left) shows the entire single crystal boule with the seed pocket highlighted. The thermal profile within the furnace has been set up so that growth would start approximately halfway through the seed pocket. The centre of Figure 5.23 show the electron micro graph of the seed pocket cut cross sectionally along the length. Three areas have been analysed with EBS D and are highlighted with red rectangles. Figure 5.23 (right) shows the three regions. The image at the bottom shows the region where the crystal started to grow. The purple region represents the (001) seed. The crystal started to grow following the orientation of the seed on the right side of the image. However, on the left side, the presence of multiple grains is observed. As the growth continued, the grains grew larger and larger as emphasized by the upper two regions in Figure 5.23 (right). These findings confirm what the pole figures have shown, i.e. the presence of several grains throughout the boule.

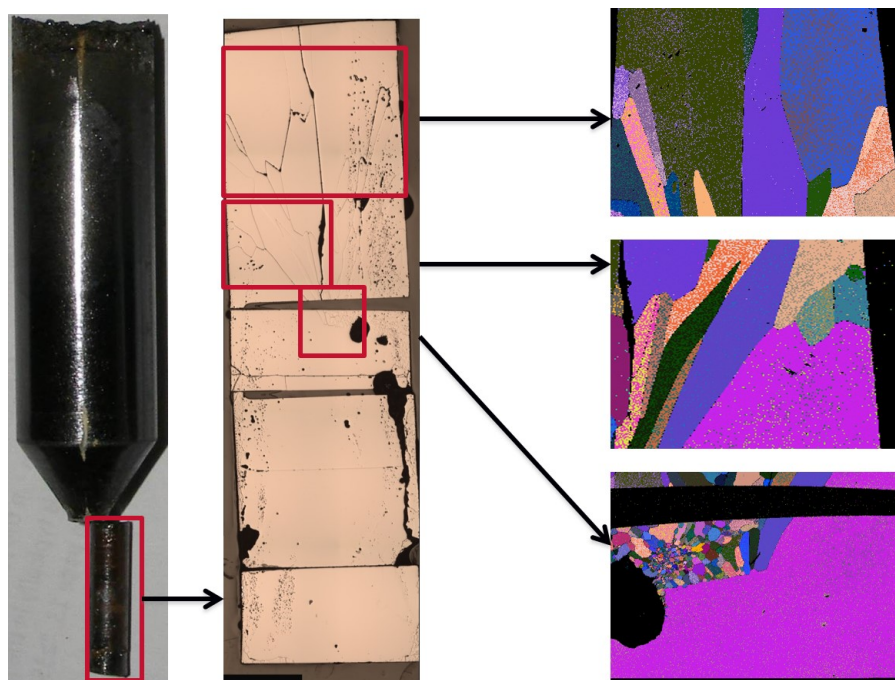


FIGURE 5.23: Image of the entire single crystal boule grown (left), cross sectional electron micrograph of the seed pocket (middle, courtesy of Buehler customer service laboratory) and three different areas investigated with Electron Back scatter Diffraction with Electron Back scatter Diffraction (right). The EBSD figures are mirror images of the regions highlighted in red on the electron micrograph and reveal regions with different crystallographic orientations (different colours) associated with grains.

5.3.2.3 Energy Dispersive X-ray Spectroscopy

In an attempt to find the cause of the unwanted nucleation, the first question asked was whether any chemical segregation played any role. By comparison with the previous run, the crystal grown within this run was modified with Mn. Therefore, to determine the chemical distribution, Energy Dispersive X-Ray Spectroscopy (EDX) has been performed around the region where the compound started to crystallise from the seed. The position of the region was roughly known as a result of the thermal profile done prior to crystal growth. EDX images are presented in Figure 5.24. The electron image (top, left) reveals the interface between the seed (lower side) and the nucleated grains (upper side), as previously seen in the EBSD image. The following images are chemical maps of the same region. All elements (Pb, In, Nb, Mg, Mn, Ti and O) seem homogeneously distributed. Although EDX results show no signs of Mn segregation at the interface, the effect may be more subtle. To completely eliminate Mn as contributing to unwanted nucleation, an identical crystal growth experiment would be required where a composition with no Mn should be grown.

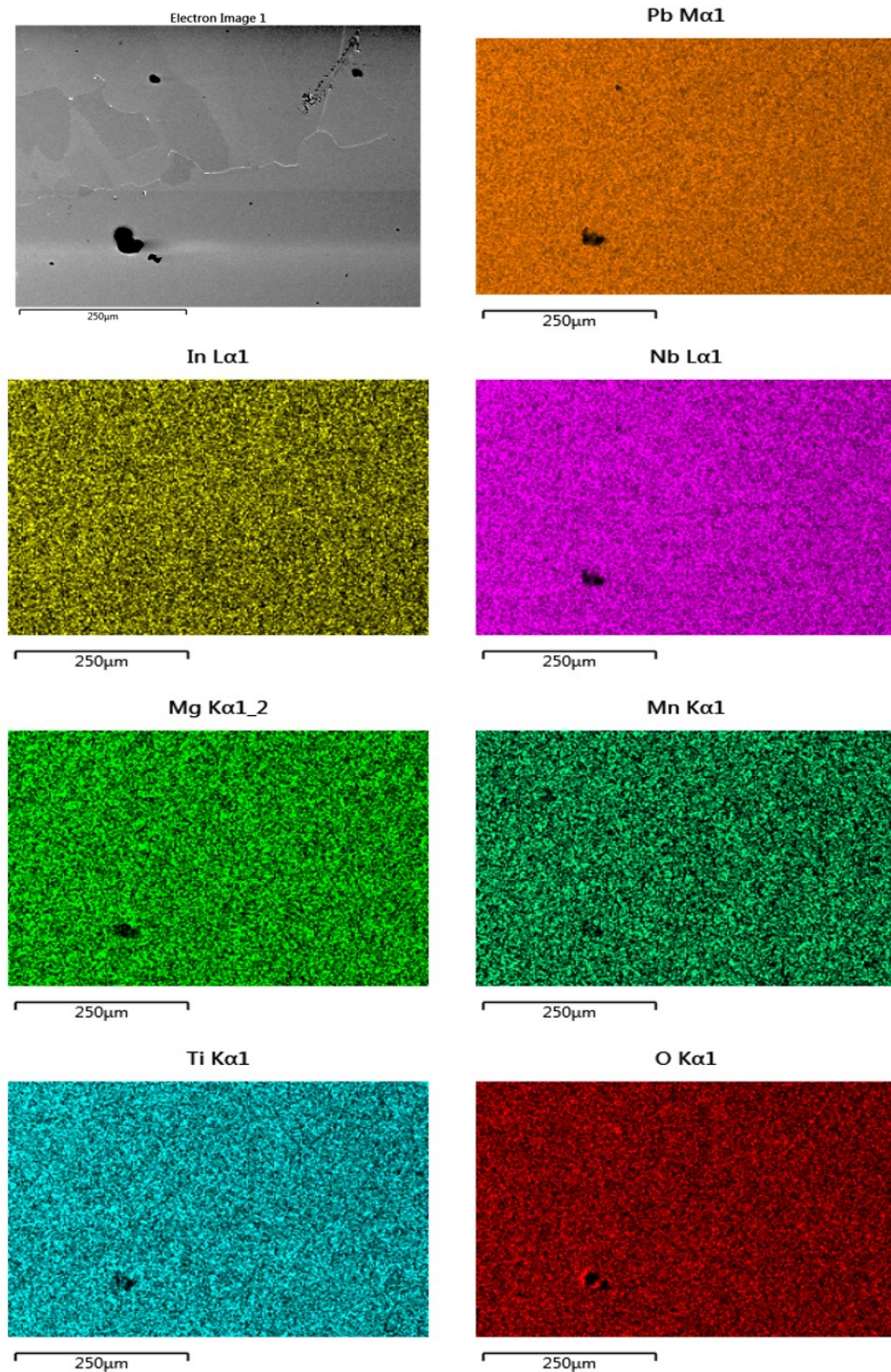


FIGURE 5.24: Energy Dispersive X-ray Spectroscopy performed at the interface seed - crystallised compound. The top-left image represents the electron micrograph revealing the seed in the bottom half of the image and the crystallised grains in the upper half of the image. The following images are chemical maps showing the distribution of each element in the compound for the same region as the electron micrograph. All chemical elements are homogeneously distributed.

5.3.2.4 Preparation for next run

Within this run an attempt at growing a Mn modified PIN-PMN-PT single crystal from a (001) oriented seed has been made. However, unwanted nucleation has been observed from the start of the growth as shown by EBSD images. EDX analysis has ruled out the existence of segregated chemical elements which could have potentially lead to unwanted nucleation. Therefore, another explanation must be found.

It has been previously noted that the (001) is the slowest and most difficult growth direction compared with (011) and (111). In addition, it has been shown [103] that the moving speed influences the liquid-solid interface shape and position - increasing the moving speed favors a concave interface, whilst decreasing the moving speed favors a more convex interface, as shown in Figure 5.25.

To test whether the lowering speed was the cause for unwanted nucleation, it has been decided to run a new growth experiment at a speed of 0.2 mm/h, which is to a moderate extent lower than 0.5 mm/h used for B2. The following section presents the result of B3 growth experiment.

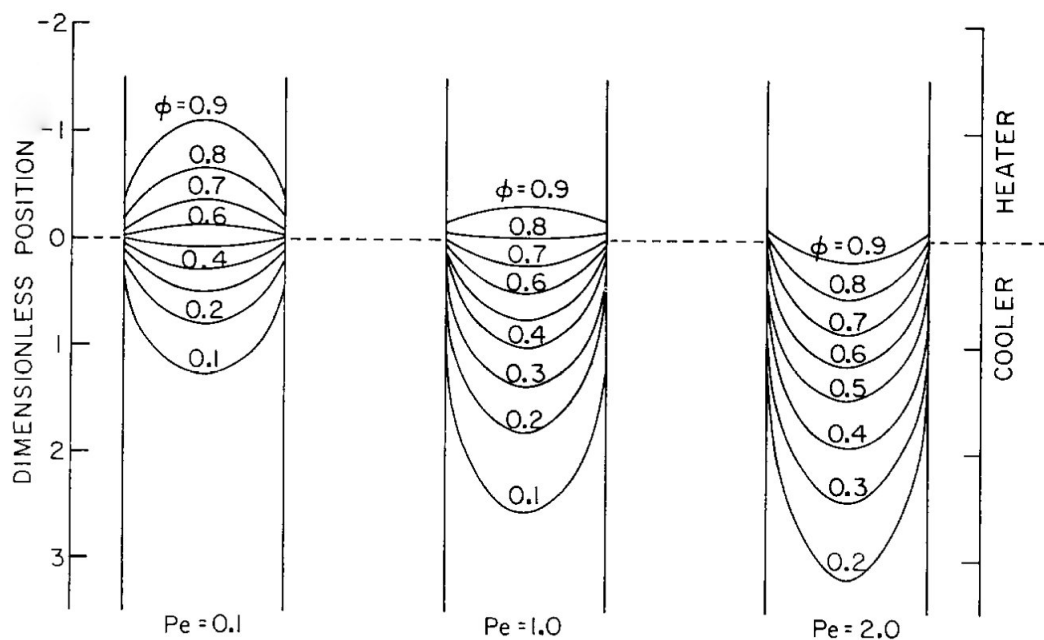


FIGURE 5.25: Influence of the moving rate on the liquid-solid interface shape and position. Pe is the ratio of heat carried by movement to heat conduction and is therefore associated with the moving speed. $Pe=0$ for a stationary ampoule and increases with increasing moving rate. The interface becomes increasingly concave with Pe increasing from 0.1 to 1 and then 2, adapted from [103].

5.3.3 Seeded Growth B3

Figure 5.26 shows the crystal grown at a rate of 0.2 mm/h as it was being removed from platinum crucible.



FIGURE 5.26: Single crystal boule grown during the third run, B3, as it is being removed from the platinum crucible

5.3.3.1 Growth direction - Pole figures

The single crystal nature of the boule has been analysed by means of pole figures on a sample diced from the lower part of the boule, a few mm away from the solidus/liquidus boundary. The set of pole figures (001), (011) and (111) is shown in Figure 5.27. Each pole figure reveals the presence of multiple grains within the sample due to the random distribution of multiple poles. Therefore, it has been concluded that unwanted nucleation has occurred during growth, regardless of the lower growth rate used compared with the previous experiment.

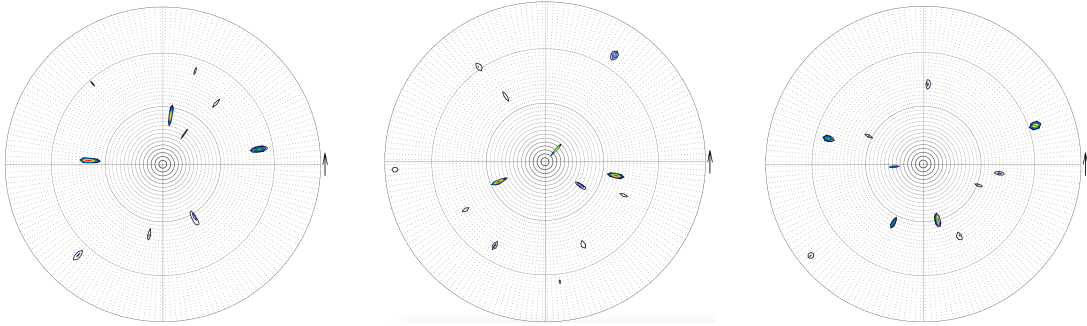


FIGURE 5.27: Pole figures obtained from a sample cut halfway through the seed pocket to investigate whether the crystal grew from the seed or nucleation has occurred as previously. The presence of multiple grains is confirmed by each pole figure, (001) (left), (011) (centre) and (111) (right).

5.3.3.2 Optical micrographs

Optical micrographs have been acquired to obtain a visual proof of the grains and are shown in Figure 5.28. Multiple grains can be observed, although they are larger than the grain previously obtained probably as a result of the lower growth speed.

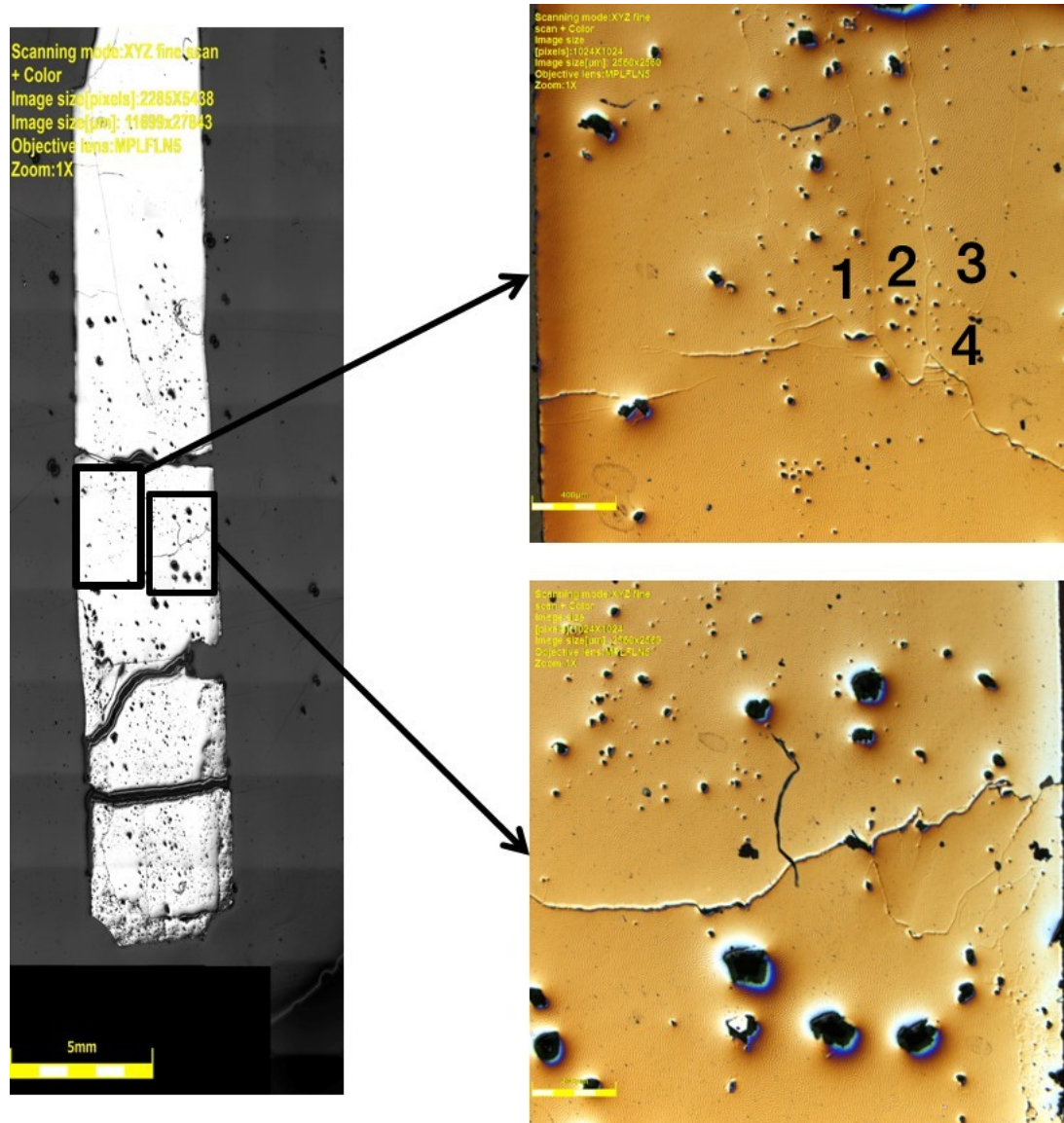


FIGURE 5.28: Optical micrograph of the B3 grown crystal - seed pocket region (left) and zoom in two regions (right). The scale bar of the left image is 5 mm and of the right 400 μm . Some grains have been numbered on the top right image to easily distinguish them.

5.3.3.3 Preparation for next run

The present experiment was designed to determine whether a lower growing speed compared with the speed used in the previous run, i.e. 0.2 vs. 0.5 mm/h, would be beneficial in growing a (001) oriented crystal from a seed and avoid unwanted nucleation. The evidence from this study, such as pole figures and optical micrographs, reveal the presence of several grains in the seed pocket region. Therefore, the lower growing speed did not prevent unwanted nucleation from occurring, although the grains were

larger than the ones found in the previous crystal. Given the difficulty of growing (001) oriented crystals reported [105], it has been decided to grow a crystal from a (011) seed, under the same conditions. The result of this experiment are presented in the following section.

5.3.4 Seeded Growth B4

The crystal grown within this experiment is shown during removal from the platinum crucible in Figure 5.29 . Having the experience of previous crystals, it has been decided that optical microscopy would suffice to assess the single crystal nature of the boule.



FIGURE 5.29: Single crystal grown during the fourth experimental run, B4 during removal from the platinum crucible

5.3.4.1 Optical micrographs

Figure 5.30 shows the optical micrograph of the crystal - region grown inside the seed pocket. The white arrows (Figure 5.30 left and zoom in, bottom-right) are pointing towards the liquidus/solidus boundary, which for this particular crystal was easy to determine owing to the difference in colour of the seeds and the grown crystal. The

seeds used were PIN-PMN-PT (light yellow), whilst the grown crystal was Mn:PIN-PMN-PT (dark grey). Approximately 2 mm away from the boundary, a polycrystalline region appears which is shown in Figure 5.30, top-right. Therefore, the images suggest that solidification has started in a single crystalline form, following the orientation of the seed. However, unwanted nucleation occurs after approximately 2 mm growth. Possible causes and solutions are discussed in the following section.

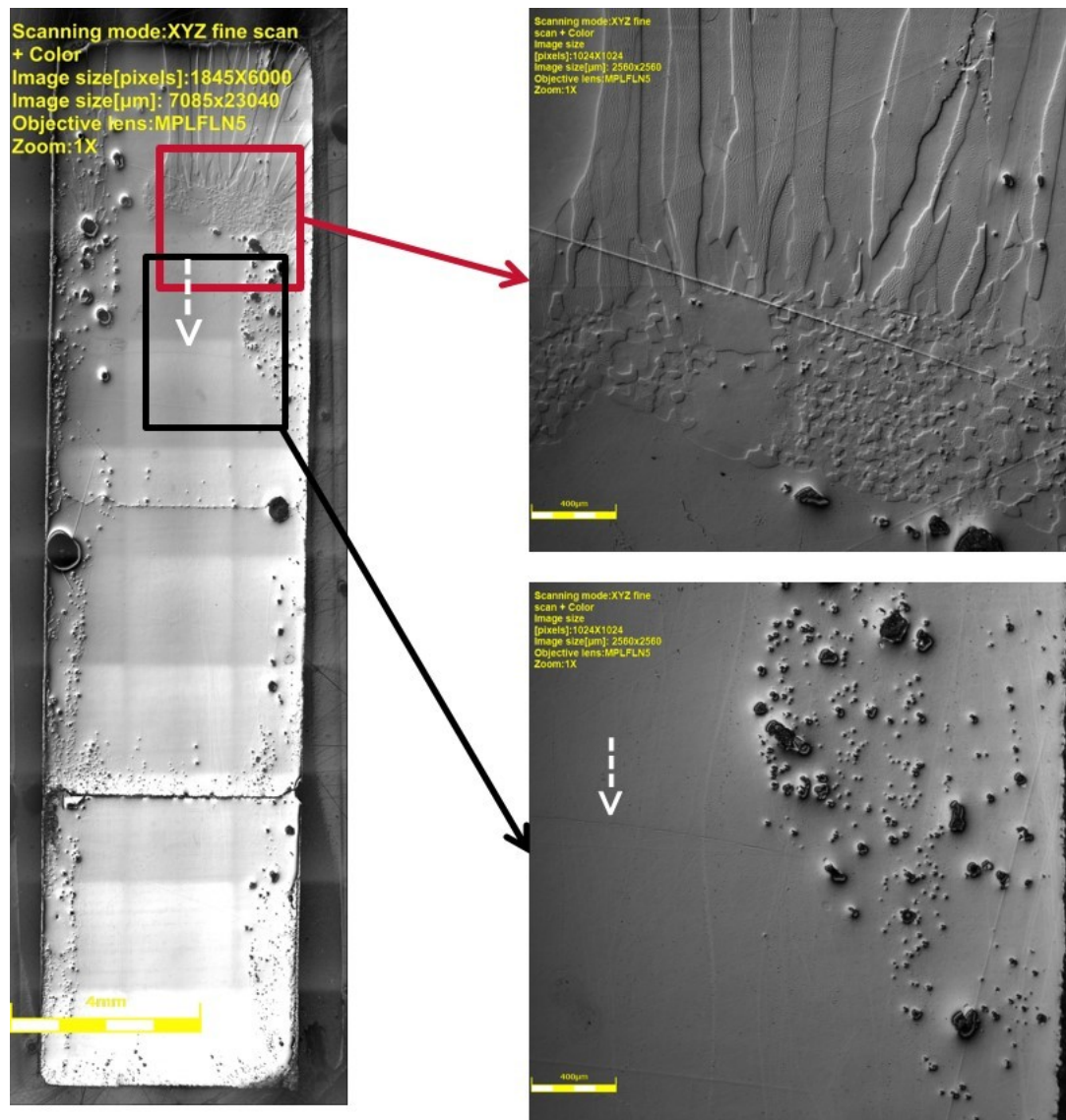


FIGURE 5.30: Optical micrograph of the crystal grown within B4 experiment - seed pocket region (left) and zoom in two regions (right). The scale bar is 4 mm for the left image and 400 μm for the right images.

5.3.5 Discussion

Unseeded and seeded crystal growth by the modified Bridgman method have been explored within this chapter. Following the results of four crystal growth experiments, two key points can be made:

1. A high quality single crystal can be easily grown when no seeds for orientation control are used.
2. When seeds are used, the growth of single crystals has been proven challenging as unwanted nucleation has occurred during each of the three seeded growth experiments.

This section discusses possible reasons for unwanted nucleation, other than chemical segregation which was discussed in Section 5.3.2.3, and highlights key factors leading to a successful single crystal growth via the seeded method.

A number of studies [3, 103, 106, 107] report that the shape and position of the liquid/solid interface are the most important factors during single crystal growth via directional solidification. In turn, the factors influencing the shape and position of the interface are:

- The temperatures in the cold and hot zones.
- The lowering rate of the crucible.
- The length of the crucible which causes an "end effect".
- The diameter of the crucible and that of the seed pocket.

The temperatures in the hot and cold zones have been discussed in Section 5.2.2 and have been chosen to obtain a slightly convex interface shape (i.e. 1355°C in the hot zone and 1150°C in the cold zone). A convex interface favors growth from the single crystal seed whilst avoiding nucleation on the crucible walls.

The crucible lowering rate has been initially set at 0.5 mm/h and was believed to be the cause of unwanted nucleation during the first seeded crystal growth experiment, Bridgman 2. However, lowering the speed to 0.2 mm/h did not stop undesirable nucleation from occurring (Bridgman 3, Bridgman 4).

Therefore, it has been concluded that the undesirable nucleation could be attributed

to temperature fluctuations within the crucibles caused by the *end effect* and by the *ratio of crucible (main body) diameter to seed-pocket diameter*. The two factors are discussed separately in the following lines.

The end effect is caused by the limited length of the crucible. Inside an infinitely long crucible the temperature field does not change and the interface position is fixed. However, inside a crucible of finite length, it has been shown that the growth speed accelerates as the crucible moves from the hot to the cold zone, despite a constant lowering rate. This behavior is shown in Figure 5.31. It is suggested that the acceleration of the growth rate may be avoided either by gradually lowering the temperature in the hot zone as the crucible moves or by using a very long crucible [106]. Furthermore, the ratio between the diameter of the crucible's main body and the diameter of the seed-pocket may lead to changes in heat transfer which may affect the axial thermal gradient. This behavior is graphically shown in Figure 5.32. The crucibles used for seeded growth within this work were 120 mm long with the inner diameter of the seed pocket 5.5 mm and the that of the main body 19 mm (drawings are provided in Appendix B). Hence, the difference between the diameter may have caused differences in heat transfer which lead to constitutional supercooling and hence multiple grains were formed.

Another factor which could have contributed to the heat transfer changes is the design of the alumina support system for the platinum crucible shown in Figure 5.7. The main body of the crucible has been surrounded by zirconia media, whilst the seed pocket was only surrounded by the alumina tube.

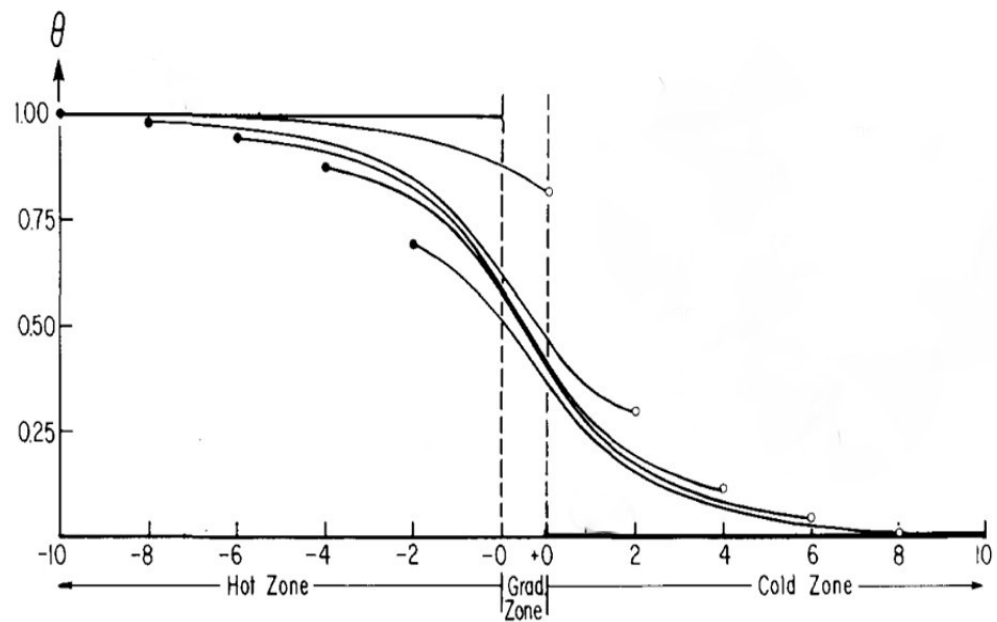


FIGURE 5.31: Progression of the thermal profile inside the crucible, as it moves from the hot towards the cold zone. The length of the crucible in this study was 11 times the diameter. From [106]

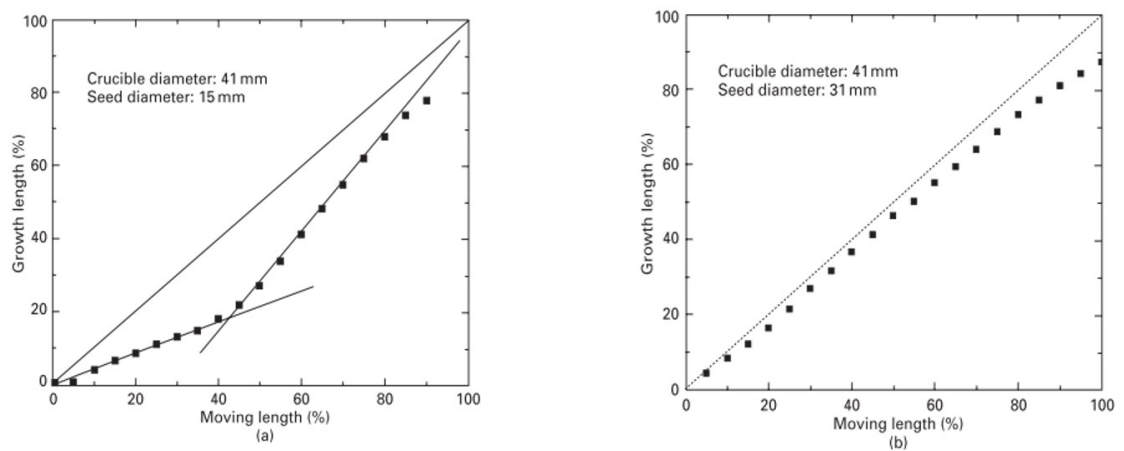


FIGURE 5.32: At constant lowering rate, the crystal growth speed accelerates if the diameter of the seed pocket is much smaller than the body of the crucible (left). The growth speeds remains constant for smaller differences in diameter. [3]

5.4 Summary and Conclusions

One aim of this thesis emphasised in Chapter 1 was to a feasibility study of growing relaxor-PbTiO₃ single crystals by Bridgman and Solid State Conversion Growth. This

chapter has addressed the growth of crystals by Bridgman. The four crystal growth experiments have investigated the following variables:

- Non-seeded versus seeded growth.
- Crucible thickness.
- Lowering speed.
- Crystallographic orientation of seeds.

A schematic diagram containing key parameters, result and the action taken from one experiment to the next of the Bridgman investigations is presented in Figure 5.33. The observations made following Bridgman experiments may be summarised as follows:

- A high quality single crystal may be relatively easy grown without a seed, by using a conical bottom shaped crucible. The preferred growth direction revealed by X-ray pole figures is (011). Chemical analysis confirmed the homogeneity of samples cut from a plate perpendicular to the direction of growth. Piezoresponse Force Microscopy was used to give an insight into the domain structure of the samples. 180° as well as 71° and/or 109° have been observed. The behavior of the imaginary versus the real impedance was described by a single semicircle implying response from the bulk only. Permittivity measurements revealed a relaxor behavior of a sample cut from the lower part of the crystal.
- The platinum crucible thickness has been reduced from 1 to 0.6 and finally to 0.4 mm with no sign of leakage. The thickness may probably be further reduced.
- Controlling orientation of crystals during growth has been proven challenging due to unwanted nucleation. Although growth speed has been reduced from 0.5 to 0.2 mm/h and the seed orientation has been changed from (001) to the less challenging (011), nucleation of multiple grains still occurred. Two possible causes are discussed - constitutional supercooling and the unreacted powder used to fill the crucible towards the bottom where pressed pellets could not be placed.

Following the results presented within this chapter, it is concluded that Bridgman may be utilised for the growth of large and highly dense single crystals. A number of factors need to be addressed in preparation for crystal growth such as: understanding of the thermal profile of the furnace, correct set up of the support system for the platinum

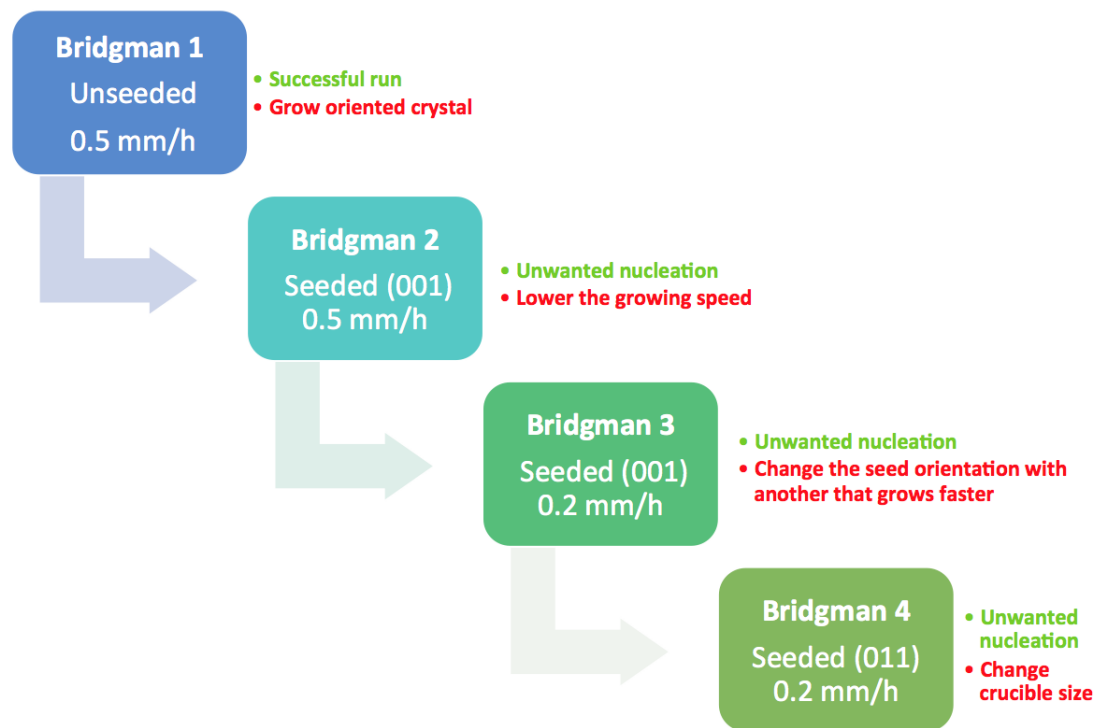


FIGURE 5.33: Summary of the Bridgman runs presenting the key parameters, as well as the result (in green) and the action taken for the subsequent run (red)

crucible to avoid major changes in heat transfer from the furnace to the melt which could lead to constitutional supercooling, choice of lowering speed, crucible dimensions which need to be chosen so that large ratios between crucible diameter and seed pocket diameter are avoided.

5.5 Limitations and Future Trends

The present study has shown that from an industrial production point of view, where single crystal growth is required and no previous experience is available, Bridgman technique may be set up relatively fast. It has been proved that self-seeded Bridgman requires little effort to be set up, whilst seeded Bridgman requires a number of experiments to determine conditions which do not encourage secondary nucleation. Specifically, seeded-Bridgman experiments should be performed with various designs of the Pt crucible and its support system to determine a design which does not favour supercooling and hence secondary nucleation. In addition, computer simulations

would be required to understand the heat transfer from the furnace to the charge and consequently to clearly describe requirements for crystal growth with no secondary nucleation.

However, two issues will still remain, namely the high cost due to the use of platinum crucibles and the compositional gradient due to Ti segregation (see Section 3.3.2). To reduce the compositional gradient, a number of solutions are suggested.

5.5.1 Bridgman method variations

5.5.1.1 Continuous Feed Growth

One solution to reduce the compositional gradient along the grown crystal has been suggested to be *Continuous Feed Growth*. Echizenya et al. [108] have shown that variation of Ti in a PMNT crystal may be controlled within 6% by using Continuous Feed Growth, compared with 20% when Conventional Bridgman Growth is used - Figure 5.34. Subsequent optimisation led to control of the Ti content within $\pm 2.5\%$ in a PIN-PMN-PT crystal [109]. The method consists of continuously pouring synthesized material into the crucible where crystal growth takes place via a feeding mechanism. Nevertheless, the method increases the complexity of the furnace design due to the feeding mechanism. Caution must be applied when designing the feeding path due to the Pb volatilisation within the crucible where growth takes place.

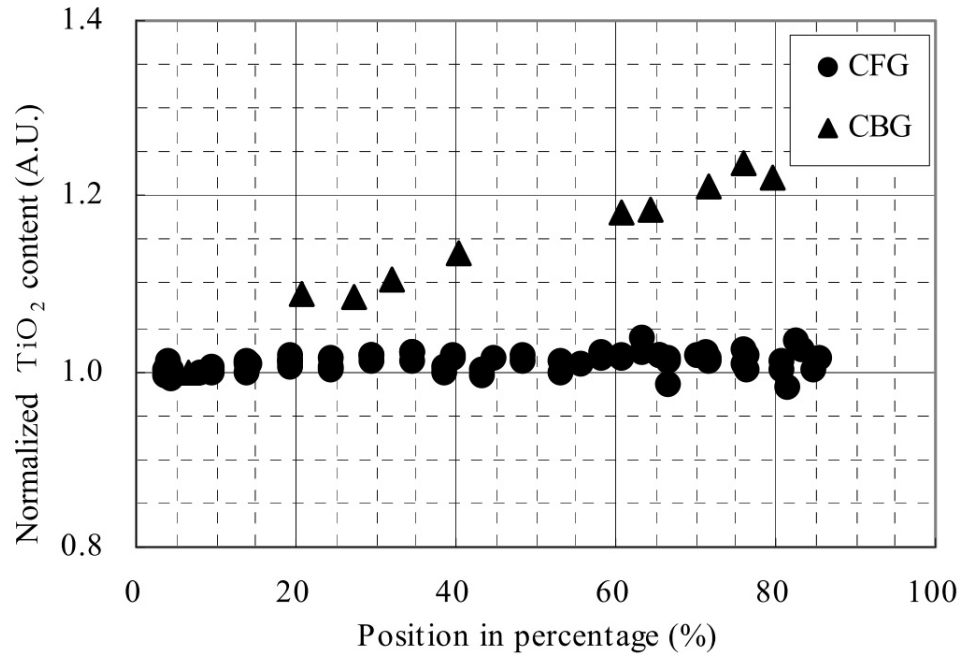


FIGURE 5.34: Ti concentration along a PMNT crystal obtained by Continuous Feed Growth (CFG) and a PMNT crystal obtained by Conventional Bridgman Growth (CBG). Ti content is normalised at 5% of the crystal position. CFG grown crystal shows a more uniform distribution of the Ti content, with variation controlled at 6% compared with 20% within the CBG crystal. From [108].

5.5.1.2 Multiround Growth

Another attempt at controlling the Ti concentration along the Bridgman grown crystal is the *Multiround Growth* reported by Wang et al. [66]. The method consists of two growth rounds in the same crucible. During the first run, a 26PIN:42PMN:32PT crystal was grown from a seed. During the second run, material with a 26PIN:42PMN:26PT composition (6% lower Ti content compared with the first formulation; composition not balanced purposely) has been fed to the crucible. The aim was to control the concentration of the entire crystal around the Morphotropic Phase Boundary - Figure 5.35. Although this approach is successful in terms of maintaining the composition around the Morphotropic Phase Boundary, variation of Ti content throughout the crystal still exists.

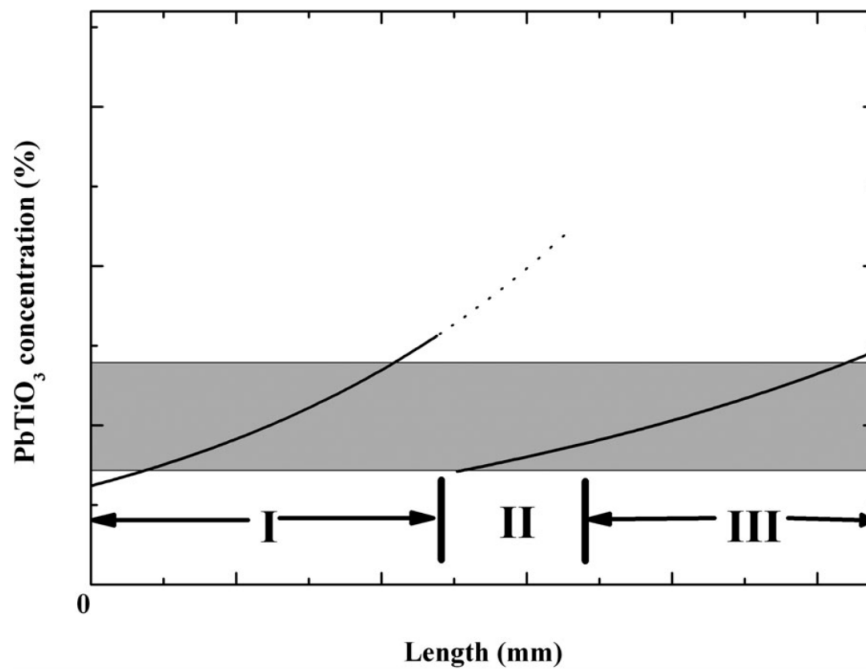


FIGURE 5.35: PbTiO_3 concentration along a crystal grown by the Multiround Growth approach. Section I and II are grown within the first run, whilst II and III are grown in the second run. Section II is remelted in the second run so that the first crystal acts as seed for the second. The grey area represents the Morphotropic Phase Boundary. Therefore, the graph shows that most of the crystal maintains a composition within the MPB. From [66].

5.5.1.3 Double Melt Approach

Tian et al. [110] have also reported an improvement in the usable section of the crystal by reducing the compositional gradient by means of a *Double Melt Approach*. The idea is different compared with the one presented in the previous subsection in that the process occurs within a sealed crucible during one single run. Half of the crystal is grown at first, followed by melt and growth of the second charge. This procedure is possible due to special design of the crucible and growth system.

5.5.1.4 Vertical Gradient Freeze

A method which does not involve crucible movement relative to the furnace has also been explored. *Vertical Gradient Freeze* method involves ramping down the power to the heater in a regulated manner so that a thermal profile moves upwards relative to the crucible [111]. Crystallisation speed is believed to be more accurately controlled and

hence the risk of undesired nucleation is minimised [112]. However, this method fails to improve the compositional gradient along the grown crystal and therefore does not represent an attractive approach for further investigations.

5.5.1.5 Float Zone Technique

An ideal method for growing relaxor-PbTiO₃ single crystals would eliminate both the compositional gradient and the expensive platinum crucible. *Float Zone Technique* seems a promising candidate. The method consists of a controlled melt zone (floating zone) which moves upwards along the material to be grown. Given the absence of a crucible, the volatilisation of Pb may be controlled by high pressure environments. However, initial experiments of growing PbTiO₃ [48] have shown that the molten zone is not stable and collapses. The instability of the molten region is explained by a strong Marangoni convection, i.e. the tendency of mass and heat to move towards regions of higher surface tension within a liquid. Consequently, considerably more work is needed to tackle the instability of the molten zone. An interesting study would consist of crystal growth trials in microgravity environment.

5.5.2 Non-melt Crystal Growth Techniques

Due to the difficulty in controlling the segregation of Ti when growth from the melt is considered, a priority should therefore be to investigate non-melt techniques.

5.5.2.1 Non-melt Bridgman

One option would be a non-melt Bridgman technique which would involve translation of the crucible with the charge through a thermal gradient but starting with temperatures right below the melting point ($\approx 10^\circ\text{C}$ or more below the melting temperature) so the charge will not be melted. At low enough translation rates a polycrystalline charge could be converted into a single crystal. The transformation would be solid to solid rather than liquid to solid as in conventional Bridgman.

5.5.2.2 Solid State Conversion Growth

Solid State is a technique which, as described in section 3.3.3, does not involve melting of the material to be grown. It has been briefly investigated by the scientific community and the technique is less complex than the non melt Bridgman suggested above. If successful, chemically homogeneous crystals could be obtained. In addition, growing crystals by this method would dramatically reduce the cost as the need for a platinum crucible is eliminated and specialised equipment (such as Bridgman furnace) is no longer needed. The next chapter aims to investigate the feasibility of growing crystals by the solid state method by providing initial investigations.

Chapter 6

Solid State Conversion Growth

Abstract

The previous chapter has shown that single crystals may be relatively easy to grow by the Bridgman method. Despite the high structural quality of the crystals obtained by Bridgman, the method has the main disadvantage of producing a compositional gradient along the boule which reduces the amount of crystalline material available for use. Therefore, a crystal growth technique able to produce homogeneous crystals would be desirable. The aim of this chapter is a feasibility study with respect to a solid state growth technique, namely Solid State Conversion Growth. The principle of the method is based on a solid-solid transformation. As the precursor compound is not melted, segregation is avoided and a chemically homogeneous crystal is obtained. A first objective of this work was a grain growth study. PIN-PMN-PT and Mn:PIN-PMN-PT compositions were prepared and the samples were sintered under different conditions of temperature. Understanding the grain growth behavior represents the basis of single crystal growth from the solid state. The second objective was to perform crystal growth experiments using single crystal seeds as nucleus grains. The results indicate that crystal growth from a seed is encouraged when a Pb-based interlayer is placed in between the seed and the polycrystal to be grown, particularly a heteroepitaxial uniform thin film of the same composition as the crystal to be grown. Although a promising method with valuable advantages such as simplicity, homogeneity and growth of crystals with predetermined shape, Solid State Conversion Growth is not a mature method and a large amount of experiments are further required to determine the conditions for growth of a crystal of useful size.

6.1 Introduction

In the introductory chapter of this thesis it has been highlighted that relaxor-PT single crystals are of great interest for underwater and medical transducers. From the three methods of growth available, limited crystal sizes may be grown by solution, whilst Bridgman produces an undesirable compositional gradient along the crystal boule. Ideally, a method which is simple, of low cost and able to produce homogeneous crystals of high structural perfection is desirable.

This chapter seeks to determine whether Solid State Conversion Growth is a viable method for growth of relaxor-PT single crystals. The study was conducted in the form of experimental analysis. Given the nature of the method, i.e. a solid-solid transformation which consists of annealing a polycrystalline sample under specific conditions as described in detail in Chapter 3, a critical step is to understand the behavior of the sample under heat treatment, particularly the grain growth behavior.

Therefore, the first step of the study was a grain growth investigation performed on PIN-PMN-PT and Mn:PIN-PMN-PT. Compositions where excess PbO is present were also prepared and analysed. PbO is known to provide a liquid phase at the sintering temperature which enhances boundary mobility and may facilitate crystal growth. In addition, PbO excess might be beneficial in diminishing the weight loss due to Pb volatilisation during heat treatment. Samples were annealed for 24 h at different temperatures to assess the extent to which grains are growing. For a crystal of useful size to be obtained, grain growth within the matrix must be suppressed and growth of a single grain, i.e. a nucleus grain must be encouraged. Due to the difficulty in controlling the growth of a single grain within the matrix, an external, large nucleus is provided in the form of a single crystal seed.

Consequently, the second step of this study was to investigate crystal growth from PMN-PT and BT crystal seeds which acted as nucleus grains. Particularly, this investigation aims to assess whether a Pb-based interlayer between the seed and the polycrystal shows any benefit in promoting crystal growth.

Although based on limited experimental results, this study will conclude on the practicality of using solid state method for single crystal growth and will also briefly describe the limitations of the technique. Future work with potential of overcoming the limitations is also suggested.

6.2 Experimental procedure

6.2.1 Sample preparation for grain growth investigations

Four different samples have been prepared for grain growth investigations, as follows: PIN-PMN-PT, Mn modified PIN-PMN-PT, 8mol% PbO excess PIN-PMN-PT and 8mol% PbO excess Mn modified PIN-PMN-PT. The formulation and synthesis procedure for PIN-PMN-PT have been given in Chapter 4. The modification with Mn has been made in a stoichiometric manner according to the formula $2\text{Pb}(\text{Mn}_{1/3}\text{Nb}_{2/3})\text{O}_3 \cdot 98(\text{Pb}(\text{In}_{1/2}\text{Nb}_{1/2})\text{O}_3 - \text{Pb}(\text{Mg}_{1/3}\text{Nb}_{2/3})\text{O}_3 - \text{PbTiO}_3)$. The PbO excess has been mixed as additive to the selected compositions during the binder mixing step. The procedure has been described in Chapter 4 of the thesis. The particle size of the synthesized powder has been analysed by laser light scattering technology (Mastersizer 2000, Malvern Instruments, United Kingdom). A small amount of powder was dispersed in water for analysis.

The powder has been compacted into 10 mm diameter pellets by uniaxial pressing followed by isostatic pressing at 200 MPa for approximately 5 minutes. The binder burn out stage has been achieved following the profile in Figure 6.1. Subsequently, the

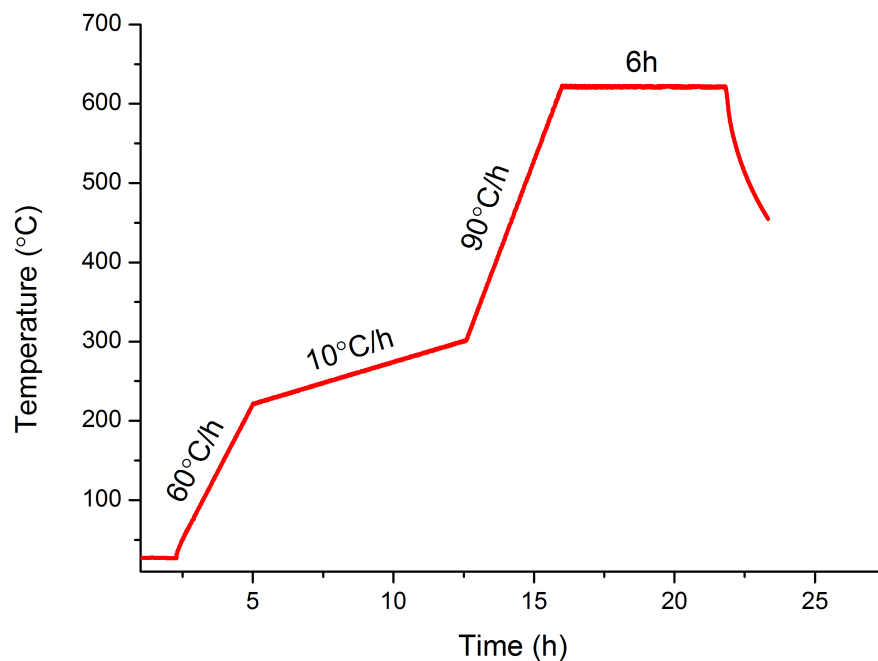


FIGURE 6.1: Binder burnout profile

samples have been placed on alumina tiles, covered with alumina crucibles and have been sintered for 24 h at 1150, 1200 and 1250°C. A heating rate of 300°C/h has been used. The phase and purity of the sintered samples have been investigated with X-ray Diffraction technique using PANalytical X'Pert Diffractometer (Phillips, The Netherlands) with a theta-theta goniometer. Density of the samples has been assessed via the Archimedes method. The procedure is described in Appendix C. The weight loss during sintering has been assessed by determining the weight of the sample before and after the heat treatment. Sintered samples have been ground and polished according to the route in Table 6.1. To reveal grain boundaries the samples have been chemically etched in a solution containing HCl and HF acids. The grain size has been analysed using OLYMPUS BX51 optical microscope (Olympus, Japan). The average grain size has been determined via the linear intercept method, as follows. For each micrograph a diagonal has been superimposed and the mean size has been determined from all the grains falling on the diagonal. To account for the real, 3D shape of the grains, Mendelson correction factor for ceramics of 1.56 has been used [113].

6.2.2 Crystal growth experiments

Following the grain growth study, two crystal growth experiments have been designed. The aim of the first experiment was to determine whether a Pb-based interlayer between the seed and the polycrystalline matrix promotes crystal growth. (001) oriented PMN-PT seeds with the size of 10x10x1 mm³ have been used. One of the two PMN-PT seeds was covered with a layer of 60 wt% Pb(II) 2-ethylhexanoate in mineral spirits [114]. The seeds have been embedded in 8mol% excess PbO PIN-PMN-PT powder by using gentle uniaxial hand pressing. Any higher uniaxial pressure would cause the seed to shatter. Subsequently, the compact has been isostatically pressed at 200 MPa for approximately 5 minutes. The samples have been placed on alumina tiles, covered with an alumina crucible and annealed at 1150°C for approximately 2 h.

The second experiment aimed to determine whether a thin film deposited on the seed is beneficial for crystal growth. (111) oriented BT seeds with the size of 10x10x1 mm³ have been used. A thin film has been deposited on one of the two seeds via Pulsed Laser Deposition. The conditions for deposition were as follows: heat up rate 20°C/min, substrate (i.e. the seed) temperature 550°C, target rotation 5 rpm, substrate rotation 5 rpm, laser energy 45 mJ, laser frequency 5 Hz, O₂ flow at 30 sccm, number of target shots 10 000, pressure inside the deposition chamber 300 mTorr, target-substrate distance 5 cm. Atomic Force Microscopy (Agilent Technologies 5420 Scanning Probe Microscope,

TABLE 6.1: Polishing procedure. Advice and products from Buehler.

Step	Surface	Abrasive Lubricant	Force (N/specimen)	Time (mm:ss)	Platen Speed (rpm)	Head Speed (rpm)	Relative Rotation
1	SiC	P400 P600 water	20	Until plane 0:40	150	60	Comp
2	TextMet P	9 μm diamond suspension diamond lubricant	20	5:00	150	60	Contra
3	TextMet P	3 μm diamond suspension diamond lubricant	20	5:00	150	60	Comp
4	Trident	1 μm diamond suspension diamond lubricant	20	3:00	150	60	Comp
5	ChemoMet	Colloidal Silica	20	1:20	100	60	Contra

Agilent Technologies, USA) was used to analyse the topography of the film deposited, whilst X-ray Diffraction (PANalytical X'Pert Diffractometer, Phillips, The Netherlands) has been used to assess whether the film has been epitaxially deposited. The seeds have been embedded in 8mol% excess PbO PIN-PMN-PT powder in the same manner as described for the first experiment. Subsequently, the pressed samples have been again placed on alumina tiles, covered with an alumina crucible and annealed at 1100°C for approximately 2 h.

Following heat treatment the samples have been cut cross-sectionally using an automatic cut-off machine (Accutom 5, Struers, Denmark) and polished using the regime in Table 6.1. Optical micrographs have been recorded with the same microscope as for grain size analysis.

6.3 Results and discussion

6.3.1 Polycrystalline precursor processing

6.3.1.1 Particle size of synthesized powder

To evaluate the extent to which grains are growing following long annealing times, the initial particle size of the synthesized powder has been assessed. Figure 6.2 shows the particle size distribution by number and volume obtained for synthesized PIN-PMN-PT, which was considered representative for all compositions prepared. By number, an average particle size of 0.4 μm has been obtained, whilst by volume, 2.2 μm .

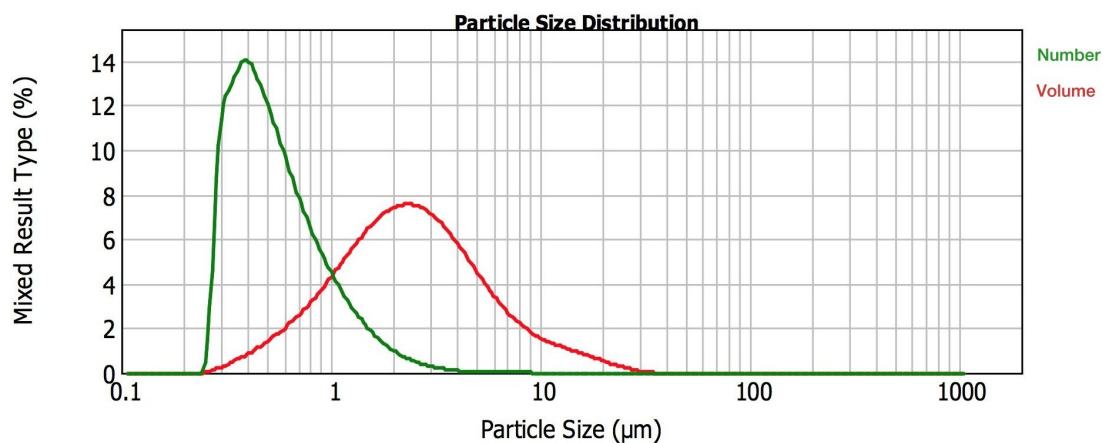
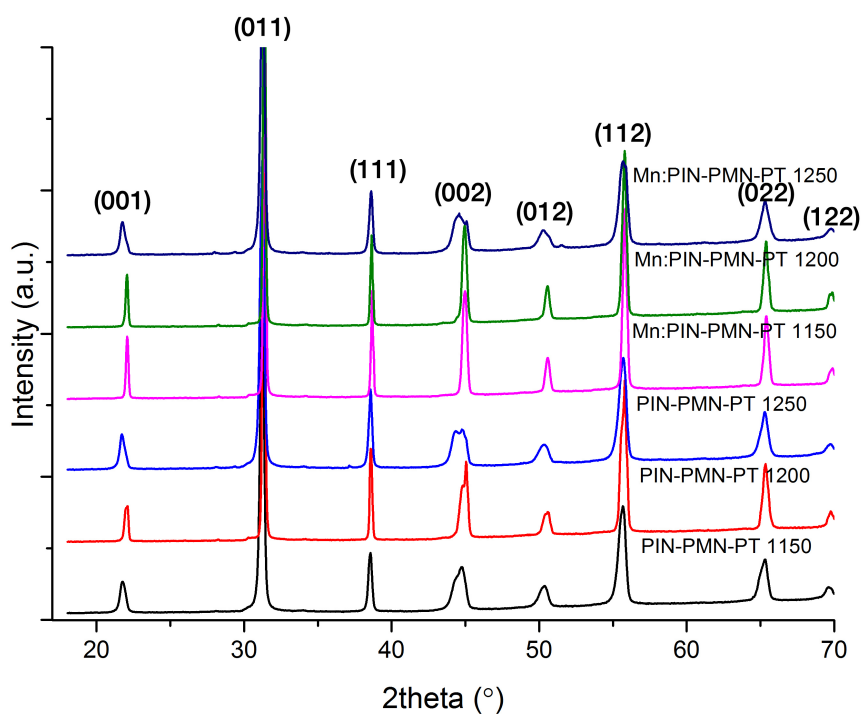


FIGURE 6.2: Particle size distribution of PIN-PMN-PT powder by number and by volume

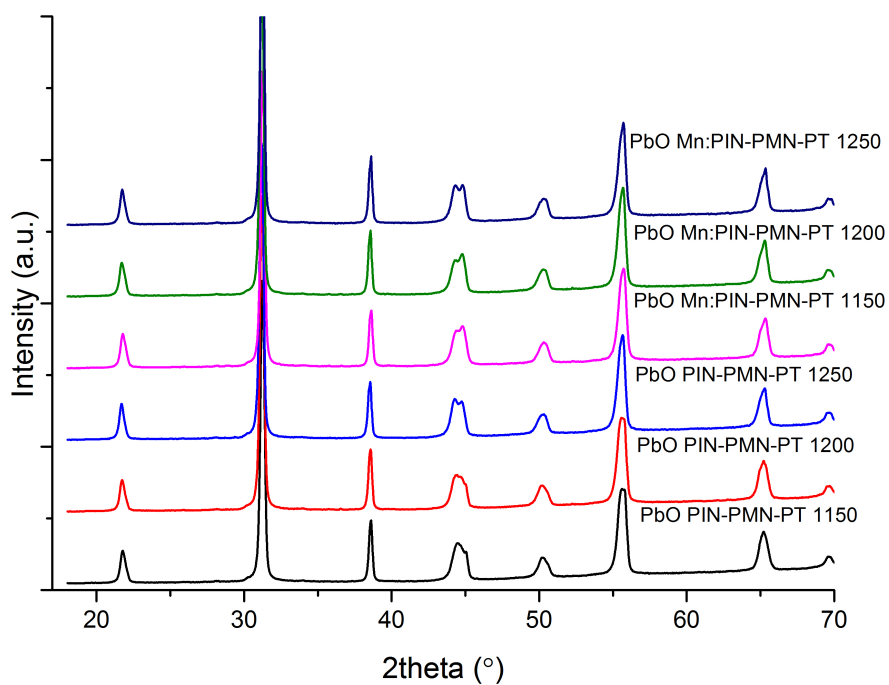
6.3.1.2 Phase analysis by X-ray diffraction

Figure 6.3 shows X-ray diffractograms for all samples. A pure perovskite phase has been obtained in each case with no secondary phases. To further investigate the crystallographic phase, the (002) peak has been analysed. When a tetragonal phase is present the peak is split as the unit cell is elongated in one direction and the spacing between (002) planes will differ slightly from the spacing between (200). On the contrary, a single peak is observed when a rhombohedral phase is present as the unit cell has all edge lengths equal (refer to Section 2.2.1 for details regarding crystallographic structures). Figure 6.3a shows the X-ray diffraction patterns for samples with no excess PbO. A tetragonal phase is revealed except for Mn:PIN-PMN-PT sintered at 1150 and 1200°C. It has been previously suggested [115] that Mn may induce a phase transformation from tetragonal to rhombohedral. This behavior is a result of the Jahn-Teller effect which causes the unit cell to distort. However, only the electron configuration of Mn^{3+} is believed to have this influence. This could potentially mean that in Mn:PIN-PMN-PT sintered at 1150 and 1200°C Mn has predominantly a valence state of 3+, although further investigations would be required to confirm (refer to Chapter 7 for a detailed study regarding behaviour of Mn in PIN-PMN-PT). A tetragonal phase is again observed in Mn:PIN-PMN-PT sintered at 1250°C revealing an influence that higher sintering temperature may have on the crystal structure. Figure 6.3b shows all samples with PbO excess sintered at different temperatures. A pure perovskite phase has been obtained in all cases with a tetragonal crystal structure.

The purpose of the X-ray diffraction study was to ensure no secondary phases such as pyrochlore is present in the samples. It has been shown that a pure perovskite phase is present in all samples, mainly with a tetragonal crystal structure. Further studies are required to determine the influence of chemical composition and sintering temperature on the crystallographic phase (i.e. rhombohedral and/or tetragonal).



(A) PIN-PMN-PT and Mn:PIN-PMN-PT sintered at 1150, 1200 and 1250°C



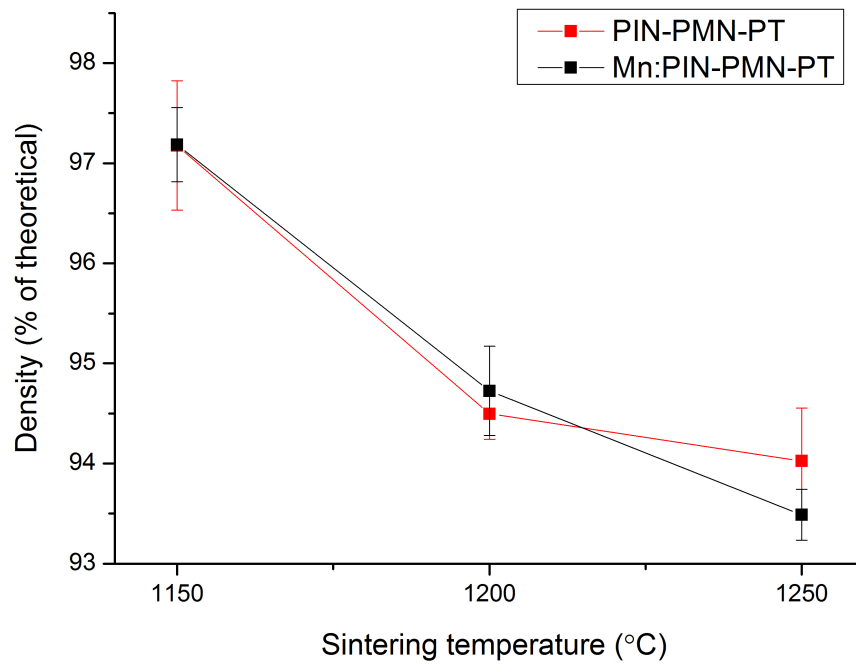
(B) PIN-PMN-PT and Mn:PIN-PMN-PT with 8mol% excess PbO sintered at 1150, 1200 and 1250°C

FIGURE 6.3: X-ray diffraction patterns recorded on all compositions prepared, sintered at different temperatures

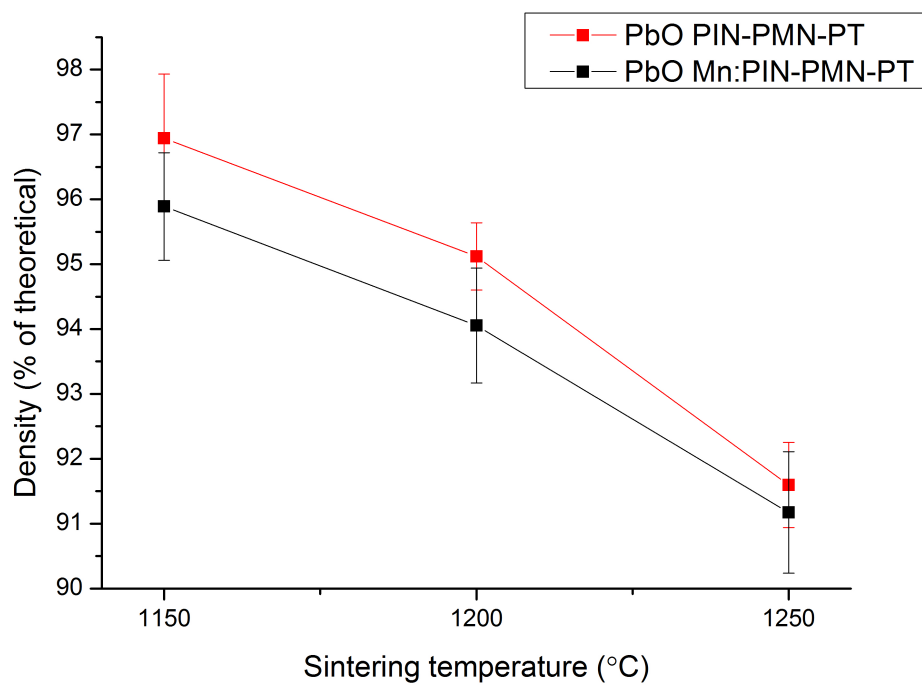
6.3.1.3 Density and weight loss

The density of the samples is graphically represented in Figure 6.4. First, the samples with no excess PbO - Figure 6.4a are discussed. No significant differences are observed when comparing samples with Mn with samples without Mn. Densities $>97\%$ of the theoretical were achieved when sintering at 1150°C . With increasing temperature the density of the samples decreases to $\approx 95\%$ for samples sintered at 1200°C and $\approx 94\%$ for samples sintered at 1250°C . Second, densities of samples with excess PbO - Figure 6.4b are discussed. When sintered at 1150°C , a density of 97% has been achieved for the Mn free sample and 96% for the Mn modified. Density decreases for samples sintered at 1200°C to 95% for the Mn free sample and 94% for Mn modified. A further decrease to 92% is observed in both Mn free and Mn modified when samples are sintered at 1250°C .

The results suggest that density decreases more rapidly with increasing temperature when excess PbO is present, due to volatilisation. The trends observed for density measurements are in agreement with weight loss measurements, presented in Figure 6.5. Samples with no excess PbO show negligible weight loss when sintered at 1150 and 1200°C and increases to 8% when sintered at 1250°C . However, when PbO excess is present, loss of 6% is observed at 1150 and 1200°C and rapidly increases to 15% , when sintered at 1250°C .



(A)



(B)

FIGURE 6.4: Density of samples sintered at different temperatures for 24 h, without PbO excess (top) and with PbO excess (bottom)

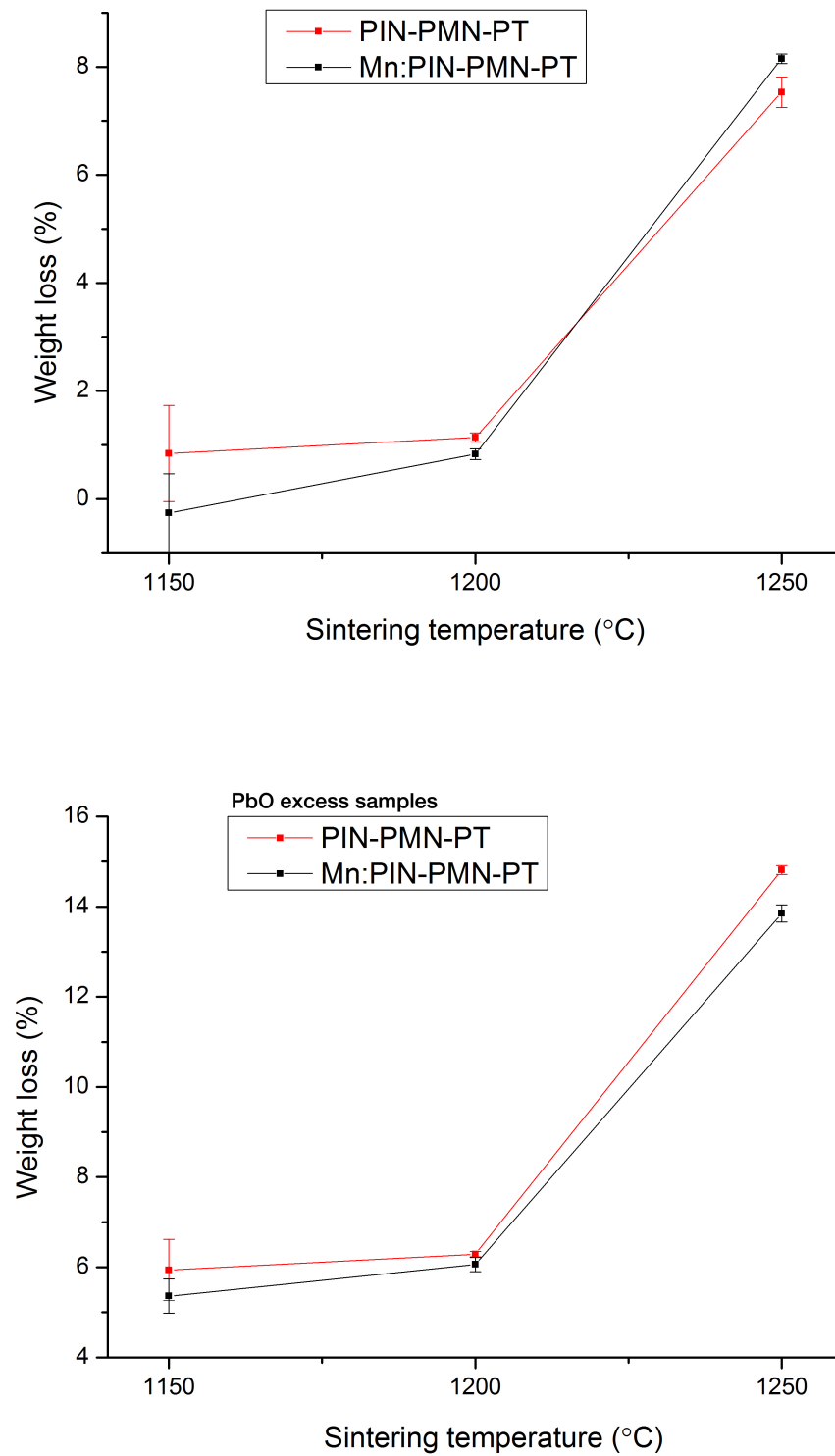


FIGURE 6.5: Weight loss of samples sintered at different temperatures for 24 h, without PbO excess (top) and with PbO excess (bottom)

6.3.1.4 Grain size analysis

Optical micrographs have been obtained on polished and chemically etched samples to investigate the influence of Mn modification, excess PbO and temperature on samples sintered for 24 h. Images of samples with no excess PbO are shown in Figure 6.6, whilst samples with PbO excess are presented in Figure 6.7. Some of the features across all images are a result of the grain pullout which has occurred during polishing. The average grain sizes for all samples imaged are represented in Figure 6.8. The difference between samples with and without Mn are not particularly prominent. The average grain size increases with temperature for all compositions prepared. However, when PbO excess is present the size of grains is significantly larger. For example when sintered at 1150°C, the size of grains in samples with no excess PbO is $\approx 6.5 \mu\text{m}$, whilst in samples with excess PbO is $\approx 13 \mu\text{m}$. No abnormal grain growth has been observed in samples with excess PbO which implied a uniform distribution of the PbO excess during material processing. In addition, with increasing sintering temperature the width of the size distribution becomes broader as suggested by the wider error bars at higher temperature.

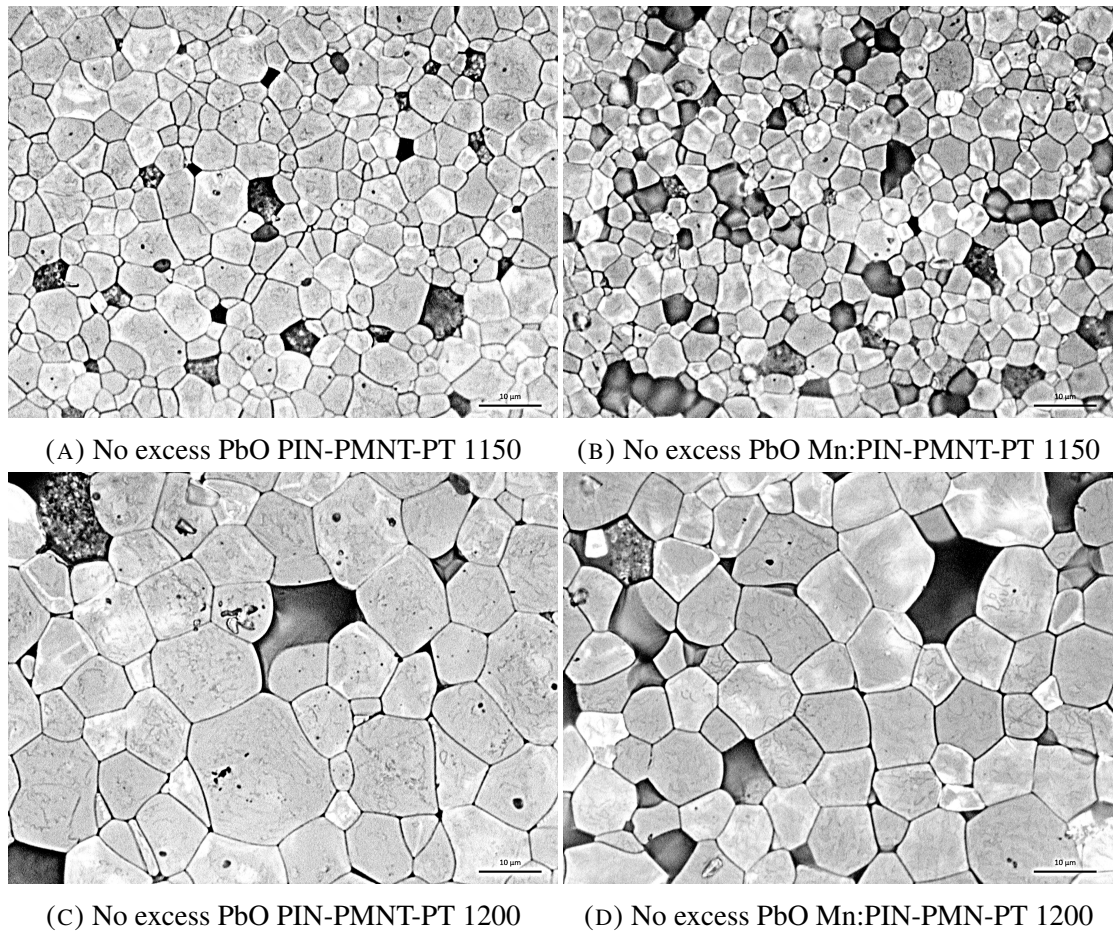


FIGURE 6.6: Optical micrographs of polished and chemically etched samples with no excess PbO, sintered at 1150 and 1200°C. Samples sintered at 1250°C proved difficult to etch and are not shown.

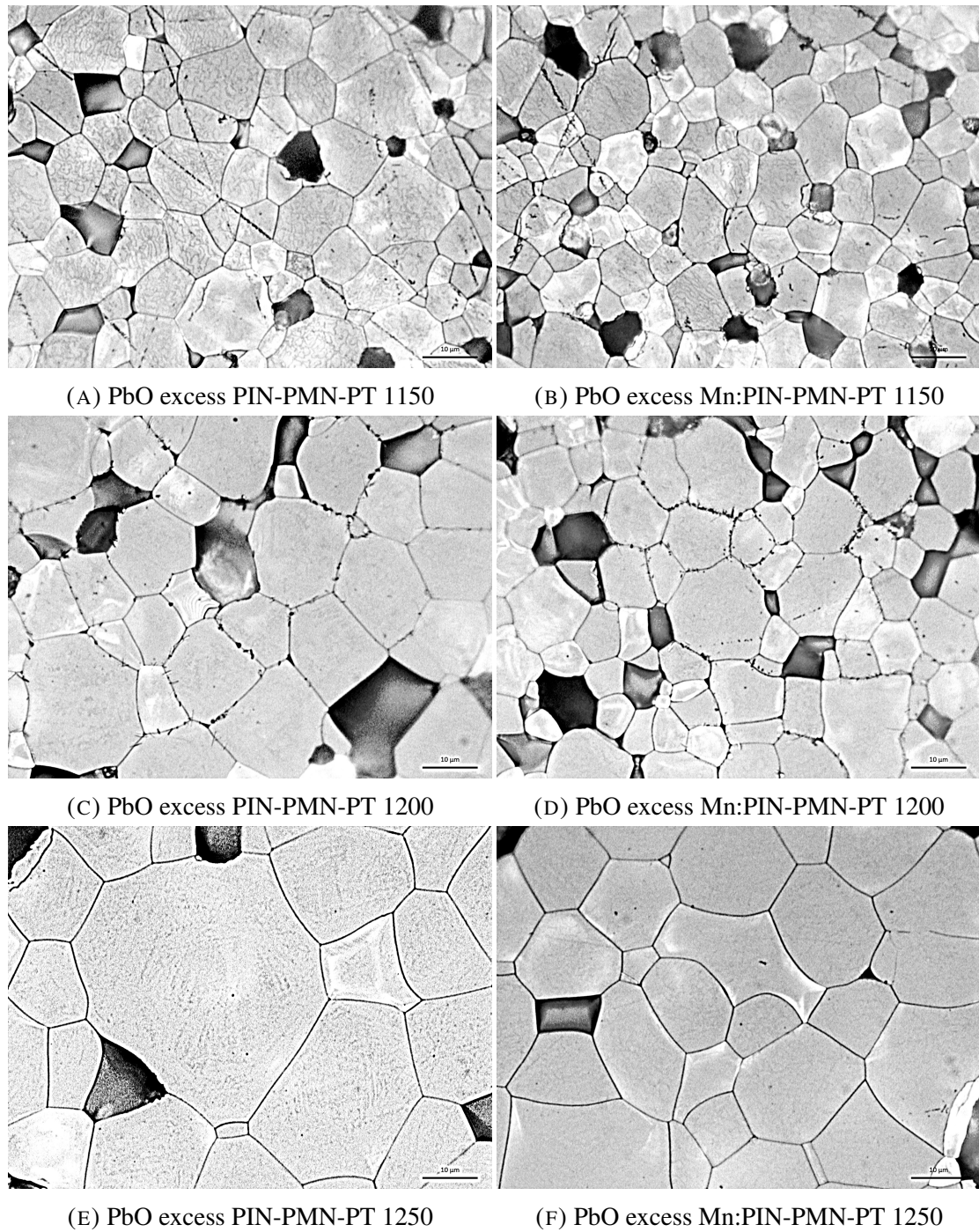
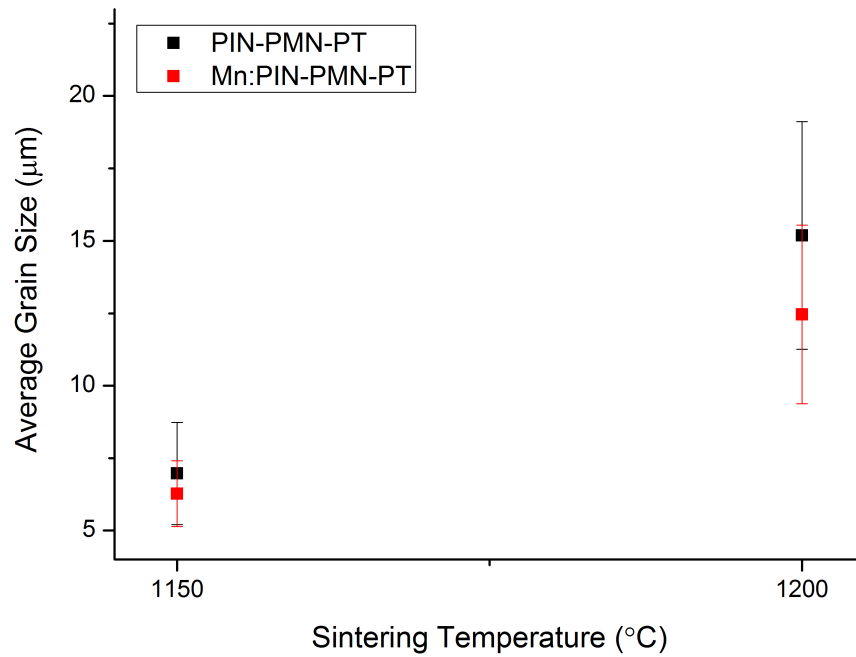
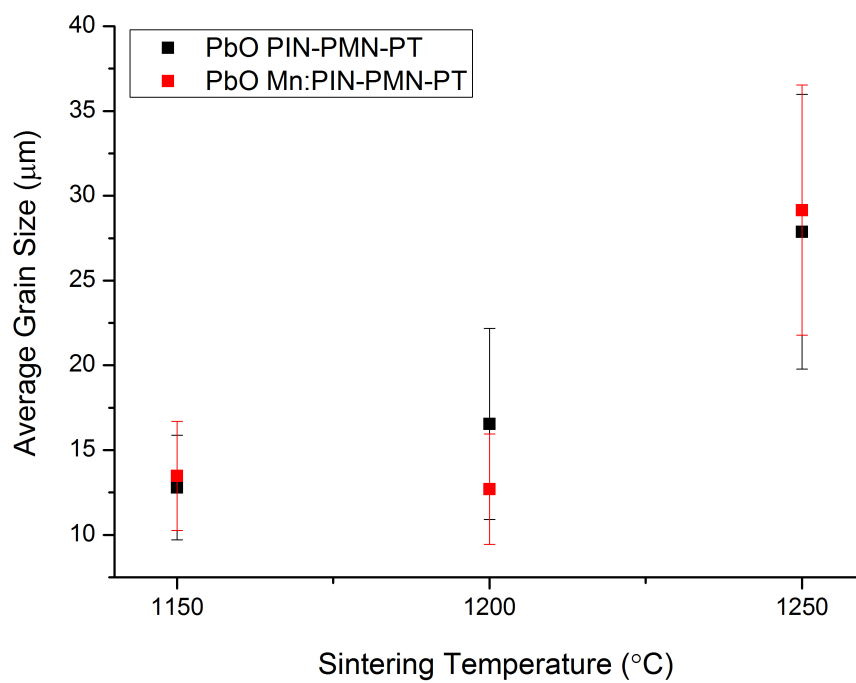


FIGURE 6.7: Optical micrographs of polished and chemically etched samples with PbO excess, sintered at 1150, 1200 and 1250°C.



(A)



(B)

FIGURE 6.8: Average grain size for samples with no excess PbO (A) and with excess PbO (B)

6.3.2 Crystal growth experiments

For crystal growth experiments, PMN-PT and BT have been chosen as single crystal seeds. The polycrystalline precursor consisted of 8mol% excess PbO PIN-PMN-PT. Mn modified formulations were not investigated as no significant differences have been observed when comparing Mn free with Mn modified compositions in terms of grain growth. The excess PbO was kept to provide the liquid phase at annealing temperature and encourage crystal growth. The annealing temperature was 1150°C or less, as any higher temperatures promoted growth of larger grains and considerably reduced the density of the samples.

6.3.2.1 Growth from a PMN-PT nucleus grain

Figure 6.9 shows optical micrographs of the crystal growth experiments when using a PMN-PT seed and when using a PMN-PT seed with a Pb(II) 2-ethylhexanoate-based layer. In the first case, very limited, non-uniform growth has been observed with a maximum of 15 μm . Another observation is that grains within the polycrystalline matrix seem to impinge on the single crystal seed which suggest the experimental conditions encouraged grain growth within the matrix in the detriment of crystal growth from the seed. In the second case, growth up to 47 μm has been observed, although it was non uniform along the seed crystal. Therefore, the following two conclusions may be drawn: (i) Pb(II) 2-ethylhexanoate-based interlayer is beneficial for crystal growth and (ii) the interlayer was not homogeneously distributed along the seed.

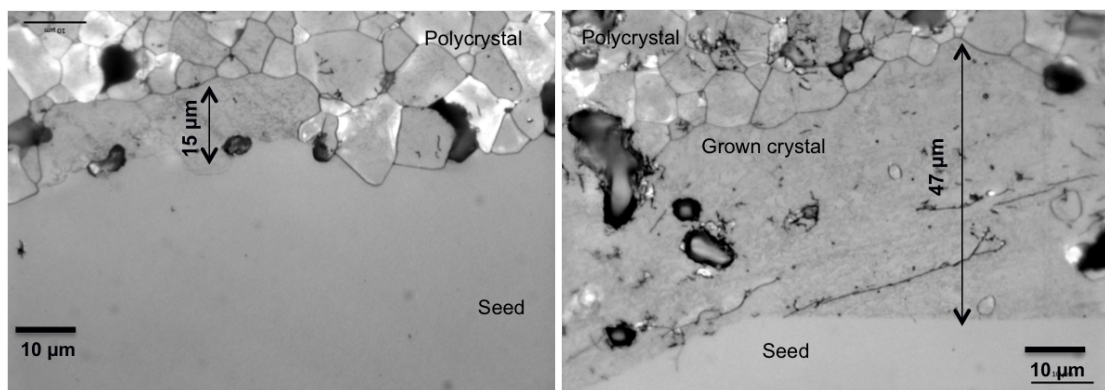


FIGURE 6.9: Growth from a PMN-PT seed (left) and growth from a PMN-PT seed with a Pb(II) 2-ethylhexanoate-based interlayer (right)

6.3.2.2 Growth from a BT nucleus grain

Experimental results concerning crystal growth from a BT seed and a BT seed with a PIN-PMN-PT deposited thin film are presented within this section. The thickness of the PIN-PMN-PT thin film deposited on the seed is expected to be ≈ 500 nm as a result of the deposition conditions used [116], although no accurate measurement has been performed within this work to determine it. X-ray diffraction performed on the seed before and after the deposition of the thin film - Figure 6.10, has revealed a single crystalline film with the same orientation as the seed, i.e. heteroepitaxial growth. Figure 6.11 shows the topography of the film. The surface roughness is 16 nm.

Figure 6.12 shows the results of the crystal growth experiments: when a BT seed has been used and when a BT seed with a thin film deposited has been used. The first experiment did not result in any crystal growth. The grains of the polycrystal seem to impinge on the seed which, as also observed in the first experiment of the previous section, implies the growth conditions encouraged grain growth within the matrix rather than crystal growth from the seed. The second experiment has proven more successful in that growth up to $42 \mu\text{m}$ has been observed. The growth was uniform all along the crystal seed. Some pores and inclusions are trapped in the grown crystal, which can be minimised by careful processing of the polycrystalline precursor.

These results show that a thin film deposited on the crystal seed encourages crystal growth.

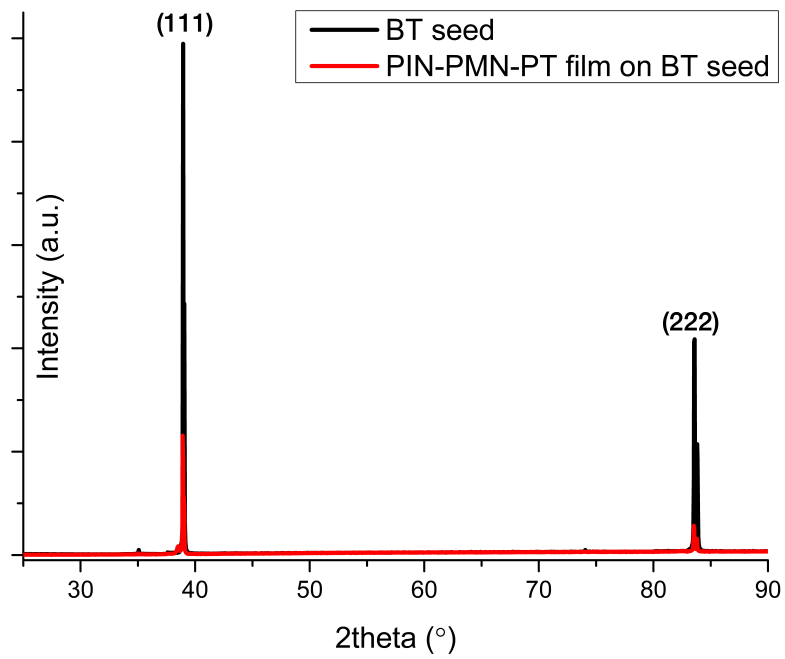


FIGURE 6.10: X-ray diffraction pattern of the BT seed and the subsequent thin film deposited

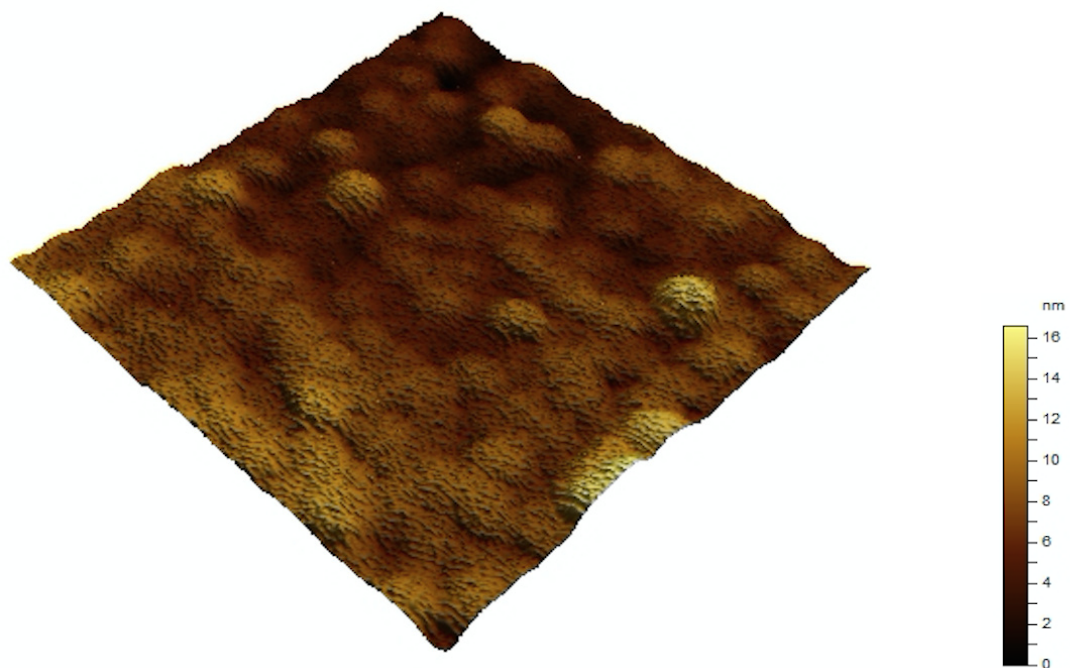


FIGURE 6.11: The surface of the deposited thin film imaged by Atomic Force Microscopy

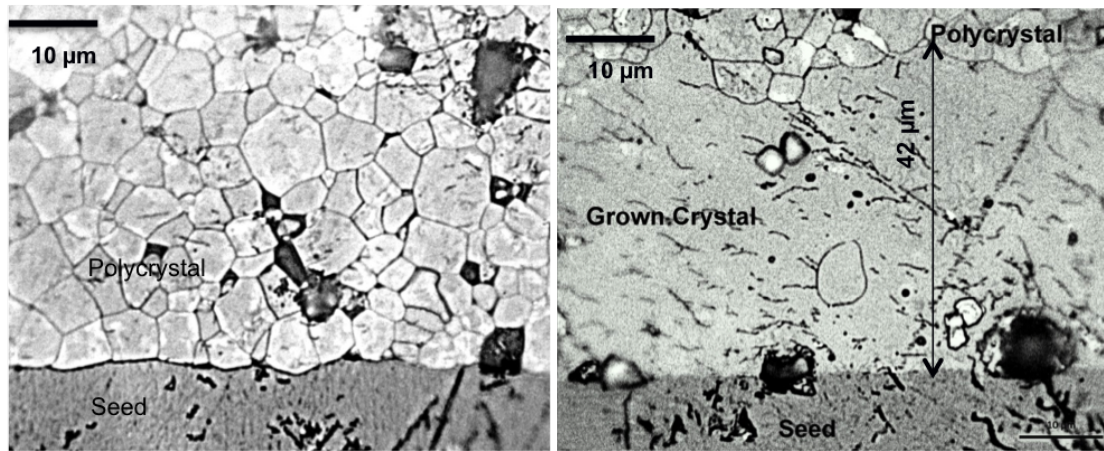


FIGURE 6.12: Growth from a BT seed (left) and growth from a BT seed with a PIN-PMN-PT thin film deposited by Pulsed Laser Deposition (right)

6.4 Summary and conclusions

In this investigation the aim was to assess the feasibility of growing single crystals by the solid state technique. Given the principle of the method which involves inhibition of grain growth within the polycrystalline matrix and stimulation of crystal growth from a seed, it is a requirement to understand the grain growth behaviour in the materials of interest to subsequently set up the conditions for crystal conversion. Therefore, the experiments have been divided in two parts, namely (i) grain growth study in PIN-PMN-PT and Mn:PIN-PMN-PT and (ii) crystal growth studies.

The first experimental study revealed that grain growth occurs in the matrix at all studied temperatures and the size of the grains increases with increasing temperature and when PbO excess is present. The samples sintered at 1150°C had an approximate density of 97% of the theoretical and it decreased to 92% at high temperature when PbO excess was present. Therefore, based on these experiments, it has been concluded that a temperature suitable for long annealing is $\leq 1150^{\circ}\text{C}$ (88% or less of the melting point).

Crystal growth experiments showed that when a Pb-based interlayer is used between the seed and the polycrystal, crystal growth is encouraged. When Pb(II) 2-ethylhexanoate based interlayer was used, crystal growth occurred from the seed although the

growth was not uniform implying that the layer was not uniformly distributed. However, when a uniform thin film with the same composition as the polycrystal to be converted was deposited by Pulsed Laser Deposition on the seed, crystal growth was uniformly promoted. However, further experiments are required to understand the mechanisms by which the thin film facilitates crystal growth. A study of the growth rate is also required. In this work, although a growth of almost $50\ \mu\text{m}$ was observed after annealing for 2 hours, it is possible that the growth rate may not be $25\ \mu\text{m/h}$. Growth may occur rapidly in the first minutes of heat treatment and subsequently slow down, particularly if the grains within the matrix also grow. Growth experiments within matrices of different grain sizes are also recommended. Such experiments would provide valuable information to help setting up conditions for growth of large crystals at relatively fast rates.

Furthermore, the present study suggests that excess PbO, although believed to minimise Pb volatilisation during long annealing, did not show improvement over the density or weight loss of the samples, but the contrary. In addition, PbO excess throughout the matrix may be an impediment in that the liquid phase provided at annealing temperature may promote grain growth and slow down the growth from the seed. Therefore, for further work it is recommended that excess PbO be avoided in the polycrystalline matrix. Nevertheless a PbO-based layer proved to be beneficial at the interface between the seed and the polycrystalline matrix.

Overall, the present study implies that a large matrix of experiments needs to be designed (i.e. a range of temperatures, compositions etc.) to find the appropriate conditions for growth of dense, defects free single crystals of significant size.

6.5 Limitations and future trends

Although the advantages of the method such as simplicity, homogeneity and growth of crystals with predetermined shape are extremely valuable, some limitations remain. The nature of the transformation which leads to crystal growth, i.e. solid-solid, presents a number of disadvantages. First, the growth rate is low when compared with liquid-solid transformations as the available energy associated with the driving force for growth is lower. Second, obtaining a high degree of structural perfection is difficult. Any defects present in the polycrystalline precursor will be transferred to the crystal. Nevertheless, reproducibility may represent an issue since the control of nucleation centers in the polycrystalline matrix seems sensitive to subtle changes in temperature

and chemical composition including impurities.

However, there are a number of changes which can be applied to the method to increase the level of success. One technique that has not been sufficiently explored is the pulse or cycling heating. Although with no sufficient evidence, it is suggested that by using cycled heating of a seed bonded to a polycrystalline matrix, growth from the seed is promoted and formation of nucleating and growing sites within the matrix are avoided. This might related to a so-called incubation time for nucleation and growth of grains. The seed acts as nucleus grain and there is no incubation time required, the seed starts to grow as soon as the critical temperature has been reached. Contrarily, within the matrix, formation of new nuclei requires an incubation time. Consequently, the cycled heating may be tuned so that the sample is kept at the growth temperature for a period of time less than the incubation time of fresh nuclei [111].

Another technique would be the use of thermal gradients across the sample, so that the crystal growth temperature would be set only near the seed-matrix interface and the temperature around the rest of the sample would be less to avoid nucleation and grain growth. However this method is relatively challenging as it requires extremely accurate control of the temperature gradient. A specialised furnace is recommended such as an Electro Dynamic Gradient Furnace which would be capable of providing a relatively narrow hot zone. A set-up similar to Bridgman could be used (section 5.5.2.1).

Another suggestion for future work is a layer-by-layer crystal conversion. The method would involve an ink-jet printer to print the piezoelectric material layer by layer onto a single crystal substrate and heat treatment after each printing step to convert the material into a single crystal layer by layer. The method does not require platinum crucibles, no melting is involved which means crystals will be homogeneous, growth is controlled for each layer separately thus overcoming the problem of grain growth within the matrix and crystals of any shape could be obtained.

Chapter 7

Advances in Understanding Mn behaviour in PIN-PMN-PT

Abstract

Piezoelectric materials with low energy losses are required for high power devices to minimise the unwanted heating effect. It has been shown that Mn modifications significantly enhance the mechanical quality factor Q_m in PbTiO_3 -based polycrystalline and multi domain single crystal ceramics. Studies suggest that Mn^{2+} enhances Q_m via defect dipole formation with oxygen vacancies and consequent pinning of domain wall movement. However, much uncertainty still exists about the behaviour of Mn when incorporated in piezoelectric oxides. Literature reported results do not seem consistent as Mn is added stoichiometrically in some cases and as additive in other cases. In addition, the valence state of Mn seems to be influenced by that of surrounding ions and vacancies and therefore, the processing conditions may also alter the behaviour of Mn. The present study aims to serve as basis towards development of a theory which explains behaviour of Mn in piezoelectric oxides taking into account the different variables. The specific objective of this research is to investigate the influence of chemical environment on properties in 2mol%Mn-modified PIN-PMN-PT polycrystals. Mn is assumed to occupy the B-site of the perovskite. For each composition prepared, 2mol%Mn substitutes sequentially 2mol% In, Mg, Ti and Nb. X-ray absorption spectroscopy, polarisation versus electric field measurements, impedance spectroscopy, permittivity, electrical losses and mechanical quality factor measurements are used to provide an insight into the behaviour of Mn-modified samples. Results indicate the presence of Mn under multiple valence states. The behaviour of Mn and hence electromechanical properties are most affected in samples where Nb content is lower rather than compositions where the content of In, Mg or Ti is altered.

7.1 Introduction and Background

7.1.1 Introduction

A large and growing body of literature investigates the influence of Mn-modification on piezoelectric oxide materials such as BaTiO₃, PbTiO₃, Pb(Zr,Ti)O₃ and other related compounds. At high fields, an unwanted heating effect is observed in the undoped materials caused by a loss of energy to mechanical damping. Therefore, the interest in this topic arises from the need of piezoelectric materials with low energy losses, i.e. high Q_m and low $\tan\delta_e$ to minimise the heating effect. Over the years researchers have tried to control the properties of piezoelectric oxide materials by means of dopants/additives. Generally, it has been shown that acceptors such as Fe, Mg, Al induce hard-like properties, whilst donors such as Nb, Ta, La induce soft-like properties. A number of studies have analysed the effect of Mn additions/modifications, typically in the range 0.5-2mol%, on piezoelectric oxide materials and a hardening effect is widely reported, i.e. enhanced Q_m . The suggested mechanism is a defect dipole formation between "negatively" charged Mn, i.e. a Mn²⁺ occupying a Ti⁴⁺ site and the positively charged oxygen vacancy [117]. According to Kröger-Vink notation¹, which will be used throughout this chapter, the dipole may be written as Mn_{Ti}^{''}- V_O^{••}. These defect dipoles are believed to develop an internal bias field which pins domain wall movement. However this statement seems to be oversimplified as evidence has been found that Mn does not always enhance Q_m . A number of other observations seem to be often ignored. First, evidence of three different valence states of Mn have been found, namely 2, 3 and 4+, where Mn⁴⁺ does not change the properties of the piezoelectric oxide materials. Second, it is unclear whether Mn is incorporated at the A-site or B-site of the perovskite (refer to Figure 2.4 for visualisation of the lattice sites). Generally it is assumed that dopants are incorporated at the B site [115], although there are studies which also prove incorporation at the A site. For example in PbTiO₃ it has been shown that Fe³⁺ and Mn²⁺ can partly occupy the Pb site [32]. It is believed that processing conditions such as temperature and atmosphere influence the site occupancy and valence state of Mn. In addition, the valence state of neighbouring atoms also seems to play an important role on the Mn behaviour. Moreover, the results in the literature often do not seem consistent due to the fact that Mn is sometimes an

¹Kröger-Vink notation is used to describe defects and their charge relative to the environment. Relevant examples include: V_O[•] = oxygen vacancy with single positive charge, V_O^{••} = oxygen vacancy with double positive charge, Mn_{Ti}['] = Mn ion with single negative charge occupying a Ti site, Mn_{Ti}^{''} = Mn ion with double negative charge occupying a Ti site

additive [118, 119] to the studied piezoelectric oxide material and some other times it is mixed stoichiometrically under the assumption of B-site incorporation. Therefore our understating of the behaviour of Mn as well as the mechanism by which Mn changes properties is very limited. The aim of this chapter is to provide a link between the findings related to Mn modifications of piezoelectric oxides. Different experiments are undertaken with the intention of achieving a more clear picture of the mechanisms behind the Mn-modified materials. This study is based on the hypothesis that Mn is incorporated at the B-site of the PIN-PMN-PT compound and the question asked is the following: *Is there a change in properties when Mn substitutes one or another chemical at the B site in solid solutions of complex perovskites?* An attempt at answering this question is made by studying stoichiometrically-designed compositions in which 2mol%Mn substitutes sequentially 2mol% In, Mg, Ti and Nb. Although single crystals are of great interest due to their enhanced properties as stated in the introductory sections of this thesis, the present study is undertaken on the polycrystalline counterparts as their preparation is not as complicated as for single crystals and the preparation time is relatively short. The study is meant to be a first step of a larger study which will include measurements on the single crystal version of the compositions of interest. The theoretical dimensions of the research is laid out in the following subchapter, namely Section 7.1.2. Four main topics are briefly reviewed - mechanical quality factor of different Mn-modified compounds, losses mechanisms, internal bias field origin and non-stoichiometry. Following the short review, experimental procedures are briefly described in Section 7.2. A detailed analysis of the observations is presented within Section 7.3 - Results and Discussion. After Summary and Conclusions in Section 7.4, this chapter also proposes further experiments for a deeper understanding of the subject - Section 7.5.

7.1.2 Background

7.1.2.1 Mechanical Quality Factor

This subsection aims to briefly review and provide conclusions based on literature on the links between mechanical quality factor Q_m and microstructure as well as chemical composition in piezoelectric Mn-modified PT-based oxides. The microstructure refers to whether the material is a single domain single crystal, a multi domain single

crystal or a polycrystalline ceramic. Table 7.1 summarises values of Q_m for the different domain engineered single crystals and polycrystals from several studies. Several conclusions may be drawn, as follows:

1. Q_m in single crystals with single domain configuration is high, even when Mn is not present. It may also be inferred that Q_m increases the further away from the MPB the composition is, in the direction of increasing the stability of the phase in which the polar direction is the same as the poling direction, for example moving away from MPB towards the R side for [111] poled rhombohedral crystals or towards the T side for [001] poled tetragonal crystals (the reader may want to refer to the phase diagram presented in Figure 2.15 and to the schematic representation of domain engineered single crystals - Figure 2.17). For example, Q_m is 1130 for [111] PMN-PT30 and it increases to 2200 for [111] PMN-PT26.
2. Q_m in undoped multi domain single crystals as well as polycrystalline materials seems to be low.
3. Q_m seems to increase for Mn-doped multi-domain single crystals and polycrystalline materials only in certain compositions. Q_m is particularly high for compositions where multiple ions with different valence states are present. This topic is particularly related to the non-stoichiometry in PT-based oxides and will be discussed separately in Section 7.1.2.4.

Although, the stated conclusions seem to be consistent throughout literature (references are provided in Table 7.1), caution must be applied as processing conditions (temperature, atmosphere) may influence the behaviour of Mn which, in turn, may influence Q_m . In addition, the measurement conditions, for example frequency, may also affect Q_m [120].

It is now necessary to discuss the mechanism giving rise to a low or high mechanical quality factor. The mechanism may be explained in terms of losses within the material which may be divided into intrinsic and extrinsic. The following subsection briefly reviews the two different types of contributions.

TABLE 7.1: Brief summary of mechanical quality factor in single domain rhombohedral 1R and tetragonal 1T single crystals, multi-domain single crystals 2R, 4R (see Section 2.3.3.4 for domain engineered single crystals) and polycrystalline materials P. In the case of single crystals where the poling direction or crystallographic phase is not specified, the domain configuration is referred to as single crystals S C only.

Material	Poling Direction	Domain Configuration	Q_m	Ref
PMN-PT	[001]	4R	140	[6]
PMN-PT	[011]	2R	750	[6]
PMN-PT	[111]	1R	2000	[6]
PMN-PT		P	75	[6]
PMN-PT30	[001]	4R	120	[121]
PMN-PT30	[011]	2R	600	[121]
PMN-PT30	[111]	1R	1130	[121]
PMN-PT26	[001]	4R	150	[121]
PMN-PT26	[011]	2R	850	[121]
PMN-PT26	[111]	1R	2200	[121]
Mn:26PIN-39PMN-35PT	[001]	1T	2000	[122]
Mn:27PIN-46PMN-27PT	[001]	4R	650	[123]
Mn:27PIN-46PMN-27PT	[111]	1R	1200	[123]
$Pb_{0.98}(Zr_{0.52}Ti_{0.48}Nb_{0.024})O_3$		P	85	[43]
$Pb_{0.96}Sr_{0.05}(Zr_{0.52}Ti_{0.46}Sb_{0.002})O_3$		P	95	[43]
$Pb_{0.97}Nd_{0.02}(Zr_{0.54}Ti_{0.46})O_3$		P	100	[43]
$Pb(Zr_{0.525}Ti_{0.472}Fe_{0.003})O_3$		P	500	[43]
$Pb_{0.95}Sr_{0.05}(Zr_{0.52}Ti_{0.44}Ni_{0.04})O_3$		P	350	[43]
$Pb_{0.91}La_{0.06}TiO_3$		P	275	[124]
$Pb_{0.925}La_{0.06}(Ti_{0.99}Mn_{0.01})O_3$		P	2400	[124]
PZT5A		P	75	[2]
PZT5H		P	75	[2]
PMN-PT29		S C	230	[2]
PMN-PT33		S C	280	[2]
PIN-PMN-PT		S C	330	[2]
PZT4		P	500	[2]
PZT8		P	1000	[2]
Mn:PIN-PMN-PT		S C	910	[2]
Mn:PMN-PZT		S C	1200	[2]
$(Pb_{0.96}Sr_{0.04})(Zr_{0.5275}Ti_{0.4675}Mn_{0.005})O_3$		P	203	[125]
$(Pb_{0.96}Sr_{0.04})(Zr_{0.525}Ti_{0.465}Mn_{0.01})O_3$		P	190	[125]
$(Pb_{0.96}Sr_{0.04})(Zr_{0.5225}Ti_{0.4625}Mn_{0.015})O_3$		P	187	[125]
$(Pb_{0.96}Sr_{0.04})(Zr_{0.53}Ti_{0.47})O_3+0.5\%MnO_2$		P	212	[125]
$(Pb_{0.96}Sr_{0.04})(Zr_{0.53}Ti_{0.47})O_3+1\%MnO_2$		P	172	[125]
$(Pb_{0.96}Sr_{0.04})(Zr_{0.53}Ti_{0.47})O_3+1.5\%MnO_2$		P	185	[125]
$(Pb_{0.96}Sr_{0.04})(Zr_{0.53}Ti_{0.47})O_3+1\%MnO_2+0.5\%ZnO+0.5\%Bi_2O_3$		P	1050	[125]
$(Pb_{0.96}Sr_{0.04})(Zr_{0.53}Ti_{0.47})O_3+0.03\%ZnO+0.02\%Bi_2O_3$		P	205	[125]
$(Pb_{0.96}Sr_{0.04})(Zr_{0.53}Ti_{0.47})O_3$		P	197	[125]
$Pb_{0.89}(Ba,Sr)_{0.11}(Zr_{0.4}Ti_{0.6})_{0.99}Mn_{0.01}O_3$		P	≈ 1250	[126]
$Pb_{0.89}(Ba,Sr)_{0.11}(Zr_{0.4}Ti_{0.6})_{0.99}Mn_{0.01}O_3+1at\%F$		P	≈ 1350	[126]
$Pb_{0.89}(Ba,Sr)_{0.11}(Zr_{0.7}Ti_{0.3})_{0.99}Mn_{0.01}O_3$		P	≈ 280	[126]
$Pb_{0.89}(Ba,Sr)_{0.11}(Zr_{0.7}Ti_{0.3})_{0.99}Mn_{0.01}O_3+1at\%F$		P	≈ 2000	[126]
$Pb_{0.90}(Ba,Sr)_{0.11}(Zr_{0.52}Ti_{0.48}Mn_{0.01})O_{3.003}$		P	660	[127]
$Pb_{0.90}(Ba,Sr)_{0.11}(Zr_{0.52}Ti_{0.48}Mn_{0.01})O_{3.003-0.01}F_{0.01}$		P	810	[127]
$Pb_{0.90}(Ba,Sr)_{0.11}(Zr_{0.52}Ti_{0.48}Mn_{0.01})O_{3.003-0.02}F_{0.02}$		P	330	[127]
$Pb_{0.90}(Ba,Sr)_{0.11}(Zr_{0.52}Ti_{0.48}Mn_{0.01})O_{3.003-0.03}F_{0.03}$		P	400	[127]
$Pb_{0.90}(Ba,Sr)_{0.11}(Zr_{0.52}Ti_{0.48}Mn_{0.01})O_{3.003-0.04}F_{0.04}$		P	720	[127]
$Pb_{0.90}(Ba,Sr)_{0.11}(Zr_{0.52}Ti_{0.48}Fe_{0.01})O_{3.003}$		P	1200	[127]
$Pb_{0.90}(Ba,Sr)_{0.11}(Zr_{0.52}Ti_{0.48}Fe_{0.01})O_{3.003-0.005}F_{0.005}$		P	1300	[127]
$Pb_{0.90}(Ba,Sr)_{0.11}(Zr_{0.52}Ti_{0.48}Fe_{0.01})O_{3.003-0.01}F_{0.01}$		P	2100	[127]
$Pb_{0.90}(Ba,Sr)_{0.11}(Zr_{0.52}Ti_{0.48}Fe_{0.01})O_{3.003-0.02}F_{0.02}$		P	1700	[127]
$Pb_{0.90}(Ba,Sr)_{0.11}(Zr_{0.52}Ti_{0.48}Fe_{0.01})O_{3.003-0.064}F_{0.064}$		P	900	[127]
$Pb_{0.90}(Ba,Sr)_{0.11}(Zr_xTi_{y-x-0.0075}Mg_{0.0075})O_{3.003}$		P	730	[127]
$Pb_{0.90}(Ba,Sr)_{0.11}(Zr_xTi_{y-x-0.0075}Mg_{0.0075})O_{3.003-0.01}F_{0.01}$		P	1610	[127]
$Pb_{0.90}(Ba,Sr)_{0.11}(Zr_xTi_{y-x-0.0075}Mg_{0.0075})O_{3.003-0.02}F_{0.02}$		P	1860	[127]
$Pb_{0.90}(Ba,Sr)_{0.11}(Zr_xTi_{y-x-0.0075}Mg_{0.0075})O_{3.003-0.03}F_{0.03}$		P	2480	[127]
$Pb_{0.90}(Ba,Sr)_{0.11}(Zr_xTi_{y-x-0.0075}Mg_{0.0075})O_{3.003-0.04}F_{0.04}$		P	1760	[127]
$Pb_{0.90}(Ba,Sr)_{0.11}(Zr_xTi_{y-x-0.0075}Mg_{0.0075})O_{3.003-0.06}F_{0.06}$		P	1000	[127]

7.1.2.2 Contribution to losses

The two types of contribution to losses, namely intrinsic and extrinsic, will be briefly discussed for single and multi domain single crystals as well as for polycrystals. For a detailed explanation of the losses mechanisms in single crystals, the reader may refer to a review by Liu et al. [120].

Intrinsic contributions are related to the crystal lattice and involve polarisation variation, i.e. rotation and/or elongation/compression. This variation leads to crystal lattice deformation which, in turn, lead to losses.

Extrinsic contributions arise, amongst other factors, from domain wall motion, defect dipoles, grain boundaries or space charges.

In single crystals with 1D domain configuration extrinsic contributions are expected to be very low, almost negligible with losses arising from polarization variation. When measured in a longitudinal mode, i.e. the applied electric field is parallel to the polarisation, Q_m is particularly high and the loss contribution is due to elongation or compression only. Q_m decreases for shear modes, i.e. the applied electric field is perpendicular to the polarisation, when polarisation rotation is involved. Furthermore, as stated in the previous subsection, Q_m increases as the composition shifts away from the MPB - towards the tetragonal side for [001] poled crystals and towards the rhombohedral side for [111] poled crystals. It is noteworthy that similar values of Q_m have been achieved for both 1R and 1T configurations, i.e. up to 2000 - Table 7.1. Although 1R configuration is expected to show a higher Q_m due to increased Young's modulus compared to 1T, the similar values have lead to the conclusion that 1R configuration is less stable and unwanted domains arise. Therefore, polarisation rotation is possible within these domains, leading to a Q_m comparable to that for 1T configurations [120]. In single crystals with multi domain configurations, rotation of polarisation is a major contributor to losses. A lowered Q_m is observed. It has been suggested that the higher the angle between the spontaneous polarisation and the applied electric field, the higher the losses. Extrinsic contributions arising from domain wall motion are also present, but they are relatively low, increasing as the composition approaches MPB where domain wall motion is easier and therefore a lower Q_m is observed.

In polycrystalline materials, the intrinsic contributions arise from the individual single crystals represented by each grain. However, the extrinsic contributions are of significant importance. From the factors giving rise to extrinsic contributions previously mentioned, domain wall movement is probably the most important. However, the presence of defect dipoles in the sample may pin this movement by means of an internal

bias field. This topic is discussed in the following subsection.

7.1.2.3 Internal Bias Field

Polarisation versus electric field loops (P-E) contain information related to defects. Robels et al. [128] suggested that defects may cause several changes to the hysteresis loop such as: slanting, change of the coercive field as well as a shift relative to the origin. The focus of this subchapter will be on the latter effect which has been suggested to be associated with an internal bias field E_{ib} . The existence of such internal field is believed to contribute to the stabilisation and pinning of domain wall movement. E_{ib} is believed to arise as a consequence of the defect dipoles alignment with the spontaneous polarisation. The alignment occurs by diffusion of the oxygen vacancy within the lattice, i.e. short range diffusion. These defect dipoles act as pinning sites for domain wall movement, as their reorientation is slow compared with ferroelectric dipoles. The model is described in detail by Robels et al [129]. However, an internal bias field may also arise from surface charges developed by secondary phases gathered around the grains in polycrystalline materials. In this case, domain walls remain mobile [32].

7.1.2.4 Non-stoichiometry

ABO_3 compounds often contain multivalent cations which lead to non-stoichiometry. For example, in $BaTiO_3$ and $SrTiO_3$, Ti^{4+} may be easily reduced to Ti^{3+} causing oxygen vacancies [72]. In complex perovskites the situation becomes more complicated. For example in Nb-modified PZT, Nb, Ti or even Pb are able to change their valency state relative to their most common ones. Therefore, Nb^{5+} can change its valence state to Nb^{3+} , Ti^{4+} can become Ti^{3+} and even Pb^{2+} might change its state to Pb^{3+} [127]. The number of scenarios increases for $Pb(In_{1/2}Nb_{1/2})O_3$ - $Pb(Mg_{1/3}Nb_{2/3})O_3$ - $PbTiO_3$ and particularly when Mn modification is performed. Mn alone may be present as Mn^{2+} , Mn^{3+} and Mn^{4+} and some possibilities are schematically shown in Figure 7.1. Much of the available literature suggest a B-site incorporation of the Mn ion [130]. However, some studies also suggest an A site incorporation under certain circumstances [124]. Site occupancy by Mn within the perovskite structure is probably a mechanism determined by processing conditions such as temperature and oxygen and /or lead partial pressures, the valency states of neighbouring atoms as well as the Goldschmidt tolerance factor (refer to Section 2.2.2 for a definition of the tolerance factor).

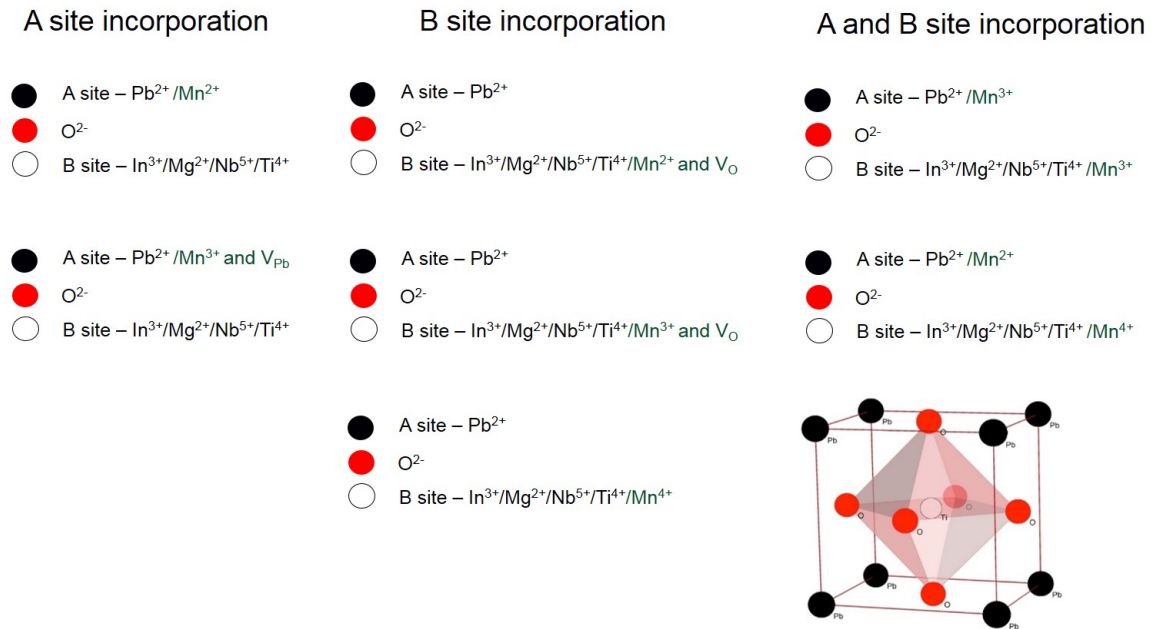


FIGURE 7.1: Mn valence state scenarios in PIN-PMN-PT. The possibilities of valence change in the case of Nb, Ti and Pb have been ignored as the number of scenarios is too large.

For example when Mn^{2+} incorporation (0.8\AA) is considered in PbTiO_3 , it can be inferred that it may fit at the A ($\text{Pb}^{2+} - 1.2\text{\AA}$) as well as at the B site ($\text{Ti}^{4+} - 0.68\text{\AA}$). If Mn occurs under the valence state of $3+$ (0.66\AA) or $4+$ (0.6\AA) it is likely that a B site will be occupied. However, a prediction to whether Mn occupies either A or B site becomes increasingly difficult in PIN-PMN-PT which has four randomly distributed ions with different ionic radii at the B-site. For reference, a table with ionic radii of the ions in the studied compound is provided Table 7.2. Overall, non-stoichiometry in Mn-modified PIN-PMN-PT may be regarded from a charge balance point of view. To achieve electro-neutrality, compensation may be achieved by oxygen vacancies, incorporation of Mn at the A-site in addition to B-site incorporation, valence change of the ions (Mn, Nb, Ti or even Pb) and, to a very small extent, free conduction electrons. Although contributions from all the stated mechanisms are expected, which one dominates seems difficult to predict and may depend on a number of factors [124, 131] such as:

- experimental conditions
- activity of PbO
- O_2 partial pressure

- processing temperature
- ionic radii
- concentration of dopant (i.e. composition of the compound).

TABLE 7.2: Ionic radii for elements in the perovskite structure studied within this work. A-site (Pb) ionic radii is given for a 12 coordination number, whilst B site (In, Mg, Nb, Ti, Mn) 6 coordination number [132]

Element	In ³⁺	Mg ²⁺	Nb ⁵⁺	Ti ⁴⁺	Mn ²⁺	Mn ³⁺	Mn ⁴⁺	Pb ²⁺
Ionic radii (Å)	0.8	0.72	0.64	0.61	0.83	0.58	0.53	1.49

The following paragraphs aim to review the influence of neighbouring atoms on the valence state of Mn in specific perovskites. The final subsection reviews the effects of the processing conditions on the valence state of Mn.

Mn and Nb simultaneous doping in PZT A study by Glinchuk et al. [133] reported an interesting behaviour in PZT doped simultaneously with Nb and Mn. The study reports a B-site incorporation and a valence state of Mn⁴⁺ only at small Nb content, i.e. $n(\text{Nb}) \leq 1.75 \text{ mol\%}$. Charge balance in this case was accompanied by Pb vacancies. With increasing Nb content, Mn³⁺ is suggested to come into existence in the region $1.75 \text{ mol\%} \leq n(\text{Nb}) \leq 1.85 \text{ mol\%}$ with elimination of Pb vacancies. A further increase in Nb concentration showed an increase in Mn²⁺ concentration. The study also suggests a relative solubility limit in Nb:PZT as follows: with increasing Nb content, the solubility limit seems to increase. In samples with Nb content lower than the Mn content, Mn seemed to concentrate at the grain boundaries. With increasing the Nb content, Mn is incorporated in the grains resulting in a more homogeneous microstructure. Therefore, an increase in Nb content seems to increase the solubility limit of Mn which seems to be linked to the requirement for excess charge balance.

A change of oxidation state of Mn (considering Mn⁴⁺ as starting point) has also been observed in (Pb,La)(Zr,Ti)O₃. It has been found that with increasing the concentration of La³⁺, the charge is compensated not only by Mn³⁺ and Mn²⁺, but also Ti³⁺.

Mn, Nb and Ni simultaneous doping in PT Amarande et al. [134] have studied Mn-modified PT doped with Ni²⁺ and Nb⁵⁺. Compositions with different contents of Ni and Nb have been investigated. When Nb content was higher and Ni-Nb gave an average valence >4+, Mn reduced and Mn²⁺ content increased. On the other hand,

when Ni concentration was increased and the average Ni-Nb valence was $<4+$, the concentration of Mn^{2+} decreases, favouring existence of Mn^{3+} and Mn^{4+} .

Mn \ Mg and F simultaneous doping in PZT Boucher et al. [135] showed that (Mn,F) co-doping leads to semi-hard materials, whilst (Mg,F) induces hardening effects including a higher Q_m . It has been shown that Mn has a valence of 4+ when incorporated into PZT. However, when F^- is also introduced at O^{2-} site, Mn seems to change its valence state gradually from 4+ to 2+ due to the F-O substitution. The (Mn,F) co-doping leads to semi-hard properties of the material. Interestingly, hard properties are reported when PZT is co-doped with (Mg,F), where Mg has essentially an oxidation state of 2+. The authors report that $\text{Mg}_{\text{Ti}}''\text{-F}^-$ defect dipole is less mobile than $\text{Mn}_{\text{Ti}}''\text{-V}_{\text{O}}^{\bullet\bullet}$, leading to a decrease in domain wall mobility.

Processing atmosphere and temperature In Mn-doped BaTiO_3 (BT), the relative proportions of 2, 3 and 4+ oxidation states of Mn depend upon the processing conditions and doping level as follows: Mn^{3+} predominates when BT is processed in oxidizing atmosphere, whilst Mn^{2+} predominates in reducing atmospheres. Mn^{4+} content increases with increasing the overall Mn content [136]. When Mn:PZT was studied, the presence of 2, 3 and 4+ oxidation states of Mn has been confirmed. It was also noticed that when sintered in oxygen atmosphere, samples showed a Q_m of 400 and when sintered in nitrogen, Q_m increased up to 1100 [137]. It has been inferred that Q_m is increased only when Mn^{2+} and Mn^{3+} are present. The sintering temperature seems to influence Q_m , too. Li et al. studied the influence of sintering temperature in $\text{Pb}(\text{Zr,Ti})(\text{Mn,Nb})\text{O}_3$. It has been suggested that a high sintering temperature encourages the appearance of oxygen vacancies. However with decreasing the sintering temperature, the concentration of Mn^{2+} increases and this also contributes to appearance of oxygen vacancies [138]. Contrarily, Izaki et al [139], when studying Mn doping in $(\text{Pb,Lu})(\text{Zr,Ti})\text{O}_3$ reported the reduction of Mn^{3+} and Mn^{4+} to Mn^{2+} to be enhanced with rising sintering temperature. Hennings et al. [124] suggested that the site distribution and valence state of Mn and Fe when added as dopants in PbTiO_3 depends strongly on the PbO and O_2 partial pressure. A low PbO partial pressure is suggested to encourage incorporation of a small amount of dopants at the A site. In addition, a high O_2 partial pressure reduces the amount of oxygen vacancies which might affect the valence state of the dopants.

These studies clearly indicate a complex behaviour and a strong dependency of the processing conditions. However, it seems to be widely accepted that the enhancement of Q_m is related to the content of Mn^{2+} and Mn^{3+} and not the overall Mn content which also exists with a 4+ oxidation state [139].

7.2 Experimental Procedures

7.2.1 Investigated Compositions

The modification with Mn has been made under the assumption of incorporation at the B-site of the perovskite - refer to Figure 7.1. 28PIN-40PMN-32PT has been chosen as the base composition. The modification has been made by sequential substitution of 2mol% In, Mg, Ti and Nb with 2mol% Mn. Seven samples have been investigated. The samples are labelled according to the ion that Mn substitutes, i.e. 0 for the Mn-free composition, In where Mn substitutes In and so on. A summary of the compositions prepared may be found in Table 7.3.

TABLE 7.3: Summary of compositions studied

Sample	Substituted ion	Assumed Mn compound	Composition				Formula
			Mn compound	PIN	PMN	PT	
0	-	-	-	28	40	32	$\text{PbIn}_{0.14}\text{Mg}_{0.133}\text{Ti}_{0.32}\text{Nb}_{0.406}\text{O}_3$
In	In	$\text{Pb}(\text{Mn}_{1/2}\text{Nb}_{1/2})\text{O}_3$	4	24	40	32	$\text{Mn}_{0.02}\text{PbIn}_{0.12}\text{Mg}_{0.133}\text{Ti}_{0.32}\text{Nb}_{0.406}\text{O}_3$
Mg	Mg	$\text{Pb}(\text{Mn}_{1/3}\text{Nb}_{2/3})\text{O}_3$	6	28	34	32	$\text{Mn}_{0.02}\text{PbIn}_{0.14}\text{Mg}_{0.113}\text{Ti}_{0.32}\text{Nb}_{0.406}\text{O}_3$
Ti	Ti	PbMnO_3	2	28	40	30	$\text{Mn}_{0.02}\text{PbIn}_{0.14}\text{Mg}_{0.133}\text{Ti}_{0.30}\text{Nb}_{0.406}\text{O}_3$
Nb1 ¹	Nb	$\text{Pb}(\text{In}_{1/2}\text{Mn}_{1/2})\text{O}_3$	4	24	40	32	$\text{Mn}_{0.02}\text{PbIn}_{0.14}\text{Mg}_{0.133}\text{Ti}_{0.32}\text{Nb}_{0.387}\text{O}_3$
Nb2 ¹	Nb	$\text{Pb}(\text{Mg}_{1/3}\text{Mn}_{2/3})\text{O}_3$	3	28	37	32	$\text{Mn}_{0.02}\text{PbIn}_{0.14}\text{Mg}_{0.133}\text{Ti}_{0.32}\text{Nb}_{0.387}\text{O}_3$
All ²	In/Mg/Ti/Nb	N/A	2.6	27.4	39	31	$\text{Mn}_{0.02}\text{PbIn}_{0.137}\text{Mg}_{0.131}\text{Ti}_{0.314}\text{Nb}_{0.399}\text{O}_3$
B4 ³	N/A	$\text{Pb}(\text{Mn}_{1/3}\text{Nb}_{2/3})\text{O}_3$	2	27.44	39.2	31.36	$\text{Mn}_{0.007}\text{PbIn}_{0.137}\text{Mg}_{0.131}\text{Ti}_{0.314}\text{Nb}_{0.412}\text{O}_3$

¹Nb1 and Nb2 are compositionally equivalent. Theoretically, Mn may replace Nb either in $\text{Pb}(\text{In}_{1/2}\text{Nb}_{1/2})\text{O}_3$ or $\text{Pb}(\text{Mg}_{1/3}\text{Nb}_{2/3})\text{O}_3$ and, depending on the compound chosen, slightly different ratios of InNbO_4 and MgNb_2O_6 are mixed during processing. However the final theoretical composition will be identical. Nevertheless, preparing the composition in both ways may give an indication of the extent to which processing may influence results.

²In All 2mol%Mn replaces 2mol% of all B-site ions.

³B4 is one of the Mn modified single crystals grown within this work - refer to Chapter 5. The valence state of Mn in this sample has been investigated as well for comparison.

7.2.2 Sample Preparation

The samples have been prepared at Thales Underwater Systems laboratory (Rydalme, Australia). Characterisation has been performed at Thales Underwater Systems (Rydalme, Australia), The Australian Synchrotron (Melbourne, Australia) and the University of Leeds (Leeds, United Kingdom). Each composition has been synthesized in a powder form by using: PbO >99.8% (Hammond Lead Products - HLP 100Y), TiO₂ >99% (Kronos - 1001), Nb₂O₅ 99.9%, In₂O₃ 99.99%, (MgCO₃)₄.Mg(OH)₂.5H₂O >99% (Aldrich) and MnO₂ (Celtic Chemicals). The columbite-like MgNb₂O₆ (MN) and wolframite-like InNbO₄ (IN) have been pre-synthesized at The University of Leeds (refer to Section 4.2 in Chapter 4). The compounds have been attrition milled using a Netzsch laboratory mill (NETZSCH-Feinmahltechnik GmbH) in tap water for 1h using 0.5 mm yttria-stabilised zirconia media. Following milling, the powders were dried and sieved through a 250 μm stainless steel sieve. After a calcination stage at 800°C for 4h, the powders have been re-milled for a further hour under the same conditions as described above. The powders have been subsequently mixed with 0.2wt%(solids) dispersant (BYK-154, BYK Additives&Instruments) and 1wt% binder (Glascal HA4, Allied Colloids) in tap water and continuously mixed in an induction-heated mixer.

The powder was pressed using a semi-automatic uniaxial press at ≈90 MPa into circular pellets with 16 mm diameter. The subsequent binder burnout process took place according to the profile shown in Figure 7.2. The pellets were sintered following the profile shown in Figure 7.3 in air. The density has been measured according to the Archimedes method (see Appendix C). Subsequently, the samples have been ground to 1.5 mm thickness using SiC paper on a TegraSystem grinder and polisher (Struers). The samples were electroded by means of silver paste fired at 540°C, followed by poling at 135°C under an electric field of 1.5 kV/mm for 10 minutes. After the poling process, the samples were removed from the oil bath and allowed to cool at room temperature.

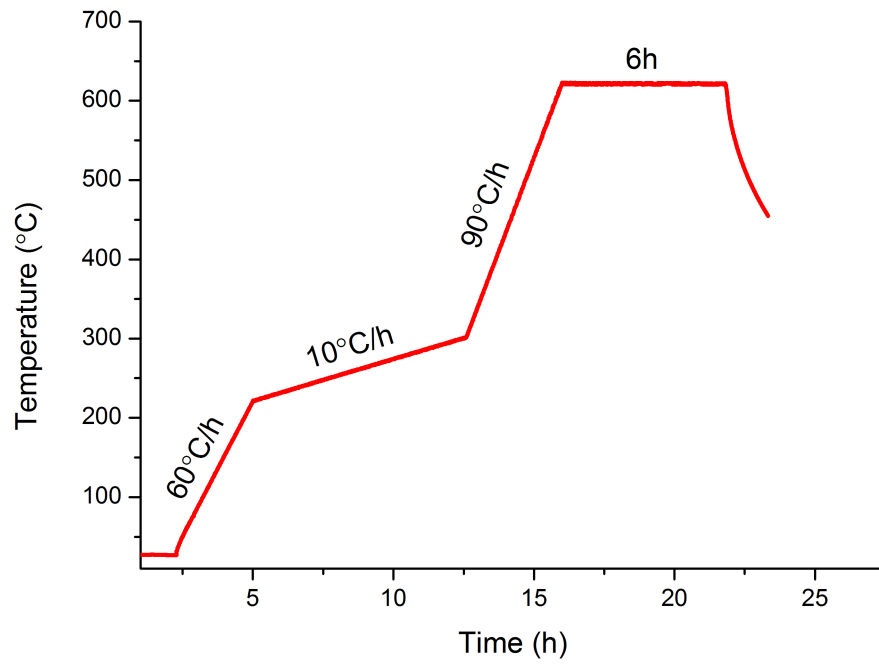


FIGURE 7.2: Binder burnout profile measured during the process

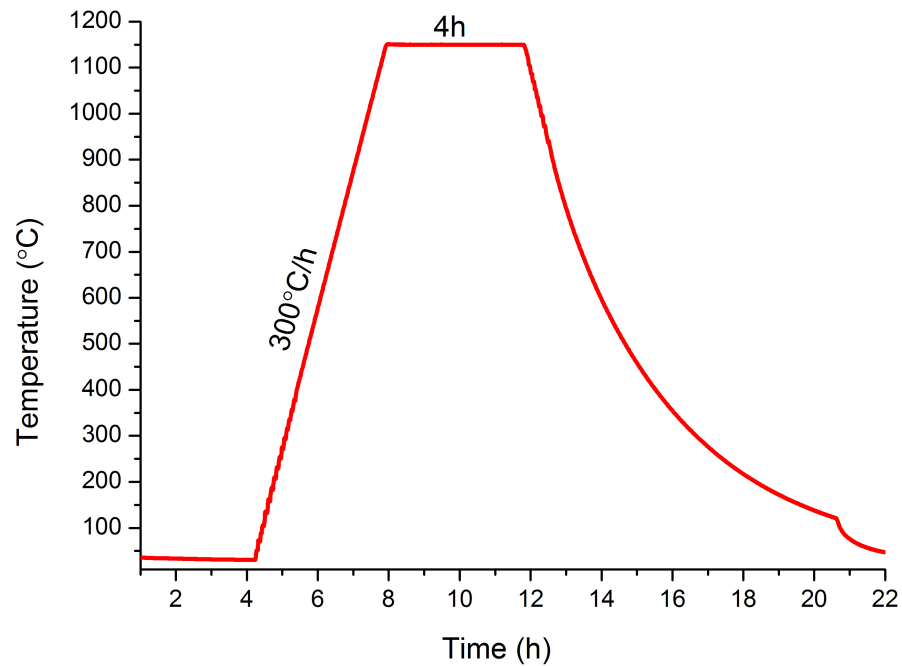


FIGURE 7.3: Sintering profile measured during the process

7.2.3 Characterisation Techniques

7.2.3.1 Investigations during sample preparation

To ensure a relevant binder burnout temperature profile is used, the weight loss as a function of temperature has been tested using a thermogravimetric analyser (Q500, TGA, TA Instruments). The calcined powders have been investigated in terms of phase with X-ray Diffraction technique using PANalytical X'Pert Diffractometer (Phillips, The Netherlands) with a theta-theta goniometer. Furthermore, OLYMPUS OLS4100 optical microscope has been used to investigate the calcined powders and the surface of the sintered samples.

7.2.3.2 X-ray Absorption Spectroscopy

X-ray Absorption Spectroscopy (XAS) has been the method of choice for determining the average valence state of Mn in each Mn containing sample. Data was collected at the XAS beamline at the Australian Synchrotron (Melbourne, Australia). The work has been undertaken by Dr Peter Kappen, Dr Bernt Johannessen and Dr Tamsyn Ross. The scans have been acquired at the Mn K-absorption edge using fluorescence detection with a 100-element HP-Ge detector (Canberra, Australia). Prior to measurements, radiation hardness has been tested on one sample by extended X-rays exposure. No change in the spectroscopic response after 30 min suggested X-rays do not alter the valence state of the investigated chemical element. The average valence state for Mn has been established by comparison with spectra from commercial manganese oxides with known valence states.

7.2.3.3 Polarisation versus Electric Field

Polarisation versus field measurements have been performed using a Precision LC Ferroelectric Tester (Radiant Technologies, USA) together with a TREK 5/80 high voltage power amplifier. The measurements were controlled by Vision Data Acquisition and Management System Software. All measurements have been taken by applying a triangular signal with a frequency of 1 Hz. Prior to full P-E loops, electric fields have been applied sequentially from 0.1 to 0.5 kV/mm with a 0.1 kV/mm step. By using Equation 7.1 the real part of the relative permittivity has been calculated at the different applied electric fields. It has been assumed that $D \cong P$ [9]. The method of extraction

of the permittivity from polarisation versus field loops is shown in Figure 7.4.

$$D = \varepsilon_0 E + P = \varepsilon_0 \varepsilon_r E \quad (7.1)$$

Furthermore, acquisition of full P-E loops allowed determination of any internal bias field, E_{ib} , as follows. A sample with no internal bias field exhibits a symmetrical hysteresis loop with respect to the x axis. However, when an internal field is present the loop shifts either to the left or right side. The internal bias field is then calculated as the difference between the coercive field measured and the coercive field calculated by centring the hysteresis loop on the x axis.

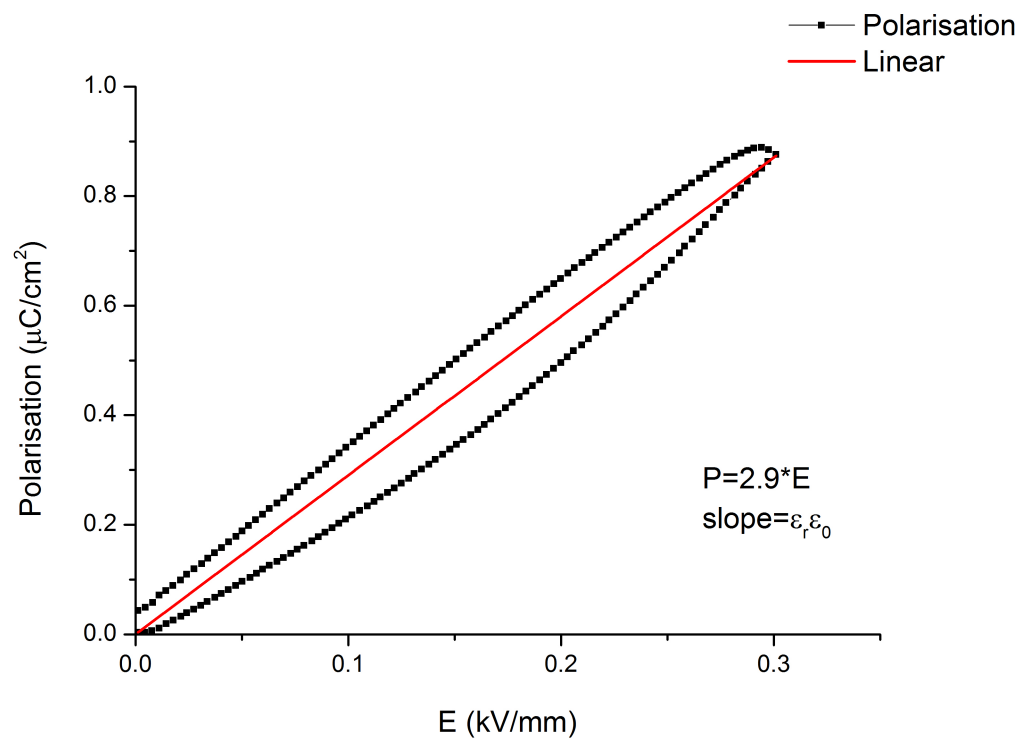


FIGURE 7.4: Method for calculation of real permittivity from PE loops

7.2.3.4 Impedance Spectroscopy

Impedance spectroscopy measurements have been performed using ModuLab XM MTS (Solartron Analytical, England) in conjunction with a tube furnace Pyrotherm (England) for testing at various temperatures. Data acquisition was controlled by ModuLab XM Software, whilst the temperature was controlled by a K-type thermocouple

placed in the vicinity of the sample and monitored via LabVIEW software. The impedance data was acquired in the frequency range 0.5 Hz - 1 MHz. ModuLab XM Software has been used to fit data obtained with an equivalent circuit and extract values for the various circuit elements.

7.2.3.5 Permittivity versus Temperature

HP 4192 Impedance Analyser has been used to record the capacitance of the samples over a range of frequencies, from -50 to 300°C. The temperature was controlled by a furnace from a Q800, DMA instrument (TA Instruments) provided with a gas cooling accessory which uses cold nitrogen generated from controlled heating of liquid nitrogen. Data acquisition was automated in a LabVIEW environment.

7.2.3.6 Mechanical quality factor

An HP 4194 impedance analyser together with a LabVIEW data acquisition software have been used to obtain the Q_m values of the sample. In addition to the measurement method stated in Section 2.3.2.4, other methods are also available. For measurements within this work Equation 7.2 has been used.

$$Q_m = \frac{f_r}{(\Delta f)_{3dB}} \quad (7.2)$$

where f_r is the frequency at which admittance is maximum or impedance is minimum (i.e. resonance frequency) and Δf_{3dB} is the 3dB width of the resonance.

7.3 Results and Discussion

7.3.1 Investigations during sample preparation

Thermogravimetric analysis has been performed on the calcined powder, after the binder mix-in step. The obtained weight loss profile is shown in Figure 7.5. It was inferred that the binder was effectively burnt by setting up a temperature around 600°C, as most of weight (associated with binder) is lost below 500°C.

Furthermore, the samples have been investigated with X-ray Diffraction to ensure a

perovskite phase has been obtained following calcination. The diffractograms are shown in Figure 7.6. A perovskite has been obtained with minor peaks associated with a non-perovskite structure. The software Highscore in conjunction with PDF4 database of the International Centre for Diffraction Data has been utilised to identify possible phases and the minor peaks were related to the following compounds: $\text{Pb}_3\text{Nb}_4\text{O}_{13}$, $\text{Nb}_2\text{Pb}_{1.5}\text{O}_{6.5}$, $\text{Pb}_{1.45}\text{Nb}_2\text{O}_{6.26}$ and/or PbO . Nevertheless, the weak peaks may also be due to $\text{Cu K}\beta$ radiation or even non-Cu radiation from the X-ray tube, such as $\text{W L}\alpha$ and further investigation is required to distinguish between the different sources for the peaks.

Optical micrographs have been collected to investigate the calcined powders - Figure 7.7. There are inhomogeneities observed in the calcined powders as suggested by the dark spots which are associated with MnO_2 agglomerations. The inhomogeneity is expected to be reduced by the second milling process. The surfaces of the samples, shown in Figure 7.8, reveal some residual chemical non-uniformity as suggested by some non-uniform grain growth during sintering, for example in Figure 7.8d and 7.8e. However, there is a possibility this is only a surface effect as the figures show the as-sintered surface. The density of the samples is shown in Figure 7.9. Densities obtained are in the range 92-94% of the theoretical. It is believed that by increasing the amount of binder used or by isostatic pressing the samples prior to sintering, values closer to the theoretical may be achieved [140].

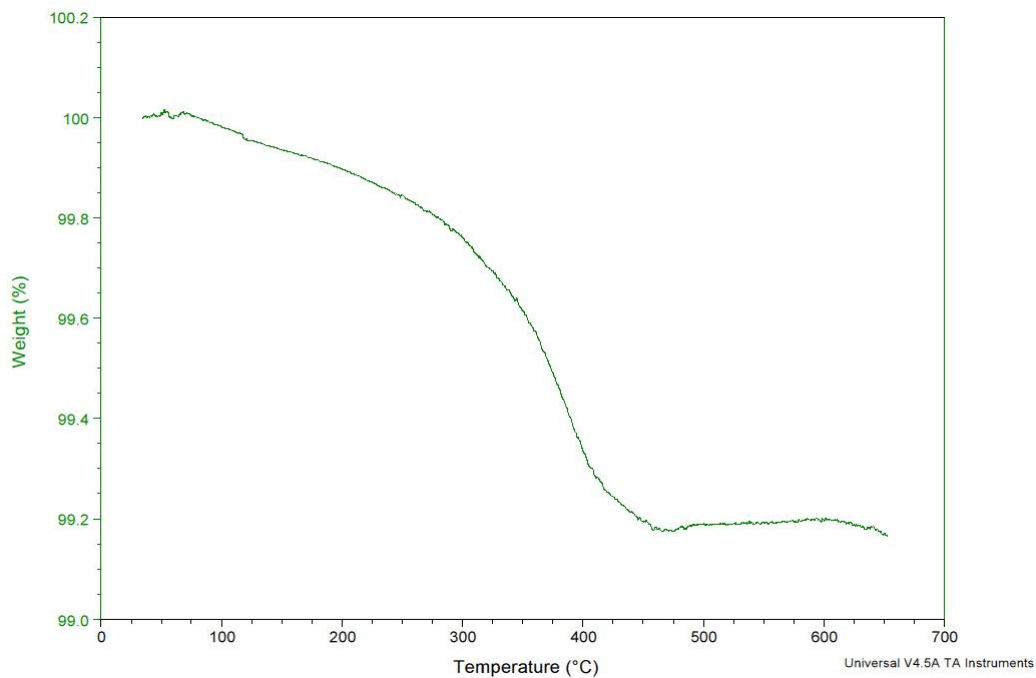


FIGURE 7.5: Thermogravimetric analysis of the powder containing binder

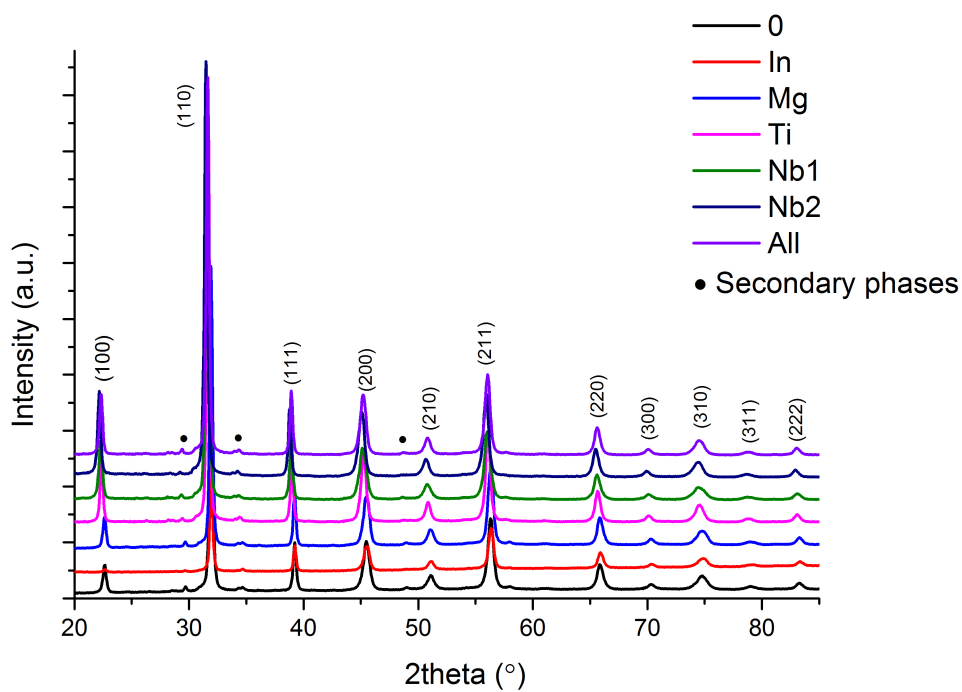
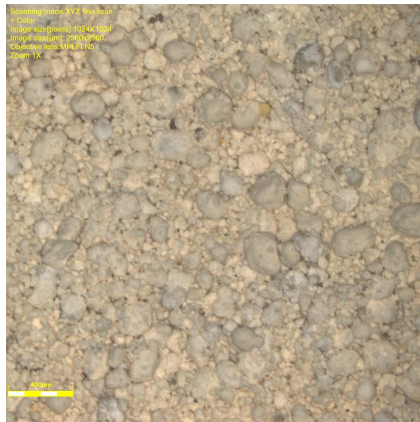
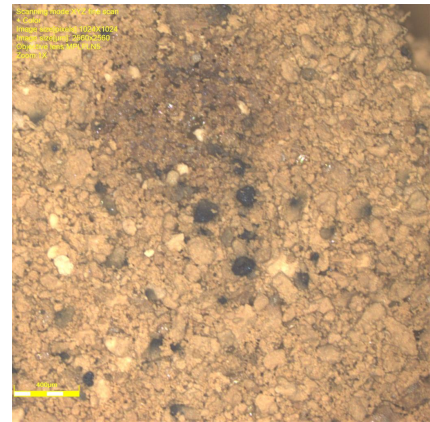


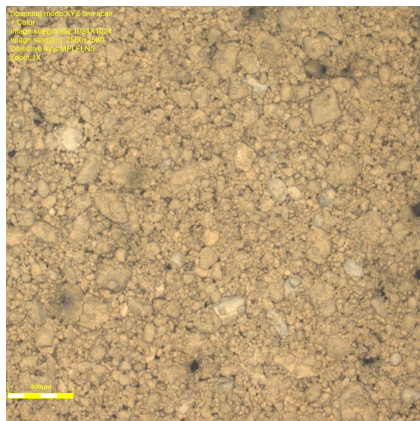
FIGURE 7.6: X-ray patterns for calcined powders.



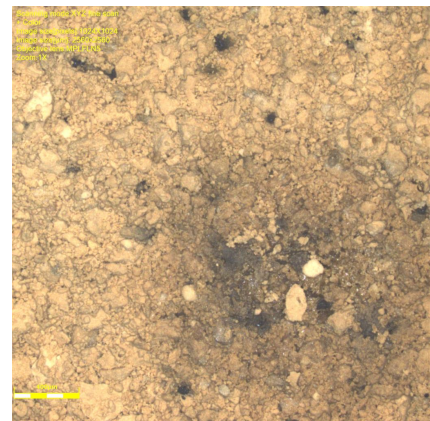
(A) 0



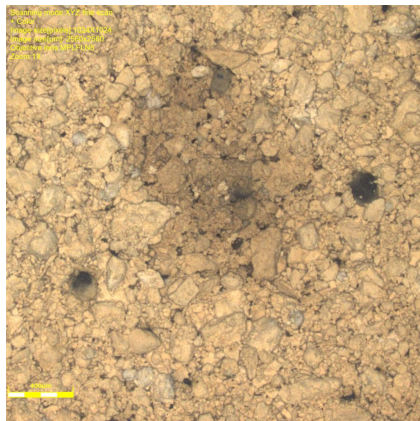
(B) In



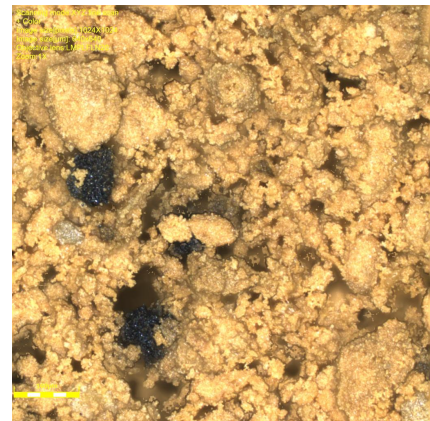
(C) Mg



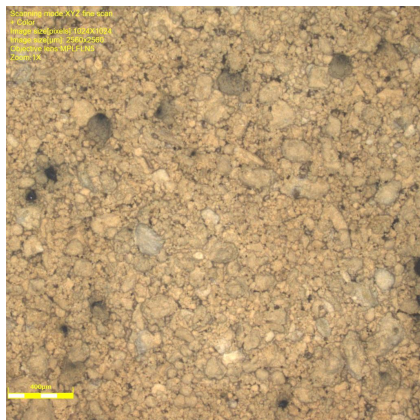
(D) Ti



(E) Nb1



(F) Nb2



(G) All

FIGURE 7.7: Optical micrographs of calcined powders. The scale bar is 400 μm.

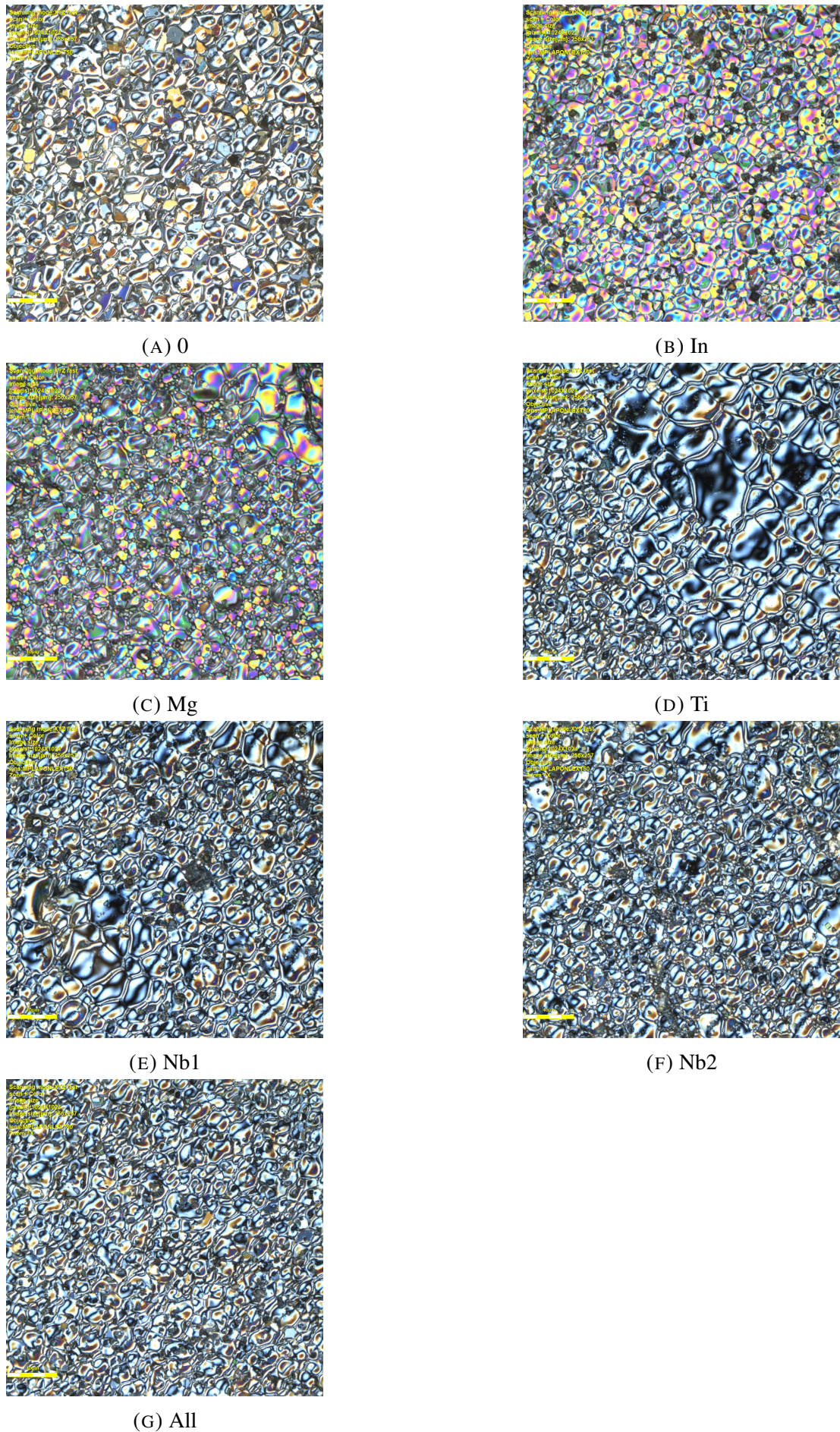


FIGURE 7.8: Optical Micrographs of sintered samples. The images have been taken on the unpolished, unetched surface. The scale bar is $400\mu\text{m}$.

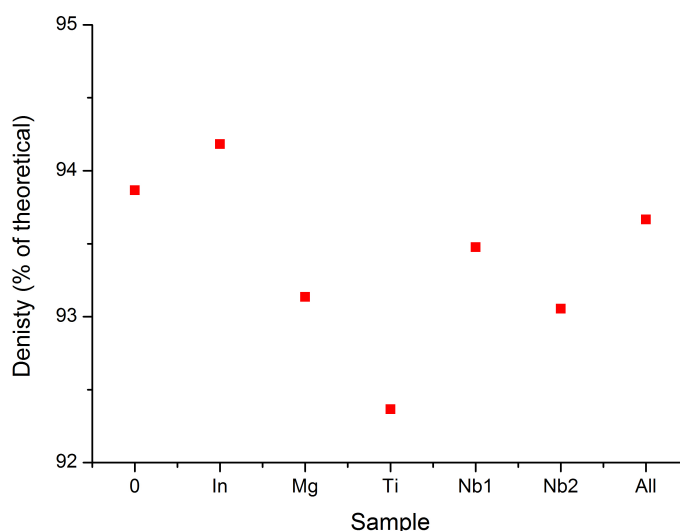


FIGURE 7.9: Density of samples obtained via Archimedes method

7.3.2 Mn Valence State

The X-ray Absorption Spectrum is shown in Figure 7.10. The equivalent average valence state as a function of absorption energy is shown in Figure 7.11. An average valence state of 3.6 has been observed for all the polycrystalline samples under investigation. A Mn-modified single crystal has also been included in the study and the average valence observed was 3.4, which is slightly lower than that observed for the polycrystalline samples. These values suggest a mixture of valence states, probably 2+, 3+ and 4+. It is believed that the difference between single crystal and polycrystals arises from the fact that compositions are slightly different. The single crystal B4 has a Mn content of 0.7mol%, whilst the polycrystals 2mol%. In addition, it is probably interesting to also note the Nb content: 41.2mol% for the single crystal and 38.7-40.6mol% for the polycrystals - refer to Table 7.3. This is relevant as it seems to be consistent with previous studies which suggested the Mn valence state is lower as Nb concentration increases - Section 7.1.2.4. The investigated single crystal had a lower Mn content and a slightly higher Nb content compared to the polycrystals which could explain the slightly lower valence state observed. Therefore, the single crystal seems to have a slightly increased concentration of Mn²⁺ and probably Mn³⁺ and less Mn⁴⁺. However, the different processing conditions should not be omitted. The single crystal has been grown in a sealed crucible which could lead to oxygen poor atmosphere and

hence to a higher concentration of oxygen vacancies which could lead to a lower Mn valence state in order to achieve charge compensation.

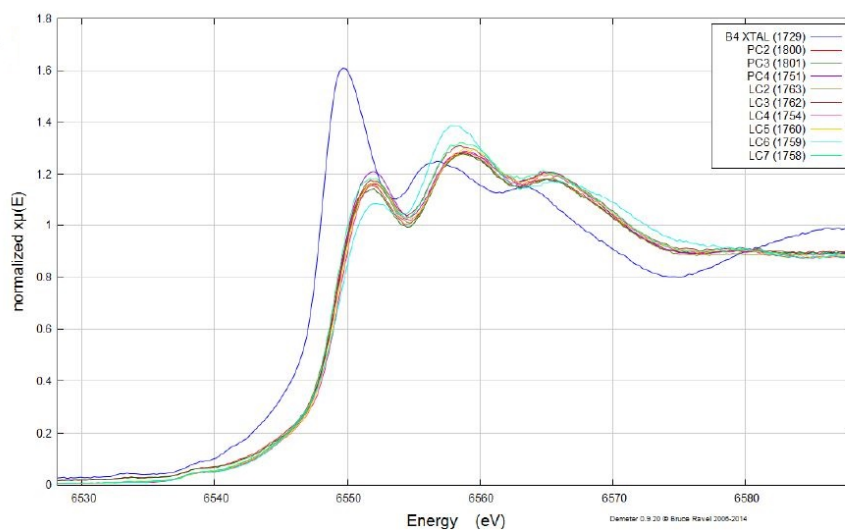


FIGURE 7.10: X-Ray Absorption Spectrum of Mn-modified samples investigated in this study (The samples In, Mg, Ti, Nb1, Nb2, All are here labelled LC2, LC3, LC4, LC5, LC6, LC7). The spectrum from Mn modified single crystal B4 (B4 XTAL) is also presented. PC samples are not investigated here. Measurements conducted at The Australian Synchrotron.

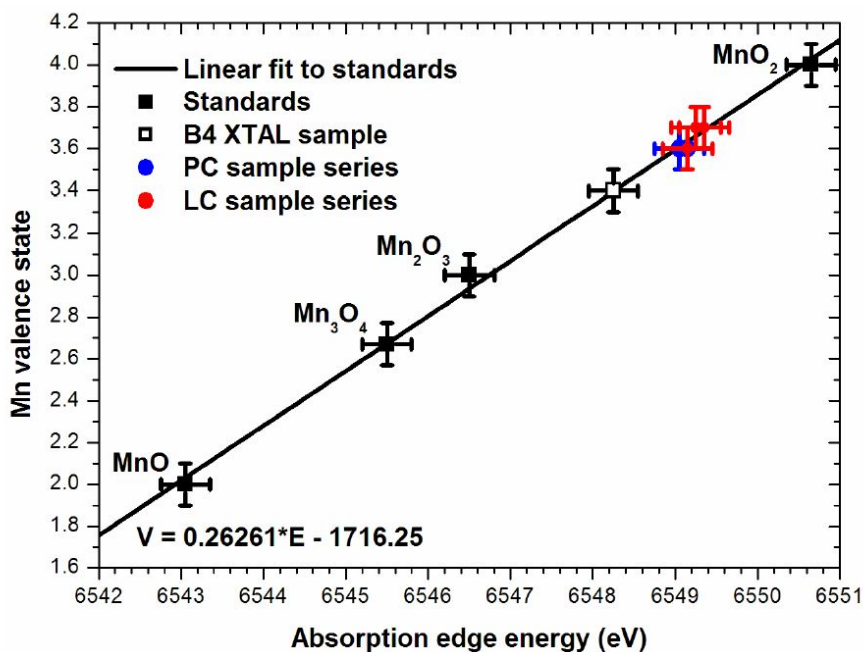


FIGURE 7.11: Valence state as a function of absorption edge energy for commercial oxides, B4 single crystal (B4 XTAL) and sample analysed within this study (The samples In, Mg, Ti, Nb1, Nb2, All are here labelled LC2, LC3, LC4, LC5, LC6, LC7). PC samples are not investigated here. Data provided by The Australian Synchrotron.

7.3.3 Permittivity versus Electric Field

Figure 7.12 shows the relative variation of the real permittivity as a function of electric field applied as calculated from polarisation - electric field loops at subcoercive field values. The following observations can be made:

- Sample 0 (i.e. undoped) shows the highest permittivity.
- Mn-modified (i.e. acceptor doped) samples show lower values compared with the undoped sample.
- Nb1 and Nb2 (i.e. samples with lower Nb content) show the lowest values amongst Mn-doped samples. In other words, when the content of Nb (donor) is lowered, the permittivity also decreases.

These observations are in agreement with previous findings which report an increased permittivity for donor doped materials and decreased for undoped and acceptor doped. To analyse the degree of linearity of the permittivity - electric field dependence, the plots are shown separately for each sample in Figure 7.13. Sample 0 shows a non-linear response, whilst in the case of Mn-modified samples the linearity increases, with the response for the In sample completely linear. A non-linear behaviour is typically associated with extrinsic effects as intrinsic contributions may only be measured in single domain single crystals where domains are absent or when the measurement is performed at temperatures close to 0 absolute when domain wall movement is frozen. In turn, the extrinsic contributions are related to domain walls activity [141]. Samples with reduced domain wall movement show more linear permittivity versus electric field dependence, which may also be interpreted as less lossy response. This behaviour is expected in Mn-modified samples.

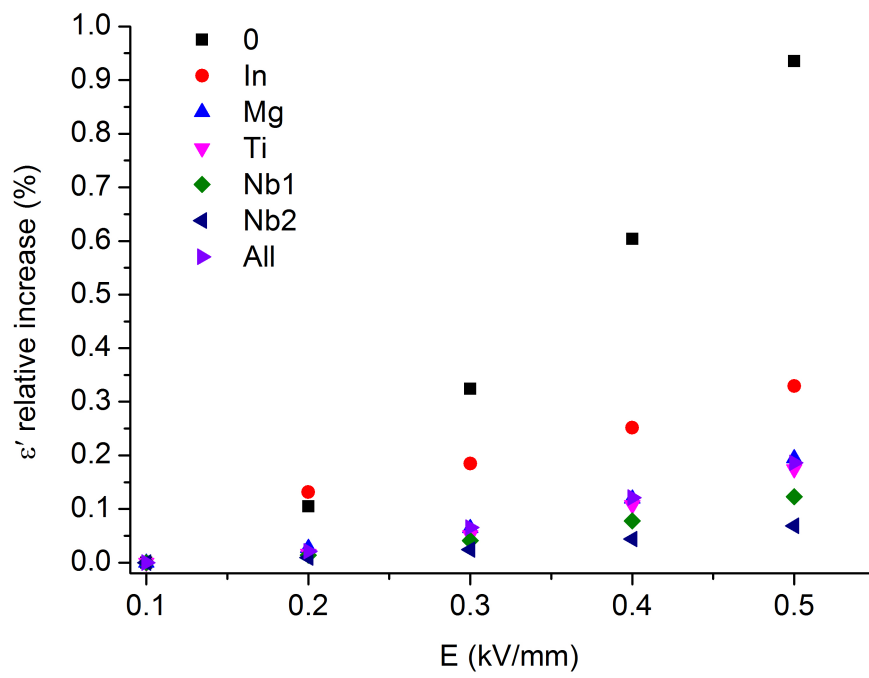


FIGURE 7.12: Real part of relative permittivity as a function of electric field

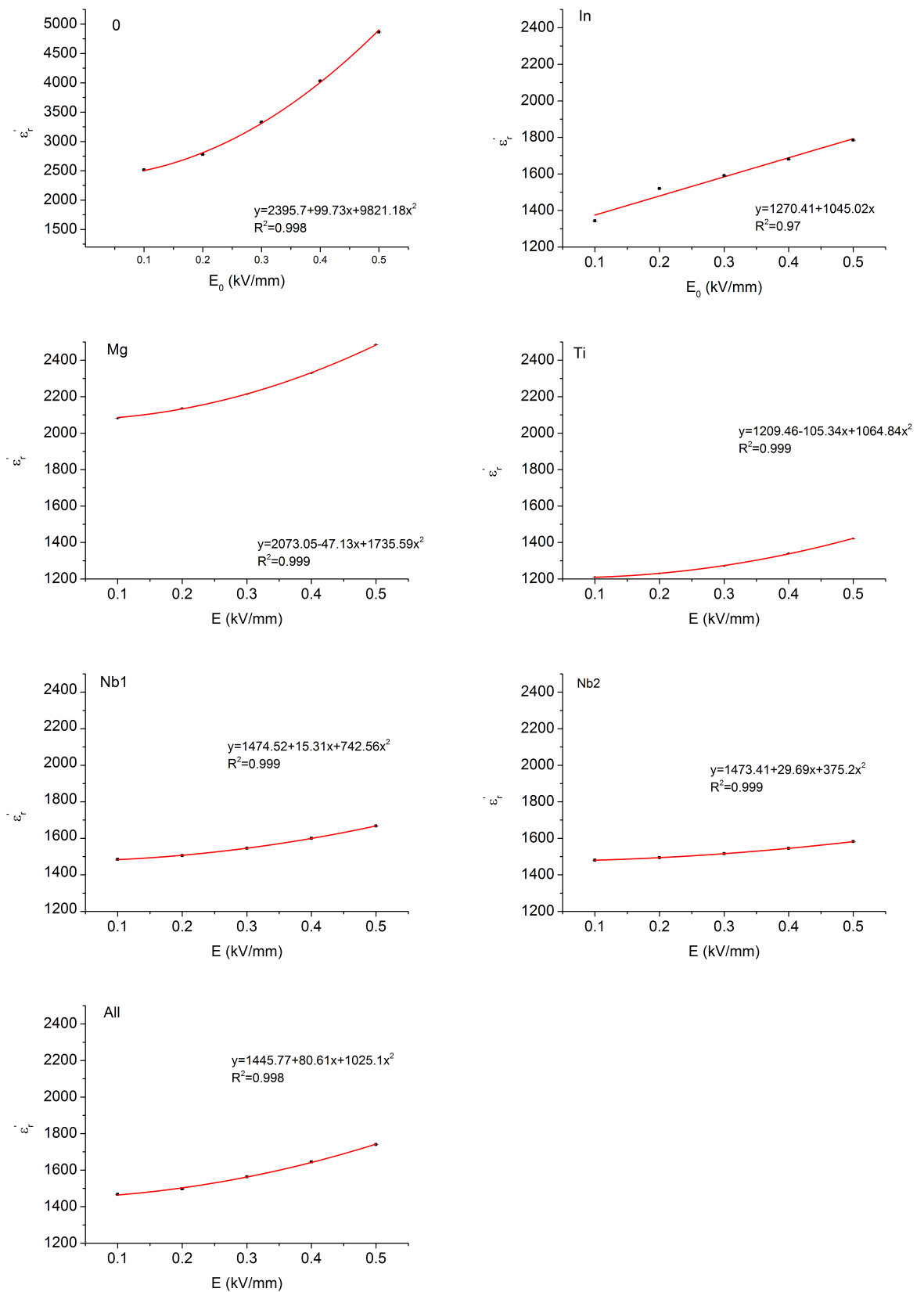


FIGURE 7.13: Real part of permittivity versus electric field. The scale is different for Sample 0 plot compared to the plots for the Mn-modified samples.

7.3.4 Polarisation versus Electric Field

Hysteresis loops are shown in Figure 7.14. The first observation is the value of the polarisation which is the highest for the Mn-free sample 0 and decreases for the Mn-modified samples. Second, the shape and position of the loops differ. The internal bias field within the samples calculated from the loops is shown in Figure 7.15. The highest bias field is observed for the Mn-free 0 and also for the samples where Mn substitutes Nb (Nb1 and Nb2), i.e. 0.1 to 0.2 kV/mm. The rest of the samples have an internal field lower than 0.05 kV/mm. The fields probably arise as a consequence of a combination of effects, i.e. $\text{Mn}_{\text{Ti}}''\text{-V}_{\text{O}}^{\bullet\bullet}$ defect dipoles and space charges from secondary phases around grains. The relatively high field observed for sample 0 is probably due only to space charges as Mn (and hence $\text{Mn}_{\text{Ti}}''\text{-V}_{\text{O}}^{\bullet\bullet}$ defect dipole) is not present in this sample.

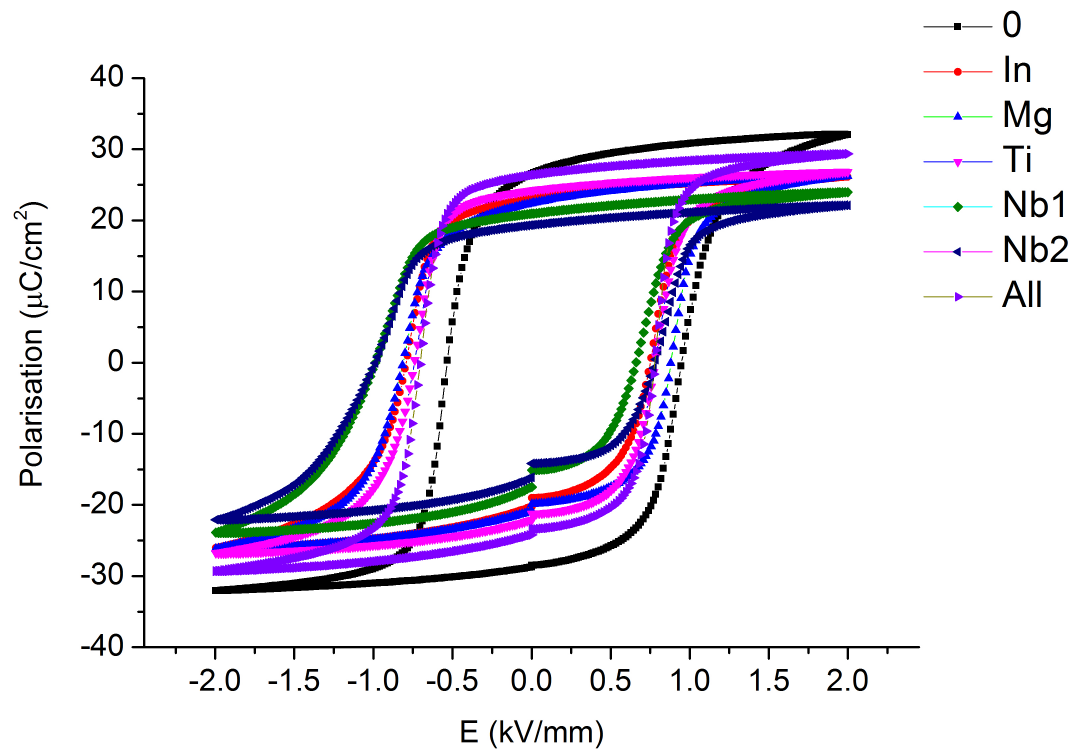


FIGURE 7.14: Polarisation versus electric field loops

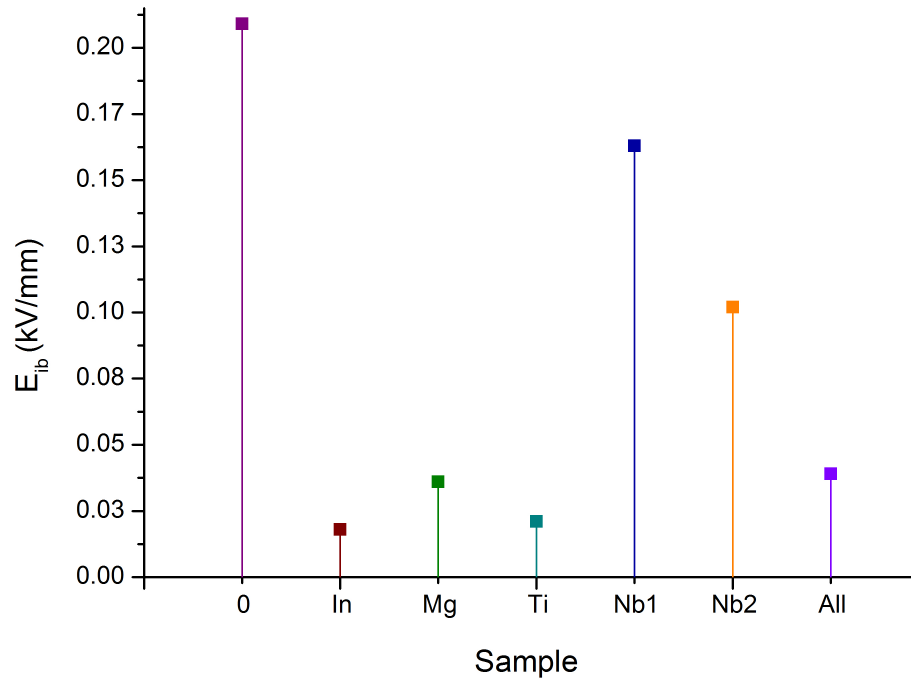


FIGURE 7.15: Internal bias field (absolute values) calculated from hysteresis loops.

7.3.5 Impedance Spectroscopy

7.3.5.1 Complex Impedance Spectrum

Impedance Spectroscopy data is first analysed under the form of complex impedance - Equation 7.3

$$Z^* = Z' + iZ'' \quad (7.3)$$

where Z' is the real part and Z'' the imaginary part of the complex impedance. Nyquist diagrams, i.e. $-Z''$ versus Z' for all samples at various temperatures are shown in Figure 7.16. Above 175°C a single semicircle is obtained in all cases. To highlight the difference between the samples, data obtained at 400°C is shown for all samples in Figure 7.17. The impedance changes and has its lowest value for the Mn-free sample and increases for the Mn modified samples. The behaviour of the imaginary part of the impedance versus frequency is shown in Figure 7.18 for all samples at 400°C and in Figure 7.19 separately for each sample. The differences in peak height together with broadening of peaks indicates a dispersion of relaxation times. This seems to be in contradiction with Nyquist plots where a single semicircle is typically associated with

a single relaxation. The single relaxation process may be modelled by an equivalent circuit formed by an ohmic resistor (R) and a capacitor (C) in parallel Figure 7.201. However, a mismatch has been found between the experimental data and the response of the RC ideal circuit. Examples of the fit with the RC equivalent circuit are given in Figure 7.203 and 7.205. By comparison with the fit, the semicircles obtained from the measured samples are suppressed, with the centre of the circle below the real impedance axis suggesting a non-Debye type of relaxation. Consequently, to account for the non-ideal behavior, the ideal capacitor (C) has been replaced by a Constant Phase Element (CPE) Figure 7.202, resulting in an improved fit - Figure 7.204 and 7.206. The R-CPE has been suggested to be a successful equivalent circuit to model the non-Debye behavior for a relatively narrow distribution of relaxation [142]. The parameters obtained for each fitting process are listed in Table 7.4. It has been previously suggested that the CPE element might be related to the distribution of relaxation times across the sample [143]. Furthermore, the parameter 'n' could be related to the width of such a distribution, with $n=1$ indicating a narrow distribution [142]. The dependence of parameter n on temperature for each sample is shown in Figure 7.21. At lower temperatures (i.e. below 175°C, the manganese free sample, 0, exhibits a relatively high n, on the order of 0.98. This value approaches the behavior of an ideal capacitor ($n \cong 1$). In the same temperature range, all Mn-modified samples exhibit significantly lower values ranging from 0.85 to 0.90. Above 175°C, n decreases and then increases again for sample 0 with the lowest value 0.93. It is interesting to note that n follows a similar trend for In, Mg, Ti and Al, increasing rapidly above 175°C (probably at the temperature of phase change), whilst it decreases for Nb1 and Nb2. These observations suggest:

- a broader distribution of relaxation for Mn modified samples compared to the Mn free sample at lower (probably below the phase transition) temperatures;
- as temperature increases, the width of this distribution further increases for Nb1 and Nb2 whilst is narrower for the rest of the samples.

The variation of the distribution width might be related to the compositional fluctuations within the samples associated with their different behaviour under stimuli. In the following subsection, an attempt is being made at explaining the relaxation distribution with calculations of mean relaxation times.

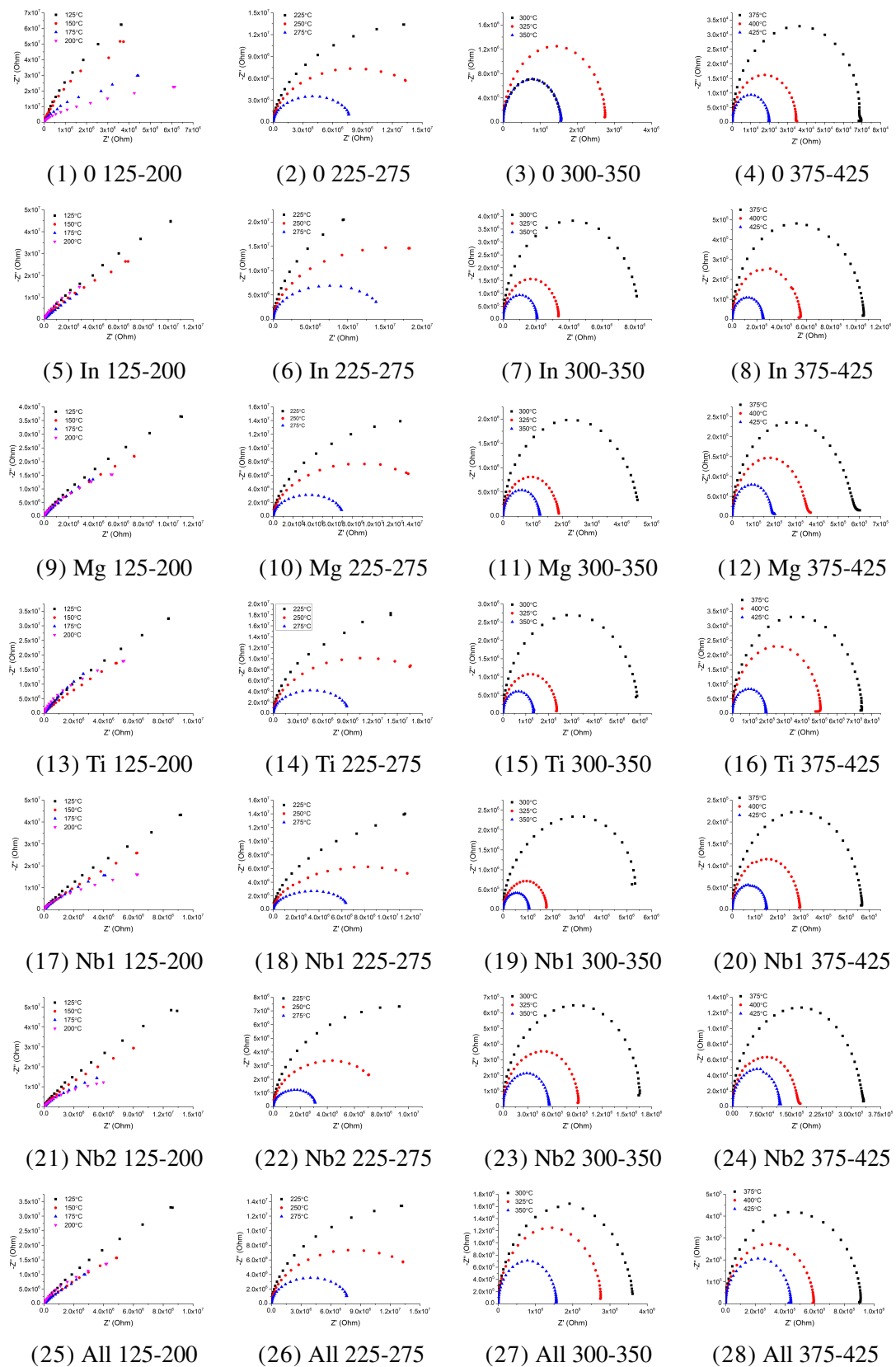
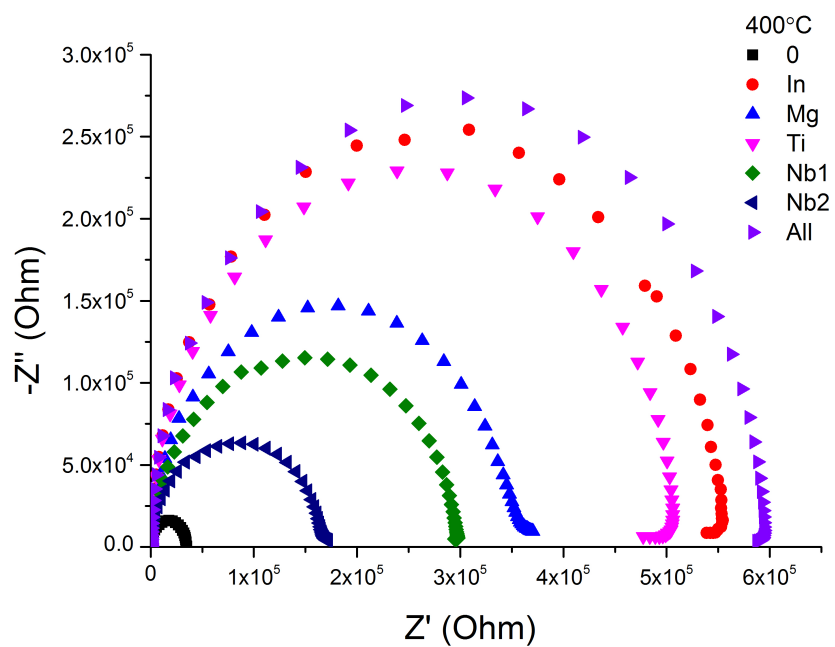
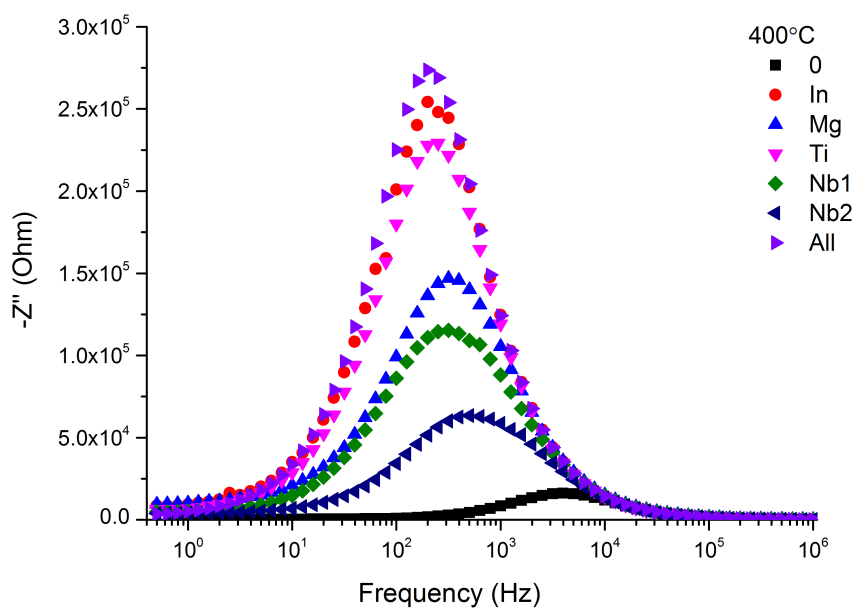


FIGURE 7.16: Nyquist plots. The caption under each figure represents the name of the sample as well as the temperature range of measured data in $^{\circ}\text{C}$

FIGURE 7.17: Nyquist plot for all samples at 400°C FIGURE 7.18: Imaginary impedance as a function of frequency at 400°C

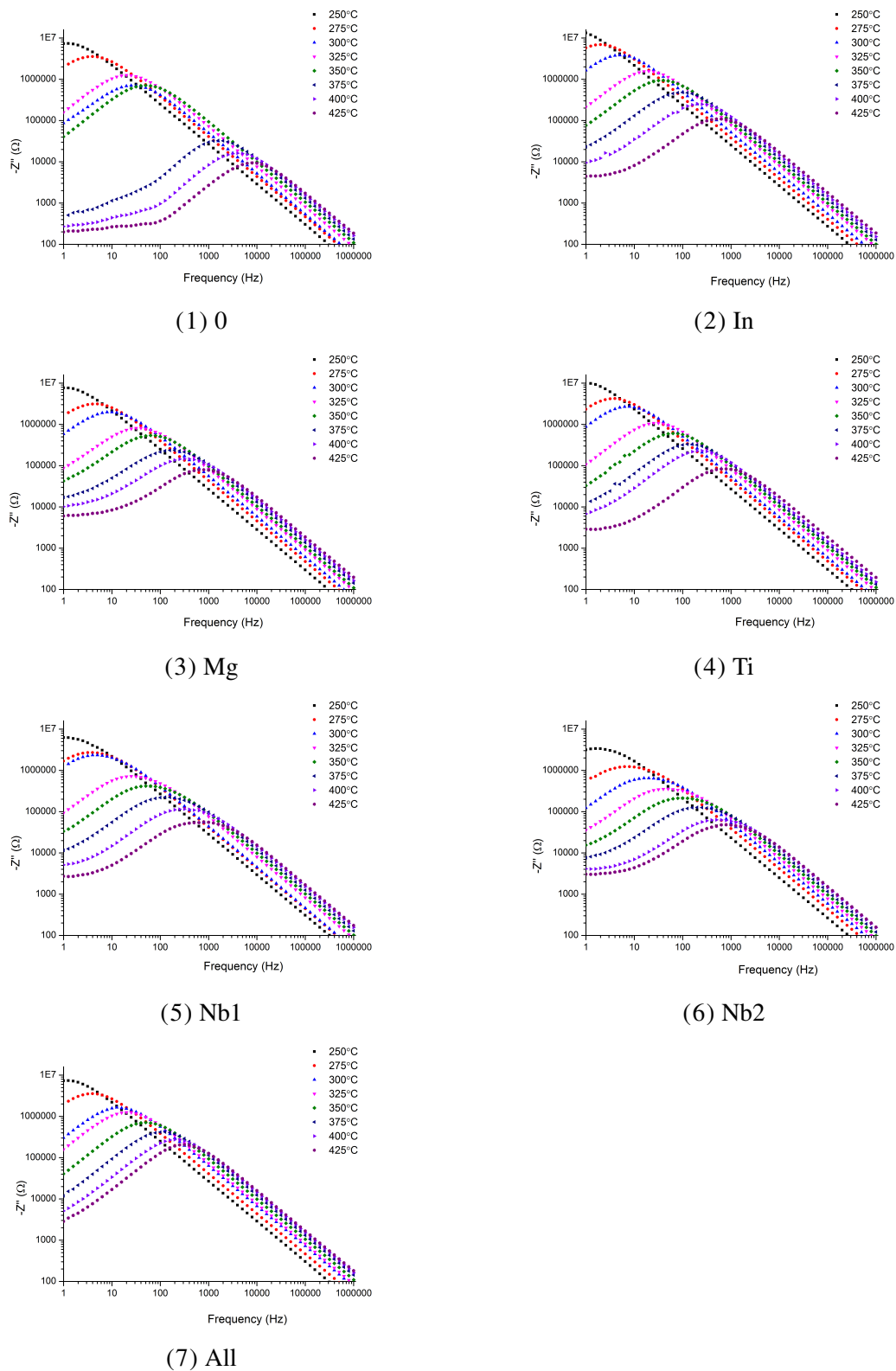
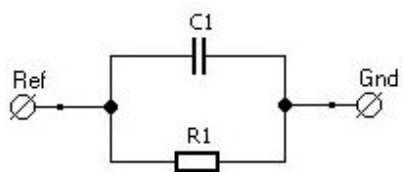
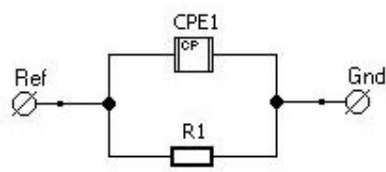
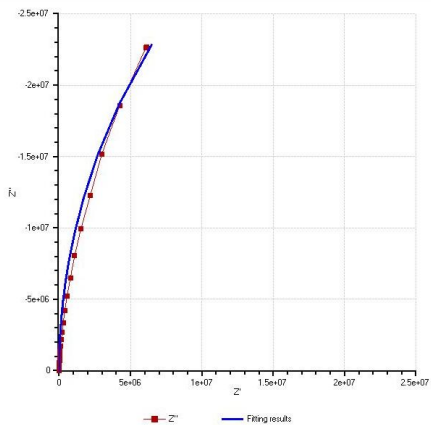


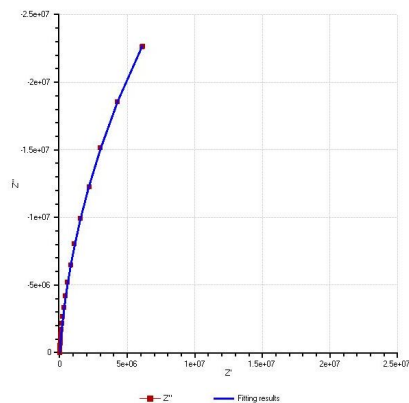
FIGURE 7.19: Imaginary part of the impedance versus frequency plots



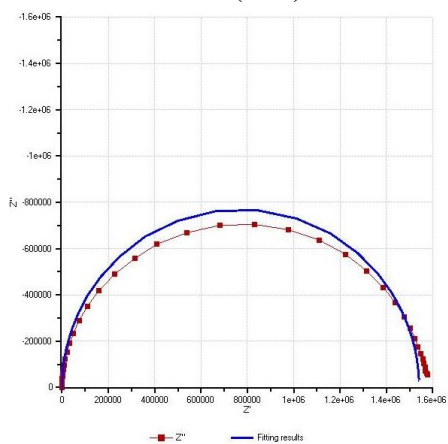
(1) RC equivalent circuit



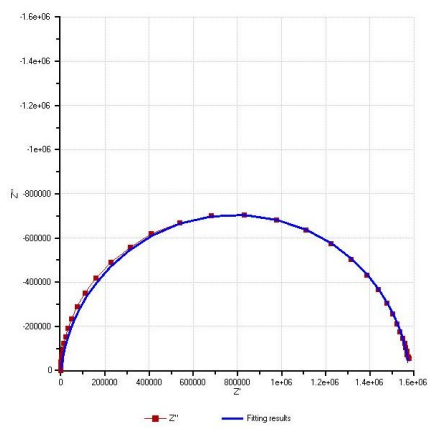
(2) R-CPE equivalent circuit



(3) 0, 200°C data (red squares) and RC fit (blue)



(4) 0, 200°C data (red squares) and R-CPE fit (blue)



(5) 0, 300°C data (red squares) and RC fit (blue)

(6) 0, 300°C data (red squares) and R-CPE fit (blue)

FIGURE 7.20: Nyquist plots fitted using ModuLab XM Software

TABLE 7.4: R-CPE parameters obtained for each fitting process

Sample	R (Ω)	Q (Fs^{n-1})	n	Sample	R (Ω)	Q (Fs^{n-1})	n
125°C				150°C			
0	2.202×10^9	5.1805×10^{-9}	0.981	0	1.165×10^9	6.259×10^{-9}	0.982
In	6.423×10^8	7.6157×10^{-9}	0.903	In	3.724×10^8	1.3065×10^{-8}	0.880
Mg	3.762×10^8	9.2723×10^{-9}	0.877	Mg	2.271×10^8	1.5604×10^{-8}	0.860
Ti	4.433×10^8	1.0574×10^{-8}	0.887	Ti	3.186×10^8	2.0513×10^{-8}	0.860
Nb1	7.292×10^8	9.9119×10^{-9}	0.905	Nb1	4.15×10^8	1.3358×10^{-8}	0.890
Nb2	5.349×10^8	6.982×10^{-9}	0.891	Nb2	2.599×10^8	1.1452×10^{-8}	0.884
All	3.766×10^8	1.03×10^{-8}	0.895	All	1.902×10^8	2.2067×10^{-8}	0.863
175°C				200°C			
0	4.303×10^8	1.0985×10^{-8}	0.951	0	1.25×10^8	1.3819×10^{-8}	0.953
In	4.719×10^8	3.1101×10^{-8}	0.872	In	1.387×10^8	2.21×10^{-8}	0.947
Mg	1.47×10^8	2.5783×10^{-8}	0.884	Mg	6.929×10^7	2.0178×10^{-8}	0.931
Ti	2.754×10^8	2.5589×10^{-8}	0.909	Ti	8.429×10^7	1.7131×10^{-8}	0.959
Nb1	1.523×10^8	2.1508×10^{-8}	0.906	Nb1	6.742×10^7	1.8673×10^{-8}	0.927
Nb2	1.062×10^8	2.3198×10^{-8}	0.864	Nb2	4.597×10^7	2.4336×10^{-8}	0.901
All	2.515×10^8	3.5815×10^{-8}	0.856	All	6.96×10^7	2.2811×10^{-8}	0.942
225°C				250°C			
0	4.378×10^7	1.2802×10^{-8}	0.945	0	1.029×10^7	9.0556×10^{-9}	0.934
In	6.214×10^7	1.3426×10^{-8}	0.961	In	3.21×10^7	9.0127×10^{-9}	0.945
Mg	3.218×10^7	1.3455×10^{-8}	0.923	Mg	1.743×10^7	9.8525×10^{-9}	0.922
Ti	4.279×10^7	1.164×10^{-8}	0.935	Ti	2.207×10^7	8.3864×10^{-9}	0.945
Nb1	3.563×10^7	1.5536×10^{-8}	0.887	Nb1	1.557×10^7	1.2056×10^{-8}	0.864
Nb2	1.751×10^7	1.8785×10^{-8}	0.884	Nb2	8.418×10^6	1.5513×10^{-8}	0.861
All	3.02×10^7	1.3083×10^{-8}	0.929	All	1.658×10^7	9.4604×10^{-9}	0.926
275°C				300°C			
0	3.394×10^6	6.726×10^{-9}	0.929	0	1.579×10^6	5.414×10^{-9}	0.929
In	1.504×10^7	5.9673×10^{-9}	0.948	In	8.306×10^6	4.4664×10^{-9}	0.949
Mg	7.161×10^6	6.5277×10^{-9}	0.917	Mg	4.592×10^6	5.4574×10^{-9}	0.919
Ti	9.268×10^6	5.4994×10^{-9}	0.939	Ti	5.972×10^6	4.6187×10^{-9}	0.937
Nb1	6.77×10^6	9.3072×10^{-9}	0.865	Nb1	5.663×10^6	8.529×10^{-9}	0.877
Nb2	3.233×10^6	1.2125×10^{-8}	0.840	Nb2	1.701×10^6	9.8881×10^{-9}	0.842
All	7.95×10^6	6.3403×10^{-9}	0.929	All	3.638×10^6	4.4093×10^{-9}	0.925
325°C				350°C			
0	360700	3.6994×10^{-9}	0.932	0	178500	2.6398×10^{-9}	0.951
In	3.404×10^6	3.1×10^{-9}	0.948	In	2.078×10^6	2.8066×10^{-9}	0.939
Mg	1.888×10^6	4.0165×10^{-9}	0.906	Mg	1.248×10^6	3.4183×10^{-9}	0.909
Ti	2.378×10^6	3.2184×10^{-9}	0.937	Ti	1.343×10^6	2.6765×10^{-9}	0.937
Nb1	1.796×10^6	6.3844×10^{-9}	0.863	Nb1	1.069×10^6	5.7991×10^{-9}	0.859
Nb2	931500	8.5435×10^{-9}	0.841	Nb2	567700	7.7808×10^{-9}	0.837
All	2.784×10^6	3.7733×10^{-9}	0.933	All	1.571×10^6	2.9323×10^{-9}	0.935
375°C				400°C			
0	69380	1.8106×10^{-9}	0.969	0	34790	1.7458×10^{-9}	0.957
In	1.068×10^6	2.4349×10^{-9}	0.932	In	552700	1.9709×10^{-9}	0.942
Mg	584700	4.1478×10^{-9}	0.867	Mg	362100	3.7636×10^{-9}	0.870
Ti	745400	2.4485×10^{-9}	0.930	Ti	503500	2.0264×10^{-9}	0.944
Nb1	573700	5.3763×10^{-9}	0.855	Nb1	299000	5.2029×10^{-9}	0.849
Nb2	333800	6.9602×10^{-9}	0.840	Nb2	170400	6.9718×10^{-9}	0.830
All	913800	2.2605×10^{-9}	0.942	All	594900	1.8716×10^{-9}	0.949
425°C							
0	19960	1.4935×10^{-9}	0.962				
In	252600	2.2389×10^{-9}	0.915				
Mg	195800	3.4028×10^{-9}	0.871				
Ti	195300	2.3301×10^{-9}	0.912				
Nb1	151900	6.8071×10^{-9}	0.822				
Nb2	122400	6.1298×10^{-9}	0.843				

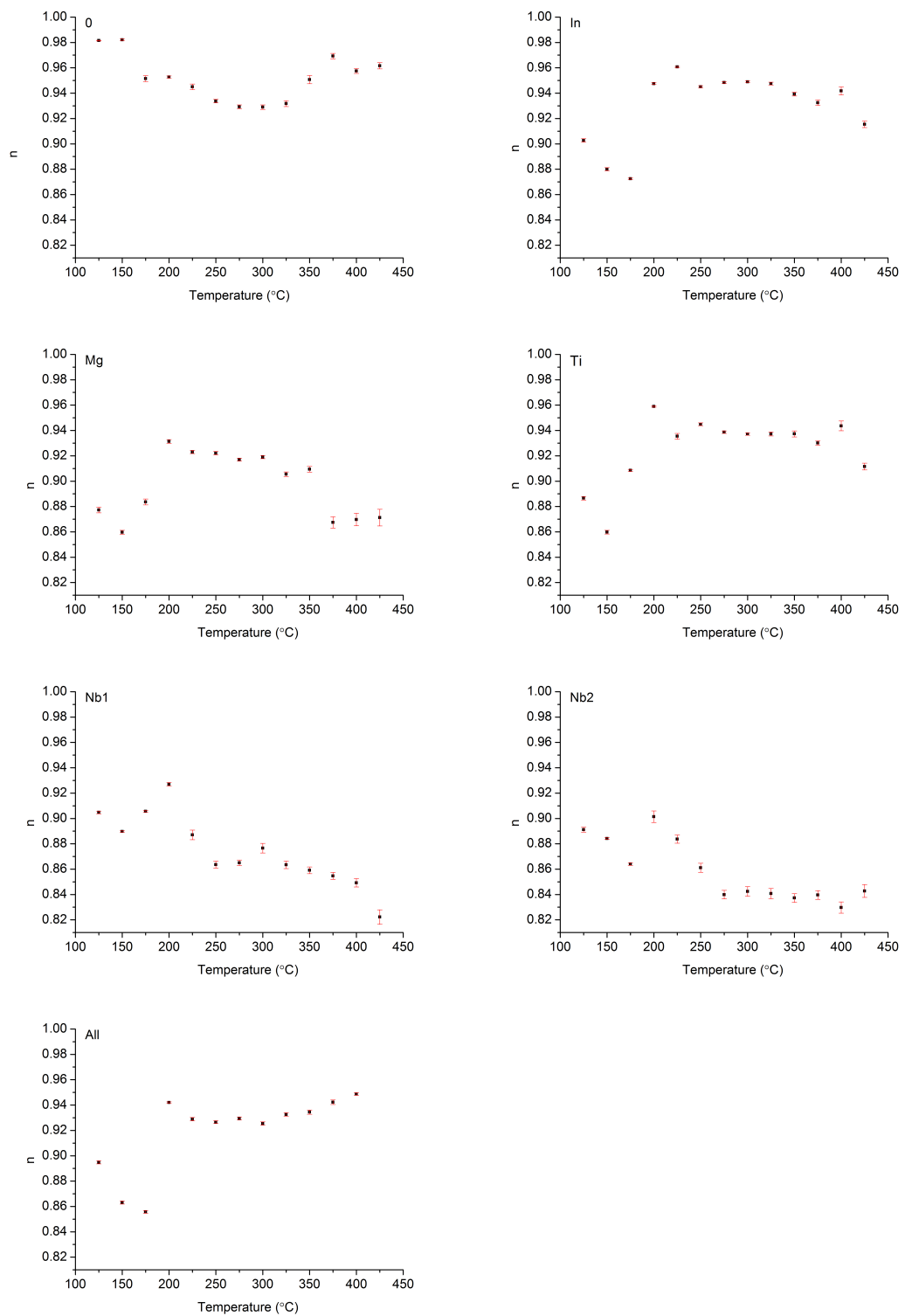


FIGURE 7.21: Evolution of parameter n with increasing temperature shown separately for each sample

7.3.5.2 Relaxation times

As pointed out in the previous subsection, data reveals a non-ideal behaviour of the samples and the presence of a CPE element is related to a distribution of relaxation times. The relaxation times (or, more realistically, a mean value for the distribution of relaxation times exhibited by the sample) have been calculated in two different ways, as follows:

1. $\tau = \frac{1}{f_0}$, where f_0 is the frequency of maximum $-Z''$ (see Figure 7.19). τ has also been calculated using the frequency of maximum imaginary modulus M'' (Section 7.3.5.3), however same results have been obtained and therefore the plots are not shown here. τ dependence on the inverse of temperature is shown in Figure 7.22. The activation energy for relaxation is calculated for each sample.
2. $\tau = RQ$, where the values for R and Q are obtained from the equivalent circuit fit and are listed in Table 7.4. The unit for τ depends on the parameter n and will be s^n [144]. The values for n are listed in Table 7.4. τ dependence on the inverse of temperature is shown in Figure 7.23. The activation energy for relaxation is calculated for each sample.

A comparison between the activation energies for τ calculated via the two different methods is shown in Figure 7.24. The plot reveals the same trend for the activation energies, i.e. a higher value for Sample 0 (0.71 and 0.65 eV) and lower values for the Mn-modified samples (0.43 to 0.55 eV and 0.39 to 0.49 eV). With regard to the relaxation time distribution function, several studies are available [143, 145]. However, it is suggested that most meaningful way to describe a system exhibiting a distribution of relaxation times is by use of a normal or Gaussian distribution around a mean value $\bar{\tau}$. The explanation for this approach relies on the following expression for the relaxation time:

$$\tau = \rho_{dc} \varepsilon_0 \varepsilon'_i \quad (7.4)$$

where ρ_{dc} is the DC resistivity, ε_0 is the permittivity of free space and ε'_i the real intrinsic permittivity of the sample. The expression contains all parameters that are material specific, i.e. resistive and dielectric. In turn, these parameters may have their own distributions which are difficult to distinguish separately. ρ and ε' may depend

on crystal structure, charge transport etc. Moreover, the crystal structure depends on composition and also temperature. Therefore, the *central limit theorem* has been suggested as most reasonable theoretical approach. The theorem states that functions of a large number of independent or weakly-dependent variables may be modelled by a distribution close to the normal distribution [142]. It is probably important to also discuss the origin of the relaxation. Typically, a single RC element (or R-CPE in the present case) is associated with relaxation originating from a single source such as the bulk of the sample. However, other contributions may also be present, i.e. minor second phases, grain boundaries, electrodes etc. The purpose of the next subsection is to briefly discuss the origin of the relaxation.

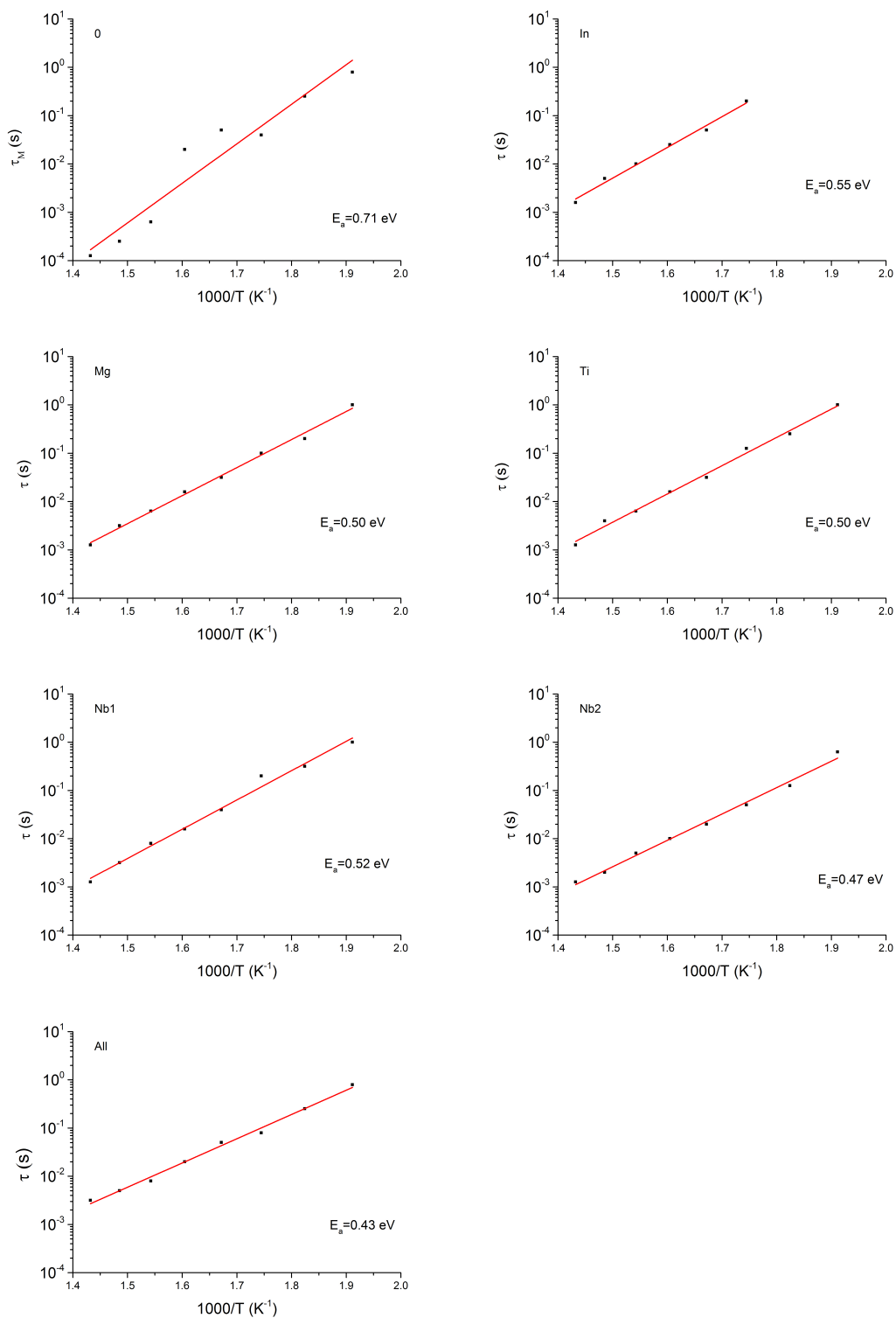
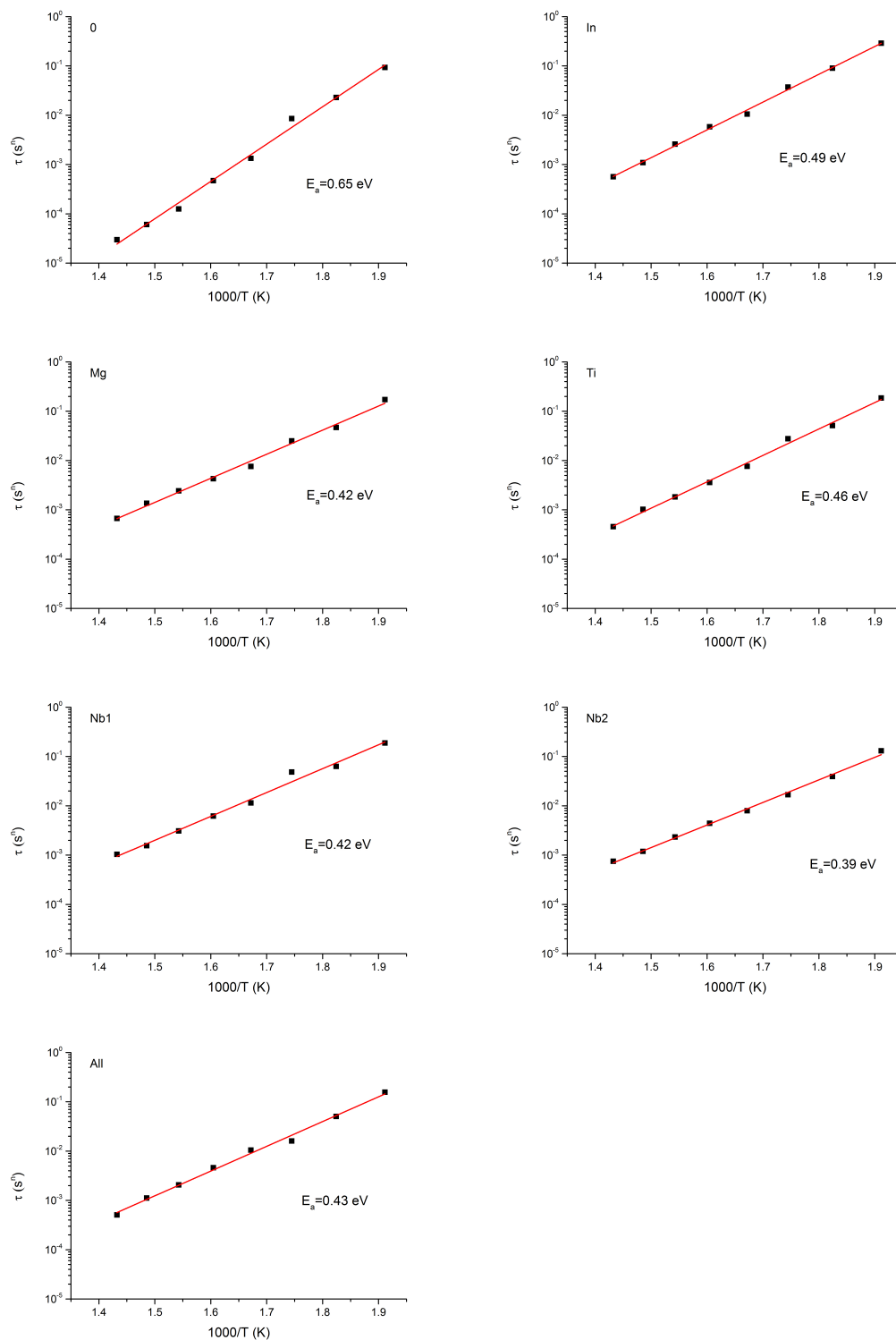


FIGURE 7.22: Relaxation times obtained with $\tau = \frac{1}{f_0}$, where f_0 is the frequency of maximum $-Z''$

FIGURE 7.23: Relaxation times obtained with $\tau=RQ$

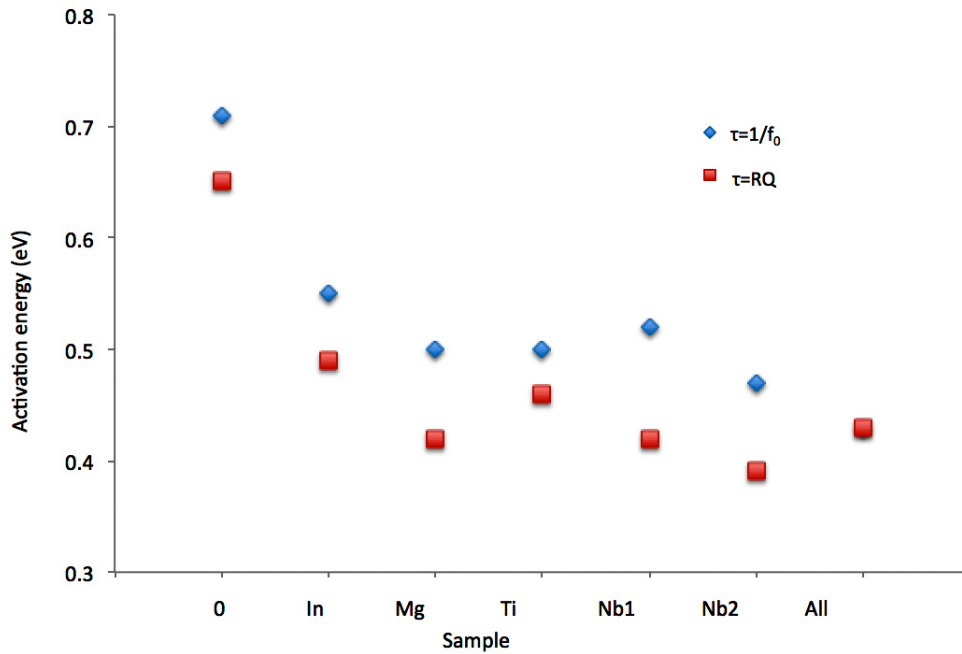


FIGURE 7.24: Activation energies for relaxation plotted for $\tau=\frac{1}{f_0}$ and $\tau=RQ$

7.3.5.3 Origin of the Relaxation Process

The single semicircles obtained for the impedance spectra above 175°C and shown in Figure 7.16 are typically associated with a single (or narrow distribution) relaxation process arising from the bulk of the sample. No contributions from grain boundaries, second phases, electrodes or other sources are obvious which would be associated with more than one semicircle in the spectra. However, other contributions may still be present and their existence may be investigated by careful analysis of the "ends" of the impedance spectrum, i.e. the low and high frequency regions. Alternatively, interpreting impedance data from the modulus point of view may also give an insight into less significant contributions to the relaxation process. This approach will be used here. The modulus is defined according to Equation 7.5 and it can be calculated using Equation 7.6.

$$M^* = M' + iM'' \quad (7.5)$$

$$M^* = i\omega C_0 Z^* \quad (7.6)$$

with ω the angular frequency and $C_0 = \frac{\epsilon_0 \cdot A}{d}$, where C_0 is the capacitance of the measuring cell in vacuum, A the electrode area, d the separation between the electrodes and

ε_0 the permittivity value in vacuum. A and d were chosen to match the sample dimensions. The imaginary part of the modulus is plotted at temperatures above 250°C for each sample in Figure 7.25. The plots show a shift of the peak to higher frequencies with increasing temperature. This result is not unexpected and it is associated with a decrease in relaxation time with increasing temperature, since the frequency of the peak

$$M''(\omega_{max}) = \frac{C_0}{2C} \quad (7.7)$$

Irvine, Sinclair and West [146] have suggested the origin of the relaxation may be identified from the value of the capacitance of the RC ideal circuit. Table 7.5 summarises the different contributions to relaxation with the associated capacitance values from [146]. However, in the present work, a non ideal behaviour is observed and a pseudocapacitance may be calculated according to Equation 7.8.

$$C = Q^{\frac{1}{n}} R^{\frac{1}{n}-1} \quad (7.8)$$

The values obtained are listed in Table 7.6 and seem to fall under three categories: grain boundary, bulk and surface layer.

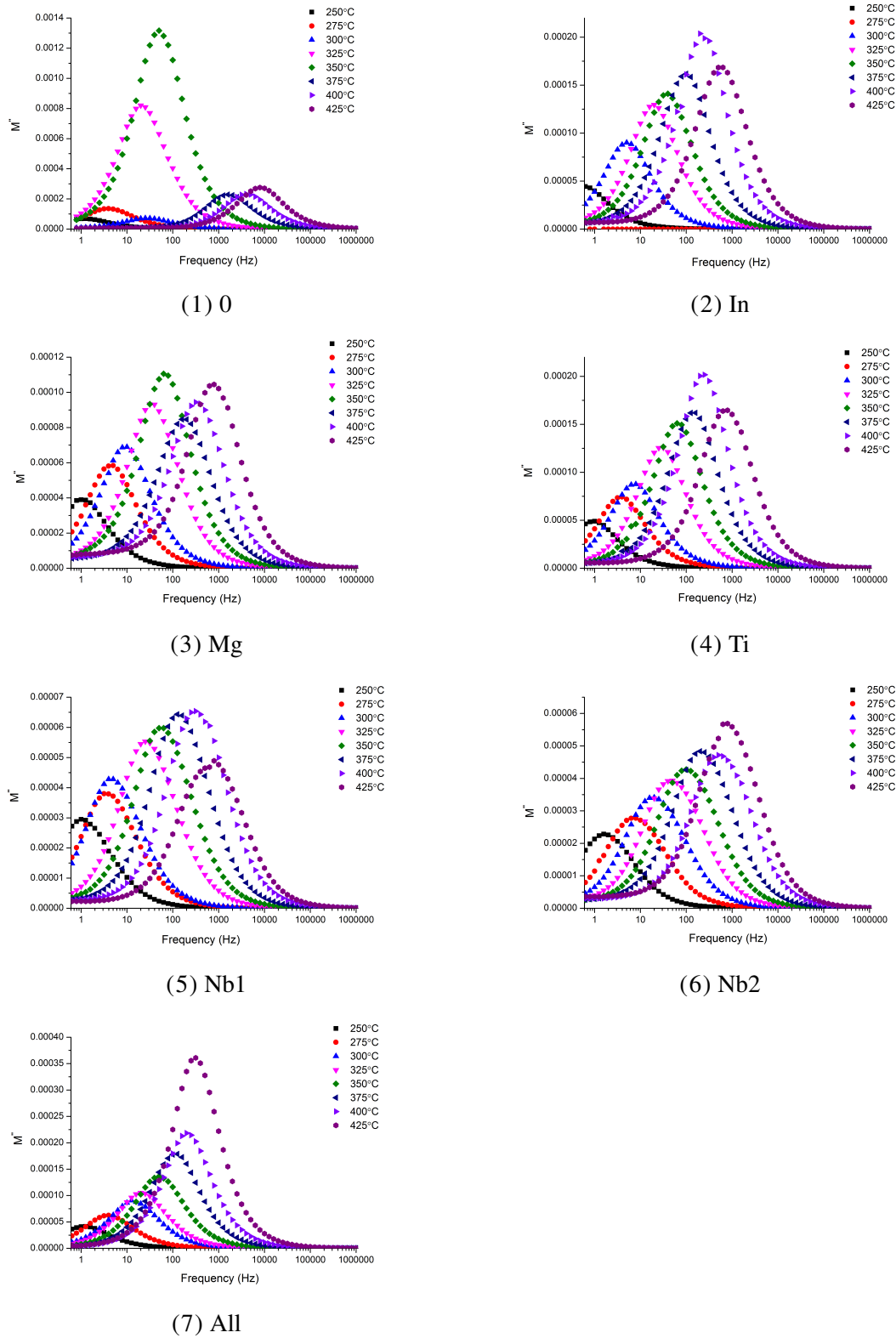


FIGURE 7.25: Modulus versus frequency plots

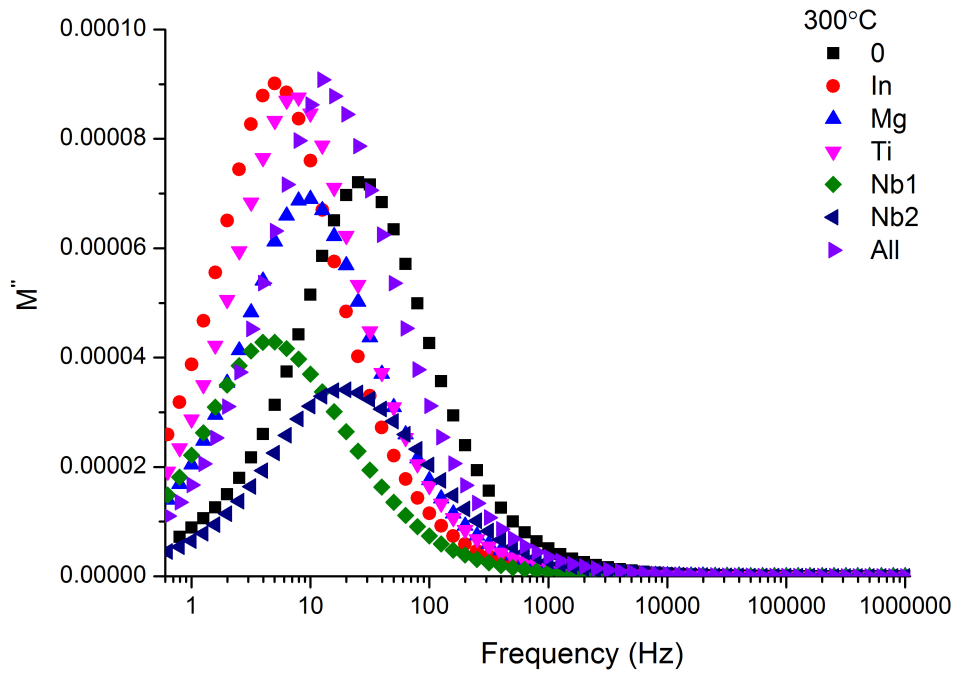


FIGURE 7.26: Imaginary part of the modulus for all samples at 300°C

TABLE 7.5: Capacitance and associated relaxation origin, classification by Irvine, Sinclair and West [146]

Capacitance (F)	Relaxation Origin
10^{-12}	bulk
10^{-11}	minor second phase
$10^{-11} - 10^{-8}$	grain boundary
$10^{-10} - 10^{-9}$	bulk
$10^{-9} - 10^{-7}$	surface layer
$10^{-7} - 10^{-5}$	sample - electrode interface
10^{-4}	electrochemical reaction

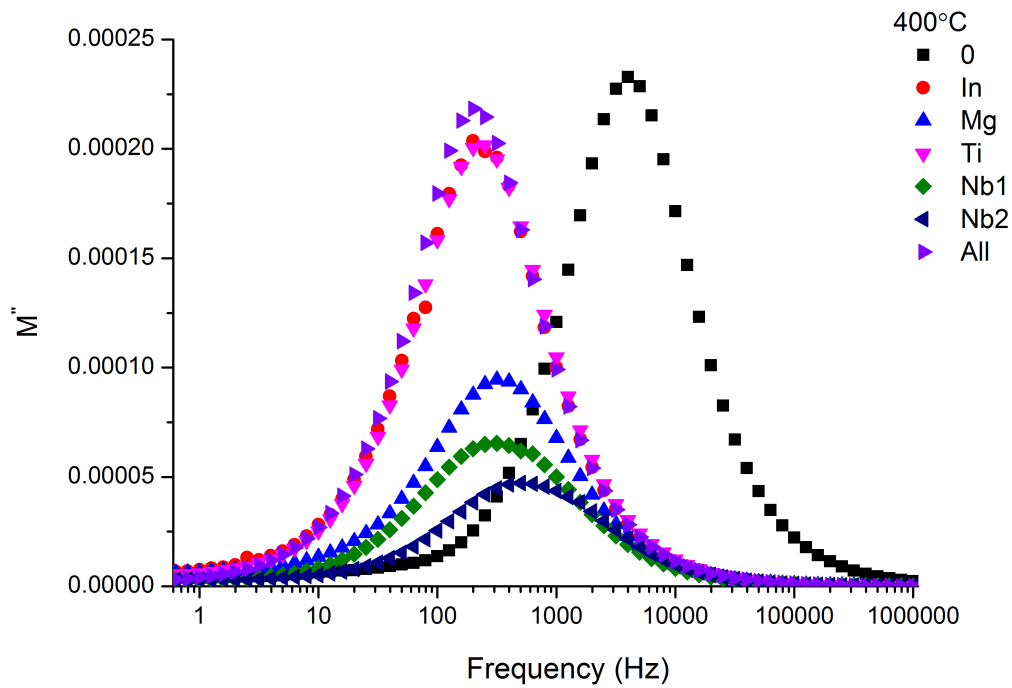


FIGURE 7.27: Imaginary part of the modulus for all samples at 400°C

TABLE 7.6: Pseudocapacitance (F) calculated calculated using the parameters R, Q, n obtained from fitting data with R-CPE_C equivalent circuit

T (°C)	0	In	Mg	Ti	Nb1	Nb2	All
125	5.42×10^{-9}	9.04×10^{-9}	1.10×10^{-8}	1.29×10^{-8}	1.22×10^{-8}	8.20×10^{-9}	1.21×10^{-8}
150	6.49×10^{-9}	1.62×10^{-8}	1.92×10^{-8}	2.79×10^{-8}	1.65×10^{-8}	1.32×10^{-8}	2.77×10^{-8}
175	1.19×10^{-8}	4.61×10^{-8}	3.07×10^{-8}	3.11×10^{-8}	2.43×10^{-8}	2.67×10^{-8}	5.19×10^{-8}
200	1.42×10^{-8}	2.35×10^{-8}	2.07×10^{-8}	1.74×10^{-8}	1.90×10^{-8}	2.46×10^{-8}	2.35×10^{-8}
225	1.24×10^{-8}	1.33×10^{-8}	1.25×10^{-8}	1.11×10^{-8}	1.44×10^{-8}	1.62×10^{-8}	1.22×10^{-8}
250	7.65×10^{-9}	8.39×10^{-9}	8.49×10^{-9}	7.60×10^{-9}	9.26×10^{-9}	1.12×10^{-8}	8.17×10^{-9}
275	5.04×10^{-9}	5.23×10^{-9}	4.95×10^{-9}	4.53×10^{-9}	6.05×10^{-9}	6.54×10^{-9}	5.05×10^{-9}
300	3.76×10^{-9}	3.74×10^{-9}	3.94×10^{-9}	3.63×10^{-9}	5.57×10^{-9}	4.60×10^{-9}	3.16×10^{-9}
325	2.28×10^{-9}	2.41×10^{-9}	2.41×10^{-9}	2.32×10^{-9}	3.15×10^{-9}	3.42×10^{-9}	2.71×10^{-9}
350	1.77×10^{-9}	2.01×10^{-9}	1.98×10^{-9}	1.84×10^{-9}	2.52×10^{-9}	2.71×10^{-9}	2.01×10^{-9}
375	1.36×10^{-9}	1.58×10^{-9}	1.65×10^{-9}	1.52×10^{-9}	2.01×10^{-9}	2.19×10^{-9}	1.55×10^{-9}
400	1.13×10^{-9}	1.29×10^{-9}	1.40×10^{-9}	1.34×10^{-9}	1.65×10^{-9}	1.75×10^{-9}	1.30×10^{-9}
425	9.85×10^{-10}	1.12×10^{-9}	1.15×10^{-9}	1.10×10^{-9}	1.54×10^{-9}	1.60×10^{-9}	1.14×10^{-9}

7.3.5.4 Conductivity

The dc conductivity is investigated within this section. The following formula has been used to calculate the conductivity

$$\sigma = \frac{l}{RA} \quad (7.9)$$

where A and l are the area of the electrodes and the thickness of the sample and R is the resistance of the sample determined from the equivalent circuit fit - Table 7.4. Figure 7.28 shows the conductivity as a function of temperature for all samples. Activation energies have been calculated in regions where the conductivity showed a linear behaviour. Above 175°C, the activation energy for the undoped, 0 sample is $E_a=1.1$ eV. For the doped samples E_a ranges from 0.69 to 0.77 eV.

Below 175°C a well defined change in slope is observed for In, Mg, Ti and All. The calculated E_a for this region is around 0.1 eV. These results together with previous observations provide some support for understanding the behaviour of Mn modified samples, where the following processes are involved.

Oxygen Vacancies Formation The formation of oxygen vacancies is a complex process which depends on three main factors:

- surrounding oxygen partial pressure
- stoichiometry of the sample
- ability of chemical constituents to change their valence state.

Under relatively low oxygen partial pressure during sample preparation (i.e. sintering) oxygen from the sample may be lost to the surrounding atmosphere according to the following reaction:



The neutral defect generated may be progressively ionized as follows:



Therefore, two electrons may be generated this way which can contribute to conduction. This aspect will be discussed later within this section.

Furthermore, oxygen vacancies may be generated upon incorporation of ions with a lower valence state than the ion it replaces. For example a Mn^{2+} replacing a Ti^{4+} in $PbTiO_3$ may generate an oxygen vacancy for charge balance.

Nevertheless, certain ions may also control the oxygen vacancies. Under certain circumstances, for example under high enough oxygen partial pressure during processing, a Mn ion may contribute to the filling of an oxygen vacancy by changing its valence state as follows:

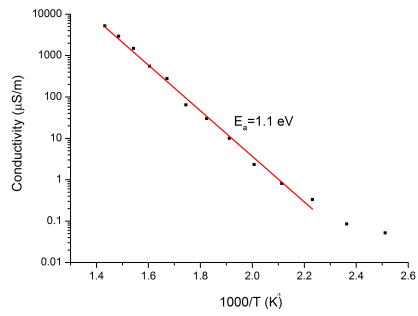


Polaron Hopping Electron hopping also referred to as polaron hopping is a conduction mechanism model for certain oxides and it might be regarded as the equivalent for band conduction in semiconductors [13]. The polaron model is valid when ions sitting on equivalent sites with oxidation states differing by unity exist in the lattice. For example Ti in $PbTiO_3$ has been suggested to act as trapping centres for the electrons generated during oxygen vacancies formation (described in the previous paragraph) according to Equation 7.15, thus providing a polaron hopping mechanism of conductivity described by Equation 7.16.

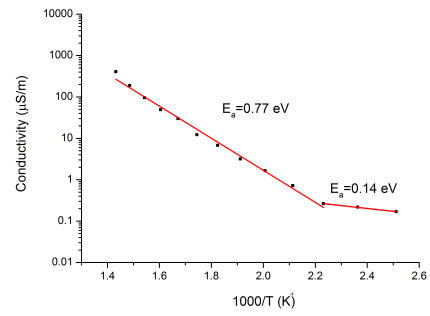


Therefore, a polaron is represented by an ion acting as a *perturbing positive charge* which polarizes the lattice locally. Considering the samples investigated within this work, in addition to Ti, Mn may also act as a polaron, contributing to the hopping conduction mechanism as follows:

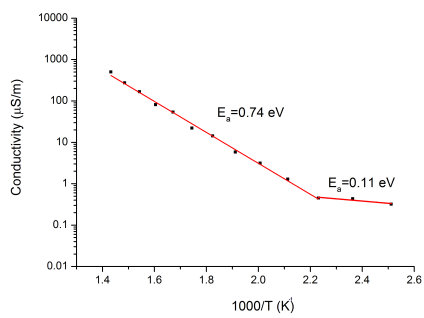




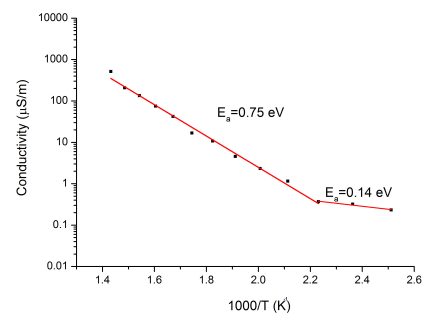
(1) O



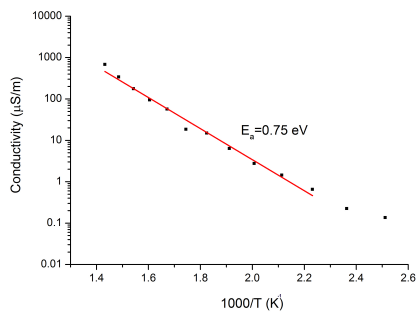
(2) In



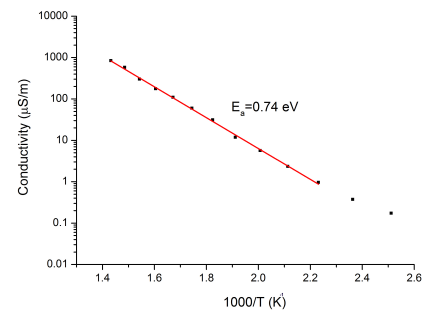
(3) Mg



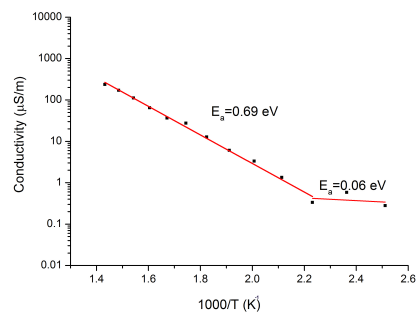
(4) Ti



(5) Nb1



(6) Nb2



(7) All

FIGURE 7.28: Conductivity versus the inverse of temperature and their and their calculated activation energies

Electron exchange has been suggested to also be possible at the Nb and Pb sites although further research is needed for confirmation. Mg and In cannot contribute to this type of conduction mechanism as their valence is fixed, i.e. 2+, 3+.

Ionic Conduction This type of conduction is possible within the investigated samples due to the existence of oxygen vacancies which diffuse through the lattice. This process may be described as follows:



Defect Dipole Formation Electron Paramagnetic Resonance measurements have confirmed the formation of $Mn_{Ti}^{\bullet\bullet} - V_O^{\bullet\bullet}$ defect dipoles [147]. Oxygen vacancies are trapped at the $Mn_{Ti}^{\bullet\bullet}$ reducing the ionic conduction. A question which may arise is: *Why only Mn seems to form defect associates with oxygen vacancies as other negatively charged ions are also present, i.e. $Mg_{Ti}^{\bullet\bullet}$?* The answer might be related to the enthalpy of association. Previously, Mn and Fe doped $SrTiO_3$ has been studied and the authors [148] suggest a higher value for the enthalpy of association in the case of Mn when compared with Fe. Therefore, in the studied compounds, Mn could have a much higher enthalpy of association compared with the other B-site ions. However, more experiments and calculations are needed to validate this explanation.

To summarise this subsection, the conduction in the studied samples is described by a combination of mechanisms which involve oxygen vacancy formation, electronic conduction via polaron hopping and ionic conduction via oxygen vacancy diffusion. It has been previously shown that different conduction mechanisms may coexist, for example electronic-ionic in MgO [72]. The total conductivity will be the sum of conductivities from individual mechanisms, as follows:

$$\sigma_i = \sigma_1 + \sigma_2 + \dots + \sigma_i \quad (7.22)$$

In addition, in terms of charge carrier concentration and mobility, the conductivity has the following expression:

$$\sigma_i = c_i z_i e \mu_i \quad (7.23)$$

where c_i is the concentration, $z_i e$ the particle charge and μ_i the mobility. It can be inferred that the contribution of each conductivity is a function of concentration and

mobility of the charge carriers. At low temperatures, i.e. $<175^\circ$, the conduction mechanism in In, Mg, Ti and AlI seems to be due to electrons (or holes), as suggested by their low activation energy around 0.1eV. This mechanism is probably a result of the ionized oxygen vacancies as well as reduction of Mn during processing. However, above 175°C , E_a is 1.09eV for 0 and around 0.7 for the rest of the samples. The activation energy of oxygen vacancies is around 1eV [149] and therefore ionic conduction via oxygen vacancies seems to be the dominant mechanism for 0. The lower activation energy in the Mn-modified samples could be explained by the presence of mixed electronic-ionic conduction with an increased electronic conduction and a decreased ionic conduction when compared with 0. First, the increased electronic conduction may be explained by the presence of Mn which reduces during processing. Second, the decrease of the ionic contribution to conduction may be explained by the presence of Mn_{Ti}'' which act as trapping centres for oxygen vacancies forming $\text{Mn}_{\text{Ti}}''\text{-V}_\text{O}^{\bullet\bullet}$ defect dipoles [147]. The less obvious change in activation energy for 0, Nb1 and Nb2 could be explained in terms of free oxygen vacancies concentration. 0 lacks Mn_{Ti}'' trapping centres and therefore all oxygen vacancies can contribute to conduction. Nb1 and Nb2 have a lower Nb^{5+} content which could be associated with a lower Mn^{2+} and Mn^{3+} concentration. This could be linked to less Mn_{Ti}'' trapping centres and therefore less trapped oxygen vacancies.

7.3.6 Dielectric measurements versus temperature

The relative permittivity measured in the frequency range 0.1 - 100 kHz is shown in Figure 7.29. At lower frequencies the permittivity is higher as several types of polarisation contribute to the response (i.e. interfacial, ionic, dipolar, electronic, space charges etc.). On the contrary, at higher frequencies the main contribution to the permittivity is electronic, therefore the permittivity decreases. Another observation is that a more pronounced frequency dispersion is observed for Mn-modified samples, as opposed to sample 0.

The temperature of maximum dielectric permittivity at 100 kHz is listed in Table 7.7, however no particular trend is observed. This behaviour is also illustrated in Figure 7.31.

The dissipation factor has been also measured in the frequency range 0.1 - 100 kHz and is shown in Figure 7.30. All Mn modified samples show a strong frequency dependence, as opposed to sample 0. To compare the samples relative to each other, the dissipation factor at 100 kHz has been plotted in Figure 7.32 for all samples. The trend observed may be explained by two dominant mechanisms for losses: domain wall motion and conductivity. Below 100°C losses in the Mn free sample are relatively high due to domain wall movement, whereas Mn modified samples have low losses due to the presence of defect associates between Mn and oxygen vacancies which pin domain wall movement. However, above 100°C, the opposite scenario is observed. With increasing temperature, the polaron hopping conduction mechanism becomes predominant. Losses are increased in Mn modified samples as the presence of Mn provides sites for polaron hopping (see section 7.3.5.4). This behaviour is consistent with the lower activation energies for relaxation observed in Mn modified samples compared with Mn free sample - Figure 7.22 and 7.23 (see Section 7.3.5.2).

TABLE 7.7: Temperature of maximum dielectric permittivity

Sample	0	In	Mg	Ti	Nb1	Nb2	All
Temperature of ϵ_{max} (°C) @100kHz	192	175	170	180	179	191	182

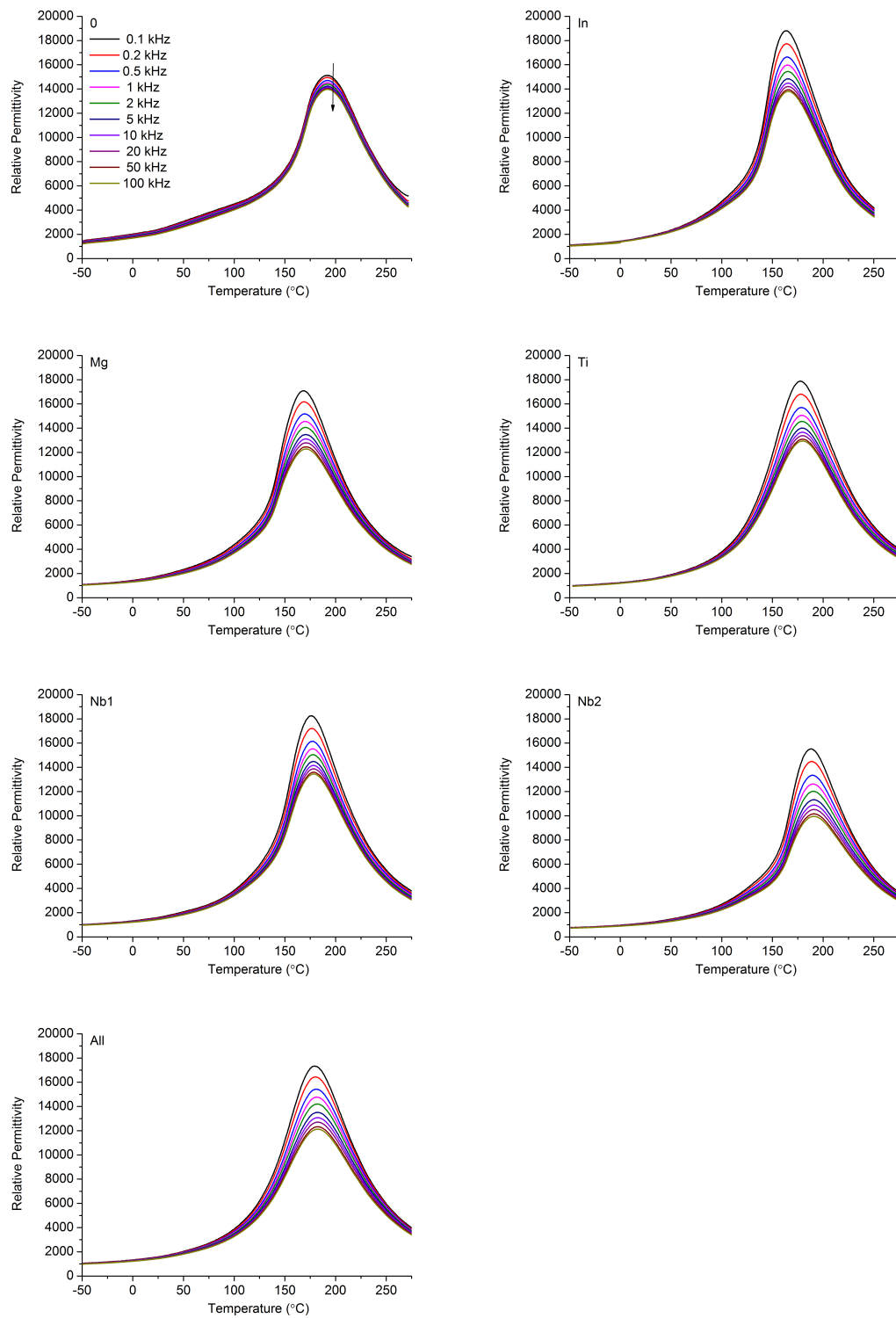


FIGURE 7.29: Relative permittivity measured in the frequency range 0.1 - 100 kHz

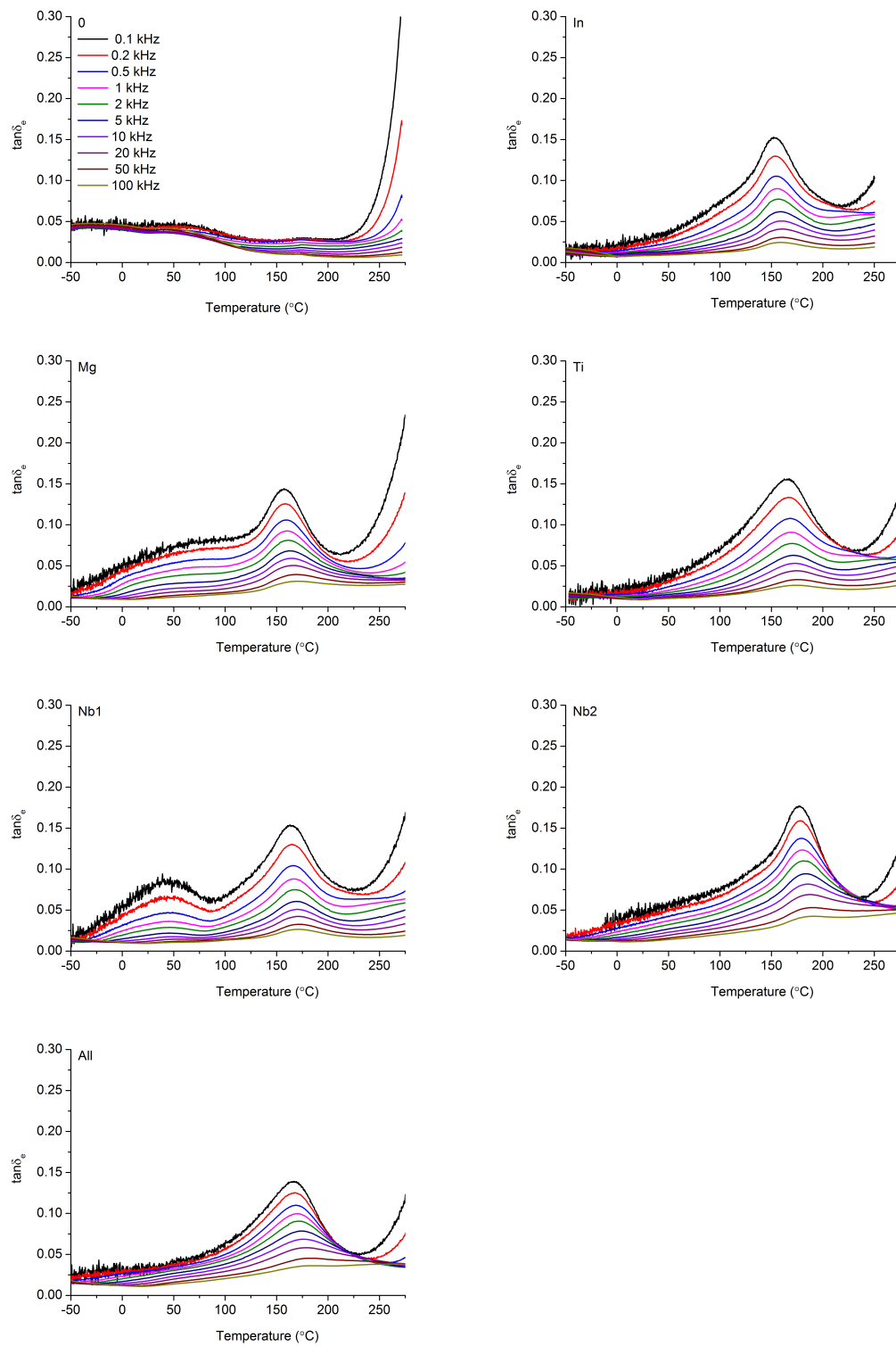


FIGURE 7.30: Dissipation factor measured in the frequency range 0.1 - 100 kHz

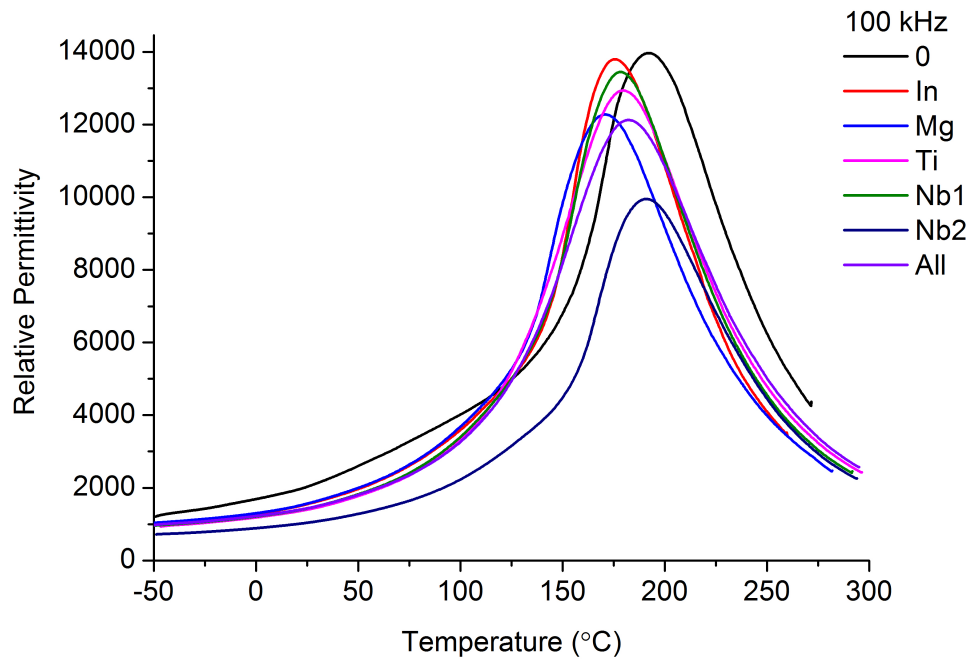


FIGURE 7.31: Relative permittivity measured at 100 kHz for all samples

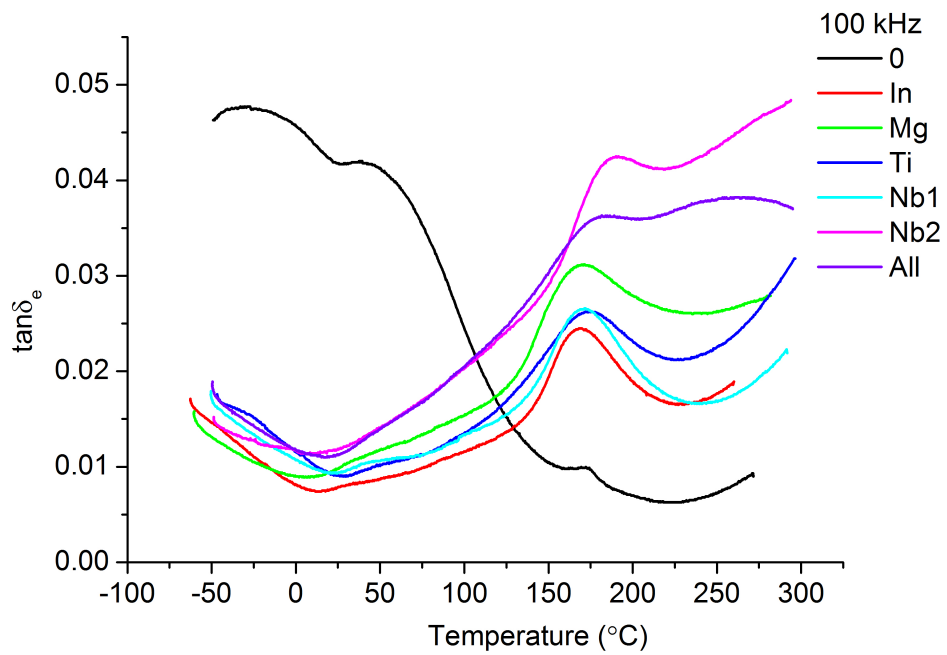


FIGURE 7.32: Dissipation factor measured at 100 kHz for all samples

7.3.7 Mechanical Quality Factor

The values for the mechanical quality factor are shown graphically in Figure 7.33. An attempt has been made at ordering the samples in the direction of decreasing Q_m . As expected, Q_m is minimum for the Mn-free sample, i.e. ≈ 100 . Mn-modified samples show a $Q_m > 800$, except Nb2 which exhibits a value of $Q_m \approx 500$. This may be related with a lower concentration of Mn^{2+} and Mn^{3+} ions in Nb2. The reason for the difference between Nb1 and Nb2 is not well understood, as they are expected to behave similarly due to the theoretically identical composition. The difference might arise as a result of processing.

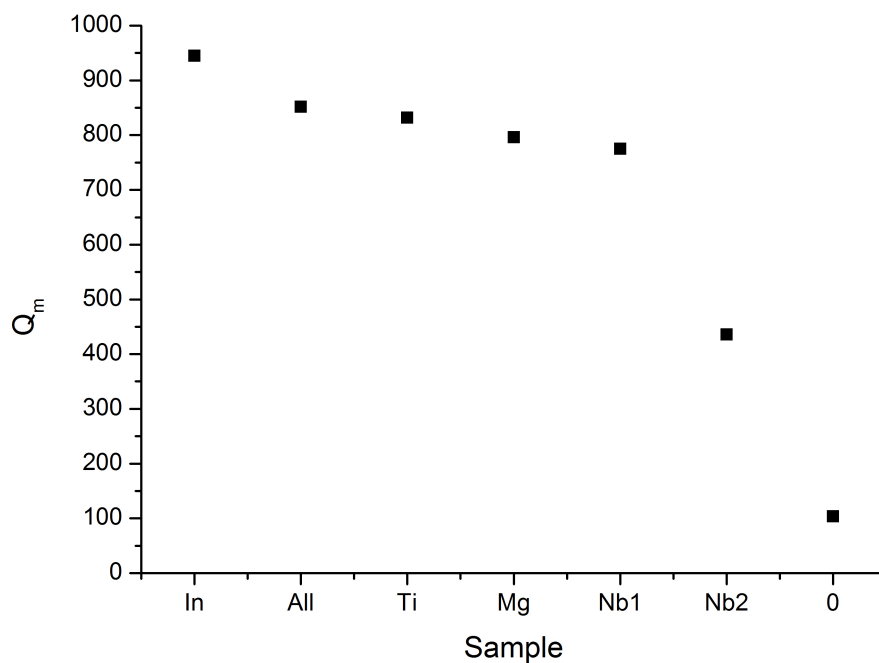


FIGURE 7.33: Mechanical quality factor

7.3.8 Property Comparison

Figure 7.34 shows the relaxation time, mechanical factor, the inverse of real permittivity measured at 0.5 kV/mm, the inverse of dissipation factor measured at room temperature and 100 kHz and the inverse of the conductivity at $\approx 500^\circ\text{C}$ for all samples. The same trend is observed for all quantities plotted and a decrease is observed in the following order: All, In, Ti, Mg, Nb1, Nb2 and 0.

The properties mentioned above have been plotted against mechanical quality factor and are shown in Figure 7.35. A variation of properties as a function of sample composition is observed, but with no clear trend. This variation may be related to the concentration of Mn^{2+} , Mn^{3+} and Mn^{4+} which seems to change from sample to sample. However the concentration change of the other B-site ions must not be omitted which may also contribute to the property variation. Further studies are required for a clear conclusion to be drawn.

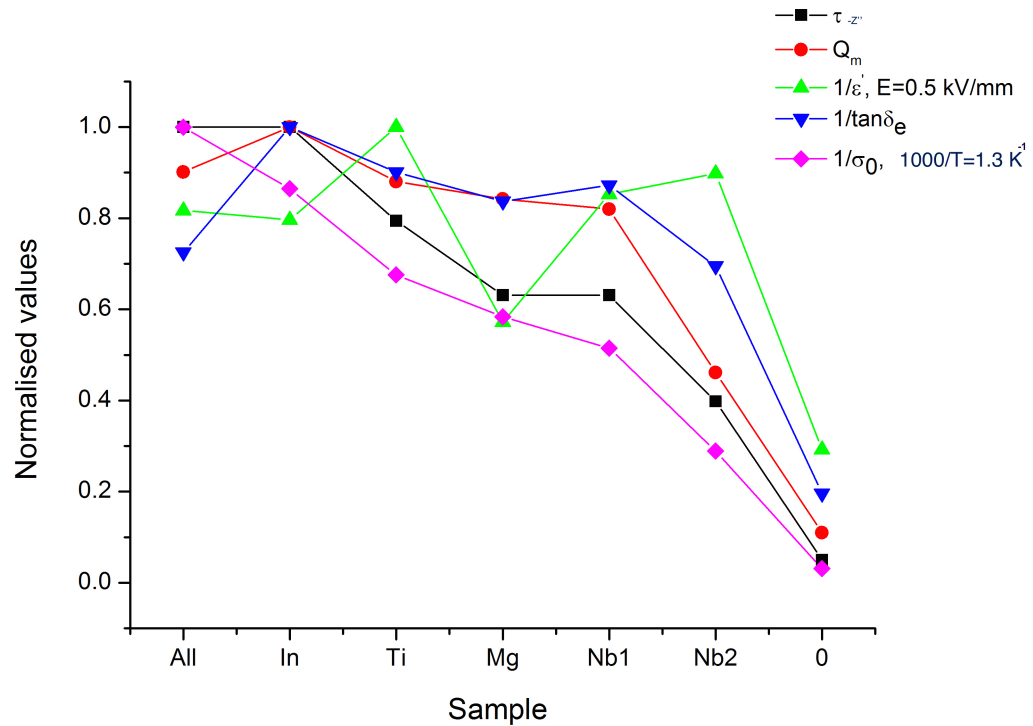


FIGURE 7.34: Normalised property values for investigated samples. The frequency of measurement for $\tan\delta_e$ was 100 kHz. The permittivity has been determined from polarisation - electric field loop using a triangular signal at 1 kHz (see Section 7.2.3.3)

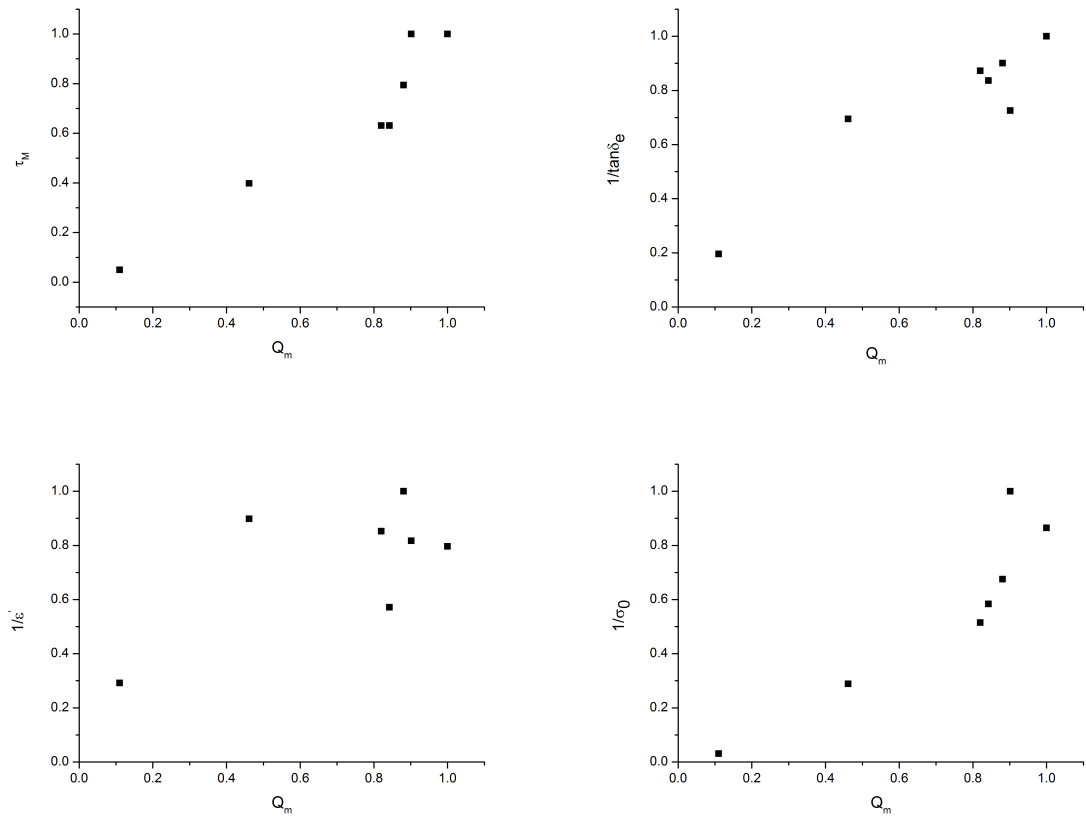


FIGURE 7.35: Properties plotted against mechanical quality factor

7.4 Summary and Conclusions

A summary of the observations made in this study is given in the following lines.

1. X-Ray Absorption Spectroscopy studies revealed an average valence state for Mn of 3.6 in all polycrystalline samples investigated within this study. This result is associated with the presence of Mn^{4+} and some Mn^{3+} and Mn^{2+} .
2. Permittivity versus electric field measurements revealed a decrease in domain wall activity for Mn-modified samples compared with the Mn-free sample.
3. Internal bias field is present in all samples with different values. It is associated with defect dipoles as well as space charges. When Mn-modified samples are compared with each other, the samples where Nb content is lower show an increased internal bias field.

4. Complex impedance measurements revealed a non-ideal behaviour described by an R-CPE equivalent circuit. A distribution of relaxation times is present and the width of the distribution is broader for samples where Nb content is lower, i.e. Nb1 and Nb2. The relaxation arises from the bulk and grain boundaries as found via investigations of the modulus.
5. A combination of conductivity mechanisms is observed: electronic via polaron hopping and ionic via oxygen vacancies diffusion. In Mn-modified samples, the ionic conductivity is decreased due to trapping of $V_O^{\bullet\bullet}$ by $Mn_{Ti}^{''}$ forming defect dipoles and the electronic conductivity is increased due to electrons which arise from Mn reduction during processing.
6. The dependence of permittivity on frequency is more pronounced in Mn modified samples.
7. The dissipation factor is high in the Mn free sample due to domain wall movement and low in the Mn modified samples due to domain wall pinning by defect associates between Mn and oxygen vacancies only below 100°C. Above 100°C losses increase for the Mn modified samples and decrease for the Mn free sample. This behaviour is explained by the electronic conduction which contributes to losses and which becomes important in Mn containing samples where Mn ions act as sites for polaron hopping.
8. The mechanical quality factor is low for the Mn-free sample and increases for the Mn-modified samples. However, a distribution of values is observed which shows that small changes in the concentration of the different ions affects Q_m .

Returning to the question asked in the introductory section of this chapter, i.e. *Is there a change in properties when Mn substitutes one or another chemical at the B-site in solid solutions of complex perovskites?*, it is now possible to conclude that different concentrations of B-site ions indeed seem to affect properties. Behaviour of Mn in PIN-PMN-PT with respect to electromechanical properties changes with changing the composition of PIN-PMN-PT. Compositions where Nb^{5+} content was lower seem to be more affected than compositions where the content of In^{3+} , Mg^{2+} or Ti^{4+} was altered. Lowering Nb^{5+} content may result in an increase in Mn^{3+} and Mn^{4+} at the expense of Mn^{2+} . The difference in Mn oxidation state was not observed in X-ray Spectroscopy studies probably due to the limitations of the technique. Further research is required to validate the findings, provide a deeper understanding of the topic and allow development of new generations of materials with controlled properties.

7.5 Future Work

Given the great interest for Mn-modified materials for use in high power devices, further research is crucial for two main reasons. First, understanding the behaviour of Mn under different circumstances will allow determination of processing conditions required to prepare materials with consistent properties. Consequently, manufacturing of large quantities of material with a narrow distribution of properties will be possible which is critical for commercialisation. Second, a deeper understanding of the mechanisms by which Mn-modification enhances properties such as the mechanical quality factor, will enable design and development of the next generation of materials with tailored properties as required by device engineers. Specifically, the following experiments are recommended as follow up of this work:

1. To clearly separate the influence of different ions on the behaviour of Mn, compositions could be designed as Mn modified PbTiO_3 with sequential additions of In, Mg, Nb, Ti.
2. Another interesting idea would be to replace a fraction of the oxygen atoms with fluorine in PIN-PMN-PT. In Section 7.1.2.4, it has been inferred that dipoles formed between magnesium and fluorine atom could also pin domains and enhance mechanical quality factor.
3. Rayleigh analysis should be applied to the different compositions to gain an insight into intrinsic and extrinsic contributions to losses.
4. High Resolution X-Ray Diffraction could be performed on samples which would give information on the crystallographic phase of samples under investigation. Consequently, lattice parameters could be calculated. Linking the results with calculations of Goldschmidt tolerance factor could give insights into the site occupancy of ions. In addition, these type of experiments would also be beneficial to confirm whether only acceptor dopants of a specific radius size (0.5 - 0.95 Å) can enhance the quality factor, as previously suggested [120].
5. Processing of samples should be performed in oxygen rich and oxygen poor conditions to determine the influence of lower/higher oxygen vacancy concentration on properties of samples with different B-site ion concentrations (as the samples investigated within this study).

6. Further Impedance Spectroscopy studies are also needed. Although the R-CPE has been shown to fit data well and provide a reasonable explanation of the mechanisms leading to such behaviour, other models could be investigated, for example the equivalent circuit based on the Concept of Mismatch and Relaxation model [150]. Such a study could provide a deeper understanding of processes at the atomic level.
7. Despite a more intricate preparation involved, research should be moved onto single crystals rather than polycrystals. In addition to the interest device engineers have in these materials, studying directly single crystals has the advantage of lacking grain boundaries and reduced pore concentration which reduces the effects influencing properties and therefore simplifies data analysis.

Summary and Conclusions

The two aims of the project were (i) to compare Bridgman and Solid State techniques for the growth of relaxor-PbTiO₃ single crystals and (ii) to investigate Mn modifications in relaxor-PbTiO₃ polycrystals, particularly how the complex chemical environment of the relaxor-PbTiO₃, represented by the presence of various ions with various oxidation states, affects the behaviour of Mn with respect to electromechanical properties.

The research conducted and the findings are summarised in the following paragraphs.

- Large and highly dense relaxor-PbTiO₃ single crystals can be obtained from the melt via the Bridgman technique. This work has shown that a single crystal with 20 mm diameter, 60 mm length and 99% density of the theoretical can be readily grown by the self-seeded Bridgman method. The major challenge was growing crystallographically oriented single crystals via seeded Bridgman technique due to secondary nucleation which occurred during growth. It is believed that the cause for secondary nucleation was ineffective heat transfer from the furnace to the platinum crucible which resulted in supercooling. In turn, the ineffective heat transfer is believed to be caused by the geometry of the crucible, i.e. length (particularly length of the seed pocket) and ratio of the seed pocket diameter to the crucible's main body diameter. This work contributes to existing knowledge of Bridgman grown relaxor-PbTiO₃ crystals by providing a critical assessment of the growth parameters (i.e temperature, growth speed, crucible design) and an evaluation of the challenge encountered represented by secondary nucleation. This information is not widely available in the literature and is of particular help to the industrial sector, for example manufacturers of conventional piezoelectric ceramics that may wish to implement Bridgman technology for single crystal growth.
- Solid State Conversion Growth was investigated as a potentially cheaper, alternative technique to Bridgman for single crystal growth. The experiments involved heat treatment of a single crystal seed attached to a polycrystalline bulk sample which theoretically induces conversion of the polycrystal into a single crystal. The results of this research suggest that a thin film of the same composition as

the material to be converted into a single crystal, deposited by Pulsed Laser Deposition onto the crystal seed facilitates bonding to the polycrystal and encourages crystal growth. When the thin film was present, 42 μm single crystal growth was observed after two hours of heat treatment, whereas no crystal growth was observed from a seed with no film deposited. Experimental investigations of crystal growth by the Solid State method where a thin film is used as interlayer between the seed and the polycrystal have not been previously reported. The finding highlights the potential usefulness of the thin film to promote crystal growth. However further studies are required to demonstrate growth of a crystal with practical size (cm range).

- Investigations on $\text{Pb}(\text{In}_{1/2}\text{Nb}_{1/2})\text{O}_3\text{-Pb}(\text{Mg}_{1/3}\text{Nb}_{2/3})\text{O}_3\text{-PbTiO}_3$ polycrystalline samples modified in a stoichiometric manner with 2mol% Mn revealed a complex behaviour of the Mn ion. It has been shown that changes in the ratios of B-site ions (i.e. In^{3+} , Nb^{5+} , Mg^{2+} , Ti^{4+}) have an influence on the Mn valence state which may be stable as Mn^{2+} , Mn^{3+} and/or Mn^{4+} . Varying the content of Nb was found to have the most pronounced influence on the Mn behaviour. Lowering the content of Nb^{5+} seems to increase the content of Mn^{4+} at the expense of Mn^{2+} and/or Mn^{3+} . The increase of Mn^{4+} content leads to an increase of electrical and mechanical losses. These results enhance our understanding of Mn modifications in piezoelectric materials. Currently, Mn modifications are the most efficient way to decrease electrical and mechanical losses in polycrystalline ceramics and multi domain single crystals. Therefore this work is beneficial to industrial manufacturers of piezoelectric materials as well as academic researchers. The overall message is that Mn modifications must be performed with caution because the material's electromechanical properties depend on the Mn valence state which in turn depends on the ratios of surrounding ions. The valence state may be influenced by other factors such as processing conditions which makes the subject of further experiments.

Further work

Single crystals, particularly relaxor-PbTiO₃ are vital for the new generation of acoustic transducers. Therefore, it is important to develop an inexpensive single crystal growth technique able to provide large and homogeneous crystals. Furthermore, Mn modified relaxor-PbTiO₃ are required for high power devices due to their low electrical and mechanical losses and it is therefore recommended to further investigate the behaviour of Mn in these materials and specifically how it can be controlled. Recommendations have been presented at the end of each experimental section, i.e. chapters 5, 6 and 7. Key recommendations are:

1. Seeded-Bridgman experiments should be performed with various dimensions of the Pt crucible to determine a design which does not favour supercooling and hence secondary nucleation.
2. The Bridgman technique is widely acknowledged as expensive due the use of Pt crucibles and to the unpreventable compositional gradient which limits the amount of material with required properties from one crystal. The compositional gradient is caused by Ti segregation during growth, a result of the liquid to solid phase transformation. One way to avoid Ti segregation is to avoid the liquid phase altogether. For example, crystal growth could be performed starting with temperatures right below the melting point ($\approx 10^\circ\text{C}$ or more lower than the melting temperature). As a consequence, lower growth rates (i.e. crucible translation speed) relative to conventional Bridgman need to be employed because the solid to solid transformation is slower than liquid to solid. This approach is similar to the Solid State technique in that it is a solid to solid transformation. However, the growth would be performed from one end to another which is specific to the Bridgman method and which offers boundary migration control.
3. Solid State Conversion experiments need to further explore the approach which involves use of a thin film at the interface between the seed and the polycrystal. Experiments need to be performed for longer periods of time with the aim of growing a cm-sized crystal.
4. Solid State typically involves heat treatment of a bulk polycrystalline material with a crystal seed attached which promotes crystal conversion. At paragraph 2 above it has been suggested to perform solid state conversion from one end

to another of the crucible as in Bridgman technique to control the boundary migration. Another approach would be to convert a polycrystalline material into a single crystal layer by layer, as follows: additive manufacturing could be used to print a layer with thickness in the micrometer range onto a crystal substrate and subsequently heat treat to convert the layer into a single crystal; the process could be repeated until a crystal with practical size is obtained.

5. This thesis has provided insights into the influence of surrounding ions on the behaviour of Mn in relaxor-PbTiO₃. Further research could explore post-processing, such as annealing of samples in reducing and oxidising atmospheres to test the influence on the behaviour of Mn. This approach might be used to stabilise the valence state of Mn which would allow tuning of the electromechanical properties.

Appendix A

Pole figures technique

When a crystalline sample is irradiated with X-rays, crystal planes diffract the X-ray beam according to Bragg's law:

$$n\lambda = 2d\sin\theta \quad (\text{A.1})$$

where n is an integer, λ the wavelength of the X-ray, d the spacing between crystal planes and θ the angle between the incident beam and the crystal plane. Knowing the specific angles θ at which a crystalline sample diffracts X-rays (can be determined by Powder X-Ray Diffraction), allows investigation of the orientation of a single crystal or the degree of preferred orientation. The technique uses the Schultz geometry schematically shown in Figure A.1. In this geometry, the X-ray source and detector are fixed at the θ angle associated with the desired plane, whilst the sample is rotated 360° around the normal direction to the sample (β) and tilted 90° from the normal direction to the sample (α). The intensity varies as the position of the sample is varied. Points where high X-ray intensities are acquired are termed *poles*. The poles are represented on a stereographic projection - Figure A.2, referred to as *pole figure* - Figure A.3. A pole figure illustrates the statistical angular distribution of the investigated crystallographic plane within the irradiated area. The presence of well defined poles at specific angles is associated with a single crystal. Typical pole figures for the (111), (100) and (110) planes in a cubic single crystal sample are shown in Figure A.4.

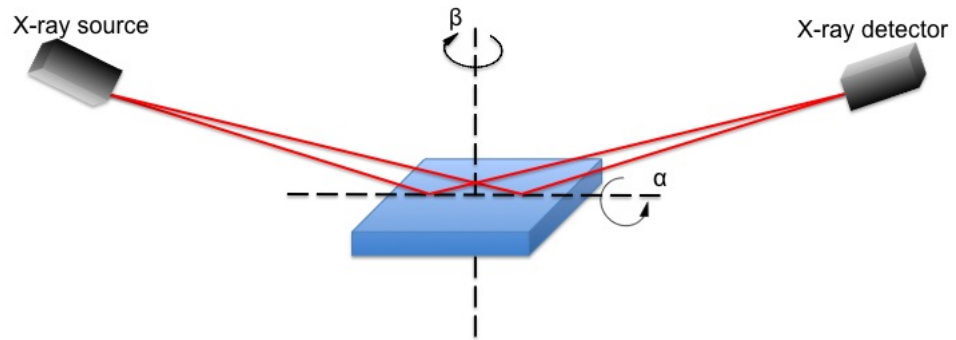


FIGURE A.1: Schultz geometry used to investigate orientation of single crystals or the degree of preferred orientation in textured crystalline samples. The X-ray beam is fixed at θ angle (red), whilst the sample is rotated 360 about the normal to the sample surface (β) and tilted 90 from the normal to the sample surface (α). Adapted from [104].

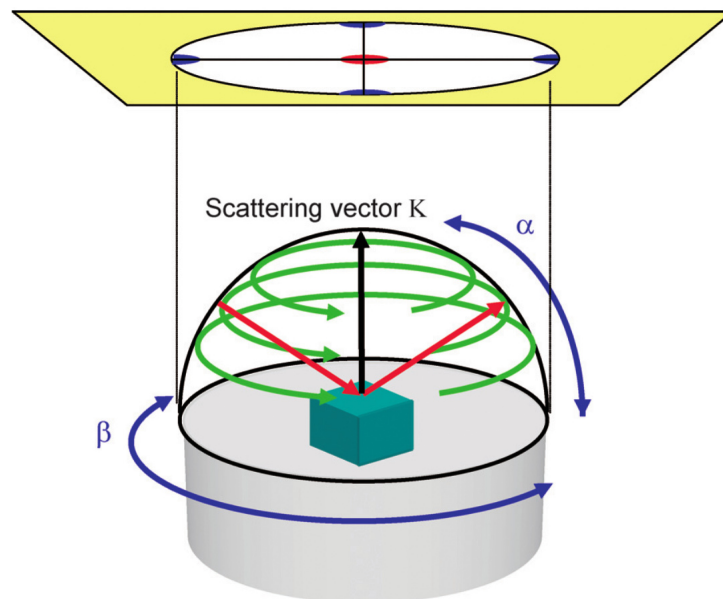


FIGURE A.2: Representation of the sample movement by varying α and β angles during investigation. The red arrows represent the fixed X-ray beam. The variation of diffracted X-rays intensity is represented on a stereographic projection [104].

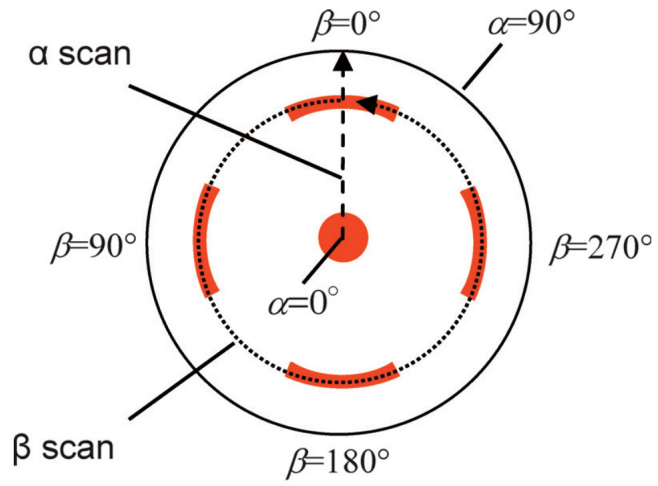


FIGURE A.3: The α and β angles on a pole figure [104].

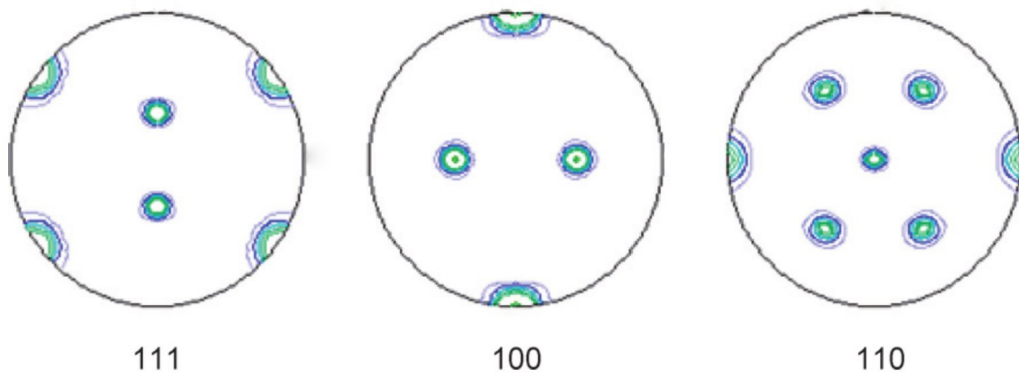
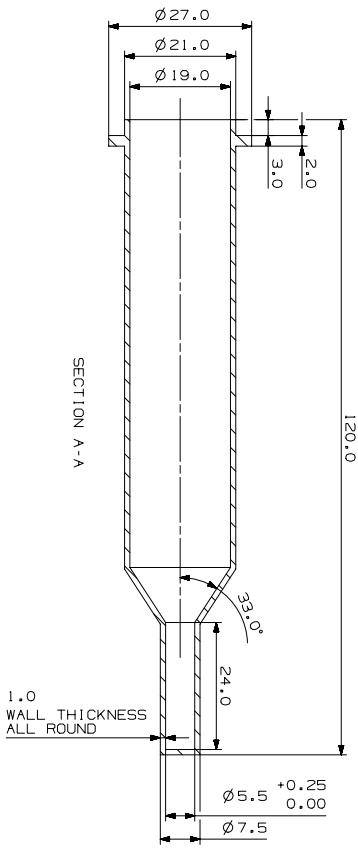
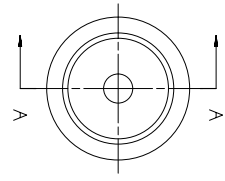


FIGURE A.4: Typical pole figures of a cubic single crystal sample for the (111), (100) and (110) crystallographic planes [104].

Appendix B

Design of Platinum Crucibles for Seeded Growth

Detailed drawings of the crucible used for seeded growth are presented in the following pages (courtesy of Robert Simpson).



DRG	SHT	NO.	1
ISSUE	NO.	1	1
DATE	1/1/2013		
3RD ANGLE PROJECTION			
ORIGINAL SCALE	DIMENSIONS IN	ESTIMATED MASS	TOLERANCES
NX CAD	2 : 1 1 : 1	MM 0.163Kg	± 0.25 U.O.S.
DEPARTMENT	TYPE	CHECKED	CERTIFIED
LMR	PROTOTYPE		
DRAWN BY	PROTOTYPE		
R. SIMPSON	FOR PARTS		
ORIGINAL DATE	PRODUCTION		
08-10-13	L. STOLICA		

REMOVE ALL SHARP EDGES AND CORNERS. TOLERANCES ON MACHINED DIMENSIONS AS FOLLOWS: 0.500 ±0.2 0.500-1000 ±0.4 UNLESS OTHERWISE STATED.

MACHINE SURFACES TO BE 3.2 OR BETTER. TOLERANCES ON MACHINED DIMENSIONS AS FOLLOWS: 0.500 ±0.2 0.500-1000 ±0.4 UNLESS OTHERWISE STATED.

DRAWN IN ACCORDANCE WITH UNIVERSITY OF LEEDS ENGINEERING PROCEDURES & CODES OF PRACTICE.

UNPUBLISHED. UNIVERSITY OF LEEDS. FOR RESEARCH PURPOSES ONLY. ALL RIGHTS RESERVED. DISCLOSED OR REPRODUCTION WITHOUT PERMISSION OF THE UNIVERSITY OF LEEDS.

UNIVERSITY OF LEEDS

© UNIVERSITY OF LEEDS 2013

PLATINUM CRUCIBLE MK-2

DRAWING NUMBER LUE0000232

SHEET No. 1 of 1

SHEET SIZE A2

Appendix C

Archimedes' principle for determining sample density

The principle of Archimedes states that an object immersed in water is lighter and the weight loss equals the weight of the liquid displaced. Therefore, the density of a sample may be determined as follows:

1. Determine m_1 , the dry weight of the sample.
2. Immerse sample in distilled water and record m_2 , the weight of the sample suspended in water.
3. The volume of the liquid displaced equals the weight loss of the object divided by the liquid's density:

$$V_{displaced\ water} = \frac{m_1 - m_2}{\rho_{water}} \quad (C.1)$$

4. The volume of the sample is:

$$V_{sample} = \frac{m_1}{\rho_{sample}} \quad (C.2)$$

5. The volume of the liquid displaced equals the volume of the sample:

$$\frac{m_1 - m_2}{\rho_{water}} = \frac{m_1}{\rho_{sample}} \quad (C.3)$$

6. The density of the sample may be calculated:

$$\rho_{sample} = \frac{m_1}{m_1 - m_2} * \rho_{water} \quad (C.4)$$

To ensure accurate value of the water density is used, the temperature of the water is recorded regularly during measurements. In addition, if air bubbles form on the surface of the samples when immersed in water, a drop of washing up liquid is used to reduce the surface tension. The set up for Archimedes density measurements is illustrated in Figure C.1.

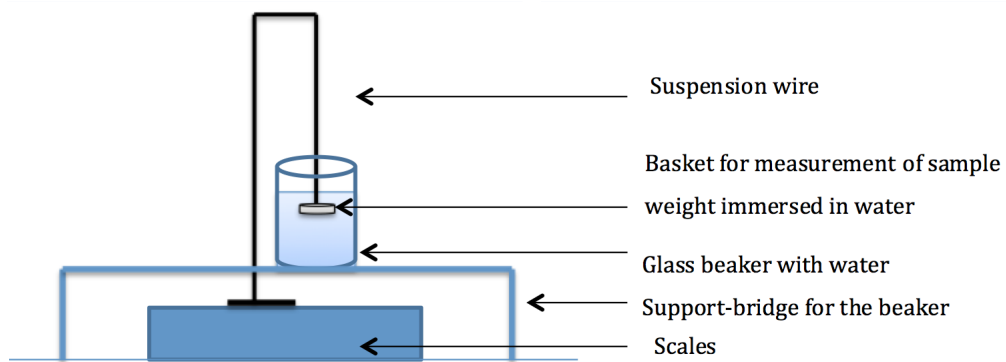


FIGURE C.1: Schematic diagram of the set-up used to determine the weight of samples immersed in water to subsequently determine the density using Archimedes' principle

Appendix D

Conferences and other activities

Conferences

1. Ferroelectrics UK 2013, Sheffield, United Kingdom
2. International Symposium on the Applications of Ferroelectrics, July 2013, Prague, Czech Republic
3. Showcase 2013 – The 4th Annual University of Leeds Postgraduate Research Conference
Poster - A smart material hidden all around us: What is it? Why research it?
4. International Symposium on the Applications of Ferroelectrics, May 2014, State College, PA, USA
Poster - Investigation of the Microstructure in $\text{Pb}(\text{In}_{1/2}\text{Nb}_{1/2})\text{O}_3\text{-Pb}(\text{Mg}_{1/3}\text{Nb}_{2/3})\text{O}_3\text{-PbTiO}_3$
5. Crystallization Centre Annual Meeting, September 2014, The University of Leeds, UK
Oral presentation - Piezoelectric single crystals
6. International Symposium on the Applications of Ferroelectrics, May 2015, Singapore, Singapore
Richardson Travel Bursary Recipient, <http://www.soci.org/news/awards/richardson/laura-stoica>
Oral presentation - Grain Growth and Crystal Growth Investigations in PIN-PMN-PT

7. Visit, University of New South Wales, October 2015

Seminar talk - Growth of piezoelectric single crystals

8. International workshop on acoustic transduction materials and devices, May 2016, State College, PA, USA

Oral presentation - Advances in Understanding Variation of Properties by Mn modification in PIN-PMN-PT

Poster, 3rd place in poster competition - Mn modifications in PIN-PMN-PT: How are electromechanical properties affected?

9. International Symposium on the Applications of Ferroelectrics, August 2016, Darmstadt, Germany

Oral presentation - Substitution of B-site ions with Mn in PIN-PMN-PT: Influence on properties

Poster - Substitution of B-site ions with Mn in PIN-PMN-PT: Influence on properties

Competition

- Materials Science and Technology Literature Review Prize 2014, The Institute of Materials, Minerals and Mining and Maney Publishing
Review paper (finalist) - Piezoelectric PbTiO₃-based single crystals: methods of growth

Industrial experience

- Industrial placement at Thales Australia, August - October 2015, Rydalmere, Australia

University visit

- Visiting PhD researcher at The University of New South Wales, Australia, September - October 2015, Sydney, Australia

Bibliography

- [1] Piezoelectric ceramics: Principles and applications. *APC International Ltd*, 2006.
- [2] Shujun Zhang and Fei Li. High performance ferroelectric relaxor-PbTiO₃ single crystals: Status and perspective. *Journal of Applied Physics*, 111(3), 2012.
- [3] Zuo-Guang Ye. *Handbook of advanced dielectric, piezoelectric and ferroelectric materials: Synthesis, properties and applications*. Elsevier, 2008.
- [4] L. Ewart. Piezocrystal applications and Gen II material properties. In *International Symposium on Piezocrystals and their Applications, London, UK, July 2015*, 2015.
- [5] Jie Chen and Rajesh Panda. Review: Commercialization of piezoelectric single crystals for medical imaging applications. In *IEEE Ultrasonics Symposium, 2005.*, volume 1, pages 235–240. IEEE, 2005.
- [6] Shujun Zhang, Fei Li, Xiaoning Jiang, Jinwook Kim, Jun Luo, and Xuecang Geng. Advantages and challenges of relaxor-PbTiO₃ ferroelectric crystals for electroacoustic transducers - A review. *Progress in materials science*, 68:1–66, 2015.
- [7] E Pluribus Anthony. Blankmap-world, 2016. URL <https://commons.wikimedia.org/wiki/File:BlankMap-World-noborders.png>.
- [8] Walter Guyton Cady. *Piezoelectricity: An introduction to the theory and application of electromechanical phenomena in crystals*. McGraw-Hill, 1946.
- [9] B. Jaffe, W. R. Cook Jr., and H. Jaffe. *Piezoelectric ceramics*, volume 3. Academic Press London and New York, 1971.
- [10] Jan Holterman and Pim Groen. *An introduction to piezoelectric materials and components*. Stichting Applied Piezo, 2012.

- [11] Nicole A Benedek and Craig J Fennie. Why are there so few perovskite ferroelectrics? *The Journal of Physical Chemistry C*, 117(26):13339–13349, 2013.
- [12] Christopher Hammond and Christopher Hammond. *The basics of crystallography and diffraction*. Oxford University Press Oxford, 2009.
- [13] Anthony J Moulson and John M Herbert. *Electroceramics: materials, properties, applications*. John Wiley & Sons, 2003.
- [14] Victor Moritz Goldschmidt. Die gesetze der krystallochemie. *Naturwissenschaften*, 14(21):477–485, 1926.
- [15] Fei Li, Linghang Wang, Li Jin, Dabin Lin, Jinglei Li, Zhenrong Li, Zhuo Xu, and Shujun Zhang. Piezoelectric activity in perovskite ferroelectric crystals. *Ultrasonics, Ferroelectrics, and Frequency Control, IEEE Transactions on*, 62(1):18–32, 2015.
- [16] John Frederick Nye. *Physical properties of crystals: their representation by tensors and matrices*. Oxford university press, 1985.
- [17] H Jaffe and DA Berlincourt. Piezoelectric transducer materials. *Proceedings of the IEEE*, 53(10):1372–1386, 1965.
- [18] August Chełkowski. *Dielectric physics*, volume 9. Elsevier Science & Technology, 1980.
- [19] Peter John Harrop. *Dielectrics*. John Wiley & Sons, 1972.
- [20] AF Devonshire. Theory of ferroelectrics. *Advances in physics*, 3(10):85–130, 1954.
- [21] Antonio Arnau et al. *Piezoelectric transducers and applications*, volume 2004. Springer, 2004.
- [22] John L Butler and Charles H Sherman. Transducers and arrays for underwater sound. *Modern acoustics and signal processing* (, 2016.
- [23] Z-G Ye, B Noheda, M Dong, D Cox, and G Shirane. Monoclinic phase in the relaxor-based piezoelectric/ferroelectric $\text{Pb}(\text{Mg}_{1/3}\text{Nb}_{2/3})\text{O}_3\text{-PbTiO}_3$ system. *Physical review B*, 64(18):184114, 2001.
- [24] B Noheda. Structure and high-piezoelectricity in lead oxide solid solutions. *Current Opinion in Solid State and Materials Science*, 6(1):27–34, 2002.

- [25] Dawei Wang, Maosheng Cao, and Shujun Zhang. Phase diagram and properties of $\text{Pb}(\text{In}_{1/2}\text{Nb}_{1/2})\text{O}_3$ - $\text{Pb}(\text{Mg}_{1/3}\text{Nb}_{2/3})\text{O}_3$ - PbTiO_3 polycrystalline ceramics. *Journal of the European Ceramic Society*, 32(2):433–439, 2012.
- [26] Fei Li, Shujun Zhang, Zhuo Xu, Xiaoyong Wei, Jun Luo, and Thomas R Shrout. Piezoelectric activity of relaxor- PbTiO_3 based single crystals and polycrystalline ceramics at cryogenic temperatures: Intrinsic and extrinsic contributions. *Applied physics letters*, 96(19):192903, 2010.
- [27] Ahmad Safari and E Koray Akdogan. *Piezoelectric and acoustic materials for transducer applications*. Springer Science & Business Media, 2008.
- [28] L Eric Cross. Relaxor ferroelectrics: an overview. *Ferroelectrics*, 151(1):305–320, 1994.
- [29] RA Cowley, SN Gvasaliya, SG Lushnikov, B Roessli, and GM Rotaru. Relaxing with relaxors: a review of relaxor ferroelectrics. *Advances in Physics*, 60(2):229–327, 2011.
- [30] G. S. Smolensky and A. Agronovskaya. *Soviet Physics Solid State*, 1:1429, 1960.
- [31] Desheng Fu, Hiroki Taniguchi, Mitsuru Itoh, and Shigeo Mori. $\text{Pb}(\text{Mg}_{1/3}\text{Nb}_{2/3})\text{O}_3$ (PMN) Relaxor: Dipole Glass or Nano-Domain Ferroelectric? *arXiv preprint arXiv:1301.3615*, 2013.
- [32] K. Carl and K. H. Hardtl. Electrical after-effects in $\text{Pb}(\text{Ti,Zr})\text{O}_3$ ceramics. *Ferroelectrics*, 17(1):473–486, 1977. doi: 10.1080/00150197808236770. URL <http://dx.doi.org/10.1080/00150197808236770>.
- [33] Dragan Damjanovic. A morphotropic phase boundary system based on polarization rotation and polarization extension. *Applied Physics Letters*, 97(6):062906, 2010.
- [34] Etsuro Sawaguchi. Ferroelectricity versus antiferroelectricity in the solid solutions of PbZrO_3 and PbTiO_3 . *Journal of the Physical Society of Japan*, 8(5):615–629, 1953. doi: 10.1143/JPSJ.8.615. URL <http://dx.doi.org/10.1143/JPSJ.8.615>.
- [35] B Jaffe, RS Roth, and S Marzullo. Piezoelectric properties of lead zirconate-lead titanate solid-solution ceramics. *Journal of Applied Physics*, 25(6):809–810, 1954.

- [36] R Clarke, RW Whatmore, and AM Glazer. Growth and characterization of pbzrxti1-xo3 single crystals. *Ferroelectrics*, 13(1):497–500, 1976.
- [37] Jun Kuwata, Kenji Uchino, and Shoichiro Nomura. Phase transitions in the $\text{pb(zn1/3nb2/3)o3-pbtio3}$ system. *Ferroelectrics*, 37(1):579–582, 1981.
- [38] S Park and Thomas R Shrout. Ultrahigh strain and piezoelectric behavior in relaxor based ferroelectric single crystals. *Journal of Applied Physics*, 82(4), 1997.
- [39] Richard E Eitel. Novel piezoelectric ceramics: Development of high temperature, high performance piezoelectrics on the basis of structure, PhD thesis, Dept. of Material Science, The Pennsylvania State University, 2013.
- [40] Marc Lethiecq, Franck Levassort, Dominique Certon, and Louis Pascal Tran-Huu-Hue. Piezoelectric transducer design for medical diagnosis and NDE. In *Piezoelectric and Acoustic Materials for Transducer Applications*, pages 191–215. Springer, 2008.
- [41] James F Tressler. Piezoelectric transducer designs for sonar applications. In *Piezoelectric and Acoustic Materials for Transducer Applications*, pages 217–239. Springer, 2008.
- [42] Shujun Zhang, Fei Li, Xiaoning Jiang, Jinwook Kim, Jun Luo, and Xuecang Geng. Advantages and challenges of relaxor- PbTiO_3 ferroelectric crystals for electroacoustic transducers – A review. *Progress in Materials Science*, 68:1–66, 2015.
- [43] Enwei Sun and Wenwu Cao. Relaxor-based ferroelectric single crystals: Growth, domain engineering, characterization and applications. *Progress in Materials Science*, 65:124–210, 2014.
- [44] M Ueltzen. The Verneuil flame fusion process: substances. *Journal of crystal growth*, 132(1-2):315–328, 1993.
- [45] Wt Zulehner. Czochralski growth of silicon. *Journal of Crystal Growth*, 65 (1-3):189–213, 1983.
- [46] WA Bonner and LG Van Uitert. Growth of single crystals of $\text{Pb}_3\text{MgNb}_2\text{O}_9$ by the Kyropoulos technique. *Materials Research Bulletin*, 2(1):131–134, 1967.

- [47] C Barry Carter and M Grant Norton. *Ceramic materials: science and engineering*. Springer Science & Business Media, 2007.
- [48] N Maffei and GA Rossetti. Float-zone growth and properties of ferroelectric lead titanate. *Journal of materials research*, 19(03):827–833, 2004.
- [49] Young-Sung Yoo, Myung-Koo Kang, Joo-Hwan Han, Hwan Kim, and Doh-Yeon Kim. Fabrication of BaTiO₃ single crystals by using the exaggerated grain growth method. *Journal of the European Ceramic Society*, 17(14):1725–1727, 1997.
- [50] Thomas Richter, Carsten Schuh, Ender Suvaci, and Ralf Moos. Single crystal growth in PMN-PT and PMN-PZT. *Journal of materials science*, 44(7):1757–1763, 2009.
- [51] Huiqing Fan, Lili Zhao, Bin Tang, Changsheng Tian, and Hyoun-Ee Kim. Growth and characterization of PMNT relaxor-based ferroelectric single crystals by flux method. *Materials Science and Engineering: B*, 99(1):183–186, 2003.
- [52] C Elissalde, F Weill, and J Ravez. Correlation between dielectric properties and nanostructure in a Pb(In_{1/2}Nb_{1/2})O₃ ceramic. *Materials Science and Engineering: B*, 25(1):85–91, 1994.
- [53] Timothy Laurence Burnett. *Growth and characterisation of bismuth ferrite lead titanate single crystals*. PhD thesis, Leeds, 2008.
- [54] Z-G Ye. Crystal chemistry and domain structure of relaxor piezocrystals. *Current Opinion in Solid State and Materials Science*, 6(1):35–44, 2002.
- [55] W Chen and Z-G Ye. Top-cooling-solution-growth and characterization of piezoelectric 0.955Pb(Zn_{1/3}Nb_{2/3})O₃-0.045PbTiO₃ [PZNT] single crystals. *Journal of materials science*, 36(18):4393–4399, 2001.
- [56] Thomas R Shrout, Zung P Chang, Namchul Kim, and Steven Markgraf. Dielectric behavior of single crystals near the (1-x)Pb(Mg_{1/3}Nb_{2/3})O₃-(x)PbTiO₃ morphotropic phase boundary. *Ferroelectrics Letters Section*, 12(3):63–69, 1990.
- [57] Naohiko Yasuda, Hidehiro Ohwa, Motoyuki Kume, and Yohachi Yamashita. Piezoelectric properties of a high Curie temperature Pb(In_{1/2}Nb_{1/2})O₃-PbTiO₃

- binary system single crystal near a morphotropic phase boundary. *Japanese Journal of Applied Physics*, 39(2A):L66, 2000.
- [58] Xiuzhi Li, Zujian Wang, Chao He, Xifa Long, and Zuo-Guang Ye. Growth and piezo-/ferroelectric properties of PIN-PMN-PT single crystals. *Journal of Applied Physics*, 111(3):034105, 2012.
- [59] Tao Li, Hamel Taylor, Xiuzhi Li, Zujian Wang, Ying Liu, Chao He, Tao Chu, Liaodong Ai, Dongfang Pang, and Xifa Long. Top-Seeded Solution Growth and properties of high T_C $\text{Pb}(\text{In}_{1/2}\text{Nb}_{1/2})\text{O}_3$ - $\text{Pb}(\text{Zn}_{1/3}\text{Nb}_{2/3})\text{O}_3$ - PbTiO_3 single crystals. *Science of Advanced Materials*, 5(9):1271–1274, 2013.
- [60] Tsuyoshi Kobayashi, Senji Shimanuki, Shiroh Saitoh, and Yohachi Yamashita. Improved growth of large lead zinc niobate titanate piezoelectric single crystals for medical ultrasonic transducers. *Japanese journal of applied physics*, 36(9S):6035, 1997.
- [61] Percy W Bridgman. Certain physical properties of single crystals of tungsten, antimony, bismuth, tellurium, cadmium, zinc, and tin. In *Proceedings of the American academy of arts and sciences*, volume 60, pages 305–383. JSTOR, 1925.
- [62] Donald C Stockbarger. The production of large single crystals of lithium fluoride. *Review of Scientific Instruments*, 7(3):133–136, 1936.
- [63] Long Li, Xiaobing Li, Xiangyong Zhao, Bo Ren, Qing Xu, Haiqing Xu, Haosu Luo, Xin Li, and Xiumei Shao. Enhanced dielectric, pyroelectric and ferroelectric properties of Mn-doped $0.15\text{Pb}(\text{In}_{1/2}\text{Nb}_{1/2})\text{O}_3$ - $0.55\text{Pb}(\text{Mg}_{1/3}\text{Nb}_{2/3})\text{O}_3$ - 0.30PbTiO_3 single crystals. *Journal of Alloys and Compounds*, 595:120–124, 2014.
- [64] Jian Tian, Pengdi Han, Xinling Huang, Huixin Pan, James F Carroll, and David A Payne. Improved stability for piezoelectric crystals grown in the lead indium niobate-lead magnesium niobate-lead titanate system. *Applied physics letters*, 91(22):2903, 2007.
- [65] Hongbing Chen, Zhe Liang, Laihui Luo, Yiyang Ke, Qi Shen, Zongren Xia, Chengyong Jiang, and Jianguo Pan. Bridgman growth, crystallographic characterization and electrical properties of relaxor-based ferroelectric single crystal PIMNT. *Journal of Alloys and Compounds*, 518:63–67, 2012.

- [66] Xian Wang, Haiwu Zhang, Di Lin, Sheng Wang, Xiangyong Zhao, Jianwei Chen, Hao Deng, Xiaobing Li, Haiqing Xu, and Haosu Luo. An effective growth method to improve the homogeneity of relaxor ferroelectric single crystal $\text{Pb}(\text{In}_{1/2}\text{Nb}_{1/2})\text{O}_3\text{-Pb}(\text{Mg}_{1/3}\text{Nb}_{2/3})\text{O}_3\text{-PbTiO}_3$. *Crystal Research and Technology*, 49(2-3):122–128, 2014.
- [67] Kevin T Zawilski, M Claudia C Custodio, Robert C DeMattei, Sang-Goo Lee, Ralph G Monteiro, Hiroyuki Odagawa, and Robert S Feigelson. Segregation during the vertical Bridgman growth of lead magnesium niobate–lead titanate single crystals. *Journal of crystal growth*, 258(3):353–367, 2003.
- [68] Shujun Zhang, Fei Li, Nevin P Sherlock, Jun Luo, Hyeong Jae Lee, Ru Xia, Richard J Meyer, Wesley Hackenberger, and Thomas R Shrout. Recent developments on high Curie temperature PIN–PMN–PT ferroelectric crystals. *Journal of crystal growth*, 318(1):846–850, 2011.
- [69] Yaoyao Zhang, Xiaobing Li, Da’an Liu, Qinhui Zhang, Wei Wang, Bo Ren, Di Lin, Xiangyong Zhao, and Haosu Luo. The compositional segregation, phase structure and properties of $\text{Pb}(\text{In}_{1/2}\text{Nb}_{1/2})\text{O}_3\text{-Pb}(\text{Mg}_{1/3}\text{Nb}_{2/3})\text{O}_3\text{-PbTiO}_3$ single crystal. *Journal of Crystal Growth*, 318(1):890–894, 2011.
- [70] Haosu Luo, Guisheng Xu, Haiqing Xu, Pingchu Wang, and Zhiwen Yin. Compositional homogeneity and electrical properties of lead magnesium niobate titanate single crystals grown by a modified Bridgman technique. *Japanese Journal of Applied Physics*, 39(9S):5581, 2000.
- [71] Ho-Yong Lee, Jong-Bong Lee, Tae-Moo Hur, and Dong-Ho Kim. Method for solid-state single crystal growth, June 19 2012. US Patent 8,202,364.
- [72] Yet-Ming Chiang, W David Kingery, and Dunbar P Birnie. *Physical ceramics: principles for ceramic science and engineering*. J. Wiley, 1997.
- [73] Shen J Dillon, Kaiping Tai, and Song Chen. The importance of grain boundary complexions in affecting physical properties of polycrystals. *Current Opinion in Solid State and Materials Science*, 2016.
- [74] Seongtae Kwon, Wesley S Hackenberger, Paul W Rehrig, J-B Lee, T-M Heo, DH Kim, and H-Y Lee. Solid state grain growth of piezoelectric single crystals. In *Applications of Ferroelectrics, 2004. ISAF-04. 2004 14th IEEE International Symposium on*, pages 153–156. IEEE, 2004.

- [75] HY Lee. Solid-state single crystal growth (SSCG) method: a cost-effective way of growing piezoelectric single crystals. *Piezoelectric Single Crystals and Their Application*, pages 160–77, 2004.
- [76] Patrick T King, Edward P Gorzkowski, Adam M Scotch, Derrick J Rockosi, Helen M Chan, and Martin P Harmer. Kinetics of $\{001\}$ $\text{Pb}(\text{Mg}_{1/3}\text{Nb}_{2/3})\text{O}_3$ -35mol% PbTiO_3 single crystals grown by seeded polycrystal conversion. *Journal of the American Ceramic Society*, 86(12):2182–2187, 2003.
- [77] SL Swartz and Thomas R Shrout. Fabrication of perovskite lead magnesium niobate. *Materials Research Bulletin*, 17(10):1245–1250, 1982.
- [78] MA Subramanian, G Aravamudan, and GV Subba Rao. Oxide pyrochlores—a review. *Progress in Solid State Chemistry*, 15(2):55–143, 1983.
- [79] M. Inada. *Japanese National Technical Report*, 23(1), 95, 1977.
- [80] R Yimnirun, X Tan, S Ananta, and S Wongsanmai. Preparation of fine-grain lead indium niobate ceramics with wolframite precursor method and resulting electrical properties. *Applied Physics A*, 88(2):323–328, 2007.
- [81] Linghang Wang, Shan Zhao, Li Jin, Fei Li, and Zhuo Xu. Effects of InNbO_4 fabrication on perovskite PIN-PMN-PT. *Journal of the American Ceramic Society*, 97(10):3110–3115, 2014.
- [82] Shujun Zhang, Jun Luo, Wesley Hackenberger, Nevin P Sherlock, Richard J Meyer Jr, and Thomas R Shrout. Electromechanical characterization of $\text{Pb}(\text{In}_{1/2}\text{Nb}_{1/2})\text{O}_3$ - $\text{Pb}(\text{Mg}_{1/3}\text{Nb}_{2/3})\text{O}_3$ - PbTiO_3 crystals as a function of crystallographic orientation and temperature. *Journal of Applied Physics*, 105:104506, 2009.
- [83] Guisheng Xu, Kai Chen, Danfeng Yang, and Junbao Li. Growth and electrical properties of large size $\text{Pb}(\text{In}_{1/2}\text{Nb}_{1/2})\text{O}_3$ - $\text{Pb}(\text{Mg}_{1/3}\text{Nb}_{2/3})\text{O}_3$ - PbTiO_3 crystals prepared by the vertical bridgman technique. *Applied physics letters*, 90(3):2901, 2007.
- [84] Xiaozhou Liu, Shujun Zhang, Jun Luo, Thomas R Shrout, and Wenwu Cao. Complete set of material constants of $\text{Pb}(\text{In}_{1/2}\text{Nb}_{1/2})\text{O}_3$ - $\text{Pb}(\text{Mg}_{1/3}\text{Nb}_{2/3})\text{O}_3$ - PbTiO_3 single crystal with morphotropic phase boundary composition. *Journal of applied physics*, 106:074112, 2009.

- [85] Shujun Zhang, Jun Luo, Wesley Hackenberger, and Thomas R ShROUT. Characterization of $\text{Pb}(\text{In}_{1/2}\text{Nb}_{1/2})\text{O}_3\text{-Pb}(\text{Mg}_{1/3}\text{Nb}_{2/3})\text{O}_3\text{-PbTiO}_3$ ferroelectric crystal with enhanced phase transition temperatures. *Journal of applied physics*, 104 (6):064106, 2008.
- [86] Supon Ananta and Noel W Thomas. A modified two-stage mixed oxide synthetic route to lead magnesium niobate and lead iron niobate. *Journal of the European Ceramic Society*, 19(2):155–163, 1999.
- [87] Supon Ananta, Rik Brydson, and Noel W Thomas. Synthesis, formation and characterisation of MgNb_2O_6 powder in a columbite-like phase. *Journal of the European Ceramic Society*, 19(3):355–362, 1999.
- [88] Wei Ji, Chee Kiang Ivan Tan, Kui Yao, Abdullah Al-Mamun, Charanjit S Bhatia, and Ten It Wong. Structural Evolution and Properties of $0.3\text{Pb}(\text{In}_{1/2}\text{Nb}_{1/2})\text{O}_3\text{-}0.38\text{Pb}(\text{Mg}_{1/3}\text{Nb}_{2/3})\text{O}_3\text{-}0.32\text{PbTiO}_3$ Ferroelectric Ceramics with Different Sintering Times. *Journal of the American Ceramic Society*, 97(10):3294–3300, 2014.
- [89] Edward F Alberta and Amar S Bhalla. Preparation of phase-pure perovskite lead indium niobate ceramics. *Materials Letters*, 29(1):127–129, 1996.
- [90] Shujun Zhang, Sung-Min Lee, Dong-Ho Kim, Ho-Yong Lee, and Thomas R ShROUT. Elastic, Piezoelectric, and Dielectric Properties of $0.71\text{Pb}(\text{Mg}_{1/3}\text{Nb}_{2/3})\text{O}_3\text{-}0.29\text{PbTiO}_3$ Crystals Obtained by Solid-State Crystal Growth. *Journal of the American Ceramic Society*, 91(2):683–686, 2008.
- [91] Zoran Samardžija, Jae-Ho Jeon, and Miran Čeh. Microstructural and compositional study of a bulk $\text{Pb}(\text{Mg}_{1/3}\text{Nb}_{2/3})\text{O}_3\text{-PbTiO}_3$ single crystal grown from a BaTiO_3 seed. *Materials characterization*, 58(6):534–543, 2007.
- [92] Seung Tae Lim, Tae Woo Kim, Su Gil Hur, Seong-Ju Hwang, Hyunwoong Park, Wonyong Choi, and Jin-Ho Choy. Effects of p-and d-block metal co-substitution on the electronic structure and physicochemical properties of InMO_4 (M= Nb and Ta) semiconductors. *Chemical physics letters*, 434(4):251–255, 2007.
- [93] Kakali Sarkar and Siddhartha Mukherjee. Synthesis, characterization and property evaluation of single phase MgNb_2O_6 by chemical route. *Journal of The Australian Ceramic Society Volume*, 52(2):32–40, 2016.

- [94] Mitsuyoshi MATSUSHIMA, Yoshihito TACHI, and Yosuke IWASAKI. Development of large diameter piezo-single crystal PMN-PT with high energy conversion efficiency. *JFE technical Report*, pages 46–51, 2005.
- [95] Guisheng Xu, Haosu Luo, Weizhuo Zhong, Zhiwen Yin, Haiqing Xu, Zhenyi Qi, and Ke Liu. Morphology and defect structures of novel relaxor ferroelectric single crystals $\text{Pb}(\text{Mg}_{1/3}\text{Nb}_{2/3})\text{O}_3\text{-PbTiO}_3$. *Science in China Series E: Technological Sciences*, 42(5):541–549, 1999.
- [96] Xinming Wan, Jie Wang, HLW Chan, CL Choy, Haosu Luo, and Zhiwen Yin. Growth and optical properties of $0.62\text{Pb}(\text{Mg}_{1/3}\text{Nb}_{2/3})\text{O}_3\text{-}0.38\text{PbTiO}_3$ single crystals by a modified Bridgman technique. *Journal of crystal growth*, 263(1): 251–255, 2004.
- [97] Linghang Wang, Zhuo Xu, Zhenrong Li, and Fei Li. Bridgman growth and thermal analysis of $\text{Pb}(\text{Mg}_{1/3}\text{Nb}_{2/3})\text{O}_3\text{-PbTiO}_3$ single crystals. *Materials Science and Engineering: B*, 170(1):113–116, 2010.
- [98] Ajmal Khan, Frank A Meschke, Tao Li, Adam M Scotch, Helen M Chan, and Martin P Harmer. Growth of $\text{Pb}(\text{Mg}_{1/3}\text{Nb}_{2/3})\text{O}_3\text{-}35\text{ mol\%PbTiO}_3$ Single Crystals from (111) Substrates by Seeded Polycrystal Conversion. *Journal of the American Ceramic Society*, 82(11):2958–2962, 1999.
- [99] Chang Eui Seo and Duk Yong Yoon. The Effect of MgO Addition on Grain Growth in PMN–35PT. *Journal of the American Ceramic Society*, 88(4):963–967, 2005.
- [100] Day J. G. Crystal growing from oxide melts - the choice of crucible materials. *Platinum Metals Rev.*, 7(2).
- [101] Xian Wang, Zhuo Xu, Zhenrong Li, Fei Li, Hongbing Chen, and Shiji Fan. Growth of the relaxor based ferroelectric single crystals $\text{Pb}(\text{In}_{1/2}\text{Nb}_{1/2})\text{O}_3\text{-Pb}(\text{Mg}_{1/3}\text{Nb}_{2/3})\text{O}_3\text{-PbTiO}_3$ by vertical Bridgman technique. *Ferroelectrics*, 401(1):173–180, 2010.
- [102] Guisheng Xu, Haosu Luo, Haiqing Xu, Zhenyi Qi, Pingchu Wang, Weizhuo Zhong, and Zhiwen Yin. Structural defects of $\text{Pb}(\text{Mg}_{1/3}\text{Nb}_{2/3})\text{O}_3\text{-PbTiO}_3$ single crystals grown by a Bridgman method. *Journal of crystal growth*, 222(1):202–208, 2001.

- [103] Chong E Chang and William R Wilcox. Control of interface shape in the vertical Bridgman-Stockbarger technique. *Journal of Crystal Growth*, 21(1):135–140, 1974.
- [104] Keigo Nagao and Erina Kagami. X-ray thin film measurement techniques VII. Pole figure measurement. *The Rigaku Journal*, 27(2):6–14, 2011.
- [105] Jun Luo. Bridgman Growth of $\langle 001 \rangle$ -Oriented 4in Diameter PIN-PMN-PT Piezoelectric Crystals. In *2016 Joint ISAF/ECAPD/PFM Conference, Darmstadt, Germany, August 2016*.
- [106] To Jasinski, WoMo Rohsenow, and AoFo Witt. Heat transfer analysis of the Bridgman-Stockbarger configuration for crystal growth: I. Analytical treatment of the axial temperature profile. *Journal of Crystal Growth*, 61(2):339–354, 1983.
- [107] Ta-Wei Fu and William R Wilcox. Influence of insulation on stability of interface shape and position in the vertical Bridgman-Stockbarger technique. *Journal of Crystal Growth*, 48(3):416–424, 1980.
- [108] K Echizenya and M Matsushita. Continuous feed growth and characterization of PMN-PT single crystals. In *Ultrasonics Symposium (IUS), 2011 IEEE International*, pages 1813–1816. IEEE, 2011.
- [109] M Matsushitata and K Echizenya. Continuous feeding growth of ternary PIN-PMN-PT single crystals. In *Applications of Ferroelectrics, International Workshop on Acoustic Transduction Materials and Devices & Workshop on Piezoresponse Force Microscopy (ISAF/IWATMD/PFM), 2014 Joint IEEE International Symposium on the*, pages 1–4. IEEE, 2014.
- [110] J. Tian, H. Pan, H. Marshall, P. Han, and S. Dynan. Growth of PMN-PT Based Single Crystals with Double Melt Approach. *2016 International Workshop on Acoustic Transduction Materials and Devices*, May 10-12,2016.
- [111] HL Bhat. *Introduction to Crystal Growth: Principles and Practice*. CRC Press, 2014.
- [112] Zibo Jiang. PMN-PT crystal of less defects and more uniformity. In *2015 Joint IEEE International Symposium on the Applications of Ferroelectrics, International Symposium on Integrated Functionalities and Piezoresponse Force Microscopy Workshop (ISAF/ISIF/PFM)*, pages 56–59. IEEE, 2015.

- [113] Richard E Chinn. *Ceramography: preparation and analysis of ceramic microstructures*. ASM International, 2002.
- [114] Tao Li, Suxing Wu, Ajmal Khan, Adam M Scotch, Helen M Chan, and Martin P Harmer. Heteroepitaxial growth of bulk single-crystal $\text{Pb}(\text{Mg}_{1/3}\text{Nb}_{2/3})\text{O}_3$ -32mol% PbTiO_3 from (111) SrTiO_3 . *Journal of materials research*, 14(08): 3189–3191, 1999.
- [115] Yudong Hou, Mankang Zhu, Feng Gao, Hao Wang, Bo Wang, Hui Yan, and Changsheng Tian. Effect of MnO_2 addition on the structure and electrical properties of $\text{Pb}(\text{Zn}_{1/3}\text{Nb}_{2/3})_{0.20}(\text{Zr}_{0.50}\text{Ti}_{0.50})_{0.80}\text{O}_3$ ceramics. *Journal of the American Ceramic Society*, 87(5):847–850, 2004.
- [116] Juan Jiang, Hyun-June Jung, and Soon-Gil Yoon. Epitaxial PMN–PT thin films grown on buffered Si substrates using ceramic and single-crystal targets. *Journal of Alloys and Compounds*, 509(24):6924–6929, 2011.
- [117] Xiaobing Li, Xiangyong Zhao, Bo Ren, Haosu Luo, Wenwei Ge, Zheng Jiang, and Shuo Zhang. Microstructure and dielectric relaxation of dipolar defects in Mn-doped $(1-x)\text{Pb}(\text{Mg}_{1/3}\text{Nb}_{2/3})\text{O}_3$ - $x\text{PbTiO}_3$ single crystals. *Scripta Materialia*, 69(5):377–380, 2013.
- [118] Hongliang Du, Zhibin Pei, Wancheng Zhou, Fa Luo, and Shaobo Qu. Effect of addition of MnO_2 on piezoelectric properties of PNW–PMS–PZT ceramics. *Materials Science and Engineering: A*, 421(1):286–289, 2006.
- [119] Xia Zhao, Wei Chen, Lixue Zhang, Jinghui Gao, and Lisheng Zhong. Effect of fabrication routes on the microstructure, the dielectric and ferroelectric properties of the Mn-doped BaTiO_3 ceramics. *Applied Physics A*, 118(3):931–938, 2015.
- [120] Gang Liu, Shujun Zhang, Wenhua Jiang, and Wenwu Cao. Losses in ferroelectric materials. *Materials Science and Engineering: R: Reports*, 89:1–48, 2015.
- [121] Shujun Zhang, Nevin P Sherlock, Richard J Meyer Jr, and Thomas R Shrout. Crystallographic dependence of loss in domain engineered relaxor-PT single crystals. *Applied physics letters*, 94(16), 2009.
- [122] Lingping Kong, Gang Liu, Shujun Zhang, and Haozhe Liu. The role of tetragonal side morphotropic phase boundary in modified relaxor- PbTiO_3 crystals

- for high power transducer applications. *Journal of Applied Physics*, 114(14): 144106, 2013.
- [123] Limei Zheng, Raffi Sahul, Shujun Zhang, Wenhua Jiang, Shiyang Li, and Wenwu Cao. Orientation dependence of piezoelectric properties and mechanical quality factors of $0.27\text{Pb}(\text{In}_{1/2}\text{Nb}_{1/2})\text{O}_3$ - $0.46\text{Pb}(\text{Mg}_{1/3}\text{Nb}_{2/3})\text{O}_3$ - 0.27PbTiO_3 :Mn single crystals. *Journal of Applied Physics*, 114(10):104105, 2013.
- [124] D Hennings and H Pomplun. Evaluation of lattice site and valence of Mn and Fe in polycrystalline PbTiO_3 by electron spin resonance and thermogravimetry. *Journal Of The American Ceramic Society*, 57(12):527–530, 1974.
- [125] VV Klimov, NI Selikova, and AN Bronnikov. Effect of MnO_2 , Bi_2O_3 , and ZnO additions on the electrical properties of lead zirconate titanate piezoceramics. *Inorganic materials*, 42(5):573–577, 2006.
- [126] Eric Boucher, Benoit Guiffard, Laurent Lebrun, and Daniel Guyomar. Effects of Zr/Ti ratio on structural, dielectric and piezoelectric properties of Mn- and (Mn, F)-doped lead zirconate titanate ceramics. *Ceramics international*, 32(5): 479–485, 2006.
- [127] L Eyraud, P Eyraud, L Lebrun, B Guiffard, E Boucher, D Audigier, and D Guyomar. Effect of (Mn, F) co-doping on PZT characteristics under the influence of external disturbances. *Ferroelectrics*, 265(1):303–316, 2002.
- [128] U Robels, JH Calderwood, and G Arlt. Shift and deformation of the hysteresis curve of ferroelectrics by defects: An electrostatic model. *Journal of applied physics*, 77(8):4002–4008, 1995.
- [129] U Robels, L Schneider-Störmann, and G Arlt. Dop234: Domain wall trapping as a result of internal bias fields. *Ferroelectrics*, 133(1):223–228, 1992.
- [130] Lian-Xing He and Cheng-En Li. Effects of addition of MnO on piezoelectric properties of lead zirconate titanate. *Journal of materials science*, 35(10):2477–2480, 2000.
- [131] Christopher M Beck, Noel W Thomas, and Ian Thompson. Manganese-doping of lead magnesium niobium titanate: Chemical control of dielectric properties. *Journal of the European Ceramic Society*, 18(12):1685–1693, 1998.

- [132] Robert C. Weast. *Handbook of Chemistry and Physics (65th Edition)*.
- [133] MD Glinchuk, IP Bykov, VM Kurliand, M Boudyš, T Kala, and K Nejezchleb. Valency states and distribution of manganese ions in PZT ceramics simultaneously doped with Mn and Nb. *physica status solidi (a)*, 122(1):341–346, 1990.
- [134] L Amarande, C Miclea, M Cioangher, MN Grecu, I Pasuk, and RF Negrea. Influence of co-dopants average valence on microstructural and electromechanical properties of lead titanate ceramics. *Journal of the European Ceramic Society*, 34(5):1191–1200, 2014.
- [135] E Boucher, D Guyomar, L Lebrun, B Guiffard, and G Grange. Effect of (Mn, F) and (Mg, F) co-doping on dielectric and piezoelectric properties of lead zirconate titanate ceramics. *Journal of applied physics*, 92(9):5437–5442, 2002.
- [136] SB Desu and EC Subbarao. Effect of oxidation states of Mn on the phase stability of Mn-doped BaTiO₃. *Ferroelectrics*, 37(1):665–668, 1981.
- [137] Toshio Kamiya, Toshimasa Suzuki, Takaaki Tsurumi, and Masaki Daimon. Effects of manganese addition on piezoelectric properties of Pb(Zr_{0.5}Ti_{0.5})O₃. *Japanese journal of applied physics*, 31(9S):3058, 1992.
- [138] Baoshan Li, Zhigang Zhu, Guorong Li, and Aili Ding. Microstructure and electromechanical properties in PMnN-PZT ceramics sintered at different temperatures. *Journal of Materials Science and Technology*, 21(3), 2005.
- [139] T Izaki, H Haneda, A Watanabe, and Y Uchida. Effects of Mn ions on the piezoelectric property of PLZT. *SUMITOMO METALS*, 45:46–46, 1993.
- [140] Bryant Peter. Personal communication, 2015.
- [141] U Robels, Ch Zadon, and G Arlt. Dip219: Linearization of dielectric nonlinearity by internal bias fields. *Ferroelectrics*, 133(1):163–168, 1992.
- [142] Rainer Schmidt. Impedance spectroscopy of electroceramics. *Ceramic Materials Research Trends*, page 321, 2007.
- [143] J Ross Macdonald and E Barsoukov. Impedance spectroscopy: theory, experiment, and applications. *History*, 1(8), 2005.
- [144] JP Diard, B Le Gorrec, and C Montella. Handbook of electrochemical impedance spectroscopy. *Diffusion Impedances*. [www. bio-logic. info/potentiostat/notes. html](http://www.bio-logic.info/potentiostat/notes.html), 2012.

- [145] SA Ktitorov. Determination of the relaxation time distribution function from dielectric losses. *Technical Physics Letters*, 29(11):956–958, 2003.
- [146] John TS Irvine, Derek C Sinclair, and Anthony R West. Electroceramics: characterization by impedance spectroscopy. *Advanced Materials*, 2(3):132–138, 1990.
- [147] Rüdiger-A Eichel. Structural and dynamic properties of oxygen vacancies in perovskite oxides—analysis of defect chemistry by modern multi-frequency and pulsed EPR techniques. *Physical Chemistry Chemical Physics*, 13(2):368–384, 2011.
- [148] Rotraut Merkle and Joachim Maier. Defect association in acceptor-doped SrTiO_3 : case study for $\text{Fe}'_{\text{Ti}}\text{V}_\text{O}^{\bullet\bullet}$ and $\text{Mn}'_{\text{Ti}}\text{V}_\text{O}^{\bullet\bullet}$. *Physical Chemistry Chemical Physics*, 5(11):2297–2303, 2003.
- [149] Donald Morgan Smyth. The defect chemistry of metal oxides. *The Defect Chemistry of Metal Oxides*, by DM Smyth, pp. 304. Foreword by DM Smyth. Oxford University Press, Jun 2000. ISBN-10: 0195110145. ISBN-13: 9780195110142, 1, 2000.
- [150] MR Shoar Abouzari, F Berkemeier, G Schmitz, and D Wilmer. On the physical interpretation of constant phase elements. *Solid State Ionics*, 180(14):922–927, 2009.